Light-driven Microswimmers and Their Applications

Von dem Stuttgarter Zentrum für Simulationswissenschaften (SC SimTech) der Universität Stuttgart zur Erlangung der Würde eines Doktor-Ingenieurs (Dr.-Ing.) genehmigte Abhandlung

Vorgelegt von

Varun Sridhar

aus Anthiyur (Indien)

Hauptberichter: Prof. Dr. Metin Sitti

Mitberichter: Prof. Dr. Christian Holm

Mitberichter: Prof. Dr. Wei Gao

Tag der mündlichen Prüfung: 20. Juli 2021

Max-Planck-Institut für Intelligente Systeme

2021

Acknowledgements

This dissertation would not have been possible without the numerous amazing people that I had the wonderful opportunity of working with. First of all, I would like to thank my advisor Prof. Metin Sitti for giving me a wonderful opportunity to work in the Physical Intelligence Department at the Max Planck Institute for Intelligent Systems, Stuttgart. I thank him very much for his warm support, guidance and freedom to peruse my research. Without his guidance throughout the dissertation it would not have been possible. I would like to thank Max Planck Society for funding this dissertation. I also like to thank Prof. Frank Allgöwer for helping me initially and being my co-supervisor. I am grateful to Prof. Christian Holm and Prof. Wei Gao for serving on my thesis committee and for all their guidance.

My heartfelt gratitude goes to Dr. Byung-Wook Park for his mentorship and his guidance through the initial phases of my PhD. Without whose guidance and help this PhD would have definitely not been possible. It was a great pleasure working with you and I was fortunate to had the chance to work with you. Thank you for all your wonderful advices throughout my PhD for my research and my personal development and for listening patiently and brainstorming endless ideas and projects.

I am very much indebted to my long-term collaborators Dr. Filip Podjaski, Julia Kröger, Vio Duppel, Dr. Alberto Jiménez-Solano and Prof. Bettina Lotsch for establishing such a fruitful collaboration without which this dissertation would not have been possible. Thank you, Filip, for all your wonderful ideas, suggestions and broadening my horizon on research.

I would like to thank my research collaborators from Physical Intelligence (PI) Department, Dr. Yunus Alpan, Dr. Joshua Giltinan, Ugur Bozuyuk, Devin Sheehan, Dr. Yan Yu, Dr. Vimal Kishore. Our TEM collaborators Dr. Surong Guo, Kersten Hahn and Prof. Peter A. van Aken and all our technical staff for always being very helpful.

I want to thank all my fellow colleagues who made my time at Physical Intelligence department very memorable, I had some of the best time in my life in company of such brilliant people, especially Muhammad Yunusa, Dr. Donghoon Son, Dr. Abdon Pena-Francesch, Dr. Guillermo Amado, Chantal Goettler, Dr. Ville Limatainen, Dr. Madhu Batuwangala, Dr. Hamed Shahsavan, Dr. Zoey Davidson, Dr. Utku Culha, Dr. Oncay Yasa, Dr. Immihan Ceren

Yasa, Gaurav Gardi, Alp Can Karacakol, Martin Phelan, my office maters Yunwoo Lee, Hyun Gyu Kim and all the other PI members and my other colleagues from other groups at MPI IS.

Last but not the least, I am very grateful to my family for their ceaseless support during my PhD, my parents S Sridhar and P Jayanthi, my uncle Ravi Palaniswamy who has always been my inspiration for research since my childhood. My amazing friends who have always been there for me throughout, Anbu Malar, Maheshwar, Sri Muthu Narayanan, Sai Prashanthi, Bharathi, Saravana Balaji, Vivek, Siva Shankar, Adthiya Bandla, Divya Bharathi, Poorani, Nivedita, Nivedha, Nikila, Nisha and all my wonderful friends here at Stuttgart for making Stuttgart an exciting place to be in. Special thanks to my fiancé Dr. Kaviya Mohankumar who has been my pillar of support, an endless source of love and motivation and for patiently listening to me always.

Abstract

Light-driven microswimmers have garnered attention for their potential use in various applications such as environmental remediation and targeted drug delivery. Most of the early development has been on the investigation of new materials, the overall swimming mechanism and the necessary control of the microswimmers. Within the domain of light-driven microswimmers, photocatalytic microswimmers have been at the forefront due to the ability to adapt already available photocatalytic materials. In this dissertation, we have advanced the field of light-driven microswimmers by introducing three new types of materials and designs. We have developed material versatility by utilizing both inorganic and organic synthetic materials for their application to light-driven microswimmers. The new designs used for swimming allowed for faster propulsion of light-driven microswimmers under low intensity UV and visible light. We demonstrated the use of a hollow mesoporous TiO_2 microswimmer that swims much faster than a solid TiO_2 microswimmer. The use of a mesoporous structure which has a large surface area, allows for faster swimming and ability to load drugs like Doxorubicin, an anti-cancer drug. The microswimmers also show enhanced environmental remediation due to the faster propulsion of the hollow mesoporous Janus TiO_2-Au microswimmer. We also present the use of a visible light responsive CoO-TiO_2 microswimmer that swims in low visible light illumination without the need for any external fuels. The microswimmers show visible light activity over a range of wavelengths. This multi-responsiveness allows for wavelength steering of the microswimmers in addition to the magnetic steering enabled by their inherent magnetic property. Finally, we demonstrate Poly(heptazine imide) (PHI), a 2D carbon nitride material for the use as swimmers, they show efficient propulsion in aqueous media not only during but after illumination creating a solar battery swimming in dark. The mechanism of propulsion is also investigated in depth for different cap structures and different fuels. The PHI based microswimmers without the presence of any cap structures display propulsion in different ionic and biological media and cellular environments, such as diluted blood, without requiring additional fuels. the swimmers can be loaded with a model cancer drug, doxorubicin (DOX), in large amounts (185% loading efficiency) without any passive release. Controlled drug release on demand is demonstrated in different pH conditions and can be triggered also by illumination while being sensitive to oxygen concentrations. Hence, through this thesis we demonstrate the use of novel photocatalytic materials for design and fabrication of light-driven microswimmers. Novel applications such as environmental remediation, drug loading and

delivery have been demonstrated using light-driven microswimmers; this would allow for the use of light-driven microswimmers in biomedical and theranostic applications.

Zusammenfassung

Lichtgetriebene Mikroschwimmer haben aufgrund ihrer Einsatzmöglichkeiten in verschiedenen Anwendungsbereichen, wie z. B. in der Umweltsanierung, der Wasserstoffentwicklung und der gezielten Medikamentenabgabe, viel Aufmerksamkeit erregt. Die meisten der frühen Entwicklungen auf dem Gebiet der Mikroschwimmer zeigten sich bei der Erforschung neuer Materialien, der Weiterentwicklung des Schwimmmechanismus und bei der erforderlichen Steuerung der Mikroschwimmer. Bei lichtgetriebenen Mikroschwimmern standen photokatalytische Mikroschwimmer im Vordergrund, da sie die Fähigkeit besitzen, bereits verfügbare photokatalytische Materialien an ihre Bedürfnisse anzupassen.

In dieser Dissertation haben wir das Gebiet der lichtgetriebenen Mikroschwimmer mithilfe der Einführung von drei neuen Materialtypen und Designs weiterentwickelt. Hierbei haben wir unseren Entwicklungsfokus auf die Vielseitigkeit der Materialien gelegt und bei lichtgetriebenen Mikroschwimmern sowohl anorganische als auch organische synthetische Materialien eingesetzt. Die drei neuen Designs zur Weiterentwicklung der Schwimmfunktion ermöglichten einen schnelleren Antrieb der lichtgetriebenen Mikroschwimmer unter UV- und sichtbarem Licht niedriger Intensität. Wir demonstrierten den Einsatz eines hohlen mesoporösen TiO_2-Mikroschwimmers, der viel schneller schwimmen kann als ein fester TiO_2-Mikroschwimmer. Das schnellere Schwimmen wird durch die mesoporöse Struktur mit ihrer großen Oberfläche ermöglicht. Zudem kann der Mikroschwimmer mit Medikamenten wie Doxorubicin, einem gängigen Chemotherapeutikum, beladen werden. Aufgrund der schnelleren Fortbewegung des hohlen mesoporösen Janus TiO_2-Au Mikroschwimmers werden außerdem deutlich bessere Ergebnisse in der Umweltsanierung erzielt. Ebenfalls präsentieren wir den Einsatz eines auf sichtbares Licht ansprechenden CoO-TiO_2-Mikroschwimmers, der bei schwacher Beleuchtung mit sichtbarem Licht schwimmt, ohne dass externe Brennstoffe benötigt werden. Die Mikroschwimmer zeigen sichtbare Lichtaktivität über einen Bereich von Wellenlängen. Diese Multi-Reaktivität ermöglicht eine Wellenlängensteuerung der Mikroschwimmer zusätzlich zur magnetischen Steuerung, die wiederum aufgrund ihrer inhärenten magnetischen Eigenschaft ermöglicht wird.

Schließlich demonstrieren wir den Einsatz von Poly(heptazinimid) (PHI), einem 2D-Kohlenstoffnitrid-Material, als Schwimmer. PHI-basierte Schwimmer zeigen einen effizienten Antrieb in wässrigen Medien nicht nur während, sondern auch nach der Beleuchtung, wodurch

eine im Dunkeln schwimmende Solarbatterie entsteht. Der Mechanismus des Vortriebs wird auch für verschiedene Kappenstrukturen und unterschiedliche Treibstoffe eingehend untersucht. Die PHI-basierten Mikroschwimmer ohne jegliche Kappenstrukturen zeigen Vortrieb in verschiedenen ionischen und biologischen Medien und zellulären Umgebungen, wie z.B. verdünntem Blut, ohne zusätzliche Treibstoffe zu benötigen. Diese Schwimmer können mit Doxorubicin (DOX), einem Modell-Chemotherapeutikum, in großen Mengen (185% Beladungseffizienz) ohne jegliche passive Freisetzung beladen werden. Die kontrollierte Wirkstofffreisetzung bei Bedarf wird unter verschiedenen pH-Bedingungen demonstriert und kann auch durch Beleuchtung ausgelöst werden, wobei sie jedoch von Sauerstoffkonzentrationen empfindlich beeinflusst wird.

In dieser Arbeit werden neuartige photokatalytische Materialien für das Design und die Herstellung von lichtgetriebenen Mikroschwimmern eingesetzt. Neuartige Einsatzgebiete wie Umweltsanierung sowie Medikamentenbeladung und -abgabe wurden aufgezeigt und der Einsatz von lichtgetriebenen Mikroschwimmern in biomedizinischen und theranostischen Anwendungen als vorteilhaft und nutzbringend demonstriert.

Table of Contents

List of Figures

Especially for the element with unit mass 148, it cannot be excluded that other educts present in DMEM contribute to its formation. 160

List of Tables

Chapter 1. Introduction

1.1 Introduction to microswimmers

The idea of microswimmers or micromotors/microrobots as they have been called, is to perform a variety of functions such as delivery drugs, remove clots or perform microsurgeries within the body or in other applications such as environmental remediation of pollutants [1-4]. These ideas have been romanticized in many science fiction novels, including Issac Asimov's novels and movies such as Fantastic Voyage, a 1960s movie, which has been the inspiration for many microswimmers researchers. The initial road map to this was conceived by Prof. Feynman in his seminal lecture on nanotechnology "There's Plenty of Room at the Bottom" in 1959 [5]. The term 'swallowing the surgeon' was coined to show the potential of microswimmers and microrobotics for applications inside the body. Robotics in general refers to large scale robots in tens of centimetres, which limits their access inside the body and also on the functions they can perform [6]. Microswimmers or micromotors refers to small scale objects in the 100s of nanometers to 100s of microns [7]. These micron scale objects are capable of performing various functions such as drug delivery, environmental sensing and remediation [8]. The small size of the microswimmers allows access to various parts of the body such as blood vessels and other narrow regions of the body where large-scale robots cannot access. They are in contrast to traditional robots which are large in size and cannot access various regions of the body and for other environmental remediation [9]. The interest in microswimmers has been growing constantly as there is a large focus on current research to improve and increase the quality of life. This creates the need for improved detection and cure of life-threatening diseases even before they become a threat [10]. It also allows for creation of patient specific medicine which has become the need of the hour [11]. In order to propel and navigate these micron scale objects, different kind of propulsion strategies are followed, their size also adds additional limitations by the amount of fuel they can carry, resulting in different kinds of propulsion mechanisms to move the swimmers [12]. The predominantly used mechanisms of propulsion are magnetic, chemical propelled, enzyme driven, thermal propulsion, Marangoni effect, ultrasonic and light driven propulsion of the swimmers [8, 13].

In terms of the materials used for swimming, they can be classified as artificial and biohybrid microswimmers. In the case of biological materials, different kinds are used; the chief among them are bacteria, spermatozoa, algae, red blood cells and macrophages. They can

be further made into biohybrids by the addition of synthetic materials to improve their control or cargo carrying ability [14, 15]. The advantage that biohybrids have over other forms of propulsion is that, biological organisms like bacteria or spermatozoa have their own propulsion fuels and sensing mechanisms which provide advantageous [16]. They can be further functionalized to carry cargo and target cellular interactions by engineering them [17]. To have microswimmers and microrobots navigate successfully throughout the body there is a need to incorporate sensing, navigation through computational control and onboard fuels to propel them [18]. Biohybrid microswimmer provides this advantage [19]. Synthetic microswimmers are created from various materials available, both natural and artificial, taking advantage of the enormous strides made in materials science and nanotechnology. Synthetic microswimmers can be driven by self-propulsion, due to fuel reactions taking place on the surface [13]. They make use of the fuel in their surroundings and are self-propelled [20]. Self-propelled microswimmers can be driven by a variety of mechanisms such as self-diffusiophoresis, electrophoresis, thermophoresis and bubble-based propulsion [21, 22]. Self-propelled microswimmers offer many advantages, in that they make effective use of the fuels in the environment around them making them attractive for various application [23]. However, on the other hand, some of them use toxic fuels which make them incompatible for their use in biological systems [24]. Synthetic microswimmers can also be propelled by the use of an external fields like magnetic, electric or acoustic fields [8]. The biggest advantage of the use of such external fields is their ability to precisely navigate the microswimmers effectively to the desired areas without the need for any external fuels [25]. The disadvantage of this type of propulsion is the global nature of the fields that are applied, which sometimes are not compatible for all the biomedical or environmental applications. Hence, it would be effective to use self-propelled microswimmers which do not use any toxic fuels and can be steered by the use of external fields like magnetic or acoustic fields [26]. The steering does not require huge global fields hence making them compatible with multiple biomedical applications [26].

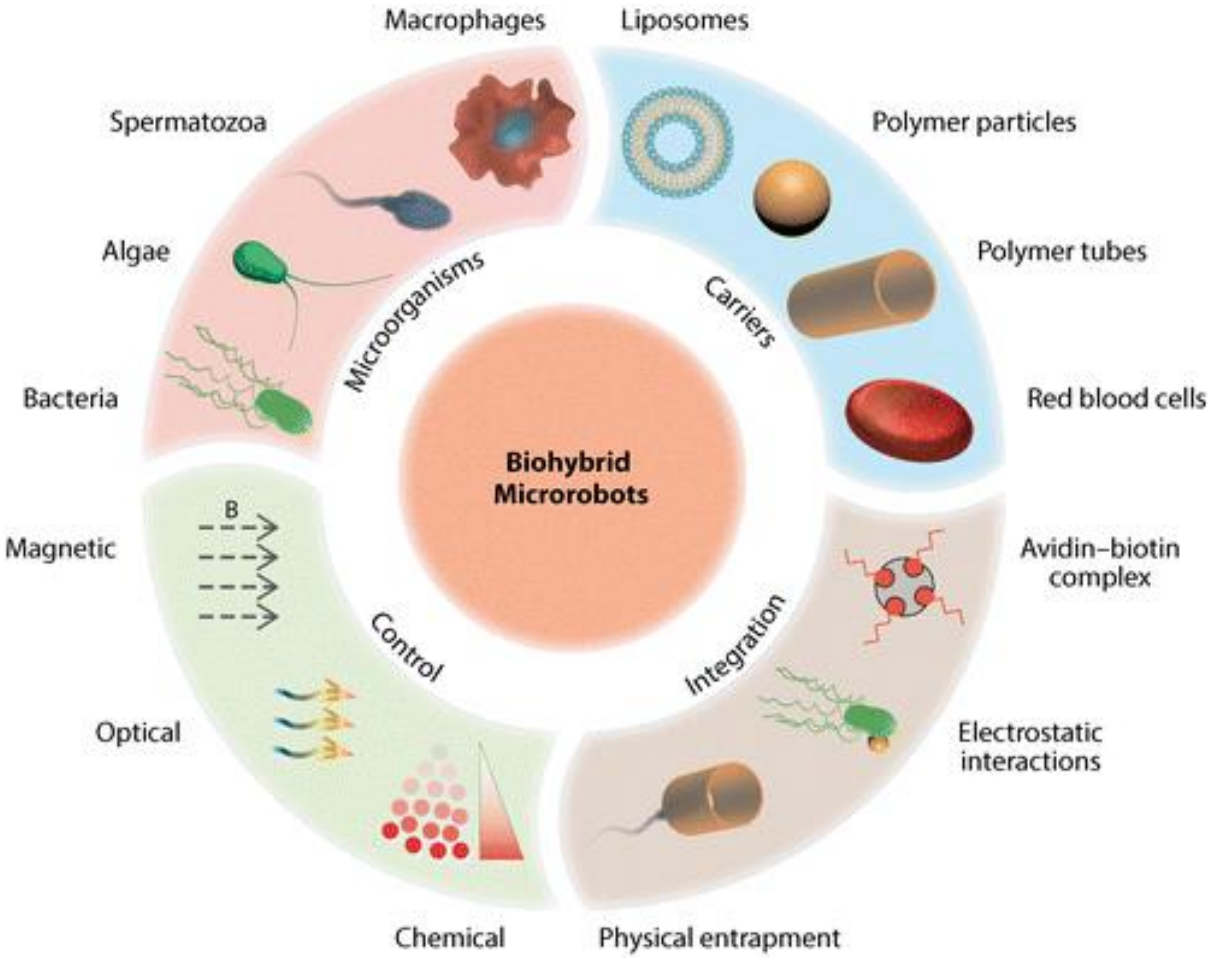

Figure 1.1 Different kinds of design, fabrication and control of biohybrid microswimmers. Reproduced from reference [15].

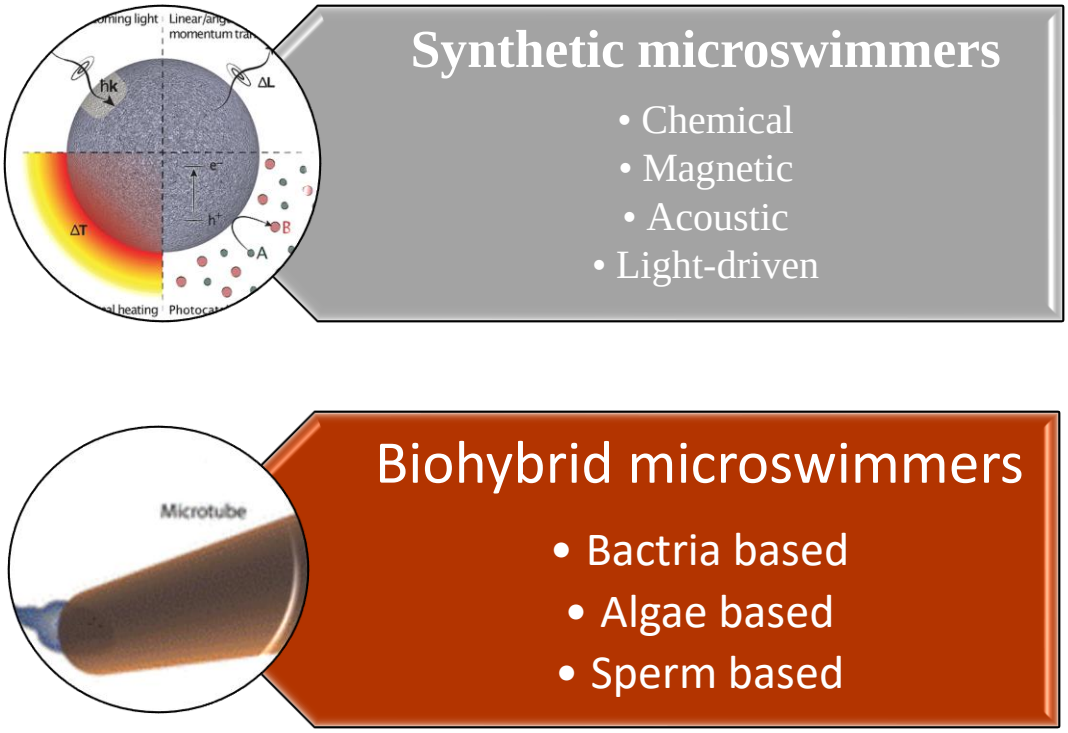

Figure 1.2 Classification of microswimmers into synthetic and biohybrid microswimmers.

1.2 Life at low Reynolds number

Unlike macroscale objects like humans or other swimmers like submarines, swimming in micro scale is very different [27]. In the micro and nano scale, the viscous forces play a more dominating role than the inertial forces, also the scaling law between micro and macro scale are different [28]. To gain an intuitive understanding on how swimming at micro and macro scales differ, imagining humans swimming in a pool of starch, the viscous forces would be very strong preventing our normal swimming strokes, resulting in us staying in the same position irrespective of how fast we move [28, 29]. The dimensional less quantity which governs the swimming in micro scale is called Reynolds number (*Re*) [30]. Reynolds number, which is a dimensionless quantity, is given by the ratio of inertial forces to viscous forces. It is given by the equation as below.

$$R_e = \frac{\rho \upsilon L}{\mu} \tag{1}$$

Where ρ is the density of medium, U is the velocity of the microswimmers, L is the characteristic linear dimension and μ is the dynamic viscosity of the medium. The Reynolds number is determined by the fluid and the dimensions of the swimmers [31]. In the case of a human swimming in water, the Reynolds number is 10^4 , whereas the Reynolds number of a

bacteria swimming in water is 10^{-4}. Most microswimmers, swim in water and hence have a Reynolds number around 10^{-4}. When Reynolds number is less than 2000, the microswimmers experience laminar flow around them [31]. The flows governing swimming in low Reynolds number was explored by Purcell in his seminal lecture on life at low Reynolds number in 1971 [28]. Under low Reynolds number conditions, the stokes equation is given by

$$\nabla p = \eta \nabla 2U + f \tag{2}$$

Where p is the pressure, U is the velocity field of the fluid, and f is the external forces on the fluid. From the equation, it can be observed that there are no inertial time dependent terms, hence the flows around the swimmer are reversible. Scallops theorem by Purcell, gave a roadmap on the conditions that are needed for the microswimmers to swim in medium. The primary condition is that, the motion of the swimmer at that instant is governed by the force is exerted at the exact instant, inertia does not play any role in the swimming. This means that constant forces are required for the propulsion of the microswimmers [28, 31]. The other condition governed by the Scallops theorem is that reciprocal motion does not produce any net motion. Hence, non-reciprocal motion is needed for the propulsion of the microswimmers. These constrains play an important role in the designing of the microswimmers for their applications. Different kinds of propulsion methods can be used to break the symmetry and make the microswimmers swim which are discussed in the later chapters.

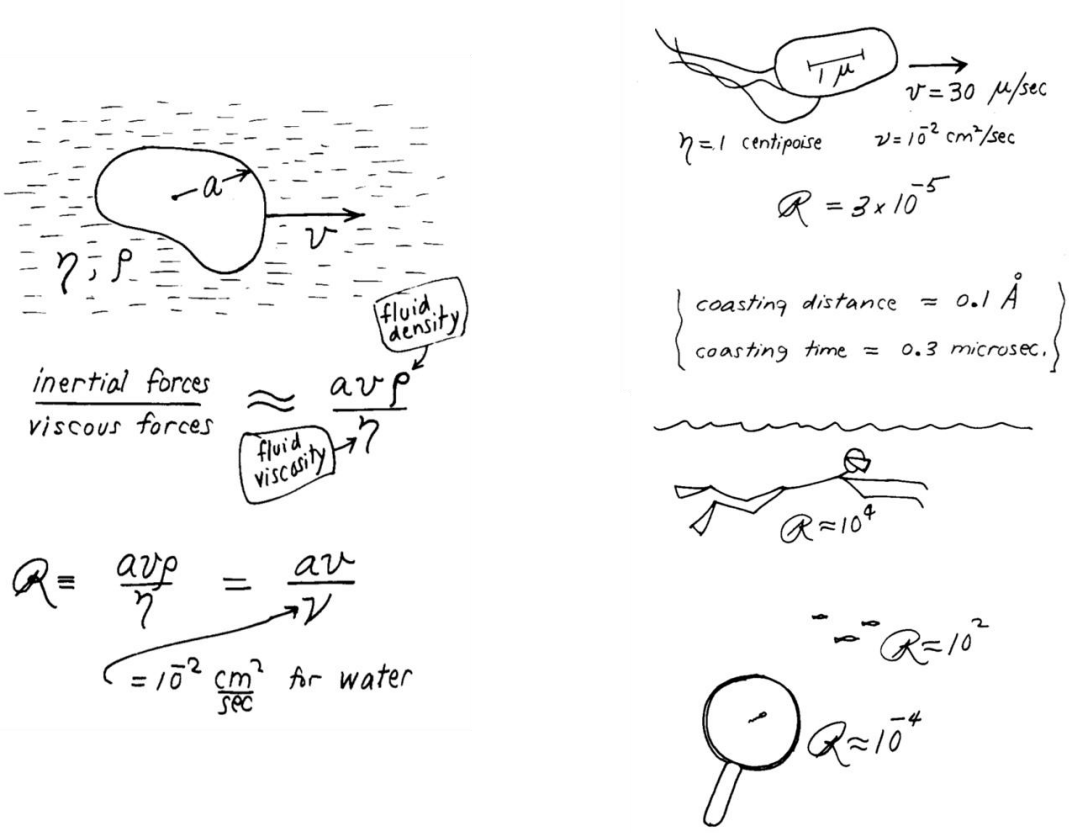

Figure 1.3 Typical life at low Reynolds number as illustrated by Purcell. Reproduced from reference [28].

1.3 Propulsion methods for microswimmer

Synthetic microswimmers can be propelled by a variety of propulsion methods such as, chemical, magnetic, acoustic and light as a fuel for propulsion [20]. One of the early microswimmers that were developed where the chemically propelled microswimmers.

1.3.1 Chemical propulsion

Chemically propelled microswimmers make use of a of catalyst, which converts fuel that converts chemical energy to mechanical energy for propulsion [8]. Different kinds of catalytic materials have been developed for the use in microswimmers. Pt was one of the initial materials that was used for chemical propulsion of microswimmers [32]. Pt chemically decomposes hydrogen peroxide (H_2O_2), the resultant products help in the propulsion of the swimmers by diffusiophoresis or electrophoresis or bubble formation [33-35]. H_2O_2 has been one of the most explored fuels for the propulsion of microswimmers [20]. The ease of decomposition allows for faster propulsion of the microswimmers, some of the highest speeds recorded in literature have been observed for H_2O_2 based microswimmers [36, 37]. Different symmetries and shapes for the Pt based microswimmers have been developed for swimming, based on the shape and

the area covered by Pt, the mechanism of swimming changes [34], enabling the exploration of different mechanisms for swimming [38]. Spherical and rod shape microswimmers are propelled through diffusiophoresis and electrophoresis, tubular structures are propelled by O_2 bubbles generation [39]. Though they are versatility for swimming, H_2O_2 fueled microswimmers suffer from a major drawback due to the toxicity of the H_2O_2. H_2O_2 is toxic to cells and organs, this limits their potential application in in vivo and medical applications [18].

In order to improve the biocompatibility of chemically propelled swimmers, different kinds of biocompatible chemical reactions are used. Among them, the reaction of magnesium with water producing hydrogen gas bubbles or using calcium carbonate in acidic conditions forming CO_2 gas bubble [40, 41]. They are used in certain vivo applications where the formation of gas bubbles does not cause any harm [22]. Magnesium based swimmers have shown drug delivery applications in stomach and Gastrointestinal tracts [17]. Different shapes and designs of the swimmers have been tested to make them more active [42]. However, they suffer from the disadvantage that gas bubbles cannot be used in circulatory system or parts which have access to the circulatory system.

Enzyme-based microswimmers are another class of chemically propelled microswimmers. They make use of the reaction of enzymes along with biocompatible fuel in their environment [43]. The high activity of the enzymes allows for the faster propulsion of the swimmers. The most commonly used enzymes for the propulsion or glucose oxidase, urease and catalase [23]. There are two classes of enzyme-based micro swimmers, the first among them was developed by Sanchez et al [44]. where they immobilized an enzyme on hollow mesoporous silica nanoparticles [45]. These enzymes then react with biocompatible fuels like urea leading to the formation of ammonia which propels the swimmers. Other works have also shown that enzymes can be mobilized on other materials like carbon nanotubes and tubular micro swimmers. The second class of enzyme-based micro swimmers were developed by Sen et al [46]. in which the enzyme by itself is used as a swimmer when they react with fuel is in the environment [47]. This method allows for chemotactical control of the microswimmers [48].

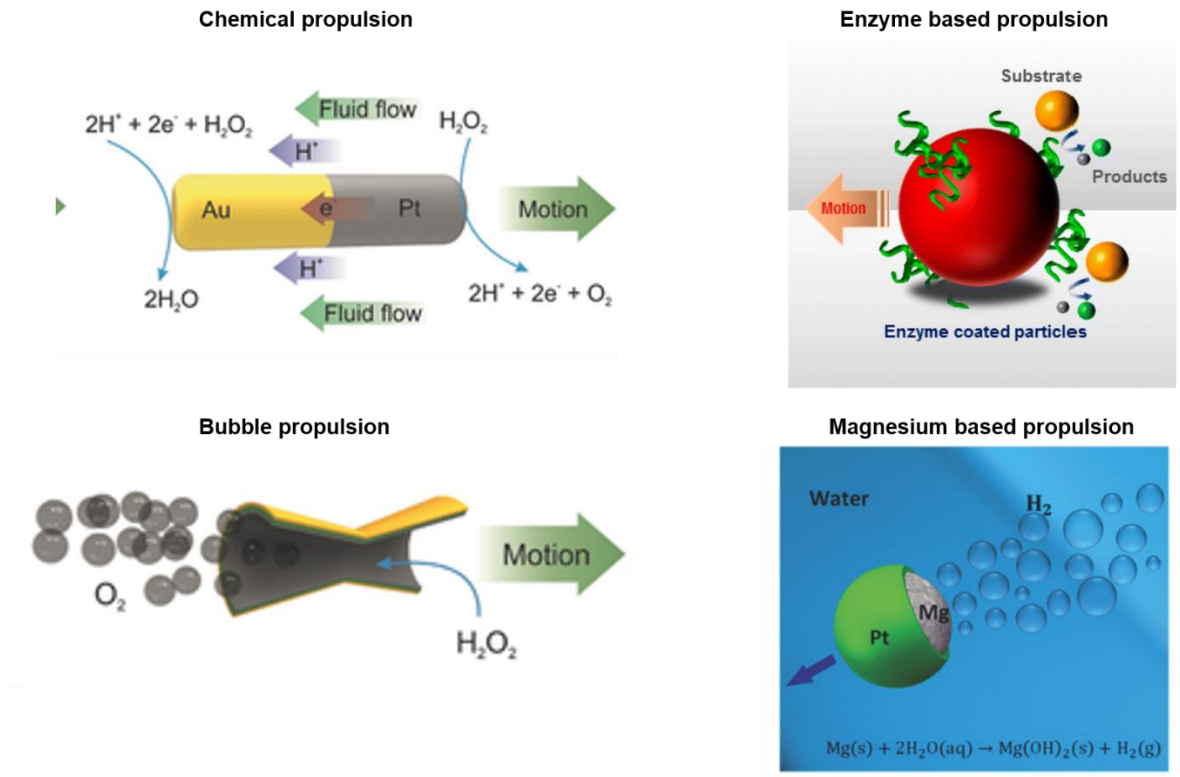

Figure 1.4 Figure showing schematic of chemical, bubble propelled, enzymatic and magnesium-based propulsion. Reproduced from references [49, 50].

1.3.2 Magnetic propulsion

Magnetic field-based microswimmers make use of the magnetic energy and transform it into mechanical energy which is available in the form of magnetic field gradient in magnetic talk to propel the microswimmers [51]. Magnetic microswimmers have the advantage that, magnetic fields of lower intensity do not harm living organisms. The magnetic field is needed for propulsion of the microswimmers is smaller hence they allow for use of magnetic microswimmers in in vivo applications [8]. The magnetic force and magnetic torque on a magnetic microswimmer is given by [52]

$$F = V(M.\nabla)B \quad (3)$$

$$T = VM \times B \quad (4)$$

Where, *V* is the volume of the object, *M* the magnetization and *B* is the magnetic flux density. To get a continuous motion of the magnetic object, the magnetic field varies spatially or temporally.

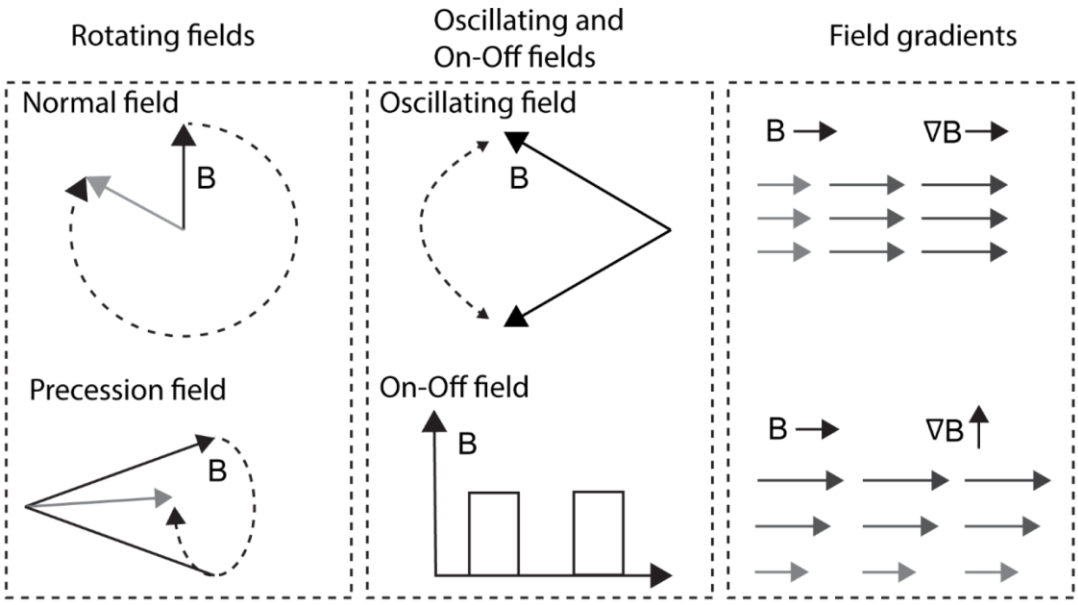

Figure 1.5 Magnetic field- and magnetic gradient-based magnetic actuation methods for magnetic microrobots. Reproduced from reference [52].

The different ways of applying the fields are rotating, oscillating, pulsed and gradient magnetic fields [8]. The type of the field being used influences the target application and the design of the microswimmers [53]. One of the most often used structures are helical structures which are made or coated with magnetic materials. Under the application of a rotating magnetic field the swimmers can be propelled and their direction of propulsion can be controlled. Different fabrications methods such as 3D microprinting, glancing angle deposition and lithography are used to fabricate theses helical structures [54-56]. These different modes of locomotion allow for the use of magnetic microswimmers in a variety of biomedical applications [57].

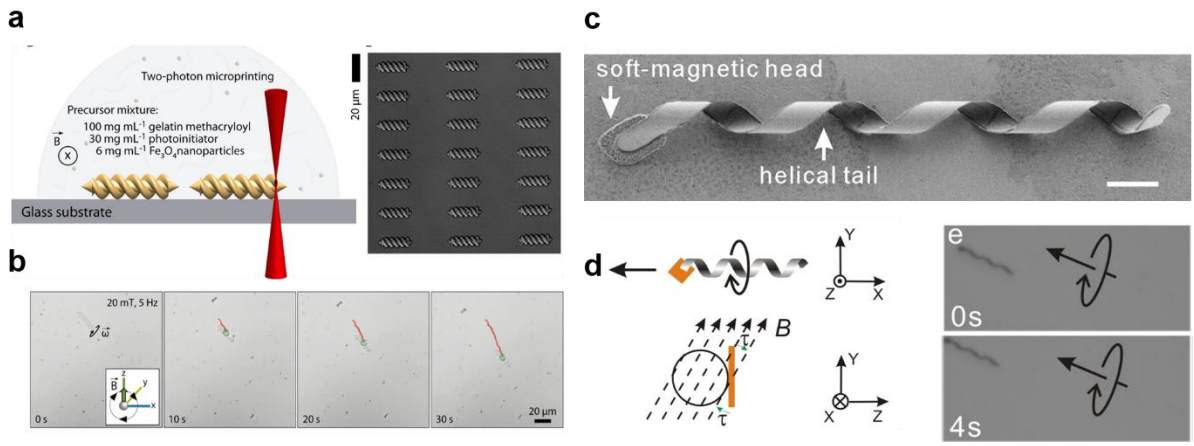

Figure 1.6 Examples of microswimmers actuated by magnetic field. a) Fabrication of double helical hydrogel microswimmer with embedded magnetic magnetic nanoparticle b) magnetic propulsion of the hydrogel microswimmers c) Helical magnetic microstructure fabricated by lithography d) magnetic propulsion of the helical structures using rotating magnetic fields. Reproduced from reference [58] [59].

1.3.3 Acoustic Propulsion

Acoustically propelled microswimmers use ultrasound fields as an external energy input to propel the microswimmers. This method is noninvasive and produces on-demand motion with good biocompatibility [60]. Ultrasound based microswimmers are propelled by acoustic radiation forces consisting of primary and secondary forces [60, 61]. One of them allows for the propulsion of microswimmers and other allows for attraction between then [62]. Ultrasound fields are biocompatible and have been clinically used in medical applications, making them one of the more biocompatible methods for propulsion of microswimmers [63]. Acoustic fields can perpetrate deep into the tissues and can generate strong streaming forces which can move the microswimmers at greater speeds. The only disadvantage is that in order to use simple non-patterned fields to propel the microswimmers, they need an air liquid interface. This creates issues in the fabrication of the microswimmers [64]. But 3D printing can be used to overcome these challenges with innovative designs that allow for the creation of air liquid interface [65]. Other designs such as tubes, cannons and rods can also be used with patterned fields [66].

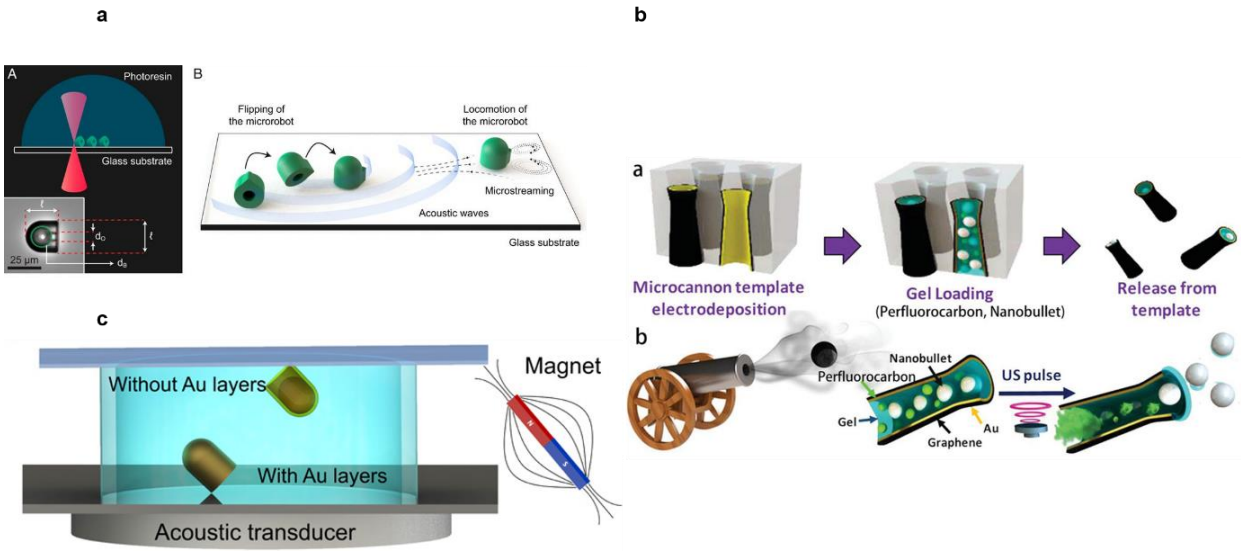

Figure 1.7 Examples of acoustic propulsion of microswimmers. a) 3D printed microswimmers that can swim under acoustic waves without the need for confinement. b) Microswimmers with cargo loaded inside them that can be triggered to release on the application of acoustic fields. c) Cap shaped microswimmers with Au layer propelled with acoustic waves. Reproduced from reference [62] [65] [67].

1.3.4 Light-driven propulsion

Light-driven microswimmers have been of interest as light as a fuel for propulsion allows for control over time and space. Light-driven microswimmers make use of different materials such as photocatalytic, photolytic, photoisomerized, photothermal and photochromic materials [68]. In the case of photo thermal microswimmers, noble metals such as gold are used to generate a thermal gradient around a particle under light illumination [69]. When light is illuminated on the noble metals due to surface plasmon resonance, the swimmers create a local heat gradient around them which in turn propels them [70]. The advantage of such photothermal is that they can be used for in vivo application due to their non-requirement of toxic fuels. But they suffer from low efficiency and requires high intensity lasers to propel them. Thermophoresis it's normally defined as the moment of the microswimmers under the effect of temperature gradient [71]. The symmetry breaking of such microswimmers is achieved when one side of the swimmers absorbs more light in comparison with the other side [72]. Hence in the present global illumination local temperature gradient is created which in turn leads to thermal diffusion of the fluid propelling the swimmer [73]. Such thermophoretic microswimmers are mostly propelled by NIR light. Traditionally gold nanostructures have been used in thermophoretic microswimmers as Au nanostructures can absorb NIR photons and convert

them into thermal energy due to surface Plasmon resonance. Such Gold nanostructures have also been used for imaging and local heating for treatment of cancer. The other major class of self-thermophoretic microswimmers are polymer-based swimmers that swim via NIR laser illumination under a photothermal mechanism [74]. He el al. showed that tubular polymer based microswimmers made of PEG and Au and Pt are deposited on the outside and inside of the tubular structure and in the presence of H_2O_2 as fuel, with increasing NIR laser intensity the swimmers swam faster due to photothermal effect [75]. Similarly, biocompatible polymer structure such as alginate-chitosan multilayers were fabricated by self-assembly techniques and Au nanostructures were grown on top of it [76]. These microswimmers when illuminated under NIR light generated propulsion due to thermal gradients created. No additional fuels were used for the propulsion of these microswimmers. Such Janus swimmers were shown to be used for drug delivery in biomedical applications. Under NIR illumination, catalytic microswimmers propelled by Pt decomposition of H_2O_2 also showed increased propulsion speed due to enhanced photothermal effect [74]. Another approach is to use light absorbing materials like carbon nanotubes for the microswimmers fabrication. Carbon nanotubes have a very high absorptive surface resulting in high light absorption. When light is incident on carbon nanotubes, the electrons get excited and subsequent relaxation of these excited electrons produces local heat which in turn propels the microswimmers. These carbon nanotubes were backed on a polymer layer and such composite swimmers under NIR laser illumination, gets heated resulting in the propulsion the swimmers [68].

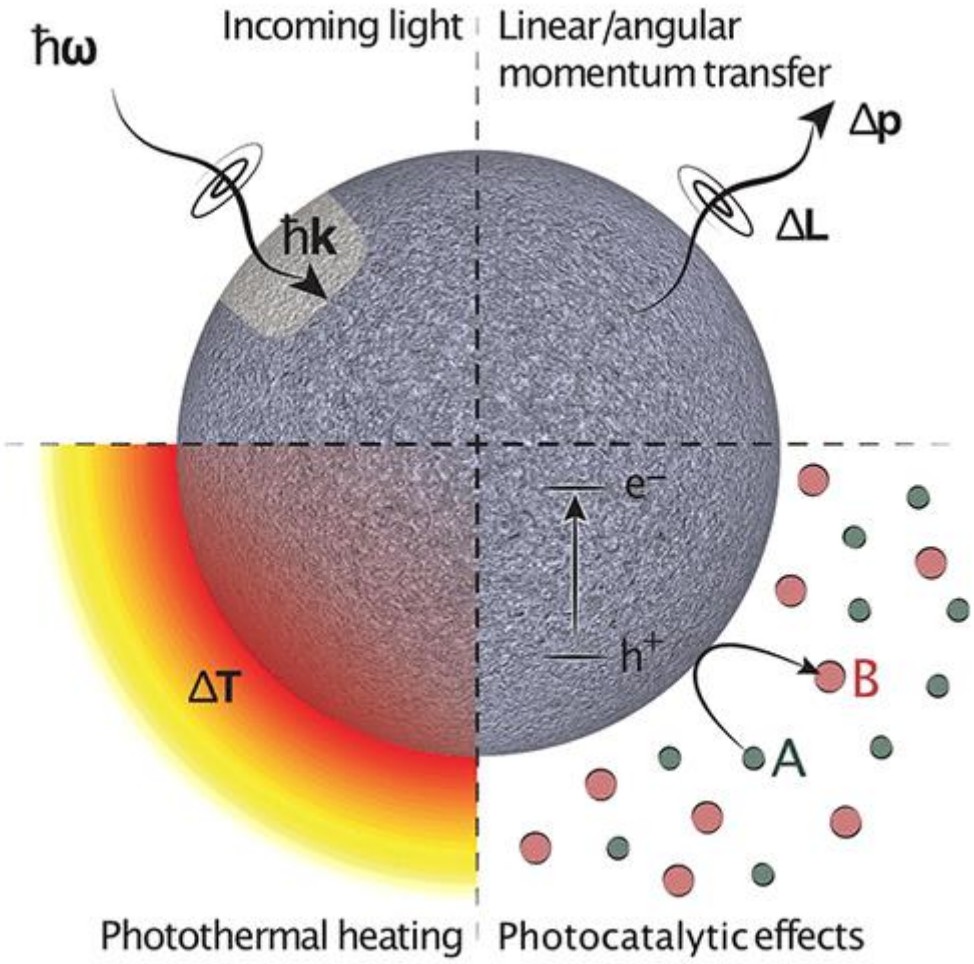

Figure 1.8 Different methods of light-triggered propulsion in synthetic microswimmers. Reproduced from reference [77].

The other major category of material used in light driven swimmers are photo-isomerization or photochromic materials, which undergo conformal changes under light illumination. Different kinds of photochromic process are used for microswimmers and soft robots' fabrication. The predominant of them are trans to cis isomerization of azobenzene dyes, photo- induced ring closing reactions and photo-tautomerism. Azobenzene are a group of dyes containing two phenol rings connected by an azo linkage giving them ability for photo switching. When the dyes are illuminated by light they absorb photons in the trans-azo band allowing for switching of from a trans to meta stable cis configuration. Azo dyes also have the ability to induce Marangoni flows around the microswimmer due to their trans-cis transformation. These flows allow for the microswimmers to be propelled under illumination. The meta stable state relaxes after some time in the absence of any illumination. Photochromic polymers could also be used as a fuel to propel passive particles, the polymer solution used as

fuel akin to H_2O_2. This allows for interesting self-organized structures that are used to study self-assembly.

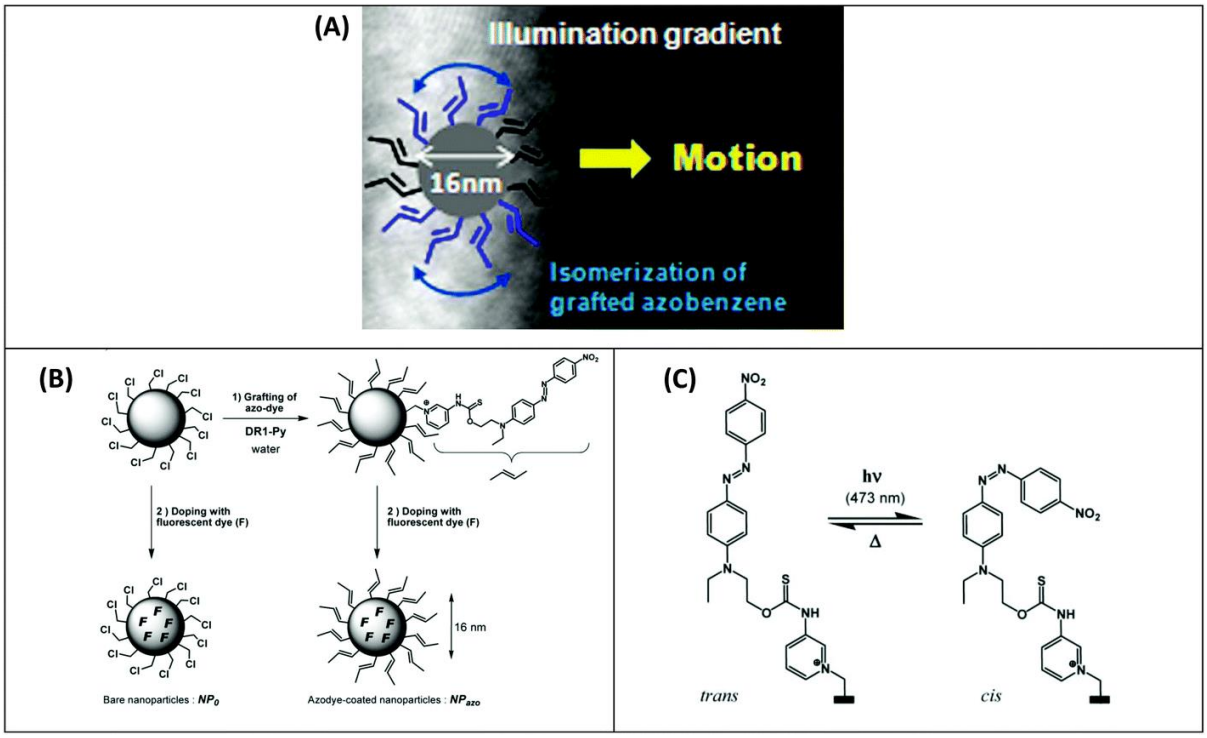

Figure 1.9 Schematic presentation of (A) the movement of azobenzene-dye-decorated polymer nanoparticles in illumination gradient, (B) preparation of non-functionalized and azobenzene-dye-decorated polymer nanoparticles, and (C) *trans* to *cis* photo-isomerization of the grafted azobenzene molecules. Reproduced from reference [78].

Some Liquid crystal elastomers (LCE) are also sensitive to light, LCEs have the ability to change their confirmations resulting in similar effects as photo chromic swimmers. Mostly LCEs are used in soft robots where their changed confirmations are locked in along with the elastomer and under illumination, these layers experience deformation due to the change in the LCE modes [56, 79].

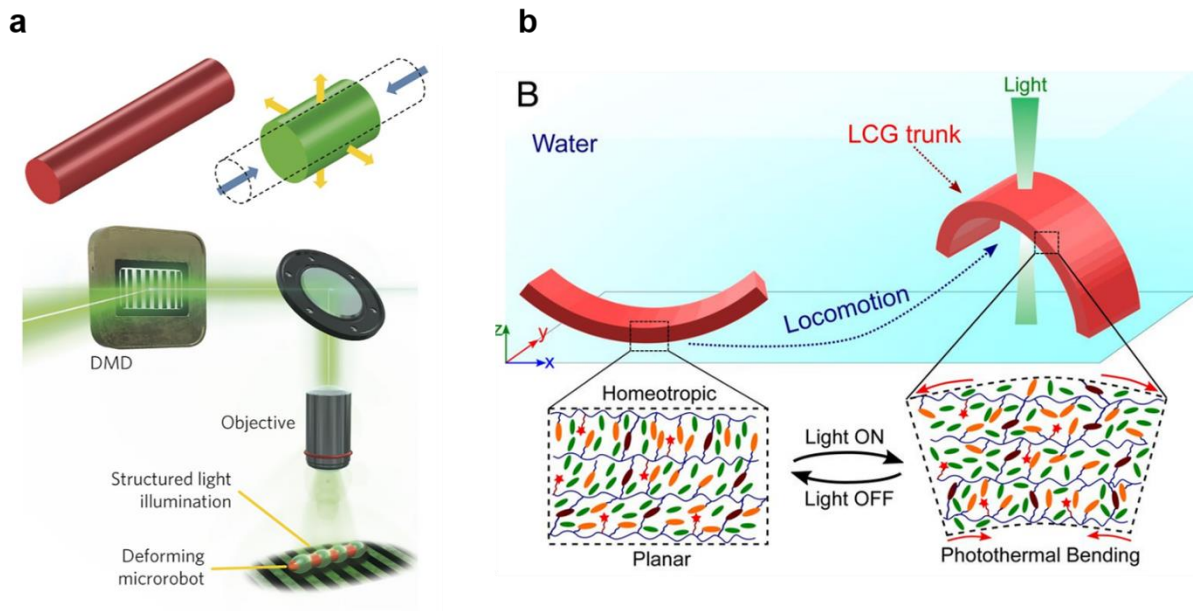

Figure 1.10 Examples of LCE materials used in light-driven actuators. a) Light-driven soft robot powered by travelling waves of expansion and contraction similar to the metachronal waves of Celia. b) Shape morphing liquid crystal elastomer based soft robot. Reproduced from references [56, 79].

1.4 Photocatalytic microswimmers

Photocatalytic microswimmers are one of the major class of light-driven microswimmers. Photocatalysis has been an extremely widely investigated field for several years with wide range of application ranging from hydrogen evolution, environmental remediation and energy storage [80, 81]. The availability of a large material library from photo catalysis can be borrowed onto light-driven microswimmers. In a classical photo catalytic reaction, the photocatalytic materials under light illumination produces electrons and holes which then migrate onto the surface of the material [82]. Under illumination electrons will be generated and transferred to the conduction band leaving the holes in the valance band. These electrons and holes then react with water or the fuel is present in the environment to form ions, molecular species or gases depending on the environment they present [83]. Different cycles of redox reactions occur around the photocatalytic surface which causes the formation of the products [83]. These products, thus form a gradient of the species under illumination around the photocatalyst surface, which in turn propels the microswimmers. These photocatalytic materials can be converted into microswimmers, if there is an asymmetric propulsion happening on one side the photocatalytic materials in comparison with the other side. This asymmetric product formation would lead to gradient formation [84]. The formation of such

gradients lead to a fluid flow around the particle in the opposite direction which leads to the propulsion of light driven microswimmers [24]. Due to this property of photocatalytic materials, theoretically any photocatalytic materials could be used to propel the microswimmer.

However, a lot of challenges occur and fabricating asymmetric designs due to the inherent design challenges that are present. The other main challenge comes in the form of low efficiency that is present in most photocatalytic materials [68]. Though the photocatalytic materials might be efficient enough for the formation of gases products such as hydrogen or oxygen and, these reactions occur slowly and not in an efficient manner. For the propagation of light driven micromotor the driving force needs to be strong enough to propel the swimmers continuously [85]. Also, in the case of light driven microswimmers powered by photo catalytic reactions, the photo catalytic reactions need to happen at a constant higher rate. The wavelength in which the swimmers produce electrons and holes also play an important role in the design of the photocatalytic microswimmers. There is a large glass of photocatalytic materials which are powered only under high UV light, which creates problems in the practical application of such swimmers. Due to these limitations, not all photocatalytic materials can be used for light driven micro swimmers.

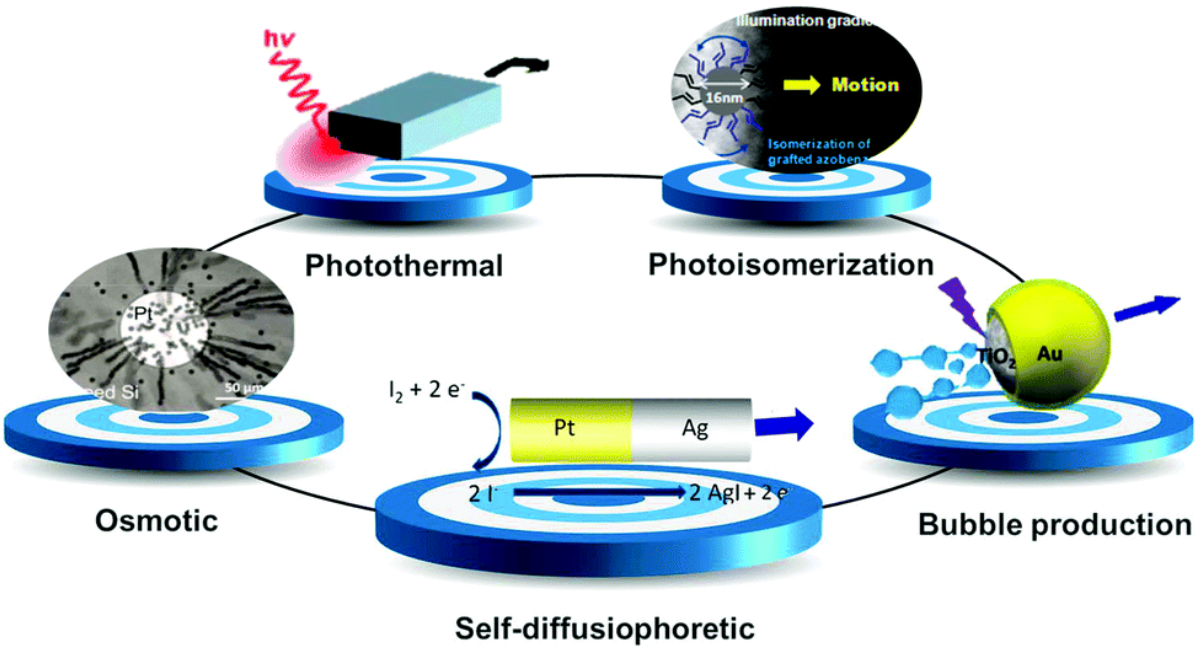

Figure 1.11 Light-driven synthetic microswimmers based on photcatalytic materials. Reproduced from reference [68].

To negate the harmful effects and application problems associated with a high intensity UV light, light-driven microswimmers propelled by photocatalytic materials need to have a relatively high efficiency under lower UV illumination intensities. Photocatalytic efficiency is usually associated with the quantum efficiency of the photo catalytic reactions. the quantum efficiency (QE%) is given by

$$\mathrm{QE} = \frac{no.\ of\ reacted\ h^+\ or\ e^-}{no.\ of\ incident\ photons} \tag{5}$$

Generally, higher the quantum efficiency of the photocatalytic materials is the stronger the propulsion behavior should be. For example the quantum efficiency values of TiO_2, one of the most widely explored photocatalytic materials is around 0.04 % where are when the photocatalytic material in combination with a co-catalytic material such as Au or Pt increases the efficiency drastically to around 4 % [86]. This 100-fold increase allows for a higher propulsion efficiency of the light-driven microswimmers under low intensity light. Doping of such metallic or non-metallic elements on the surface of photocatalytic materials increases their efficiency [80]. During the photocatalytic process there are many reaction schemes that go on such as charge separation, surface reactions and recombination. Only a small amount of charge

carriers on the surface produce beneficial redox reactions which are used for the propulsion of the micro swimmers [85]. The remaining charge getting us re-combine to form heat or photo luminescence, weakening the effect of propulsion. Hence, in order to fabricate a highly efficient light driven micro-swimmer that can be propelled under low intensity and all these design factors need to be kept under consideration [87, 88]. A major part of this thesis is focused on developing such material which can be propelled efficiently under light for potential applications such as environmental remediation, in vivo swimming and biomedical applications such as drug delivery.

1.5 Current materials used in light-driven microswimmers

The first reported work on photocatalytic from Sen et al. used TiO_2 microspheres that were propelled in UV light in pure water and methanol mixture where methanol is used for hole quenching [89]. The microswimmers moved with a speed of 10 μm/s by self-diffusiophoresis mechanism. This work opened the path for the use of different photocatalytic materials for the fabrication of light-driven microswimmers. TiO_2 has been one of the most versatile photocatalytic materials that has been used in literature [81, 90]. Their ease of fabrication, coupled with their low costs make them an interesting material for the fabrication of microswimmers. Bare TiO_2 by themselves can act as a microswimmer, the illumination direction by itself creates an asymmetry [91, 92]. But the asymmetry that is generated is not significant enough for the efficient propulsion of the propulsion. Hence, most light driven microswimmers based on TiO_2 are designed by depositing a Janus TiO_2 layer over a non-photocatalytic particle like SiO_2 [93]. The TiO_2 layer is sputtered or deposited by other thin film deposition methods on monolayers of non-photocatalytic particles [94]. This creates a Janus structure, when light is incident on the TiO_2 surface it forms electrons and holes and these charge carriers react with fuels to form product molecules. The product molecules form a gradient due to the asymmetric structure resulting in the efficient ballistic propulsion of the microswimmers. The crystallinity of TiO_2 plays an important role in their photocatalysis and hence by extension their swimming speeds [95]. Crystalline TiO_2, especially anatase phase has shown some of the highest activity under UV light [96]. Other forms of TiO_2 like the Rutile black are also used in the fabrication of microswimmers and these forms of TiO_2 though not as efficient are active in the visible spectrum of light [97, 98]. Another design strategy involved in the fabrication of microswimmers using TiO_2 is to form TiO_2 based tubular structures [99]. The tubular structures are made of TiO2 or a polymer layer with TiO_2 on the inside [100]. Pt or Au is deposited on the inside of the tubular structure to increase the efficiency of propulsion.

Tubular structures allow for bubble propulsion of the microswimmers. Bubble propelled microswimmers generally referred to as micro rockets, have the ability to be propelled at very high speeds due to the bubble ejection [27].

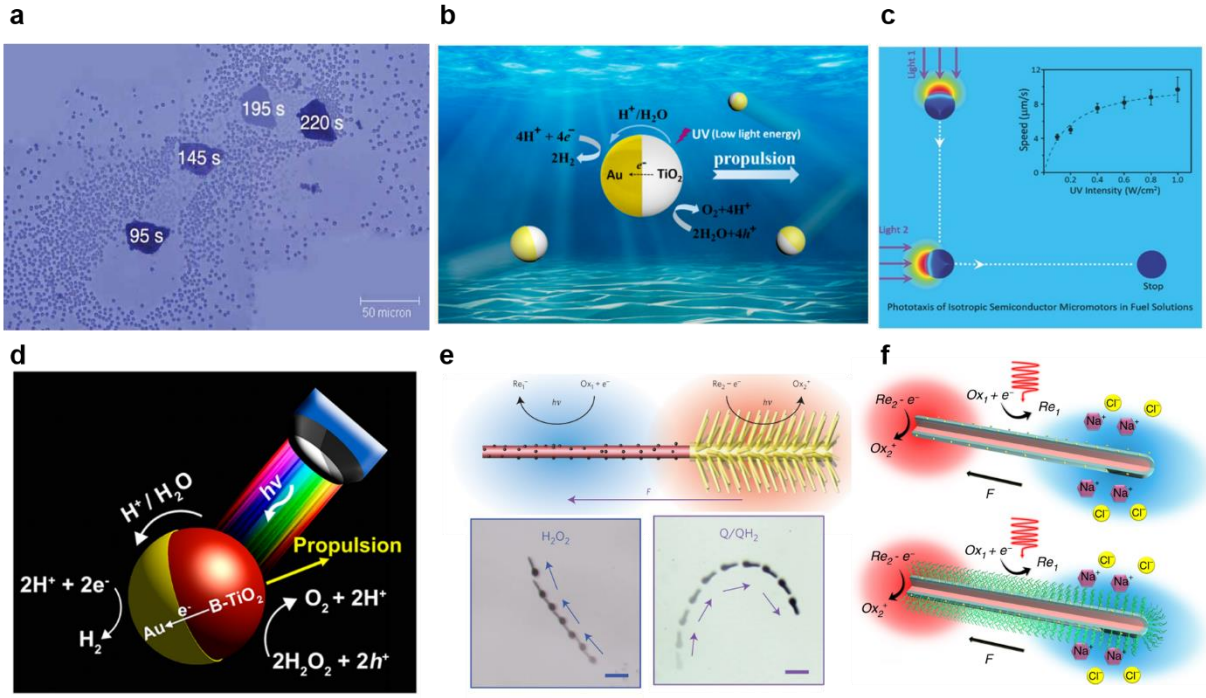

Figure 1.12 Examples of photocatalytic light-driven microswimmers: a) TiO_2-based reversable assembly with water and H_2O_2 as fuel, b) TiO_2-Au Janus microswimmer swimming in water, c) TiO_2 microswimmer without the use of any Janus cap showing phototactic behavior, d) B-TiO_2-Au Janus microswimmer showing visible light propulsion, e) TiO_2-Si based nanotrees showing positive and negative phototaxis based on their charge, and f) Si nanowire-based microswimmer with polymeric coating showing enhanced ionic tolerance. Reproduced from references [91, 98, 101-104].

Other photocatalytic materials that are used for microswimmers are ZnO [105-107], AgCl [108] , Cu_2O [109], CdS and Si nanowires [110, 111]. AgCl is photocatalytically unstable under UV light, thus under illumination AgCl breaks down into Ag+ and Cl- ions causing self-diffusiophoresis [112]. Ibele et al studied AgCl based micropumps in which an AgCl layer is immobilized onto the surface and when light is illuminated on them the ions results that are formed results in the flow and pumping action of the fluids involved [113]. Even in the absence of fuels like H_2O_2 AgCl microswimmers can be propelled in DI water under illumination due to a multi-step decomposition reaction resulting in the formation of Cl^- and H^+ ions [89]. When a Ag layer was used as a backing layer beneath AgCl, and in the presence of H_2O_2, Ag metal

can also be oxidized by H_2O_2. This results in interesting oscillatory and reversible conversion of Ag under illumination. After the illumination is switched off the reaction of ions is reversible, resulting in the back formation of AgCl [114].

Similarly, in the case of Silver phosphate (Ag_3PO_4), reversible reactions forming silver and phosphate ions under illumination which resulted in transitions between repulsion and attraction resulting in schooling behavior of the microswimmers [115]. Chemophoretic effects have also been demonstrated by such light driven swimmers under illumination due to the distribution of ions which the swimmers can follow from a region of low concentration to a region of higher concentration.

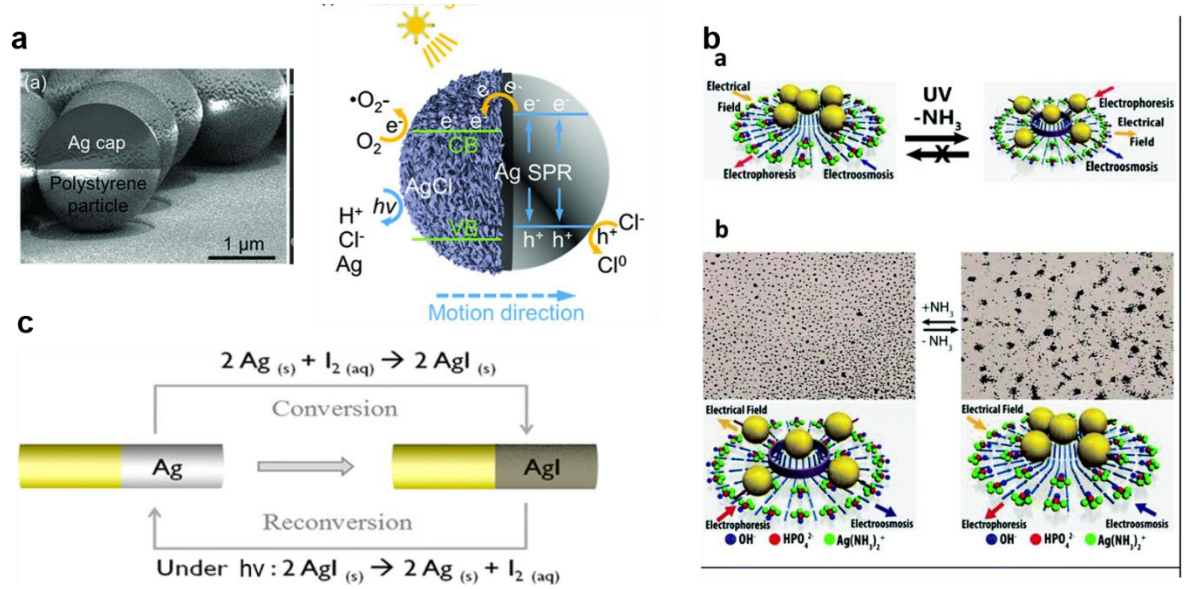

Figure 1.13 a) Schematic image for visible light absorption process of Janus PS/Ag/AgCl micromotors based on the SPR effect. b) Reversible schooling behaviour observed on Ag_3PO_4 based light-driven microswimmers. c) Schematic image of AgI based light-driven microswimmer. Reproduced from references [116] [115].

ZnO has similar photocatalytic properties as TiO_2 and ZnO microswimmers have been found active under UV light and cause the propulsion of such microswimmers in the presence of fuels such as H_2O_2 [105]. Though ZnO is not as efficient as a photocatalyst as TiO_2, the additional photocorrosion reaction of ZnO with H_2O_2 under illumination results in their enhanced propulsion. ZnO reacts with H_2O_2 to form Zn ions, this reaction is accelerated under UV illumination [117]. Similar reactions are observed by CdS based swimmers under visible light illumination [118]. Photocorrosive swimmers though efficient in propulsion suffer from drawbacks on biocompatibility due to the harmful ions they form under illumination. The other

major group of visible light driven microswimmers use Si nanowires, one of the most known semi-conducting material available [104, 119]. These nanowires can be used in conjunction with a p and n junction Si nanowires or along with Pt or Au at one end as co-catalysts for the propulsion [120].

1.6 Mechanism of propulsion

The two primary methods of propulsion of light driven microswimmers are self-diffusiophoresis and self-electrophoresis. These two mechanisms along with osmotic effects are commonly used mechanisms in the propulsion of chemical and light-driven microswimmers.

1.6.1 Self-diffusiophoresis

Self-diffusiophoresis in a mechanism in which there is an asymmetric release of products due to reactions happening on the surface. There is an asymmetric release of products and the different rates of cations and anions, due to this the charged particle can be propelled in the solution. The dominant force is the Coulomb interaction between the charged microswimmers surface and the oppositely charged Debye layer [13, 24].

1.6.2 Self-electrophoresis

Self-electrophoresis or electrolier diffusiophoresis process has been widely observed for bimetallic microswimmers such as Au-Pt rods what swim with H_2O_2 as fuel [32]. The Pt catalyzes H_2O_2 resulting in a flow of electrons from the Pt side to the Au side. In addition to the surface reaction the charge flow between the layers leads to an electric field which causes fluid flow around the microswimmer thus causing faster propulsion of the swimmer. The same mechanism can be extrapolated to light-driven microswimmers which are combined with cap structures such as Au or Pt [121]. In these cases, the reactions occur on both sides leading to an enhanced propulsion of light-driven microswimmers. This has been observed by comparing the speed of different microswimmers such as TiO_2-Au, TiO_2-SiO_2 [8, 120]. These mechanisms have also been studied in detail in this thesis in chapters 4 and 5.

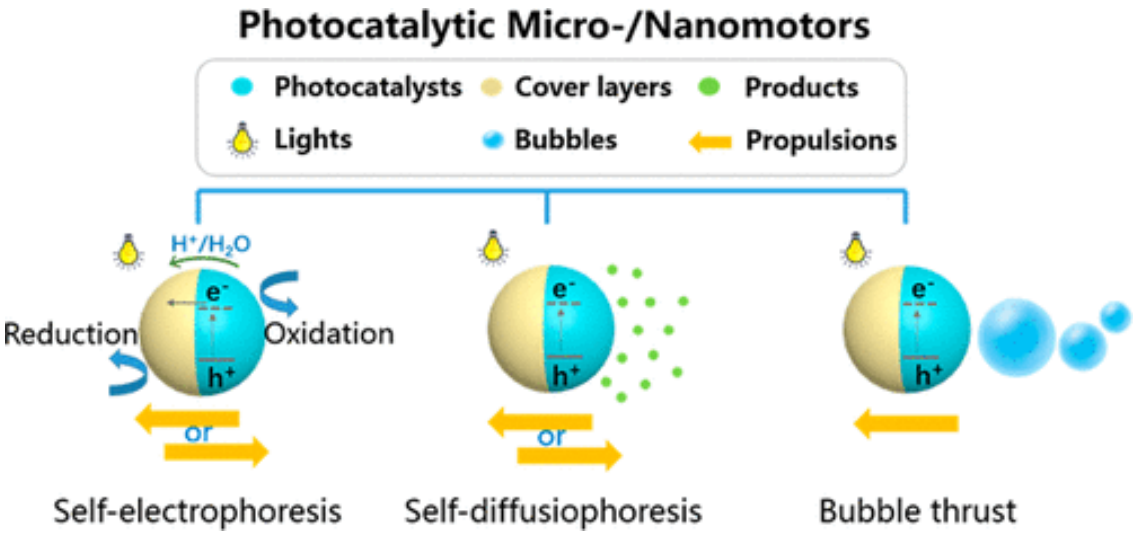

Figure 1.14 Propulsion mechanisms of photocatalytic light-driven microswimmers. Reproduced from reference [122].

1.7 Light-driven microswimmers for biomedical applications

One of the main thrust application of light-driven microswimmers is in biomedical applications. Though demonstrations, including cargo loading, sensing and tissue penetration. However, there is no complete demonstration of their applications in real cell environments or under realistic cell conditions [123]. The primary challenges lie in their biocompatibility, efficiency of loading, ion tolerance and presence of biocompatible fuels in the environment [123]. In this thesis we aim to tackle these challenges to enable the application of light-driven microswimmers in biomedical applications.

One of the primary problems in using light-driven microswimmers is their swimming in high ionic strength conditions. Most of the available literature within light-driven microswimmers is focused on swimming in aqueous solutions [124]. Thought different wavelength responsiveness and fuels have been used the swimming still takes place in the aqueous solutions. Most light-driven microswimmers swim either via self-diffusiophoresis and self-electrophoresis mechanisms [122]. Both these mechanisms involve the presence of electric fields around the particles due to the products and charge carriers that are formed due to the photocatalytic process. The electric field and the product gradients are greatly affected by the presence of ions arounds in the surrounding strength. High ionic strength in the surrounding layer collapse the Debye layer thickness around the particle. The EI50 number has been introduced previously as a measure of the ionic concentration at which the speed of the microswimmers is reduced by 50% [104].EI50 is less than 0.1 mM for self-diffusiophoretic

and self-electrophoretic swimmers [125], reaching up to ~4 mM for geometrically optimized systems addressing this problem [104]. For practical applications an EI50 value of more than 100 mM is needed. Paxton et al derived a modified equation which governs this by combining Helmholtz-Smoluchowski and Ohm's law, the equation is given by

$$U = \frac{\mu_e J}{k} \tag{6}$$

where μ_e is the electrophoretic mobility, J is the current density of the electrochemical reaction, and k is the conductivity of the bulk solution. In order to overcome these limitations, different strategies can be adopted to negate the issues that arise due to the Debye layer collapse. The use of ionic conductive surfaces and interfaces that would permit the ions in the salt environment to pass through the microswimmer body without affecting their propulsion. The other way could be the use of large porous interfaces which would allow for complete solution movement through the microswimmer body. These strategies are further explored in this thesis, especially in Chapter 5 to enable their potential biomedical applications.

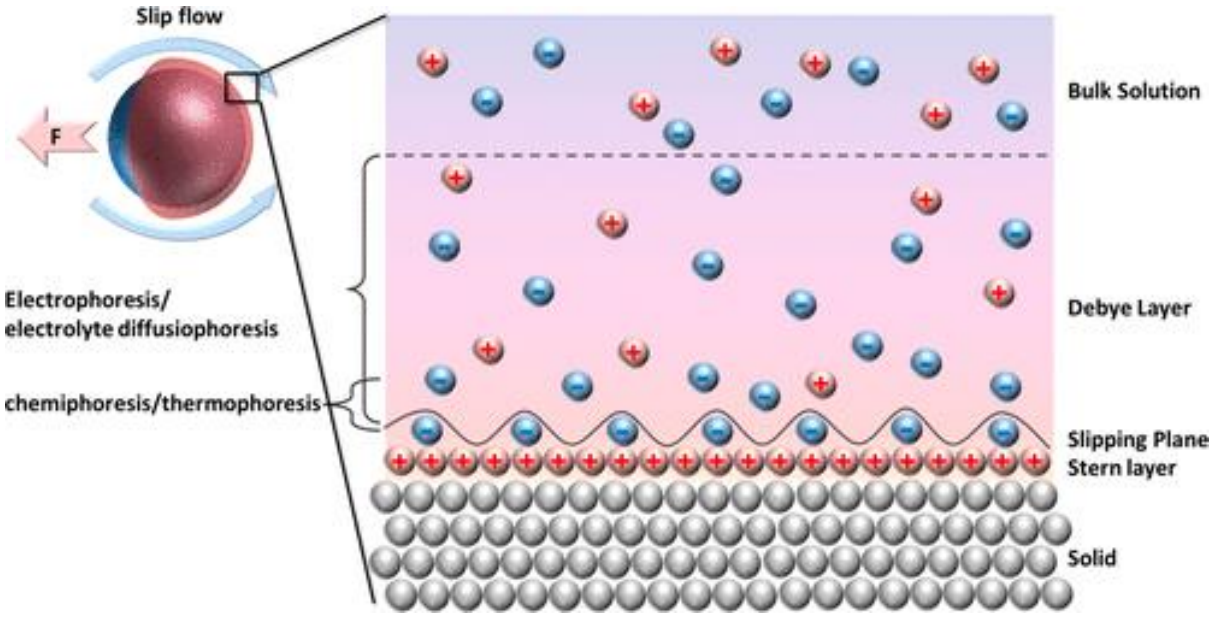

Figure 1.15 Schematic of the different propulsion mechanisms of light-driven microswimmers and their interaction regions. Reproduced from reference [123].

Most light-driven microswimmers use chemical fuels to enhance the photocatalytic reactions, thereby enhancing the propulsion speed of the microswimmers. Most of the swimmers are propelled by H_2O_2 or alcohols as fuels [8]. These fuels are not biocompatible and hence cannot be use in biomedical applications. There are other fuels such as Urea and Glucose that are predominantly used for enzyme-based microswimmers [126]. But glucose

being an alcohol has also been shown to power light-driven microswimmers, though the required concentration is higher than what is naturally present in the cell environment. In certain redox shuttles that allow for efficient transport of the ions between the two halves of the microswimmers are employed. They improve the overall efficiency of swimming in the microswimmers. However most of them currently in use are not biocompatible, but there are certain shuttles akin to the ones used by bacteria and cells within the body, which can be used to aid in the propulsion of light-driven microswimmers [127]. Fuel-free microswimmers propelled by various photocatalytic reactions taking place in pure water would be one of the ideal fuels. The only drawback they suffer from is the higher energy input required for these reactions which could cause bottlenecks in their applications.

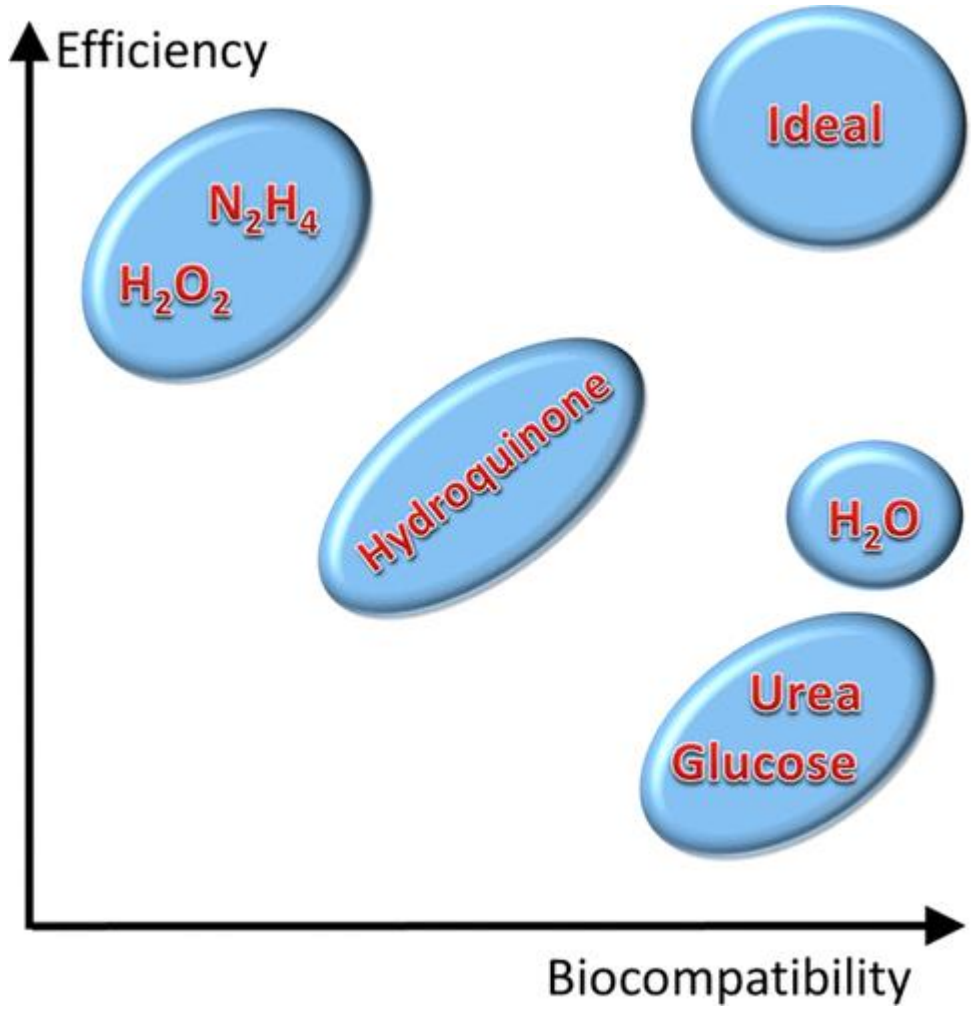

Figure 1.16 Different fuels as a function of propulsion efficiency and biocompatibility. Reproduced from reference [123].

1.8 Outline

The field of light-driven microswimmers has been growing at breakneck speed in the recent years. Most of the early development has been on the investigation of new materials, the overall swimming mechanism and the necessary control of the microswimmers. Within the domain of light-driven microswimmers, photocatalytic microswimmers have been at the forefront due to the ability to adapt already available photocatalytic materials. The fruitful knowledge available from the photocatalysis community clubbed with the knowledge of designing microswimmers can be readily transferred to fabricating light-driven microswimmers. However, not all photocatalytic materials can be used directly and this presents bottle necks in the fabrication of asymmetric structures. One of the most sought-after use of microswimmers is their potential application for biomedical applications, hence tailoring such light-driven microswimmers for their potential application in drug delivery and other biomedical applications has been paramount in light-driven microswimmers. The mechanism of swimming in such biological medium presents a different set of challenges such as availability of the fuels, their cargo carrying ability, the use of biocompatible wavelengths and the interactions with the ions present in biological environments. In this thesis we aim to address all these challenges and to present a schematic to enable the use of light-driven microswimmers in biomedical and environmental applications.

The overall goal of this thesis is to introduce new materials and designs in the field of light-driven microswimmers. The key objectives are to investigate inorganic and organic photocatalytic material, to be used for light-driven microswimmers. The different designs for their fabrication are also explored. Their designs are modified to allow for loading of drug molecules and their respective release. The other key fundamental question on the origins of the surface reactions that governs the mechanism of propulsion was also looked into. Chapter 1 surveys the current state of art in materials, controls and the challenges in light-driven microswimmers. An over view of the different propulsion mechanisms used for microswimmers, their governing physics, the mechanisms of swimming in light-driven microswimmers and the current challenges that are prevailing are presented. In Chapter 2, we present TiO_2 an inorganic photocatalyst as the material of choice for the fabrication of light-driven microswimmers. A novel hollow and mesoporous structure for light-driven microswimmers was explored. The influence of the enhanced surface area on the propulsion efficiency was looked into. This then compared with the standard solid TiO_2 microswimmers and three-fold increase in their propulsion speed can be observed. Further, this novel design

can be controlled by magnetic guidance by the addition of magnetic films which do not impact the swimming speeds. As a potential proof of concept, the hollow mesoporous TiO_2 microstructure was shown to have enhanced cargo loading of anti-cancer drugs like Doxorubicin. They also further showed enhanced environmental remediation of organic pollutants due to the swimming of the microswimmers which was demonstrated by the use of a model pollutant.

In Chapter 3, we continue the use of inorganic materials for the light-driven microswimmers. but the use of harmful UV light which presents challenges in practical applications of light-driven microswimmers. In order to avoid it, CoO a highly efficient photocatalytic material, which is also magnetic, was explored for the fabrication of microswimmers. Different fabrication methods were explored for the use of CoO-TiO_2 Janus microswimmers. The use of duel UV and visible light responsiveness of such microswimmers allows for the wavelength control of them. We have demonstrated wavelength and magnetic control of the low intensity visible light propelled microswimmers which has potential for many biomedical applications.

In Chapter 4, the possibility of exploring an organic photocatalytic material for light-driven microswimmers was explored. So far, photocatalytic microswimmers have been limited by the requirement of continuous illumination. Here, Poly(heptazine imide) (PHI), a 2D carbon nitride material is used for the swimmers, which show efficient propulsion in aqueous media not only during but after illumination (for about 30 min after their 30-s prior illumination due to their solar-battery swimming). Contrary to the mainstream reports, oxygen reduction rather than hydrogen evolution being responsible for propulsion with alcohol fuels. This allows for better understanding and modelling of light-driven microswimmers. Balancing reaction conditions, the realization of light-induced intrinsic charging of a microswimmer, enabling sustained ballistic propulsion in dark through discharge of accumulated energy.

In Chapter 5, other advantageous properties of PHI based microswimmers are explored. The use of PHI microswimmer without the use of Janus caps, allows for further broadening of their potential applications. Their unique structural and morphological porosity allows for the movement of ions in salt environments, such as those present in human body, enables them to be used for light induced propulsion in physiologically relevant conditions. PHI was also found to be biocompatible. Their structural properties enable stable drug uptake, which can be used

for biomedical applications. They display smart and intelligent release behavior by being sensitive to oxygen concentration in its environment and pH.

Finally, the last chapter summarizes our results and present a future outlook for light-driven microswimmers and its potential applications.

This dissertation combines below four journal papers, which are edited and revised to match the context of this dissertation. All publications are properly cited in the relevant sections of the dissertation.

List of papers:

1. **V Sridhar**, BW Park, M Sitti, "*Light-Driven Janus Hollow Mesoporous TiO_2–Au Microswimmers*", **Advanced Functional Materials** 2018, 28, 1704902.
2. **V Sridhar**, BW Park, S Guo, PA van Aken, M Sitti, "*Multiwavelength-Steerable Visible-Light-Driven Magnetic CoO–TiO_2 Microswimmers*", **ACS Applied Materials & Interfaces** 2020, 12, 21, 24149–24155.
3. **V Sridhar**, F Podjaski, J Kröger, A Jiménez-Solano, BW Park, BV Lotsch, M Sitti, "*Carbon nitride-based light-driven microswimmers with intrinsic photocharging ability*", **Proceedings of the National Academy of Sciences** 2020, 117 (40) 24748-24756.
4. **V Sridhar**, Y Alpan, V Kishore, J Kröger, L Grunenberg, F Podjaski, BV Lotsch, M Sitti, "*Biocompatible Carbon nitride-Based Light-driven Microswimmer Propulsion in Biological and Ionic Media with Responsive On Demand Drug Delivery*", (under review)

Other articles beyond the scope of this thesis are:

1. J Giltinan*, **V Sridhar***, U Bozuyuk, D Sheehan, M Sitti, "3D Microprinting of Iron Platinum Nanoparticle-Based Magnetic Mobile Microrobots", **Advanced Intelligent Systems** 2021, 3: 2000204. (* Co-first authors)

Chapter 2. Light-Driven Janus Hollow Mesoporous TiO_2-Au Microswimmers

Designing of light driven microswimmers plays an essential role in making them available for practical applications. In this chapter, the advantages of using a hollow and mesoporous structure for light-driven microswimmers is explored. Hollow mesoporous TiO_2 is used as a model structure and the influence of this on their propulsion speed and functionality is studied in this chapter. The use of hollow mesoporous structure allows for their applications in environmental delivery and drug delivery applications. The results of this chapter have been previously published in reference [128]. Dr. Byungwook park assisted in designing and performing the experiments, analyzing the experimental data and drafting the manuscript published in reference [128].

2.1 Introduction

Light is one of the major sources of energy in nature. Photoactive semiconductors (e.g., TiO_2) have attracted significant interest in the past decade in various fields, such as photocatalysis, solar cells, sensors, and environmental remediation [90]. When ultraviolet (UV) light is incident on TiO_2, the UV photons excite electrons from the valence band to the conduction band of TiO_2, producing an excess of electrons on the surface of TiO_2 [82, 83]. Since the first work demonstrated by Hong et al. [101], significant progress has been made in designing TiO_2-based microswimmers by employing new material designs, doping, and morphology [91, 92, 96, 98-101, 103, 129, 130]. Although different materials, such as WO_3 [131], BiOI [132], Cu_2O [109], and Si [33, 133], have been applied for developing microswimmers, many reports have been focused on light-driven TiO_2 microswimmers under UV. This can be attributed to higher energy within UV photons, resulting in higher propulsion due to the ease of surface evolution of the generated photoelectrons from the surface [134]. Two major factors hampering potential use of such TiO_2 swimmers in potential applications are their incapability of carrying functional cargos and their low speed [135]. Using hollow TiO_2 would allow for loading of cargos for applications like targeted active drug delivery and environmental remediation [136, 137]. Moreover, Shiraishi et al. [138] reported that porous TiO_2 performs a more rapid photochemical reaction when compared to a conventional non-porous TiO_2. This enhanced activity is due to the high surface area created by the porous structure, thus making it easier for the generated

photoelectrons to move to the surface. Hollow structure provides advantages such as lower density (e.g., better neutral buoyancy), higher surface to volume ratio [139], and higher interaction with both outer and inner shells [140]. Hollow mesoporous structures provide for better light harvesting in comparison with solid structures, because they have better light absorption due to the thinner shells [141]. Hollow structures also enhance dye degradation due to Mie scattering inside the hollow shells [142]. Availability of increased photons leads to increased electrons generated on the surface.

In this chapter, we propose Janus hollow mesoporous TiO_2/Au (JHP-TiO_2-Au) microswimmers propelled at a speed of up to 48.5 μm/s under 15.5 mW/cm^2 intensity of UV light. Such speed is higher in comparison with previous works on Janus solid TiO_2/Au (JS-TiO_2-Au) microswimmers [96, 98] while requiring less UV light intensity. Due to the photocatalytic activity improved by the hollow mesoporous structure, JHP-TiO_2-Au microswimmers move faster than JS-TiO_2-Au ones. Figure 1(a) illustrates the microswimmer design. We demonstrate the influence of hollow mesoporous structure on the swimming speed of TiO_2/Au microswimmers, which affects degradation of methylene blue dye. We also demonstrate drug loading and active delivery of an anticancer drug (doxorubicin) by JHP-TiO_2-Au microswimmers. Our work provides a new design and fabrication method for light-driven microswimmers with increased swimming speed and directional guidance. An overall schematic of this is shown on Figure 2.1.

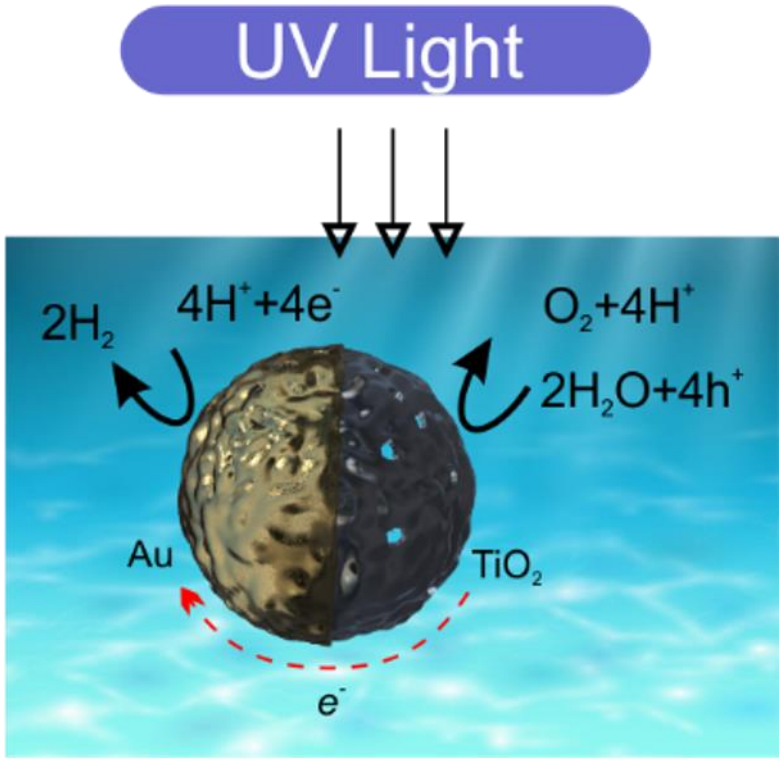

Figure 2.1 Schematic of Janus hollow porous (JHP)-TiO_2-Au microswimmers under illumination. Reproduced from reference [128].

2.2 Fabrication of JHP-TiO_2

Cationic PS spheres are purchased from Sigma-Aldrich. These PS particles are used as a template for synthesis of hollow mesoporous TiO_2 (HP TiO_2). The particles are fabricated by nucleating TiO_2 on top of the PS microparticles. The PS acts as a template for the fabrication of the HP-TiO_2. The synthesis is done by dispersing 1 mL of the template PS particles is dispersed in 10 mL ethanol. 0.76 g of PVP(Sigma-Aldrich) is added to 100 mL ethanol, and after vigorous stirring, PS template particles are added to it. 960 µL of titanium isopropoxide (TTIP, Sigma) is added to 15 mL absolute ethanol. This solution is added to the stock solution containing PS particles. PVP helps in stabilising the suspension allowing TiO_2 to precipitate on the surface of PS. The solution is stirred for 45 minutes at 800 rpm resulting in the formation of TiO_2 shells over the PS cores. To increase the thickness of the TiO_2 shell, subsequent precipitations of TiO_2 are carried out. The older TiO_2 shells act as a nucleation point for the subsequent precipitation. The thickness of the shell is increased after two subsequent additions of TTIP precursor. The resulting solution containing TiO_2 shells is filtered and washed several times to remove the residual PVP. These particles are then annealed at 450°C for 10 hours resulting in the removal of the PS core and formation of anatase hollow mesoporous TiO_2

shells. The schematic of fabrication is shown of Figure 2.2. A monolayer of the resulting particles is drop casted on a Si wafer and 10 nm Au layer is sputtered on them. The fabrication of monolayer is carried out as shown on Appendix A. The resulting Janus particles are collected in water. For control experiments, the solid TiO_2 particles are fabricated by precipitating a titanium alkoxide [143, 144], which in our case is titanium (IV) butoxide. 1 mL of titanium (IV) butoxide is added to 40 mL of ethanol containing a small amount of water. The resulting solution is incubated in room temperature for 3 hours. The resulting precipitate is filtered and washed many times with ethanol. The Au/TiO_2 Janus particles are formed by the same method as before [96]. These particles are used for control experiments. A schematic of the fabrication scheme of the microswimmers is shown on Figure 2.2.

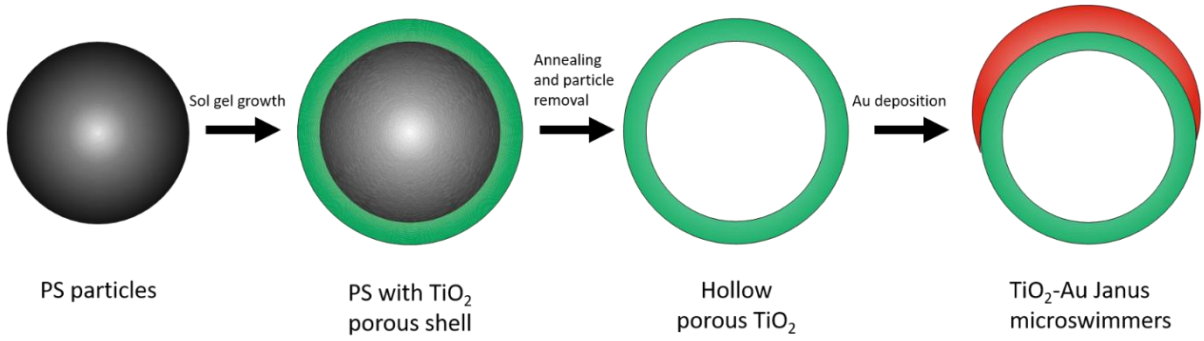

Figure 2.2 Fabrication scheme for JHP-TiO_2-Au microswimmers.

2.3 Characterization of JHP-TiO_2-Au microswimmers

The fabricated JHP-TiO_2-Au microswimmers are characterised by SEM, transmission electron microscopy (TEM), energy dispersive x-ray spectroscopy (EDX), and x-ray diffraction (XRD). The SEM images in Figure 2.3 show a JHP-TiO_2-Au microswimmer. An image contrast could be observed between the upper and lower layers indicating the presence of two different materials in a Janus shape.

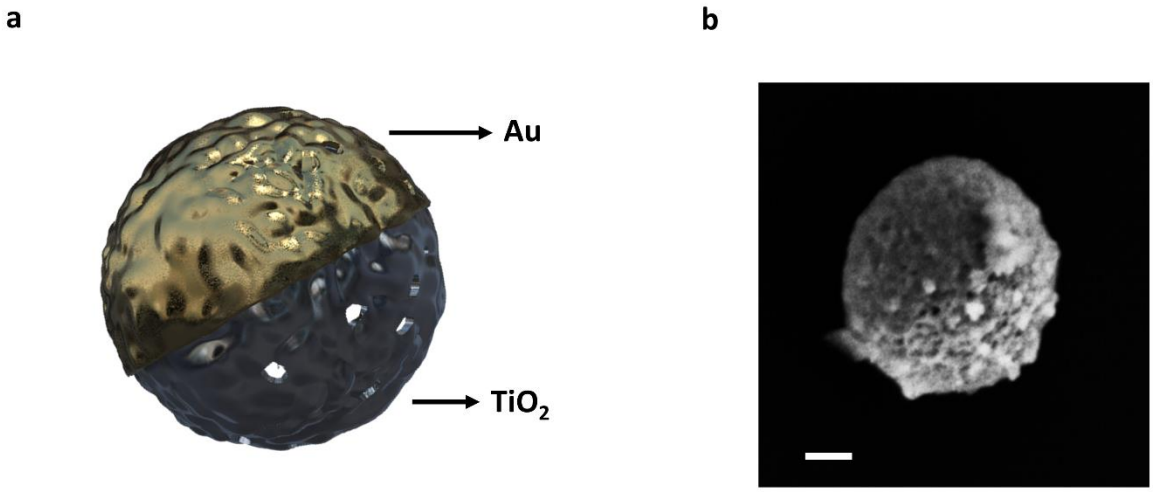

Figure 2.3 Schematic and SEM of JHP-TiO_2-Au microswimmers. (a) Overview of the proposed light-driven Janus hollow mesoporous TiO_2/Au (JHP-TiO_2-Au) microswimmer design. (b) Scanning electron microscopy (SEM) image of a JHP-TiO_2-Au microswimmer. Scale bar represents 0.2 μm. Reproduced from reference [128].

The size distribution of the particles under the SEM show that most of the microswimmers are around 1 μm. The size distribution of the particles was measured from the SEM images using the ImageJ software and is shown on Figure 2.4.

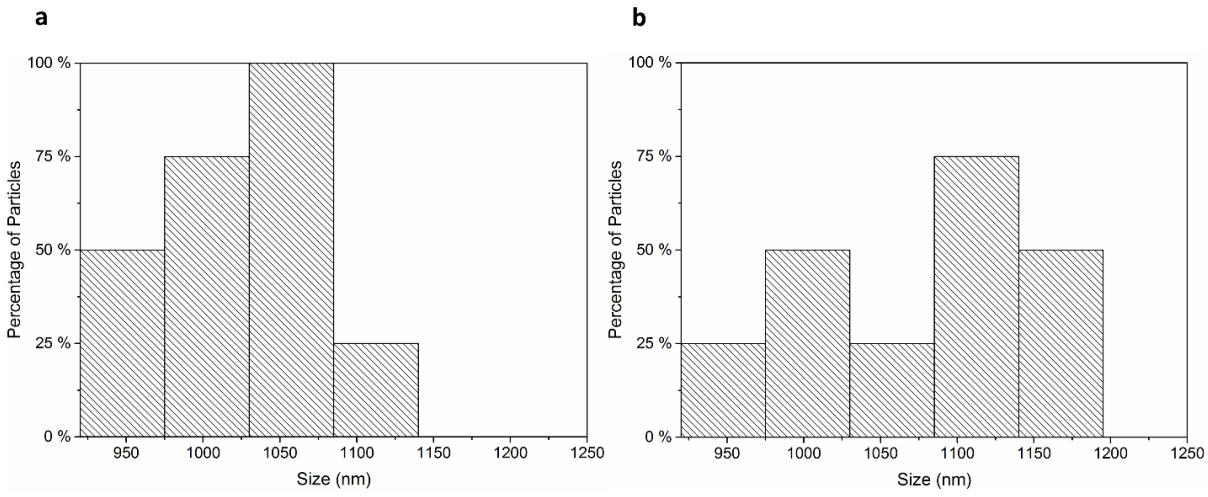

Figure 2.4 Particle size distribution of, (a) JHP-TiO_2-Au and (b) JS-TiO_2-Au microswimmers (N=10) obtained from SEM images of the particles.

Scanning transmission electron microscopy-high angle annular dark field Imaging (STEM-HAADF) imaging, energy-filtered transmission electron microscopy (EFTEM) imaging, and electron energy loss spectroscopy (EELS) measurements were conducted with the Zeiss SESAM microscope and a Nano 36 DC sputtering machine from Kurt Lesker (Hastings, UK). The microscope is equipped with an electron monochromator (CEOS, Heidelberg) and the MANDOLINE energy filter. Figure 2.5 shows the mesoporous morphology of the JHP-TiO_2-Au microswimmer and magnified regions on the surface of HP TiO_2 from the TEM. A bright image contrast between the hollow cavity and the outer shell is observed. The shell on the outer layer appears darker due to the increased thickness and the lighter regions indicate the hollow cavity in the middle. Due to sol-gel growth, TiO_2 sphere body is not completely regular. Pores show up as brighter spots between the darker spots. Different regions have different growth rates, due to the differences in the nucleation on TiO_2 surface. The surface area of the particles are increased due to these surface irregularities [145]. It can be seen that the pores are non-uniform and irregular with different sizes. The different shades of darkness are due to difference in degree of crystallization of TiO_2. The d-spacing is found to be 0.35 nm, which corresponds to the (101) lattice of the anatase phase. The Au half cap appears brighter on the image.

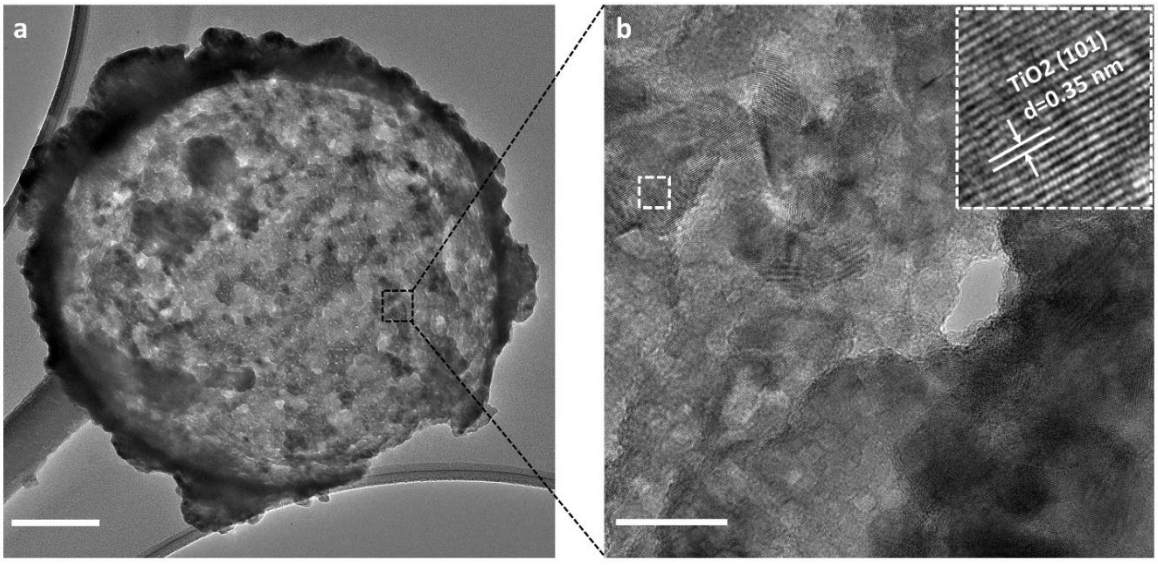

Figure 2.5 Transmission electron microscopy (TEM) images of JHP-TiO_2-Au microswimmers. (a) TEM image of spherical hollow mesoporous TiO_2. Scale bar is 0.2 μm. (b) Magnified TEM image of hollow mesoporous TiO_2 microswimmer with brighter regions indicating the pores surrounded by darker crystallized regions, different shades of darkness indicate the degree of crystallinity. Scale bar is 20 nm.

EELS is performed on the Janus particles, which provides information on the composition of various elements present on the cap structure. It is also useful in effective identification of low atomic number elements like O on the layer. Figures 2.6c-e show the elemental maps of Ti, O, and Au in green, blue, and red, respectively. Figure 2.6f shows the overlaid images of Ti and Au indicating the presence of half capping of the Au layer. The surface area of the HP structure is estimated using nitrogen adsorption-desorption isotherms.

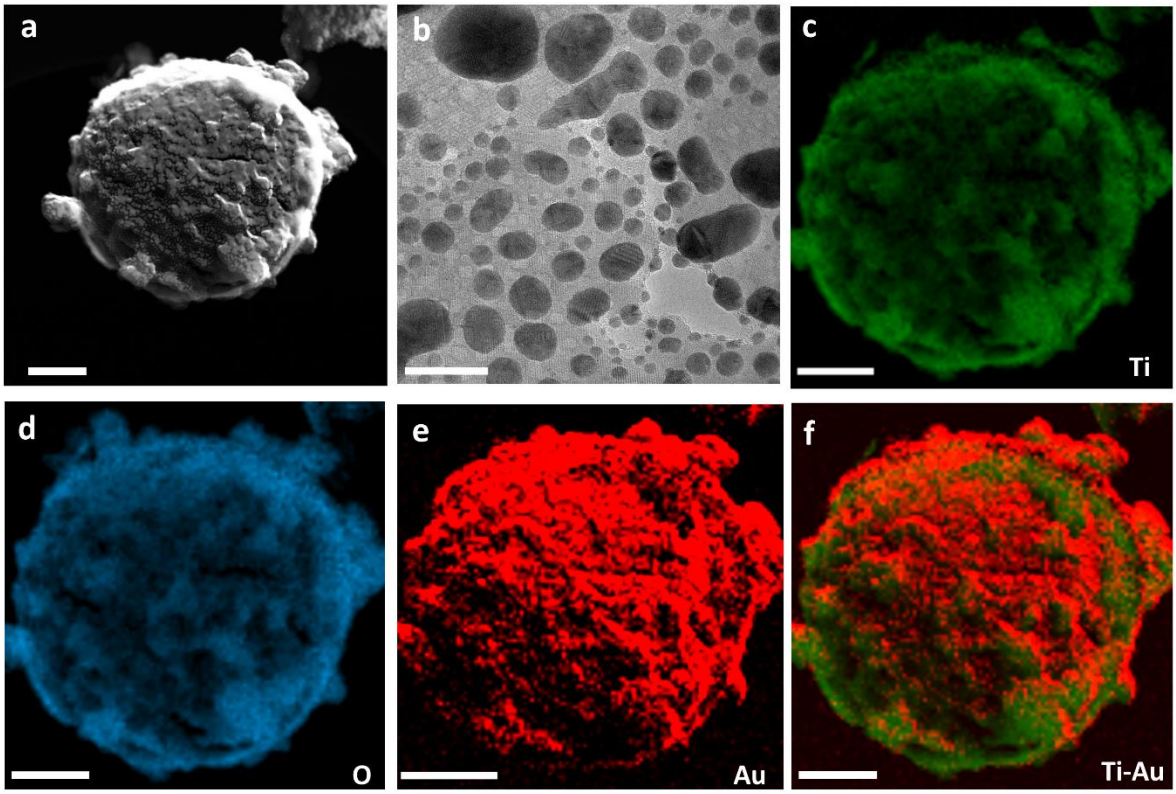

Figure 2.6 EELS images of JHP-TiO_2-Au microswimmers. (a) TEM image of a spherical hollow mesoporous TiO_2 microswimmer with gold cap. (b) Brighter regions indicate the pores surrounded by darker crystallized regions, different shades of darkness indicate the degree of crystallinity. Electron energy loss spectroscopy (EELS) color-coded elemental map of (c) Ti, (d) O, (e) Au, and (f) Ti and Au combined. Scale bar in (a,c-f) is 0.2 μm. Scale bar in (b) is 20 nm. Reproduced from reference [128].

From Brunauer-Emmett-Teller (BET) theory, the surface is found to be 57.11 m^2/g from N_2 desorption isotherm. From the adsorption and desorption curves obtained using nitrogen adsorption-desorption isotherms, a type IV adsorption isotherm indicating the presence of mesoporous structure is observed as seen on Figure 2.7a. The pore size, as indicated from the Barrett-Joyner-Halenda (BJT) desperation data, is about 4.8 nm as seen on Figure 2.7b. This

concurs with the observations from pore size distribution in the TEM image. The average pore radius from the BET method confirms the presence of the mesoporous structure [146]. The XRD data in Figure 2.7c confirms the presence of only anatase phase in the annealed hollow mesoporous (HP) TiO_2 particles. The peaks are fitted using Bruker XRD software (Diffrac.Suite) and anatase peaks are found at (101), (004), (200), (105), (211), and (204), indicating the presence of a single anatase phase without impurities. The presence of a single anatase phase allows for the faster swimming due to better absorption of the UV light.

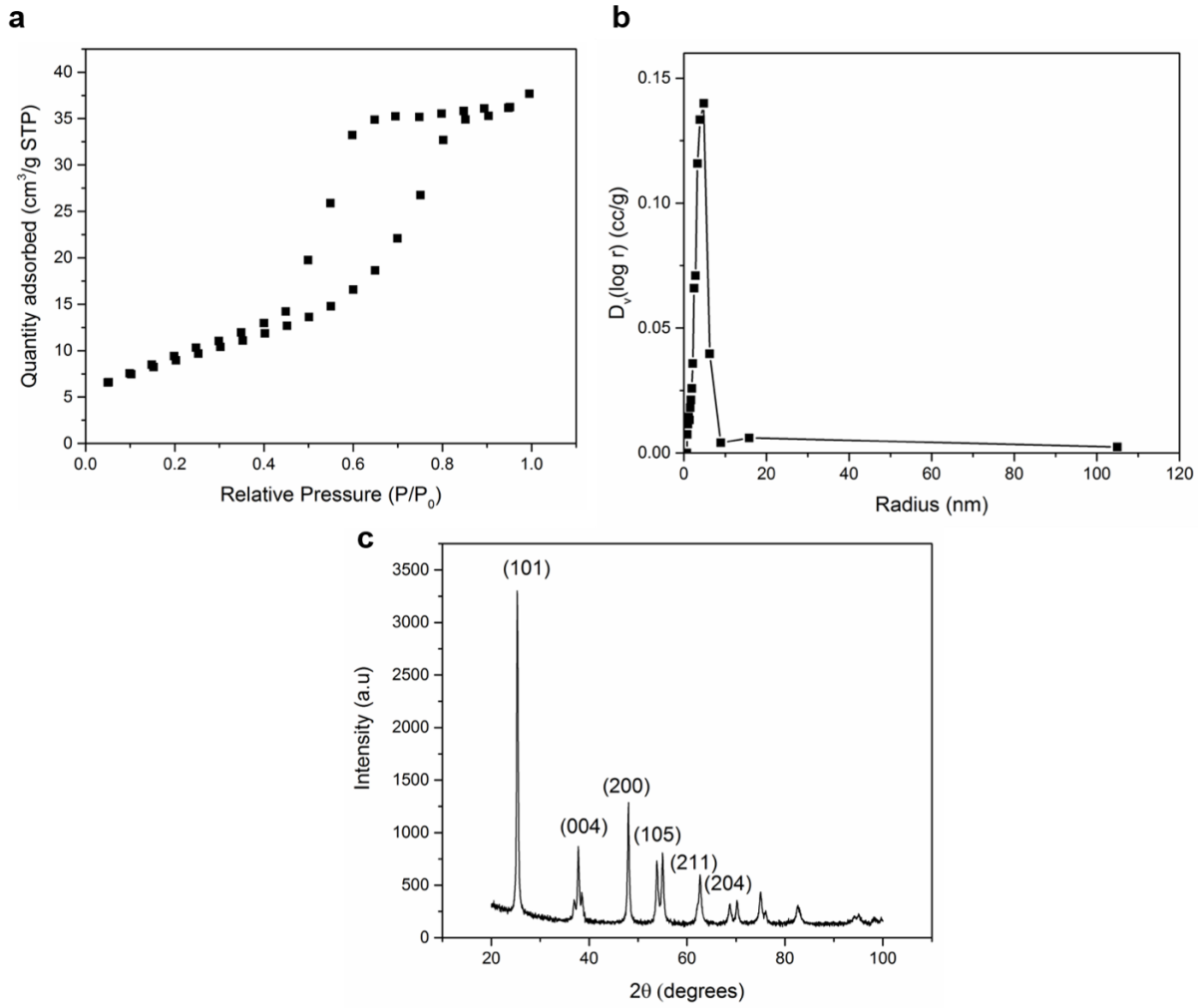

Figure 2.7 Material characterization of JHP-TiO_2-Au microswimmers. (a) Nitrogen adsorption and desorption isotherm for mesoporous TiO_2 samples annealed at 400°C indicating the presence of a mesoporous structure on the surface. (b) BarrettJoyner-Halenda (BJH) pore size distribution curve of the JHP-TiO_2-Au indicates that the average diameter of nanopores is about 4.8 nm. (c) X-ray diffraction data for hollow mesoporous TiO_2 annealed at 400°C showing the formation of only anatase phase.

2.4 Microswimmers swimming characterization

2.4.1 Setup for swimming

In order to measure the swimming properties of the microswimmers, a Thorlabs M365L2 (Germany) UV lamp is used for illumination through a Zeiss Axio A1 inverted microscope. The videos are recorded from the microscope using a LD Plan-NeoFluar 40x objective lens and Axiocam 503 CCD camera at 62 frames per second. The light path through the objective of the microscope causes focusing effect on the objective plane of the imaging.

2.4.2 Speed, mean square displacement and diffusion coefficient calculation

The swimming behaviour of the swimmers is systematically investigated by two-dimensional mean square displacement (MSD) analysis on the captured videos using a custom MATLAB code. Propulsion of JHP-TiO_2-Au microswimmers is achieved by illuminating them with this UV light with 365 nm wavelength and intensity of 15.5 mW/cm^2. The swimmers are tracked for 15 seconds. Initially the swimmers are tested under deionized (DI) water without the presence of any additional H_2O_2. Ten JHP-TiO_2-Au microswimmers from different sample batches are tracked for each condition. The mean speed of the JHP-TiO_2-Au microswimmers in DI water under UV light is 9.2±0.5 μm/s. To test the increased activity due to the mesoporous structure, various concentrations of H_2O_2 are used. At 0.1% concentration of H_2O_2, the average speed of solid JS-TiO_2-Au microswimmer is 10.5±1.2 μm/s. The average speed of JHP-TiO_2-Au microswimmers is 37.3±2.6 μm/s, which is more than three times the speed in comparison with the JS-TiO_2-Au microswimmers as seen on Figure 2.d. This value also compares with the speed of JS-TiO_2-Au microswimmers from the literature with the same UV light intensity [96]. H_2O_2 is used as it provides an increased proton gradient for swimmers enabling them to swim faster under illumination. Figure 3a shows the MSD plots for JHP-TiO_2-Au microswimmers and solid TiO_2-Au swimmers with 0.1% H_2O_2 under illumination.

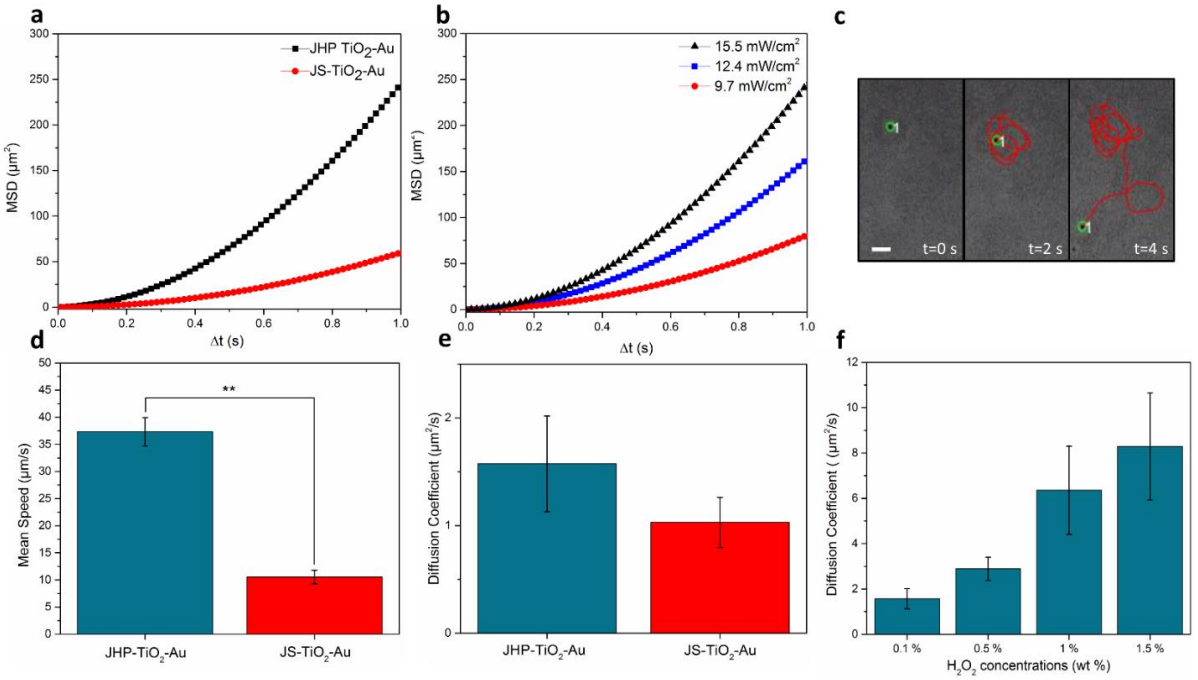

Figure 2.8 Swimming characterization of JHP-TiO_2-Au microswimmers (a) Two-dimensional mean square displacement (MSD) experimental data for the JHP-TiO_2-Au and JS-TiO_2-Au microswimmers at 0.1% H_2O_2. (b) MSD data for the JHP-TiO_2-Au microswimmers with different intensities of light at 0.1% H_2O_2. (c) Snapshot images of a JHP-TiO_2-Au microswimmer placed in an aqueous environment with 0.1% H_2O_2 at various time intervals. Scale bar is 5 μm. (d) Average (N=5) mean speed of the JHP-TiO_2-Au and JS-TiO_2-Au microswimmers under 0.1% H_2O_2 at 100% UV light intensity (15.5 mW/cm^2) with p=0.0077. (e) Average (N=5) diffusion coefficient of the JHP-TiO_2-Au and JS-TiO_2-Au microswimmers under 0.1% H_2O_2 at 100% UV light intensity. (f) Average (N=5) diffusion coefficient of the JHP-TiO_2-Au microswimmers under different H_2O_2 concentrations (0.1-1.5%) at 100% UV light intensity. Reproduced from reference [128].

The MSD plots of both microswimmers show a ballistic trajectory in the first 1 second of the tracking as seen on Figure 2.8a and b. The MSD is plotted over both shorter and longer time intervals. The MSD is given by the formula

$$\langle \Delta L \rangle^2 = 4D\Delta t + v^2\tau_R \qquad (7)$$

where D is the diffusion coefficient, $\langle \Delta L \rangle^2$ is the mean squared displacement, t is the time, V is the velocity and τ_R is the inverse rotational diffusion coefficient. In the longer time intervals ($\Delta t \gg \tau_R$) where t is the time and τ_R is the inverse rotational diffusion coefficient, there is a constant change in the direction of propulsion due to rotational Brownian motion. In short time intervals the MSD plot shows a characteristic curved plot versus time to indicate the ballistic

motion. In longer time intervals the curve shows diffusive behavior with an enhanced diffusion coefficient. By showing this crossover from ballistic to enhanced diffusive behavior we can observe that there is an active propulsion of the microswimmers due to the light and the swimmer is just not active Brownian as shown in other light-driven microswimmers. This also helps in ruling out drift as a factor for propulsion of the microswimmers. Figure 2.9 shows the MSD over longer time intervals.

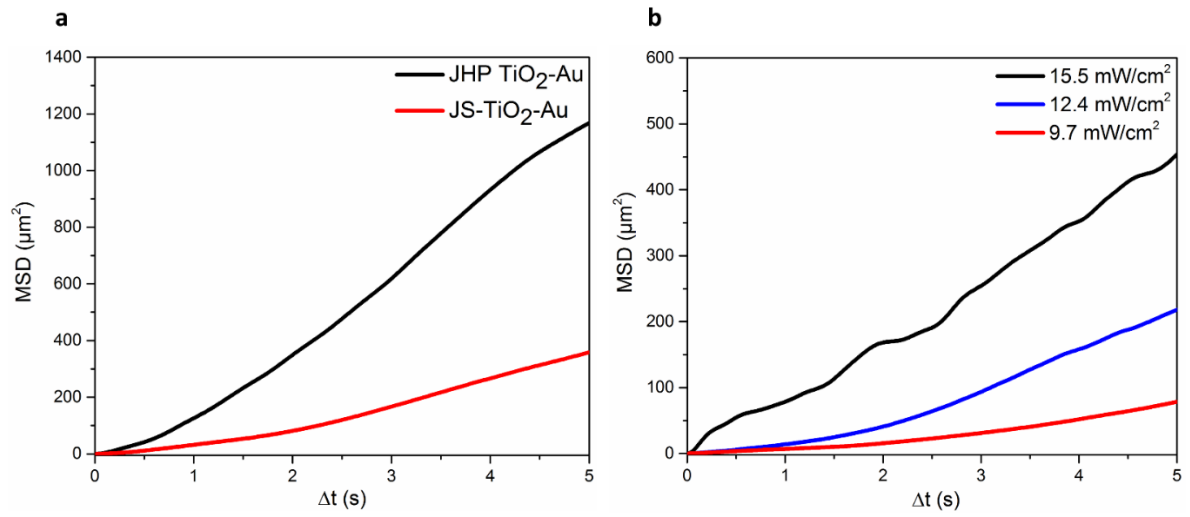

Figure 2.9 (a) Two-dimensional MSD experimental data for the JHP-TiO_2-Au and JS-TiO_2-Au microswimmers at 0.1% H_2O_2 at longer time intervals. (b) MSD data for the JHP-TiO_2-Au microswimmers with different intensities of light at 0.1% H_2O_2 at longer time intervals.

The effective diffusion coefficient (D) is calculated from the MSD data as $D=MSD/(i.\Delta t)$. For the case of two-dimensional (2D) trajectory analysis of the videos, $i=4$. D values for JHP-TiO_2-Au and JS-TiO_2-Au microswimmers under 0.1% H_2O_2 are estimated to be 1.6±0.4 and 1.0±0.2 $\mu m^2/s$, respectively. It can be seen that even at low UV intensity (15.5 mW/ cm^2), the speed of the microswimmers is higher than with other TiO_2 microswimmers found in the literature [96, 98, 147]. This result is attributed to the hollow mesoporous structure of the proposed microswimmers. The structure of the microswimmers provides an increased electron transport to the surface, followed by better charge transfer to the surface of Au, thus enabling better charge separation between different layers.

2.4.3 Effect of intensity on propulsion speed

In order to investigate the effect of light intensity on the microswimmers, three different intensities of UV light are tested. Different UV intensities induce different number of photons.

This gives the relation between incoming photons and swimming speeds. The swimmers are tested under irradiances of 9.7, 12.4, and 15.5 mW/cm^2 UV intensity. The resulting MSD plots of the microswimmers are shown in Figure 3b. The mean speeds of the microswimmers are estimated to be, 17.0±1.9 μm/s, 24.3±1.7 μm/s, and 37.3±2.6 μm/s for 9.7, 12.4, and 15.5 mW/cm^2 UV intensities, respectively. The mean speeds increase with the intensity of light, because a higher number of UV photons are available to excite the electrons from valence band to the conduction band of TiO_2 as the light intensity increases. They generate a greater number of electrons on the surface, causing an increased self-electrophoresis of the particles, which means that the swimmers would move at higher speeds under more intense light sources.

2.4.4 Effect of fuel on propulsion speed

Various concentrations of H_2O_2 are tested to determine the effect of different concentration of H_2O_2. The light intensity is kept constant for various concentrations of 0.1%, 0.5%, 1%, and 1.5% of H_2O_2 at 15.5 mW/cm^2 UV intensity. The speed of the microswimmers increases with increase in the H_2O_2 concentration. With increasing concentration of H_2O_2, the proton concentration gradient on the surface of the microswimmers increases. This is characteristic of conventional catalytic microswimmers [12]. The proton gradient directly corresponds with the electron-hole formation in TiO_2. The diffusion coefficients for different H_2O_2 concentrations are shown in Figure 3f. At concentrations of 0.1%, 0.5%, 1%, and 1.5% H_2O_2, the diffusion coefficients are found to be 1.6±0.4, 2.9±0.5, 6.3±1.9, and 8.3±2.4 μm^2/s, respectively. With increase in H_2O_2 concentration, the diffusion of microswimmers increases. This can be observed in the supplementary videos. At higher H_2O_2 concentrations, the microswimmers show greater rotational diffusion. Their higher translational speed and current experimental limitations in rotational motion tracking prevent accurate estimation of their rotational diffusion.

2.5 Mechanism of propulsion

The enhanced speed of JHP-TiO_2-Au microswimmers in comparison with solid TiO_2 ones can be attributed to higher surface area and longer diffusion length of the carriers due to the hollow structure [136, 148]. The higher surface area of hollow mesoporous TiO_2 allows faster diffusion of photo-injected electrons from TiO_2 to the Au layer. The size of hollow TiO_2 particles is comparable to the wavelengths of the incoming UV radiation. This brings faster migration of the generated electrons to the surface. Hollow structure allows for the formation of higher density of electrons at the surface, because the incoming UV photons do not penetrate deeply into the TiO_2 layer, aiding in increased generation and transport of electrons to the interface of

TiO_2.

The propulsion mechanism of the JHP-TiO_2-Au microswimmers is based on light-induced self-electrophoresis, which occurs when an asymmetric structure with a self-generated electric field moves due to the asymmetric distribution of ions [32]. The self-generated electric field causes an asymmetric distribution of ions in the medium. This variation in ionic concentration in turn propels the particles [33]. When UV light is incident on the Janus particles, the UV photons cause charge separation in JHP TiO_2. The incoming photons excite the electrons from the valance band of TiO_2 to its conduction band. These electrons then move to the surface of TiO_2. At the interface, there is a Schottky junction [149, 150]. These electrons are injected into the Au layer, which acts as a sink for the incoming electrons. The porous nature of the interface helps in enhanced charge transfer from TiO_2 to the Au layer. On the TiO_2 side, there is an accumulation of protons (H^+) due to the oxidation of H_2O_2 and H_2O. The accumulation of protons on the TiO_2 side and electrons on the Au side causes an opposing fluid flow in the medium due to the motion of the ions in the fluid, thus propelling the JHP-TiO_2-Au microswimmers with the Au side forward. This motion of the Janus swimmers is analogous to the swimming behaviour of Pt-Au bimetallic swimmers catalysed by H_2O_2 [12]. To further confirm the propulsion mechanism, control experiments of the microswimmers swimming in 0.1 M NaCl are performed. The presence of higher salt concentration stops the motion of the swimmers, because Na^+ and Cl^- ions lower the proton mobility, inhibiting the electrical double layer of the swimmers. SiO_2-Au particles are used as control to check for thermophoretic movement of the Janus microswimmers under UV light. Previous reports have shown thermophoresis of Au-capped particles under near infrared (NIR) light [151]. 10 nm-thick Au is sputtered on 1 µm-diameter SiO_2 particles. These particles are illuminated with UV light and their MSD is calculated. The SiO_2-Au particles do not exhibit any directional motion when UV light is incident on them. Hence the motion of JHP-TiO_2-Au microswimmers is only due to self-electrophoresis occurring between the TiO_2 and Au layers.

2.6 On/Off control

In many potential applications, such as targeted delivery, it is essential to stop the motion of swimmers at places of interest. Light-driven swimmers are advantageous in this regard. The swimmers move only in the presence of UV light, which acts as a fuel. In the absence of light they stop instantaneously. Only when the UV light is turned on, there is self-generated active propulsion. Such active propulsion of the particles stops when the UV light is switched off, where the particles undergo only random Brownian motion. This switchable motion adds more

control to the motion of the swimmers. The snapshots of stop and go motion at different time intervals of the swimmer are shown in Figure 2.10. The instantaneous speed of swimmers is plotted against time in Figure 2.10.

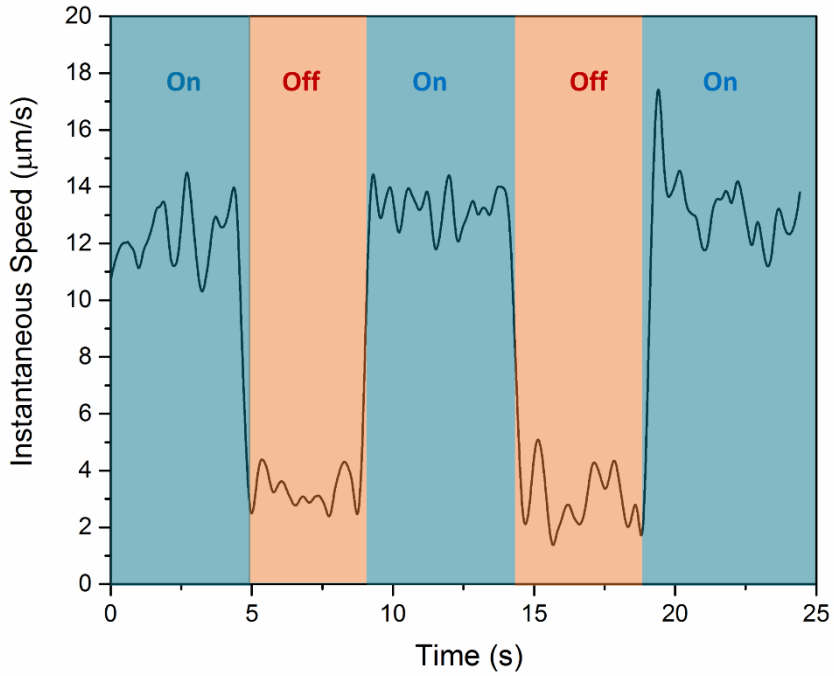

Figure 2.10 On/off speed control of a JHP-TiO_2-Au microswimmer when UV light is turned on (blue color) and off (orange color) under 0.1% H_2O_2 at 60% UV light intensity. Reproduced from reference [128].

2.7 Magnetic control of microswimmers

Controlling the direction of light-driven microswimmers is also one of the critical parameters for their potential applications. The control can be achieved in two ways: phototactically controlling them based on the direction of incident light [133] and remote magnetic steering [96]. Magnetic steering remains one of the most reliable ways to achieve precise control in comparison with phototactic control. Magnetic steering is achieved by incorporating a thin magnetic layer between the semiconducting TiO_2 and conducting Au layers. In our microswimmers, a 5 nm-thick layer of Co is sandwiched between the TiO_2 and 10 nm-thick Au layers. Co, being a conductive material, does not adversely affect the electron transfer between the TiO_2 and Au layers. There is still some electron loss at the Co interface, but it is small [96]. Co, being ferromagnetic and easier to deposit, enables easy steering control of microswimmers. A small magnetic field (~8 mT) is used to steer them. Figure 2.11 shows the directional swimming trajectories of the JHP-TiO_2-Co-Au microswimmers. It can be seen that,

as the angle of the magnetic field lines is controlled, the swimmers approximately follow the direction of the field.

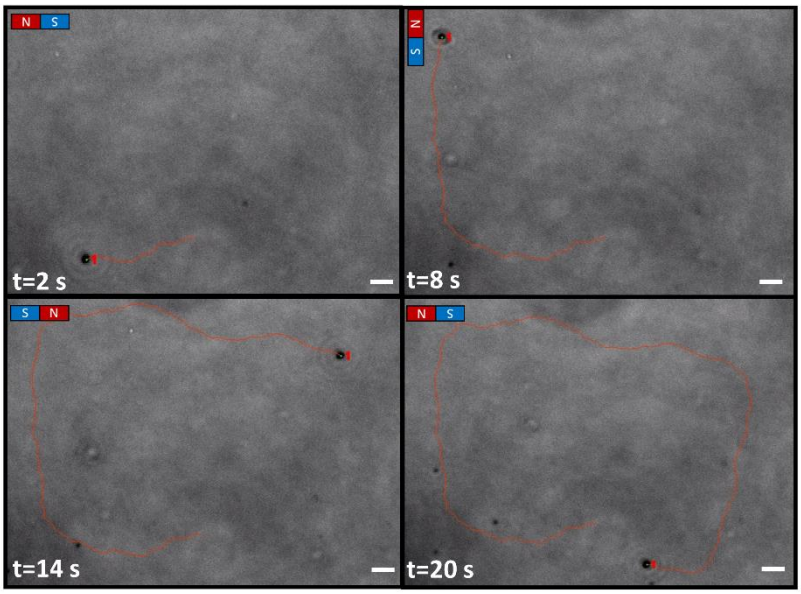

Figure 2.11 Snapshots of a magnetically guided JHP-TiO_2-Au microswimmers with a Co layer at various time intervals under 0.1% H_2O_2 at 20% UV light intensity. Scale bar is 5 μm. Reproduced from reference [128].

2.8 Active photocatalytic degradation

Environmental remediation of organic pollutants and dyes has been extensively explored using photocatalytic materials, such as TiO_2 and g-C_3N_4. Conventional dye degradation systems suffer from poor micromixing and mass transfer within the solution, which hinders the higher rate of degradation. Active matters and microswimmers enable rapid micromixing of the solutes when they swim in the solution [147]. This enables more active sites to be in contact with the dye, thus enabling faster degradation. TiO_2 as a photocatalytic material has been extensively used for dye degradation.

In this chapter, we demonstrate increased photocatalytic activity of JHP-TiO_2-Au microswimmers causing higher rate of degradation of methylene blue (MB) dye as a model pollutant. The photocatalytic degradation of the dye is studied by illuminating 10^{-6} M MB dye solution containing JHP-TiO_2-Au microswimmers under UV light. A solution containing 1 mg ($2.7x10^6$ microswimmers) of JHP-TiO_2-Au microswimmers is added to the dye solution containing 1.5% H_2O_2. The number of swimmers is counted in a haemocytometer. The resulting solution is stirred for 15 minutes before illumination to remove any dissolved oxygen present. The dye solution is removed at periodic intervals and their absorbance is measured

using a UV-Vis spectrophotometer. The dye degradation is estimated from the absorbance at different time intervals. The microswimmers show increased catalytic activity due to their active motion, causing higher intermixing of the solution. Due to this higher intermixing, more active sites of TiO_2 are on contact with the MB dye. To demonstrate the increased catalytic activity, dye degradation tests are performed with MB. The dye degradation is carried out in a solution of MB with microswimmers and 1.5% H_2O_2 under UV illumination. The effect of H_2O_2 on MB in the presence of UV has already been studied in the literature, where they do not show any significant degradation [152]. The average speed of JHP microswimmers in 10^{-6} M MB dye solution is found to be 16.5±2.3. This is 1.7 times faster than the speed of swimmers in pure water. This value is higher than previously published work on JS-TiO_2-Au microswimmers [147]. This shows the increase in speed is due to the combined effects of MB and the hollow porous structure. The degradation is also studied in a time-dependent manner using a UV Vis Spectrophotometer. Figure 6a shows the UV Vis spectrum of the dye during different degradation times in the presence of the JHP-TiO2-Au microswimmers. Figure 2.12b shows the kinetics of the MB degradation in the presence of microswimmers. The degradation degree of MB reaches 97% in 60 minutes. This is much higher than other Fenton systems using swimmers. This increased degradation is attributed to the increased local intermixing of the solution during the motion of microswimmers. Magnetically controlled JHP-TiO_2-Co-Au microswimmers can also be used for dye degradation. These swimmers can then be recovered using magnetic fields after the degradation is complete and reused again [153].

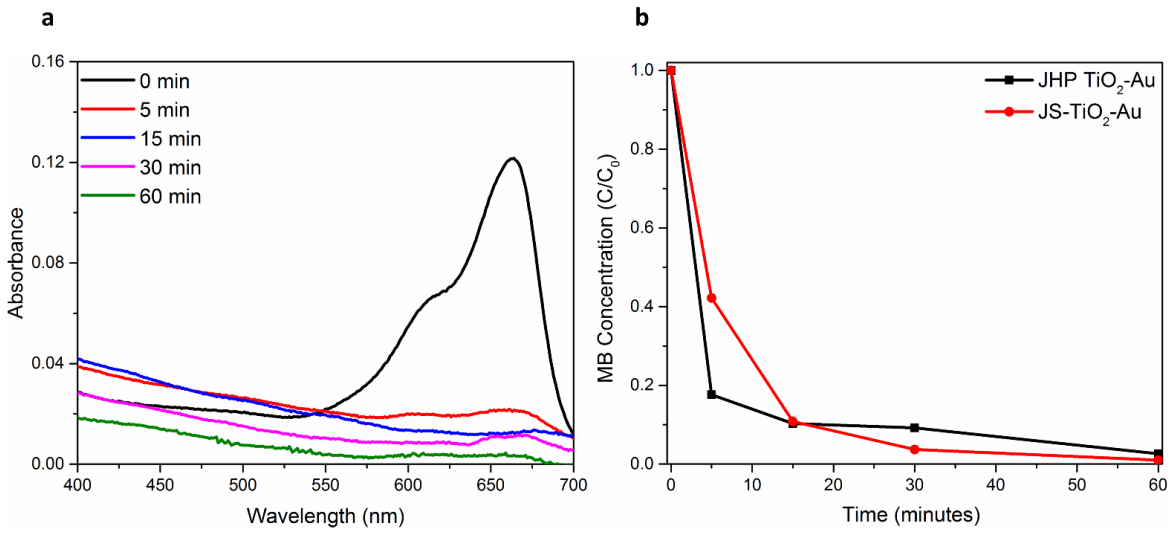

Figure 2.12 Environmental remediation of JHP-TiO_2-Au microswimmers. (a) UV-Vis spectrum of 10^{-6} M solution of methylene blue dye during different degradation times in the presence of JHP-TiO_2-Au microswimmers under 1.5% H_2O_2 at 100% UV light intensity. (b) Kinetics of methylene blue degradation in the presence of JHP-TiO_2-Au and JS-TiO_2-Au microswimmers. Reproduced from reference [128].

2.9 Doxorubicin loading

The drug loading ability of JHP-TiO_2-Au microswimmers is performed by loading 100 µg/mL solution of doxorubicin hydrochloride (DOX, Sigma-Aldrich) into the hollow mesoporous structure. JHP-TiO_2-Au microparticles are incubated in 1 mL of the DOX solution in DI water [154]. The resulting solution is stirred for 6 hours and subsequently rinsed to remove the free DOX. The DOX-loaded JHP-TiO_2-Au microswimmers are collected by centrifugation and suspended again in DI water and their swimming behavior is examined. Hollow mesoporous structures have been explored as carriers for different substances like drugs, biomolecules, and quantum dots [155], because they can have very high loading capacity of such substances due to their very high surface-to-volume ratio [156]. On the other hand, light-driven microswimmers with guidance control are potential active drug carriers in non-toxic fluids. In this chapter, we demonstrate the loading anticancer drug DOX on the JHP-TiO_2-Au swimmers. The DOX molecules are adsorbed on the surface of TiO_2 pores by electrostatic interaction [157]. The DOX-loaded microswimmers move in the presence of 0.1% H_2O_2 under UV illumination (15.5 mW/cm^2). The mean speed is shown to be 11.7 ± 1.1 µm/s. Figure 2.13a and b show the fluorescent images of the JHP-TiO_2-Au microswimmers with and without DOX loading. Figure 2.14 shows the MSD plot of the DOX- loaded microswimmers swimming

under UV illumination. The mean speed of the JHP-TiO_2-Au microswimmers is reduced by more than three times after DOX loading. This can be attributed to the adsorption of DOX molecules on the pores of hollow mesoporous structures [158], which could partially inhibit the flow and transfer of electrons on the surface of TiO_2 pores. The reduced electron flow between the TiO_2 and Au layers lowers the self-electrophoresis and thus the speed of the microswimmers. For swimming and delivering drugs in physiological fluids, the salt concentration needs to be low and the decreased speed of the drug-loaded swimmers needs to be improved, which are future works.

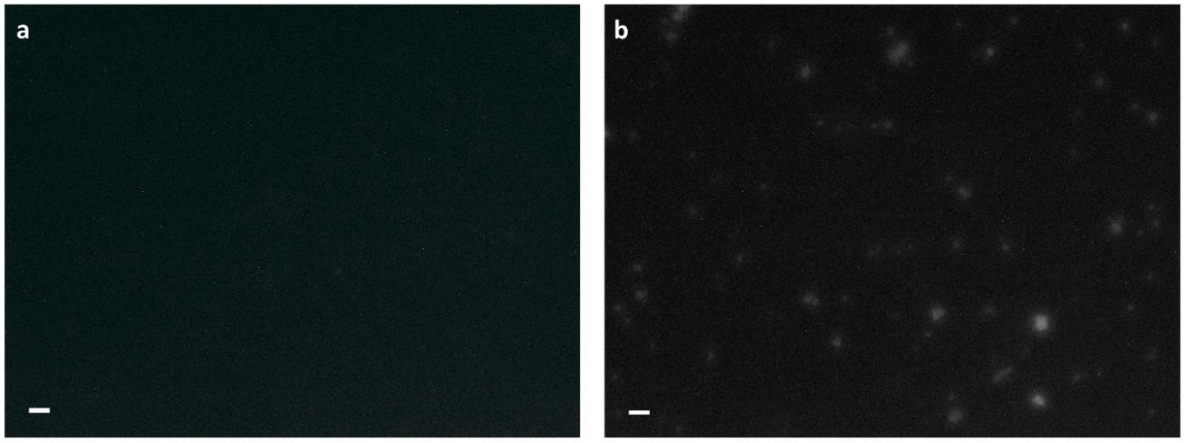

Figure 2.13 DOX loading on JHP-TiO_2-Au microswimmers. (a) Fluorescence image of JHP-TiO_2-Au microswimmers without DOX. (b) Fluorescence image of JHP- TiO_2-Au microswimmers loaded with DOX. The excitation and emission wavelengths were set at 470 nm and 525 nm. Scale bars represent 5 μm.

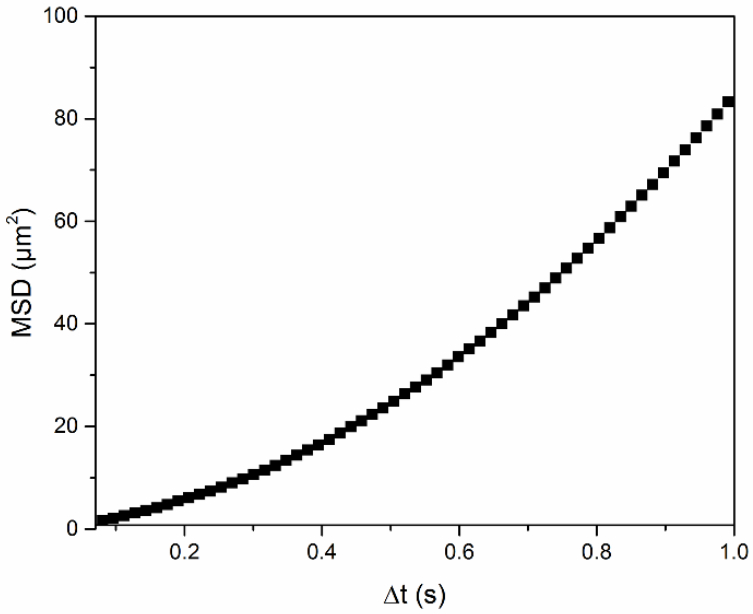

Figure 2.14 MSD experimental swimming motion data for the JHP-TiO_2-Au microswimmers loaded with DOX at 0.1% H_2O_2 at 15.5 mW/cm^2 UV illumination.

2.10 Summary

In this chapter we have developed a new design and fabrication methodology for creating JHP-TiO_2-Au microswimmers for environmental remediation and targeted active drug delivery. JHP-TiO_2-Au microswimmers show enhanced swimming speeds under low UV light intensity both in the presence and absence of H_2O_2. We find that the increased surface area by constructing the hollow mesoporous structure may be the most crucial factor for the enhanced swimming speed of microswimmers. The microswimmers exhibit directional motion under magnetic guidance with use of a thin Co layer. We have demonstrated their potential in environmental applications and targeted active drug delivery as a proof of concept. In order to enable the use of light-driven microswimmers in biological applications, visible light needs to be used instead of UV and toxic fuels like H_2O_2 need to be eliminated.

Chapter 3. Multiwavelength-steerable visible light-driven magnetic CoO-TiO_2 microswimmers

While current light-driven microswimmers require high light intensities, UV light or toxic fuels to propel them, powering them with low intensity UV-free visible light without fuels is essential to enable their potential high-impact applications. Therefore, in this chapter, a new material for light-driven microswimmers in the form of CoO is introduced. Janus CoO-TiO_2 microswimmers powered with low-intensity, UV-free visible light inside water without using any toxic fuels like H_2O_2 is proposed. The microswimmers show propulsion under full spectrum visible light with 17 times lower intensity than the mean solar intensity and UV light. The direction of swimming changes with the change of illumination from visible to UV light. In addition to being responsive, they are wavelength steerable and exhibit inherent magnetic properties enabling magnetic steering control of the CoO-TiO_2 microswimmers. The use of a low intensity fuel free propulsion enables their potential biomedical applications. The results of this chapter are reproduced from reference [159]. Dr. Byungwook Park and Prof. Metin Sitti contributed to the discussions and edited the manuscript. Dr. Surong Guo and Prof. Peter Van Aken performed and analyzed the EEL experimental data on reference [159].

3.1 Introduction

Chemically powered synthetic microswimmers have been inspired by natural biological motors for propulsion and control [12, 160, 161]. Their propulsion can be controlled by modulating the type of chemical reactions, such as catalytic or enzyme microswimmers. Also, light is an excellent power source for microswimmers, and light-driven microswimmers have shown tremendous potential for various applications, such as environmental remediation [80], drug delivery [162], and self-assembly [86]. Photocatalytic semiconductor materials have been mainly used to design light-driven microswimmers [86]. The most commonly-used semiconductor photocatalysts in light-driven microswimmers are titanium dioxide (TiO_2) [128] [163], and its various modifications [164, 165], ZnO [107], AgCl [89, 97, 108, 166], BiOI [167], $BIVO_4$ [168], Si [111, 119, 167], Cu_2O [109], Cu [97], SOM [169], CdS[170, 171], alloy [172], and Fe[170, 173]. Most of them are active only in the ultraviolet (UV) region, while the

microswimmers active in the visible light region require redox shuttles or other fuels to propel them. From these photocatalysts, Ag/AgCl-based microswimmers only have shown relatively high swimming speeds under visible light illumination [97]. When it comes to their potential applications, such as environmental remediation, they seem to be quite limited for the selection of the light source. Moreover, most of light-driven microswimmers often rely on using H_2O_2 to enhance their propulsion [174]. The addition of H_2O_2 would be many potential pitfalls in their practical applications due to their inherent toxicity.

Cobalt monoxide (CoO) can be an excellent candidate to create light-driven microswimmers. It has one of the highest overall photocatalytic efficiency (~5%) under visible light [175], and has the ability to break down water into both hydrogen (H_2) and oxygen (O_2) [176]. It also has the ability to break down water without the presence of any external reagents or donors. Initially, only CoO nanopowders showed increased catalytic activity, while CoO micropowders was found to be very less active in the presence of light [177]. Then, CoO microparticles with the specific crystallographic lattice structure have recently been found to be active in the presence of visible light [81, 178], unlike TiO_2 absorbing photons in the UV region [179]. Though the UV photons have more energy, they are not so widespread in the sun light. CoO is known to absorb light mostly in the visible and NIR regions [180]. To increase the activity of micron scale CoO micropowders, a CoO-TiO_2 heterojunction is used [181, 182]. The CoO-TiO_2 microswimmers can have both visible and UV light absorption capability [183]. Such property is due to the broader energy gap of the heterojunction, hence absorbing different light wavelengths.

In this chapter, we show that photocatalytic composite CoO-TiO_2 Janus microswimmers can be propelled by both low-intensity visible and UV lights. This was the first work to show the use of CoO for applications to microswimmers. In comparison with other light-driven micrswimmers in the literature [111, 165, 167], these microswimmers have one of the highest swimming speeds under UV-free visible spectrum and low-intensity light in the absence of any external fuels. We also demonstrate that the propulsion direction can be also changed with applied different wavelengths of light, where CoO is reactive to the visible light and TiO_2 is reactive to the UV light, creating another type of steerable microswimmers based on the incident wavelength, without the need for phototaxis to steer them. The use of wavelength-based steering enables potential applications of CoO-TiO_2 microswimmers in steerable navigation and cargo delivery. In addition, these microswimmers can be steered by

external magnetic fields due to the magnetic properties of CoO, without deposition of an additional magnetic layer during the fabrication process [184].

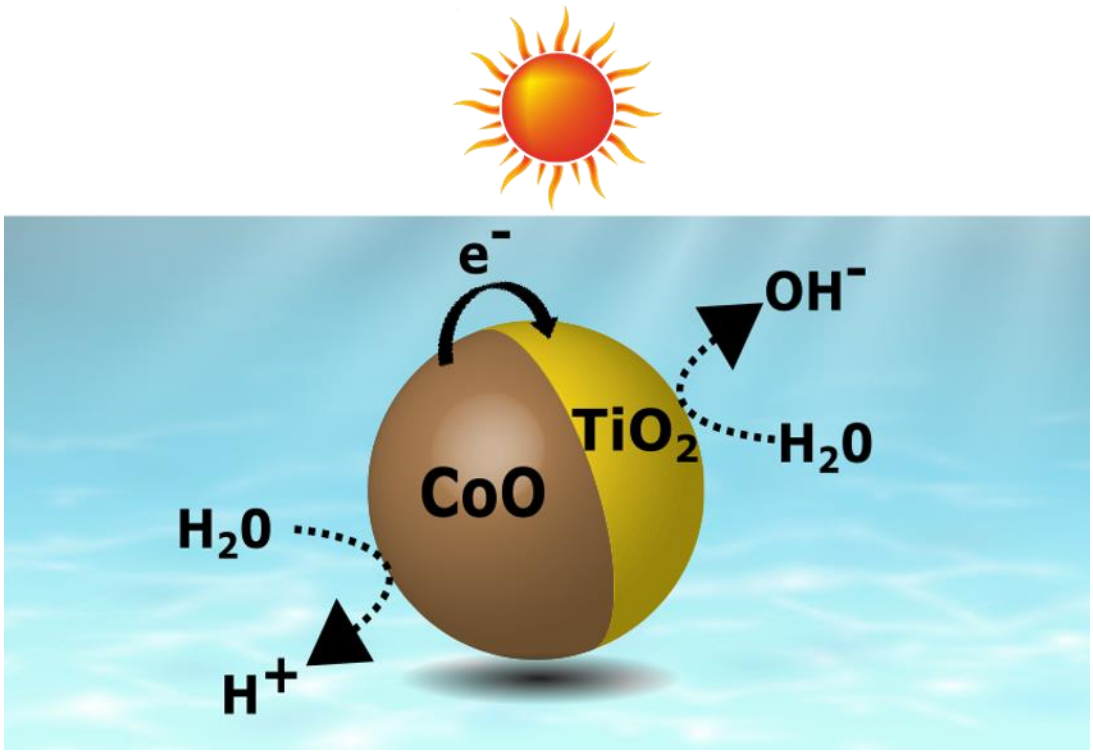

Figure 3.1 Schematic of CoO- TiO_2 light-driven microswimmer swimming in water. Reproduced from reference [159].

3.2 Microswimmer fabrication

3.2.1 Methods to create CoO-TiO_2 Janus particle

Two different approaches were taken in fabricating a CoO-TiO_2 based light-driven microswimmer. CoO is the less stable oxide of Co, due to these annealing steps have to be carried out to form CoO. Initially a 40 nm thin layer of CoO is sputtered on TiO_2 microparticles, the CoO is sputtered from a CoO target. The partial pressure of oxygen in the sputtering system is controlled so that the thin film is deposited as oxide and not as metallic Co. These CoO/Co_3O_4-TiO_2 Janus particles are then annealed in a rapid thermal annealing setup. They are annealed in a N_2 atmosphere at 400 ^oC with a raise of 10 ^oC/s and then held at that temperature for 400 s and then further ramped down to room temperature at the same rate. The rapid ramp of the temperature helps in the formation and crystallization of CoO. These Janus particles are then further characterized with XRD to determine to see if the CoO is single phase or has impurities of Co_3O_4.

In the second method Co_3O_4 microparticles have a size distribution of 2-6 µm. These microparticles are spherical in nature. Co_3O_4 microparticles are deposited on a silicon wafer by drop casting. A 40 nm-thick TiO_2 layer is sputtered on them. These Janus Co_3O_4-TiO_2 particles are then annealed in Ar atmosphere at 1000^oC in a systematic annealing to reduce Co_3O_4 to CoO. [175] Initially, the temperature is ramped up to 800^oC in 30 minutes and further heated to 1000^oC in 2 hours. The temperature is then held at 1000^oC for 10 hours. This dwell time allows for a stable CoO crystal structure. The annealing process helps in crystallizing the CoO microstructure. The Ar atmosphere allows the oxygen from the cobalt to diffuse resulting in the reduction of Co_3O_4 to CoO. [175] This process also crystalizes the TiO_2 to its rutile phase. The Ar is circulated at 25 Sccm throughout the annealing process. It is then subsequently cooled down to 900^oC in 30 minutes and then to room temperature in 10 hours. The slow cooling is essential to maintain the crystal structure and to prevent reoxidation of CoO. It also makes them photoactive. The annealing process makes the microswimmers reactive to the visible light. A reduction in size occurs due to annealing resulting in a smaller size dispersion of 1-4 µm. The particles are then sonicated and removed from the surface. These microswimmers are then used for characterization and swimming. We produce thousands of particles each run. There is batch variation due to the variation of particle coverage when doing a drop casting of the CoO particles.

3.2.2 Characterization of CoO-TiO_2 microswimmers

The CoO-TiO_2 microswimmers are fabricated by depositing a TiO_2 thin film on Co_3O_4 microparticles to create Janus particles and subsequent annealing under controlled conditions to form an annealed and crystalized Janus CoO-TiO_2 microswimmer. Scanning electron microscopy (SEM), transmission electron microscopy (TEM), x-ray diffractometry (XRD), x-ray photoelectron spectroscopy (XPS), electron energy-loss spectroscopy (EELS), and diffuse-reflectance spectroscopy (DRS) are used to characterize the structure, crystallinity and absorption spectra of the fabricated microswimmers. SEM and EDS are used to inspect their shape and element distribution. Additionally, XRD and XPS are used to confirm their formation of a CoO core. In the case of sputter deposited CoO, it is also found that there is a single CoO phase but with some Co3O4 impurities. The XRD data in Figure 3.2 of the CoO particles after annealing shows the presence of only CoO and not Co_3O_4.

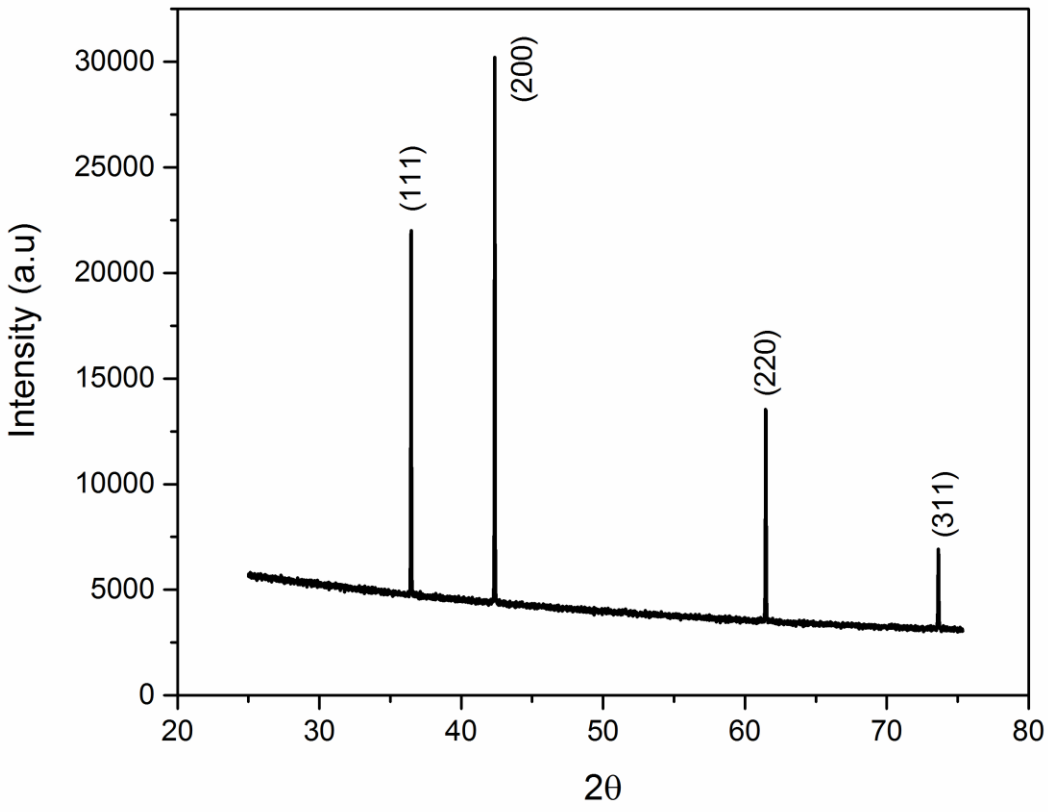

Figure 3.2 XRD of CoO-TiO_2 microswimmers with peaks indexed.

Their optical properties are characterized by EELS and DRS. A schematic of the Janus CoO-TiO_2 microswimmer is shown in Figure 3.4a. The SEM image in Figure 3.4b shows the

presence of TiO_2 half cap on the CoO particle, and Figure 3.3 shows that all of the particles have a Janus structure and their corresponding EDX. We observe that It can also be seen that the particles are not perfectly half capped, due to the inherent nature of sputtering deposition some particles have more than 50% and some have less than 50% and this coverage appears to be stochastic. Particles smaller than 2 µm have more than 50% coverage and particles larger than 4µm have less than 50% coverage. The contrast difference between the two layers indicates the presence of a Janus particle. It can also be seen that the CoO is faceted because of the crystallization that occurs when CoO is formed.

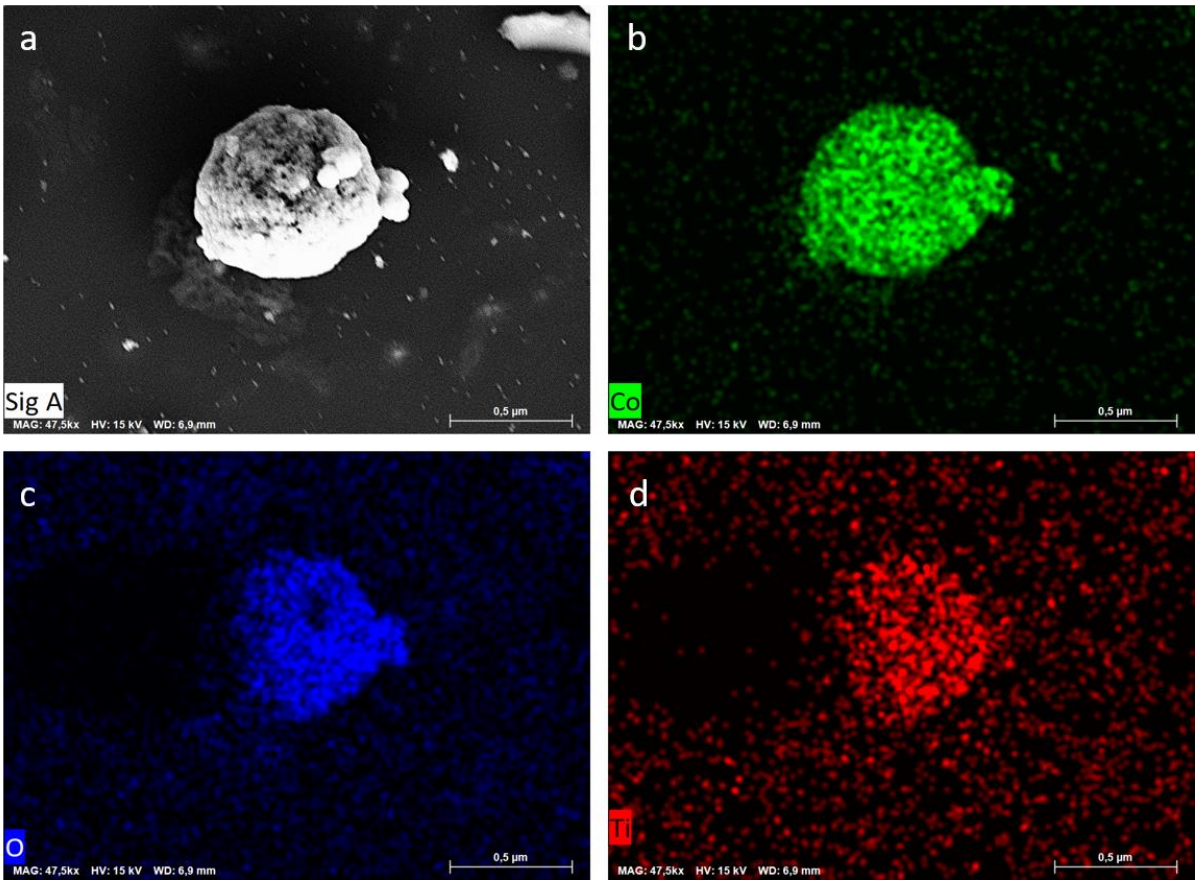

Figure 3.3 SEM and EDX of CoO-TiO_2 microswimmers. a) SEM image of CoO-TiO_2 microswimmers b-d) Co, O and Ti channel EDX images of two different CoO-TiO_2 microswimmers.

This crystallized structure results in formation of a porous surface, increasing the surface area of the microswimmers. We used energy-dispersive x-ray spectroscopy (EDS) in a scanning transmission electron microscope to qualitatively map the distribution of the major constituent elements of O, Ti, and Co in a CoO-TiO_2 particle. The signals of Ti, Co and O elements on Figure 1c, d also indicate the presence of a Janus structure. The XPS data is used to conclusively prove the presence of CoO. Figures 3.4e show the XPS spectrum of Co 2p of

CoO microparticles. The XPS spectrum of CoO shows characteristic peaks of shoulders for the main $2P_{3/2}$ and $2p_{1/2}$ indicating the presence of a pure CoO phase. DRS is used to give information on the optical bandgap and absorption spectrum of the material. A Carry 5000 UV-Vis-NIR spectrometer with an integrating sphere is used for DRS. The slope of the DRS is used to calculate the optical bandgap of the material using the Kubelka-Munk function $\mathrm{F(R)} = (1-R)\mathrm{F} = (1-R)^2/2R$, where R is the reflectance. Figure 3.4f show the DRS data for the CoO particles. The results show an onset absorption at 450 nm with additional absorptions from 600 nm. In this case, the optical bandgap of the synthesized CoO microparticles is 2.5 eV.

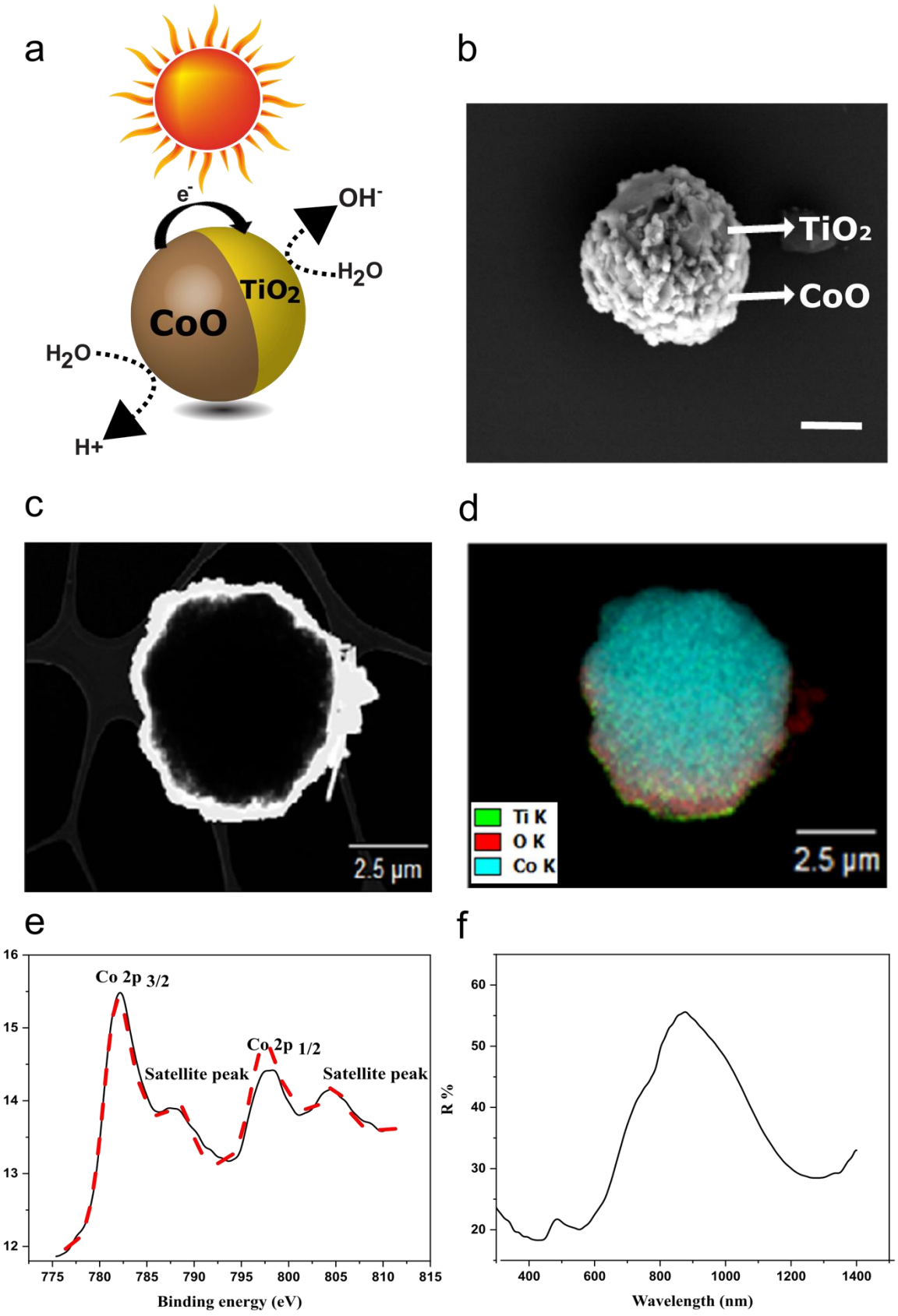

Figure 3.4 Characterization of CoO-TiO_2 microswimmers. a) Schematic of the proposed CoO-TiO_2 Janus particle-based microswimmers. b) SEM image of a CoO-TiO_2 microswimmer.

Scale bar: 1 µm. c) TEM image of the microswimmer. d) EELS data of O and Co and Ti in the microswimmer. e) XPS data of Co in the microswimmer with red dotted lines indicating the theoretical fitting. f) DRS absorption of CoO microswimmers and the resulting optical absorption energies from the Kubelka-Mulk function. Reproduced from refernece [159].

3.2.3 EELS characterization

EELS is a powerful tool to probe the electronic structure and response of an object in a broad spectral range, covering the ultraviolet to the infrared, with a nanometre-spatial resolution. Scanning transmission electron microscopy-based electron energy loss spectroscopy (STEM–EELS) measurements were performed with the sub-electron-volt sub-angstrom microscope (SESAM, Zeiss, Oberkochen, Germany) at an acceleration voltage of 200 kV. The full convergence and collection angles were 14 and 13 mrad, respectively. The acquisition time for each EEL spectrum was 1.5 s. EDX spectrum imaging was conducted with Thermo Scientific NORAN EDX-System. As seen in Figure 3.4a and b, the fabricated microswimmer has a broad absorption band from 0.5 to 4.0 eV, covering the spectral range of the infrared, the visible and the ultraviolet light. Apparently, the local absorption varies from spot to spot, because it is sensitive to the local environment and the interaction geometry. The peak on spectrum 1 (indicated by the red triangle) is at 3.1 eV, which is close to the rutile TiO_2 bandgap of 3.13 eV. Another peak on spectrum 4 (indicated by the red triangle) displays at 1.78 eV, possibly corresponding to the CoO bandgap of 1.76 eV.

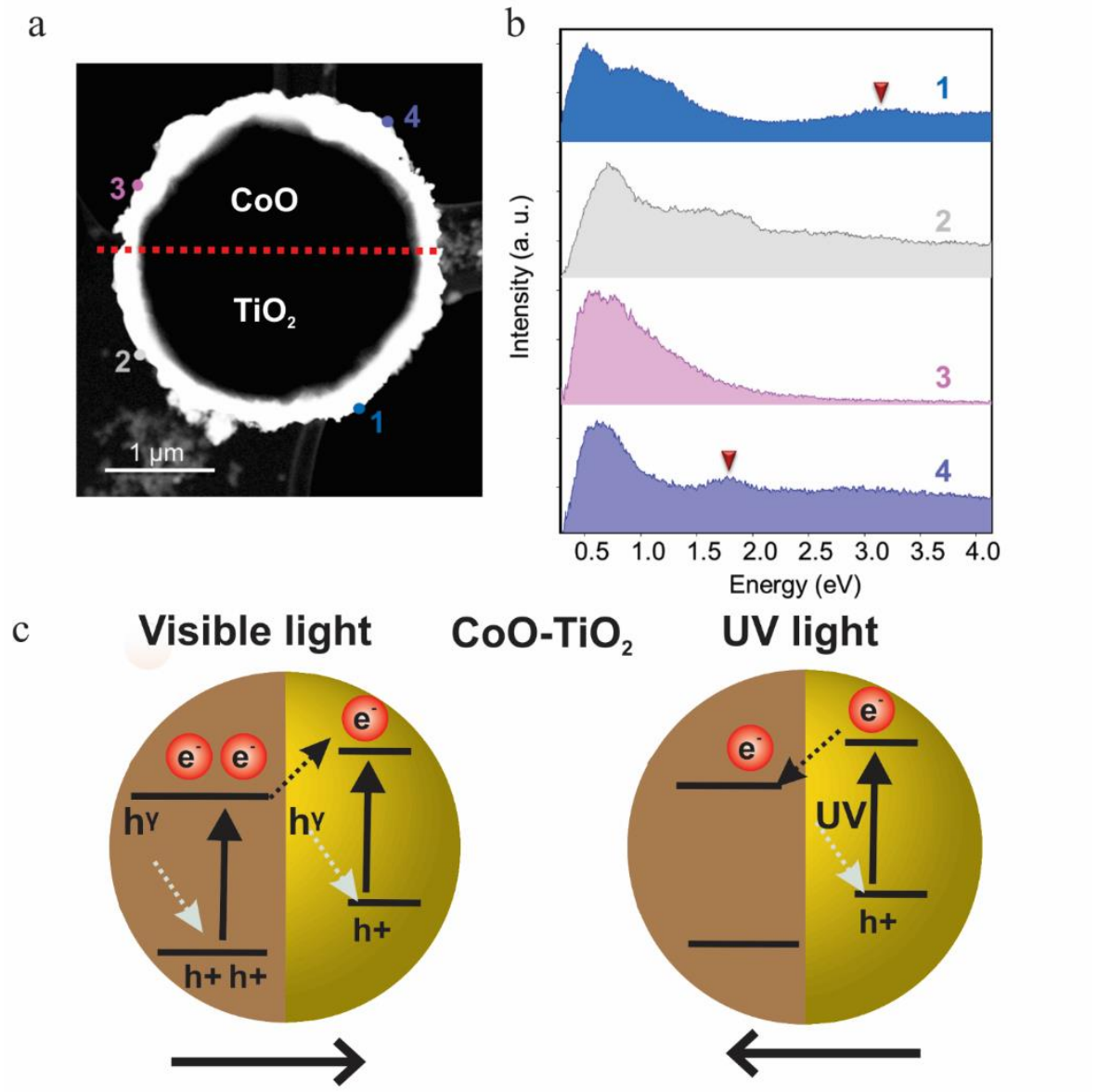

Figure 3.5 EELS analysis and mechanism of swimming. a) High-angle annular dark field (HAADF) imaging of a CoO-TiO_2 microswimmer deposited on a thin carbon film. b) Four zero-loss-peak-subtracted electron energy loss spectra (EELS) acquired around the same particle as labeled in the HAADF image. c) Band structure of the CoO-TiO_2 microswimmer under visible and UV illumination. Reproduced from reference [159].

3.3 Swimming under visible light

3.3.1 Setup for swimming

In order to measure the swimming properties of the microswimmers, a Thorlabs M365L2 (Germany) UV lamp is used for illumination through a Zeiss Axio A1 inverted microscope. The videos are recorded from the microscope using a LD Plan-NeoFluar 40x objective lens and Axiocam 503 CCD camera at 62 frames per second. The light path through the objective of the microscope causes focusing effect on the objective plane of the imaging. In the case of visisble light propulsion, the white light comes from the top through a Zeiss optical LED with a wide wavelength region as shown on Figure 3.5.

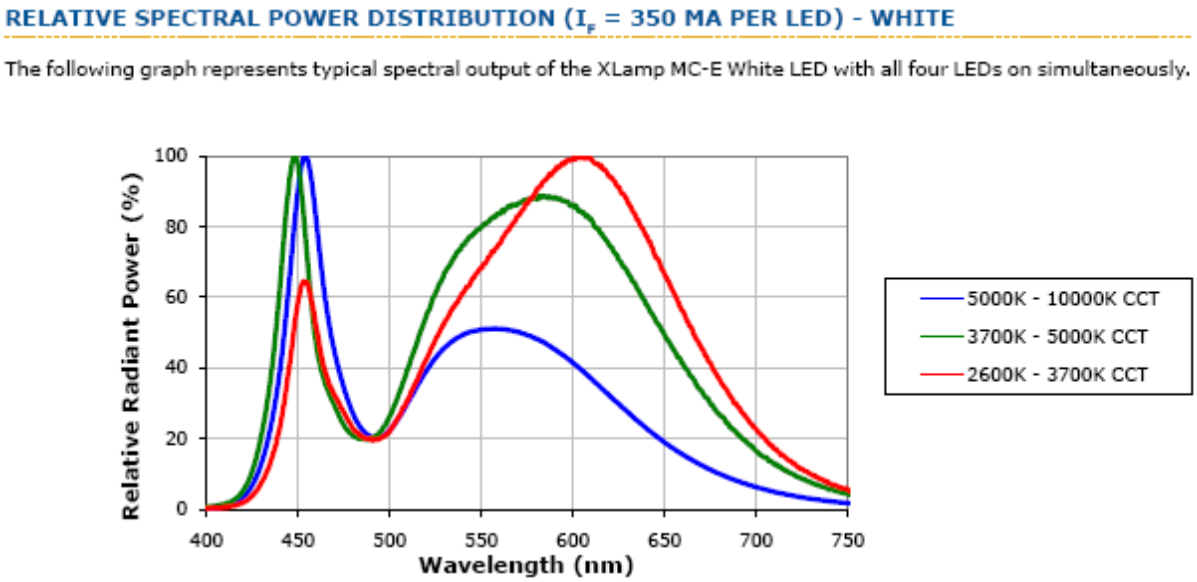

Figure 3.6 Spectrum of visible light used for propelling CoO-TiO_2 microswimmers with a 3700-5000K CCT used (Information from Carl Zeiss).

3.3.2 Swimming under visible light

A broad-spectrum white-light LED with intensity of 6 mW cm^{-2} is used to propel the microswimmers. The spectrum of the visible light has two major peaks at 450 nm and 590 nm with no peaks at the UV region, as shown in Figure 3.5. Such intensity of the light used is lower than the other visible light-driven swimmers in the literature.[185] meaning that our swimmer design may have higher swimming efficiency. The mean light intensity is 100 mW cm^{-2}, which is 17 times lower than intensity of light used for swimming. Moreover, our microswimmers do not require any additional fuel for propulsion, where water just acts as their fuel. Figure 3a shows the mean-square-displacement (MSD) plots of their swimming trajectories under visible-light illumination. The videos are recorded from the microscope using a LD Plan-

NeoFluar 40x objective lens and Axiocam 503 CCD camera at 62 frames per second. The swimming behaviour of the swimmers is systematically investigated by two-dimensional MSD swimming analysis on the captured videos using a custom MATLAB code.

When the microswimmers are illuminated by visible light, they swim with a mean speed of 11.5 ± 0.7 μm s^{-1}, as shown in Figure 3.6b. Twenty microswimmers from different sample batches are tracked to calculate such mean speed. It is likely that some of the microswimmers in a production batch may not be active, due to the inhomogeneous temperature distribution inside the annealing chamber. When it comes to the swimming mechanisms of the microswimmers under visible light, two mechanisms can be considered. First, the microswimmers swim due to a photocatalytic water splitting. The modified phase structure of TiO_2 allows band bending shown in Figure 3.6c, which may allow the transfer of electrons to the TiO_2 conduction gap, creating an electric dipole around the particle. It is likely that the combined bandgaps of CoO-TiO_2 may break down water to photogenerated products at the hydrogen and oxygen evolution potentials, due to the occurred redox reaction [103, 186-188]. Secondly, the microswimmers move due to self-electrophoresis mechanism due to the transfer of electrons between the two halves of the Janus structure. An ionic salt solution (1 M NaCl) is used to verify this mechanism. Under the illumination, no propulsion is observed. When the microswimmers in 0.5% H_2O_2 solution are illuminated, no increase in propulsion is observed as seen on Figure S5. This may be due to the presence of NaCl inhibiting the Debye layer during the propulsion of the microswimmers. The presence of salts affects the ionic mobility on the surface of the microswimmers, leading to the ions recombining on the surface of the microswimmers [189]. Moreover, the swimming speed can be regulated by the light intensity. The mean speed of the swimmers at intensity of 1 $mWcm^{-2}$ is 2.07 ± 0.11 μms^{-1} at 3 $mWcm^{-2}$ is 6.2 ± 0.2 μms^{-1} and 11.5 ± 0.7 μm s^{-1} at 6 $mWcm^{-2}$. The lower speed of the microswimmers can be attributed to the lower energy of the photons in the incident light. Plasmonic microswimmers like AgCl [97] have shown higher speeds in the presence of blue light, but they are photo-corrosive and work by breaking down to Ag^+ and Cl^- ions under illumination, resulting in ionic contaminants limiting their use to potential environmental applications. Other light-driven microswimmers driven at low light intensities[167, 172, 190] depend on addition of donors and redox shuttles for swimming in water. To the end, the CoO-TiO_2 microswimmers perform the highest swimming speed at a low-intensity, full-spectrum visible light through photocatalytic water splitting without the use of redox shuttles, compared to the previous studies [84, 97], due to better absorption of visible light, resulting in higher photocatalytic activity.

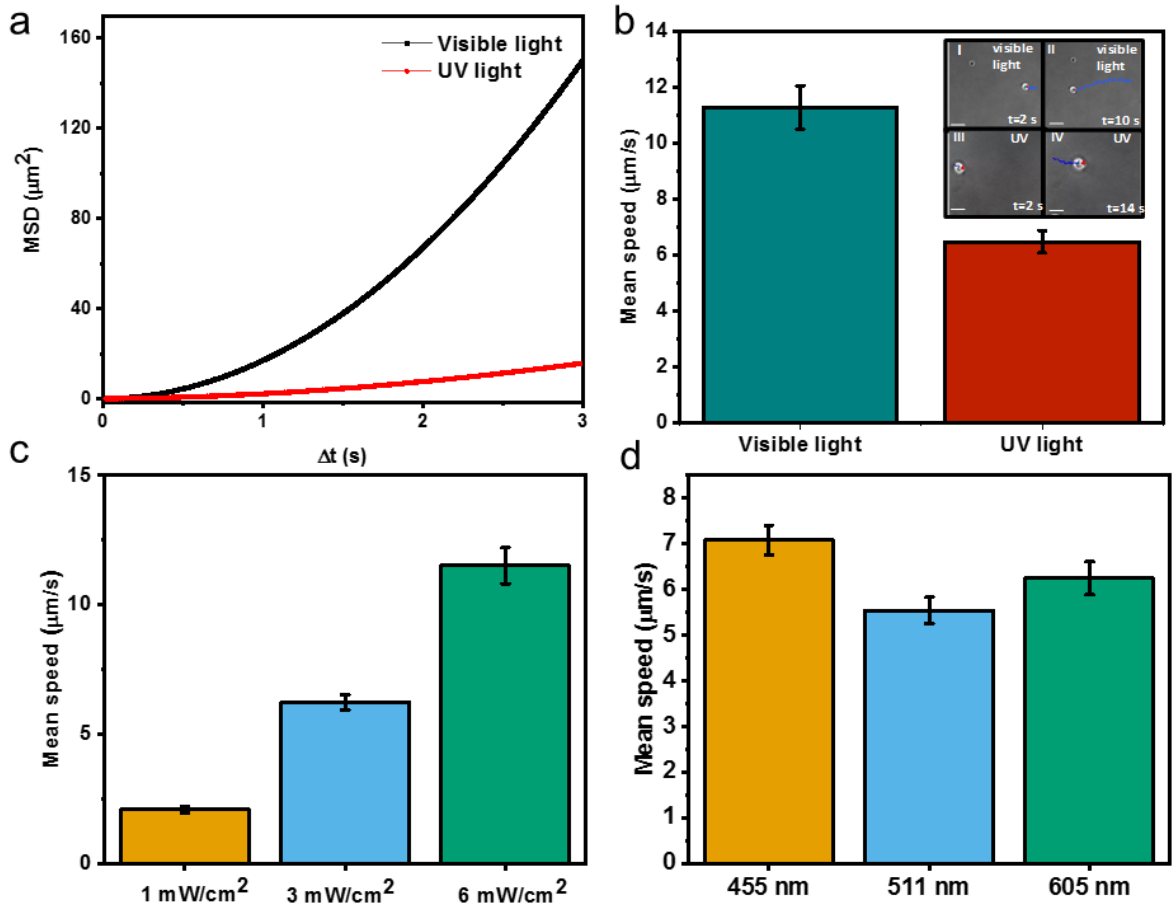

Figure 3.7 Swimming characterization of CoO-TiO_2 microswimmers. (a) Average (N=20) mean-square-displacement (MSD) data as a function of the time interval for the CoO-TiO_2 microswimmers in water under the visible and the UV light. (b) Average (N=20) mean speeds of the visible and UV light-driven swimmers with p=0.028, the error bars represent standard error of mean. Inset photos: Snapshot images of the swimmers, placed in an aqueous environment at various time intervals under both visible (I, II) (Supporting Video 1) and UV (III, IV) (Supporting Video 2) light illumination. c) Average (N=20) mean speed of the different intensities of visible light-driven swimmers, the error bars represent standard error of mean. d) Average (N=20) mean speed of the different wavelengths of visible light-driven swimmers, the error bars represent standard error of mean. Reproduced from refernece [159].

3.3.3 Switching the swimming direction under different light wavelengths

Thorlabs M365L2 (Germany) UV lamp with 365 nm wavelength and 15.5 mW cm^{-2} is used for illumination through a Zeiss Axio A1 inverted microscope When UV light is incident on the microswimmers, the TiO_2 side becomes more active as it absorbs the UV light effectively. In this case, the propulsion is due to light-driven self-electrophoresis, with the TiO_2 side becoming the driving side. The visible light-driven and UV light-driven microswimmers move

with a mean speed of 6.5 ± 0.4 µm s^{-1}. The MSD and mean speed are shown in Figure 3a and b. When the UV light is incident on the microswimmer, TiO_2 absorbs the photons due to the energy gap of 3.2 eV resulting in charge transfer to the CoO. The mechanism of propulsion is similar to other TiO_2-based microswimmers in the literature [96, 128], and their mechanism is further validated in 0.5% H_2O_2 solution. These microswimmers show increased propulsion indicating TiO_2 breaks H_2O_2 under the UV light as shown in Figure 3.7. The change in the active cap side makes the microswimmers move in a direction opposite to the direction they move under the visible light illumination.

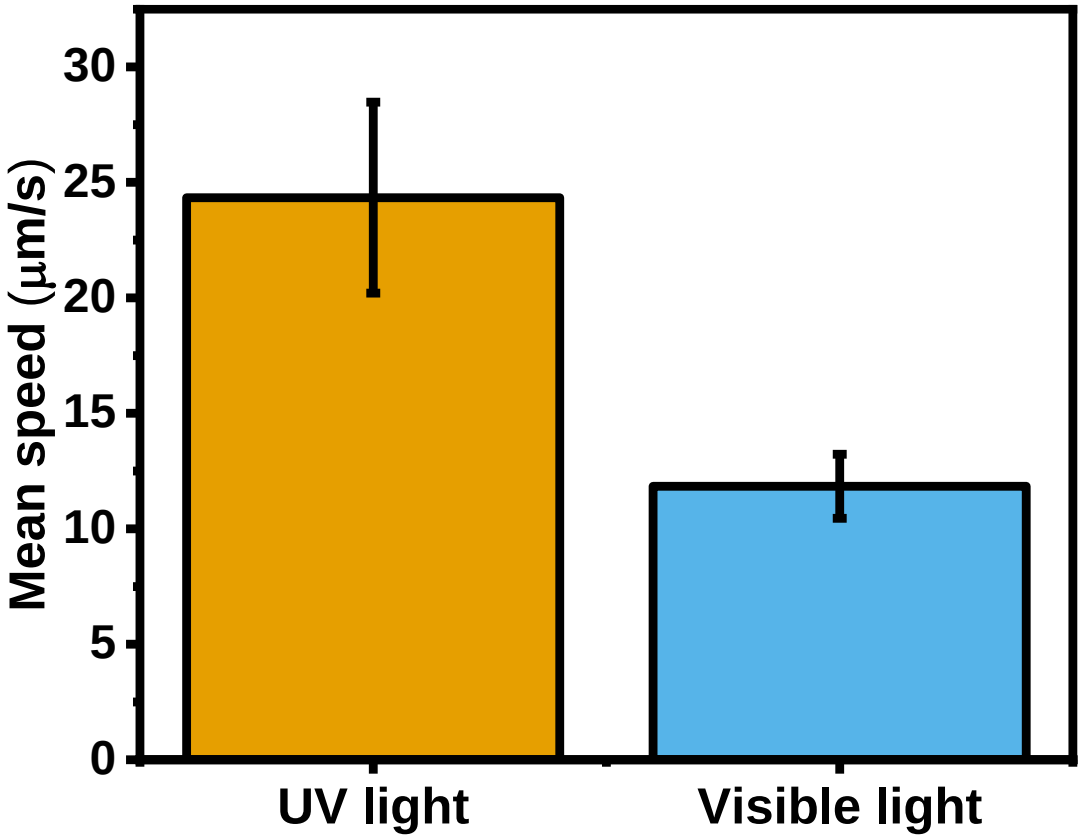

Figure 3.8 Mean speed of CoO-TiO_2 microswimmers with 0.5% H_2O_2 as fuel. Reproduced from refernece [159].

The visible light used for propulsion of the swimmers is broad spectrum, ranging from 400 to 700 nm. In order to measure the dependence of CoO-TiO_2 swimmers on the wavelength of illumination, three wavelengths in the visible light, 455 nm, 511 nm and 605 nm at 20 mW/cm^2 intensity are selected. The mean speeds of the swimmers at different wavelengths are

shown in Figure 3.6d. The fastest swimming speed is 7.1 ± 0.3 µm/s at 455 nm and the slowest one is 5.5 ± 0.3 µm/s at 511 nm. This is due to the presence of an absorption peak of CoO around 450 nm, while the absorption is the lowest at 511 nm resulting in a lower speed. The mean speed of the swimmers in individual wavelengths is still two times lower than the mean speed under the visible light, indicating that our swimmers absorb a plethora of wavelengths, enabling better charge separations and thus faster mean speeds.

3.4 Guiding the CoO-TiO_2 microswimmers

3.4.1 Wavelength control

Controlling the swimming direction without use of phototaxis enables additional degrees of freedom for the control of light-driven microswimmers. Thus, the CoO-TiO_2 microswimmers have the unique ability that, the direction of their propulsion can be changed by illuminating visible or UV light on the same swimmer. The use of different wavelengths of light enables activation of different layers of the microswimmers, causing the microswimmers to change their swimming direction depending on the symmetry of the Janus structure. However, they are inherently asymmetry formed during the fabrication process and crystallization, resulting in an imperfect Janus structure. In Figure 3.8a, the trajectories of five different CoO-TiO_2 microswimmers from different batches are monitored to confirm the symmetry effect. The microswimmers are first illuminated with visible light and then successively illuminated with UV light. Under visible light illumination, they become the driving side. The CoO being larger in volume within the swimmers, combined with larger sizes of the swimmers, causes them to move in a straight trajectory without much rotation or tumbling, as seen in the trajectories of the microswimmers. When the swimmers are only illuminated with UV light, the TiO_2 side acts as the driving side and the CoO side is passive, leading to a change in the swimming direction. Under UV illumination, there is a change in the electron field direction around the swimmers, with the electrons now moving from the CoO to the TiO_2 side, resulting in direction change for the microswimmers.

3.4.2 Magnetic control

A thin film of magnetic materials, such as Co or Ni, has been predominantly applied to steer the microswimmers. Additional magnetic layer, however, may lower the speed of swimming, which hampers the electron transfer between different layers of the Janus structure [128] and thus obstructing the charge separation. In the case of CoO-TiO_2 microswimmers, there is no need for an additional magnetic film coating. This unique characteristic of the microswimmers

comes from the inherent magnetic properties of CoO. CoO is known to be antiferromagnetic, though its Neel temperature is only at 298 K [191], above which they are paramagnetic. Due to the oxygen deficiency created during the annealing process, some Co is formed in the crystal lattice of CoO. Co is ferromagnetic in nature and provides the magnetic property, which can benefit performance of the microswimmers. This property of the CoO-TiO_2 microswimmers can be characterized by vibrating sample magnetometer (VSM) measurements. The hysteresis curves shown in Figure 3.8 (d) indicate the presence of Co on the swimmers making them ferromagnetic in nature. They can also be steered using relatively low-strength magnetic fields (~8 mT) applied by an external permanent magnet. The direction of the microswimmers can be controlled by changing the direction of the applied external magnetic field. Figure 3.8c shows the trajectory of the microswimmers under the applied magnetic field.

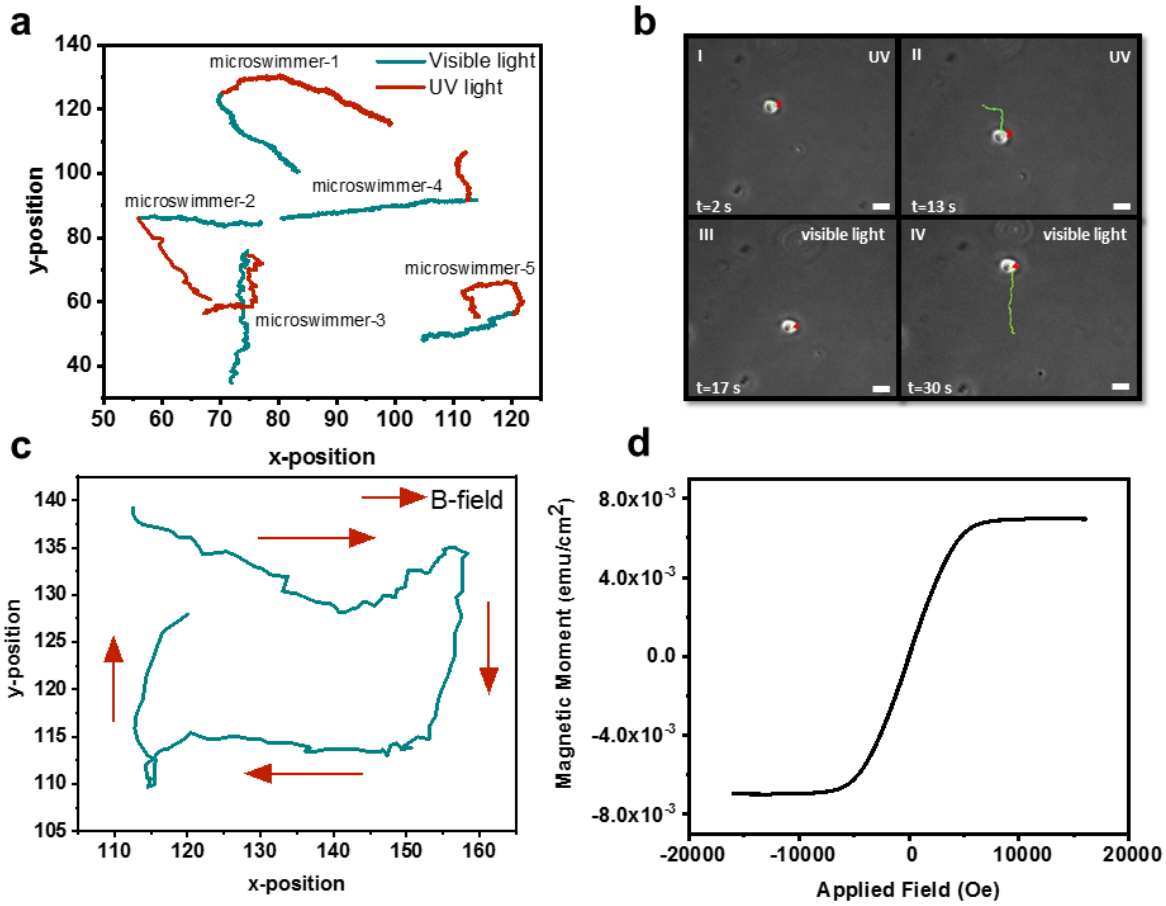

Figure 3.9 Magnetic and optical control of microswimmers. a) Trajectories of wavelength control of the CoO-TiO_2 microswimmers under visible and UV light b) Snapshots of the microswimmer video (Supporting Video 3) at various time intervals with UV light (I, II) and visible light (III, IV). Scale bar: 5 µm. c) Trajectory of the magnetically-guided microswimmer

under the visible light at various time intervals. Scale bar: 5 μm. d) VSM data showing the magnetic properties of the microswimmer. Reproduced from refernece [159].

Multiple cycles of successive light switching between visible and UV wavelengths result in change in direction each time (Figure 3.9). Hence, the direction of swimming can be reversed when the type of the illumination is changed, which is potentially controlled by regulating the wavelength of light. This wavelength-dependent direction change enables another mode of control for light-driven microswimmers, which to the best of our knowledge, has not been explored in the literature yet. This wavelength-based steering combined with their ability to load drugs and cargos would in the porous structure of the swimmer body would enable potential applications of visible light-driven swimmers in future *in-vivo* cargo delivery applications.

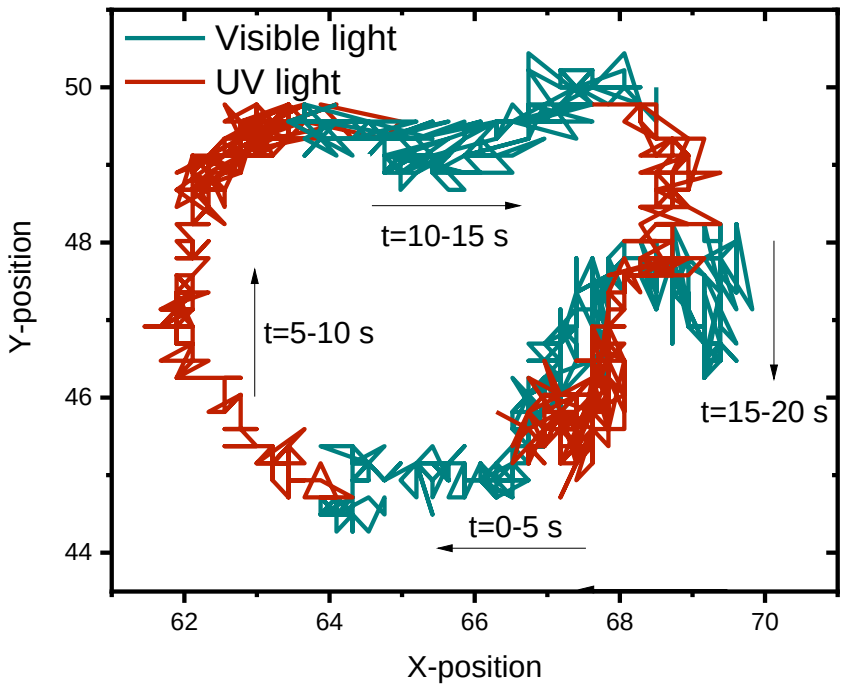

Figure 3.10 Snapshots of a light-driven CoO-TiO_2 swimmer at various time intervals with the visible light (I, II) and the UV light (III, IV). Scale bar: 5 μm.

3.5 Summary

Here, we have developed a fabrication methodology for creating multi-wavelength-responsive CoO-TiO_2 microswimmers propelled by low-intensity, UV-free, visible-light illumination. The microswimmers show enhanced swimming speeds under both visible and UV light

illumination and are multi-wavelength controllable, enabling direction change of the microswimmers by changing the wavelength of the light. The microswimmers are active under both visible and UV lights due to the unique combination of materials, allowing for selective absorption in both the sides of the Janus structure, causing the swimmers to change their swimming direction. Moreover, they can be precisely steered by the external magnetic field direction since CoO is magnetic. Such microswimmers have potential applications in target drug delivery.

Chapter 4. Carbon Nitride-based Light-driven Microswimmers with Intrinsic Photocharging Ability

So far, many photoactive molecules and materials have been adapted to serve as light-driven microswimmers by decoration with electrocatalysts [68, 85]. However, photocatalytic propulsion has mostly been realized with inorganic semiconductors, such as TiO_2 [83, 91, 92, 98, 100, 101, 103, 104, 107, 109, 119, 124, 130, 167, 192, 193] [159]. A transition to nature-inspired, organic microswimmers is thus of high interest, especially regarding potential improvements in biocompatibility, tunability and cost [194]. In recent years, organic semiconductors have become a prominent class of materials for (opto)electronics and photocatalysis [195-198], which renders them promising material candidates for microswimmers as well. In this chapter, we investigate the light-induced propulsion of PHI Janus particle-based microswimmers with caps consisting of Au, Pt and SiO_2, and we demonstrate that these properties can be exploited to realize efficient microswimmer propulsion not only in the presence, but also in the absence of light. Our findings reveal the light-induced surface catalytic processes and indicate that the reduction reaction, which is responsible for the microswimmer propulsion with alcohol donors in ambient conditions, is not the hydrogen evolution reaction (HER), but rather the oxygen reduction reaction (ORR), or more generally, the formation of reactive oxygen species (ROS), even when Pt or Au are used as co-catalysts. Under optimized conditions, our PHI-based Janus microswimmers move with comparable speeds of similar, melon type CN_x-based microswimmers and we demonstrate propulsion with visible light only [199, 200].

Making use of the dual functionality of light absorption and charge storage, we further show that light-induced charging is possible in H_2O_2, enabling persistent enhanced propulsion after the illumination was stopped, up to a duration of 24-32 times longer than the illumination period. This “solar-battery swimming” concept potentially enables new micro/nanomachine applications, such as drug delivery and environmental remediation under dark conditions, e.g., inside the human body, and *in situ* power supply for micro/nanomachines. The results of this chapter have been previously published in reference[201]. Photoelectrochemical measurements and hydrogen evolution measurements were performed by Dr. Filip Podjaski

and Julia Kroger. Dr. Filip Podjaski assisted in the design of experiments and writing of manuscript published in reference [201].

4.1 Introduction

Microswimmers are micron-scale wireless machines that are propelled in fluids by converting energy made available in their surroundings, such as chemical bonds, light, magnetic and acoustic fields [124, 202]. Such autonomous propulsion makes microswimmers highly attractive, active micro-devices in various biomedical and environmental applications [16]. While the use of sacrificial reagents can provide chemical energy for propulsion, it requires their continuous supply [12] and makes directional control difficult. Light however is abundant and one of the most widely exploited "fuels" to propel microswimmers photocatalytically [68, 122], enabling temporally and spatially controlled motion, called phototaxis [123]. Two light-driven propulsion mechanisms are possible for Janus microparticle-based microswimmers. The first mechanism is self-diffusiophoresis [203], which is induced by diffusion of catalytically converted species in solution due to the surface reactions of the photocatalyst or its capping material. The production of a concentration gradient of reduced and oxidized species leads to convection and spontaneous motion of the microswimmer along the gradient, enabling continuous propulsion [12, 27]. The second mechanism is self-electrophoresis [203], which is characterized by the transfer of electrons between the different layers of the Janus photocatalyst, generating momentum transfer (propulsion) by the formation of an electric field, which is balanced by convection of charged species generated by surface redox-reactions.

In the case of organic materials only a few examples of organic materials being used for light-driven self-diffusiophoretic or -electrophoretic propulsion have been reported [199, 200]. They rely on agglomerated, melon-based "graphitic" carbon nitrides (CN_x), which consist of strictly alternating carbon and nitrogen atoms forming heptazine units that are linked by imide bridges to one-dimensional (1D) polymer chains. Among the most recent and most active hydrogen evolution photocatalysts is poly(heptazine imide) (PHI) (Figure 4.1 a) [198, 204], a 2D CN_x with intriguing photophysical properties: [198] PHI has the ability to store photogenerated electrons in a long-lived photo-reduced state for days after illumination is stopped, with a capacity ranging up to 96 C/g [204-206]. These electrons can be discharged on demand, i.e., by the time-delayed addition of a co-catalyst that reduces water to hydrogen. As a consequence, the light and dark reactions of photocatalysis can be decoupled to produce solar fuels under dark conditions, akin to the processes occurring in natural photosynthesis [206].

This concept called *dark photocatalysis* can be extended to electrical charge transfer to realize new types of solar batteries [206, 207].

4.2 PHI Synthesis

PHI was syntesized according to a procedure described in the literature [198, 206]. In brief, melamine (5.0 g) was heated in a tube furnace in a quartz glass boat to 550°C for 12 h with a heating rate of 5°C/min under Argon (Ar)-flow. After cooling to ambient temperature, a yellow powder (2.0-2.5 g) was obtained. 1.5 g of this product (Melon) were thoroughly ground with KSCN (3.0 g), which was heated overnight to 140°C in vacuum to evaporate water. The mixture was heated in a tube furnace in an Alox boat to 400°C for 1 h and 500°C for 30 min with a heating rate of 30°C/min under Ar-flow. The Alox boat with the CN_x was sonicated two times for 15 min in 80 mL of water to disperse the yellow product. This suspension was washed six times with DI water by centrifugation (20,000 rpm). The insoluble product was dried in vacuum at 60°C overnight. The obtained PHI was used for the fabrication of microswimmers.

4.3 PHI-based Janus microswimmer fabrication

To obtain microparticles of PHI for the microswimmer preparation, 0.3 g of the material was sonicated in 200 ml DI water in an ice-cooled bath for 2 h, while shaking the suspension by hand every 30 min in addition. The obtained suspension was then centrifuged at 2000 rpm for 20 min to agglomerate smaller particles that were used for photoelectrochemical purposes. The supernatant containing larger particles was removed for the Janus particle fabrication. These were re-sonicated for 30 minutes and centrifuged at 1500 rcf. 500 µl of the stock solution with a concentration of 3 mg/ml was suspended in 10 ml ethanol, followed by further sonication for 30 minutes. 100 µl of the resulting suspension was drop cast on to the glass wafer resulting in a thin layer of the particles on the substrate. 30 nm of Pt was sputtered on top to form Janus particles. The wafer was then sonicated in water to release the particles that were then used for further experiments. The same procedure was repeated for fabrication of PHI-Au, PHI-SiO_2 and the bilayer PHI-Ni-Pt Janus particles.

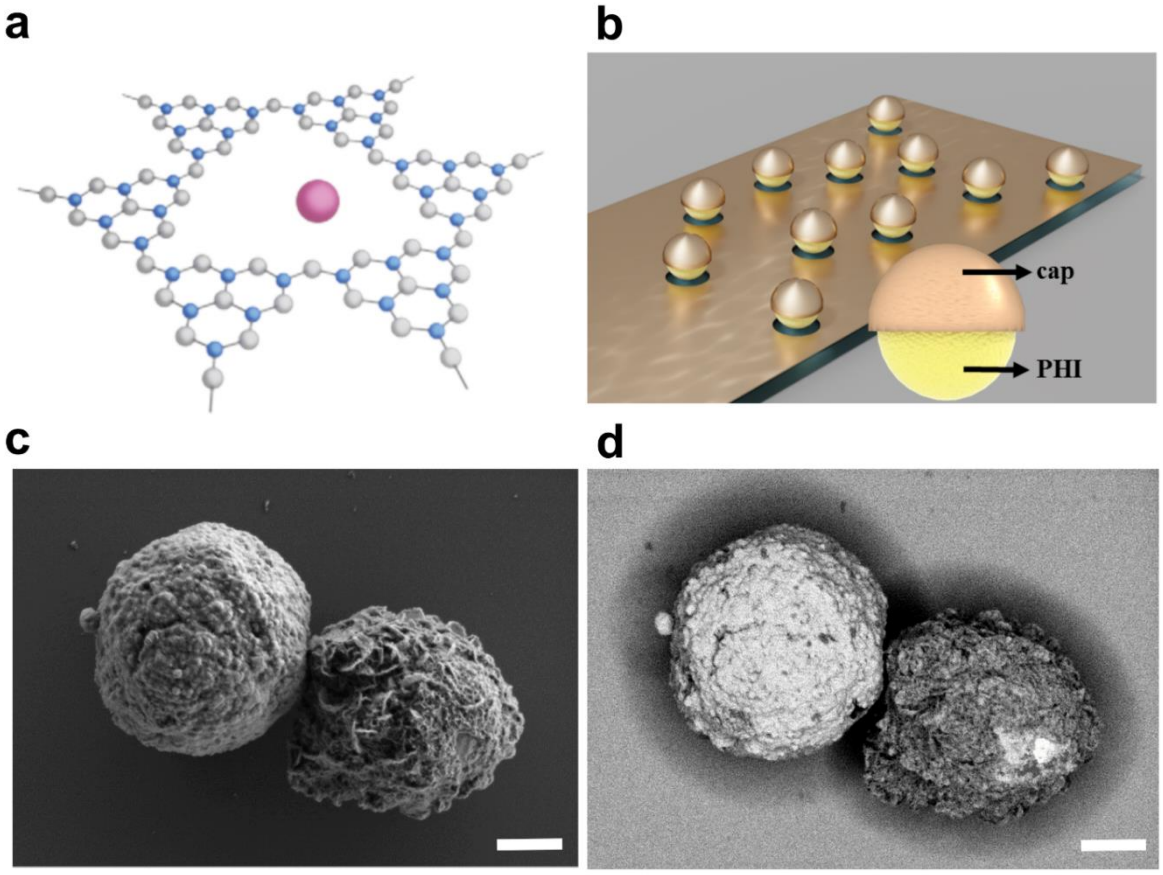

Figure 4.1 Structure of poly(heptazine imide) (PHI)-based Janus microswimmers. a) Chemical structure of PHI consisting of carbon (blue), nitrogen (grey), and hydrogen (omitted for clarity). Solvated potassium ions reside in structural pores (purple). b) Schematic of the preparation of the PHI-based Janus microswimmers by directional sputtering of cap materials (Au, Pt and SiO_2) on PHI microswimmers. Secondary electron (c) and corresponding back-scattered electron (d) images of two spherical PHI-Pt Janus microswimmers next to each other, with the Pt side facing up (left one) and the PHI side facing up (right one). The expected elemental contrast (Pt brighter) is clearly visible in d). Scale bar: 1 µm. Reproduced from reference [201].

4.4 PHI characterization

PHI-based Janus microswimmers were obtained by sonication of the bulk material and subsequent separation of particle sizes by centrifugation (see Materials and Methods section). The largest fraction was deposited on a substrate and caps were evaporated on top directionally to form Janus microswimmers, as illustrated in Figure 4.1b. Scanning electron microscopy (SEM) analysis revealed spherical shapes with a diameter of 1-3 µm (Figure 4.1c) and the back-scattered electron image showing the platinum content in Figure 4.1d. The obtained

microswimmers are not completely spherical, since they represent agglomerates of PHI nanoparticles that were separated after bulk synthesis resulting in not perfectly half-capped Janus microswimmers. Therefore, the fabricated Janus microstructures are also irregular in shape as shown in Figure 4.2.

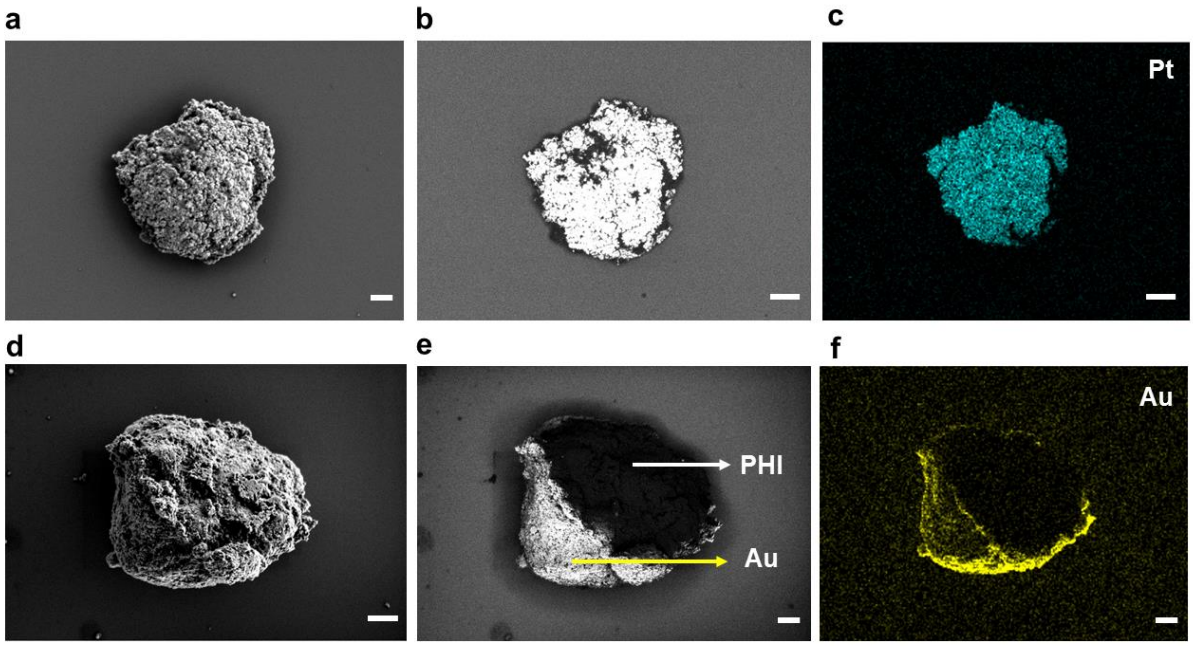

Figure 4.2 SEM and EDX images of Janus PHI microswimmers. a) Secondary electron image of a PHI-Pt Janus particle lying with the Pt face up and b) its corresponding back-scattered electron image highlighting the distribution of Pt by bright contrast. c) EDX map of a PHI-Pt Janus particle highlighting the presence of Pt on the Janus microswimmer in blue. d) Secondary electron image of PHI-Au Janus particle lying on its side. e) Corresponding back-scattered electron image highlighting the distribution of Au by bright contrast and f) EDX map of a PHI-Au Janus particle highlighting the presence of Au on the Janus microswimmer in yellow. The EDX detector is placed on the side of the chamber, thus causing shading effects. Scale bar: 1 µm. Reproduced from reference [201].

To establish the optical properties of the PHI-Pt microswimmers, the absorptance was measured Figure 4.3. The absorption edge of ~ 450 nm is similar to bulk and nanostructured PHI [207], but with an increased background, which is attributed to the metal cap. Hence, light in the blue and UV part of the solar spectrum can be absorbed and used for catalytic conversion to propel the microswimmer. The organic semiconductor PHI has a conduction band (CB) edge well negative of the reversible hydrogen electrode (RHE), approximately -500 mV versus NHE, and a valence band (VB) as positive as +2.2 V vs NHE, allowing PHI to drive multiple

redox-reactions, such as HER, ORR, and water oxidation [206-209]. The type of co-catalyst, i.e. the material used for the Janus cap, and the choice of fuel are crucial design parameters for optimized phototactic applications. To study the swimming behavior of the PHI microswimmers, we used Pt, Au and SiO_2 caps and illuminated the Janus microswimmers with visible and UV lights.

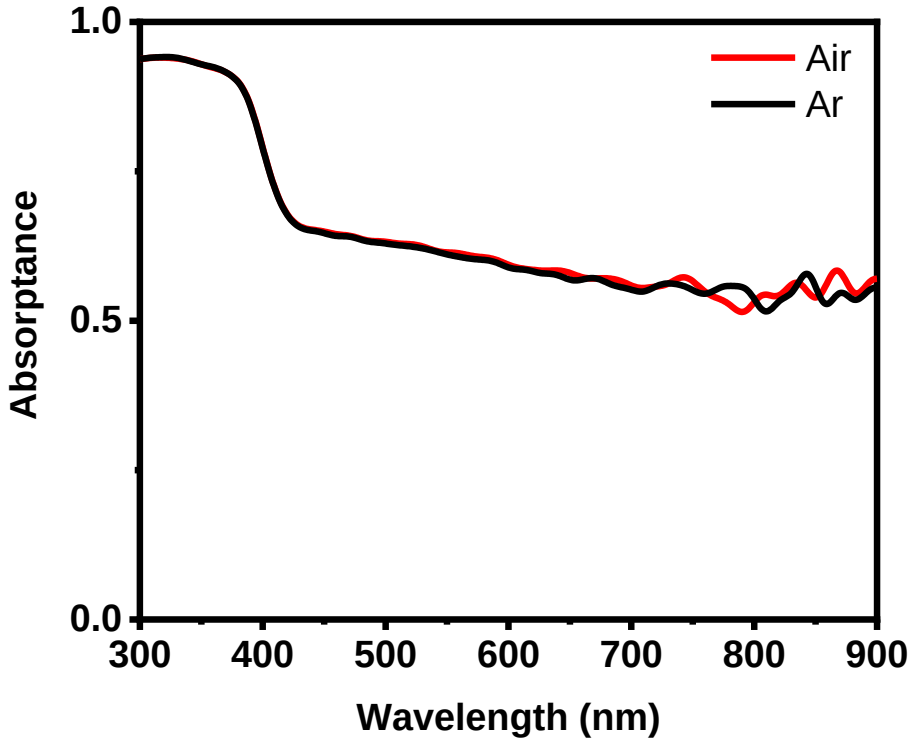

Figure 4.3 Absorptance of a PHI-Pt microswimmer suspension in water with and without O_2. The absorption onset of PHI is ~450 nm.

4.5 Microswimmer swimming characterization

4.5.1 Light intensity measurements

The spectral irradiance of the illumination in the microscope was measured at the place of the sample chamber with a calibrated Ocean Optics OCEAN-FX-XR1-ES spectrophotometer after attenuation by a neutral density filter. The results (Figure 4.4) have been normalized to the filter attenuation and to the spot size of the light beam in the microscope, which was measured to be 2.0 ± 0.5 mm in diameter, resulting in a relative experimental error of 50% after the error propagation calculation. In the case of visible light propulsion, a broad-spectrum white LED is illuminated from the top and a 470 nm light is illuminated through the microscope objective lens. The intensity of the microscope light (2 mW/cm² for the control experiments in the dark and 7 mW/cm² for imaging during UV illumination) was increased to 20 mW/cm². For

photocatalytic and photoelectrochemical experiments, the light intensity was directly measured by a calibrated Thorlabs S310C / PM100D power meter.

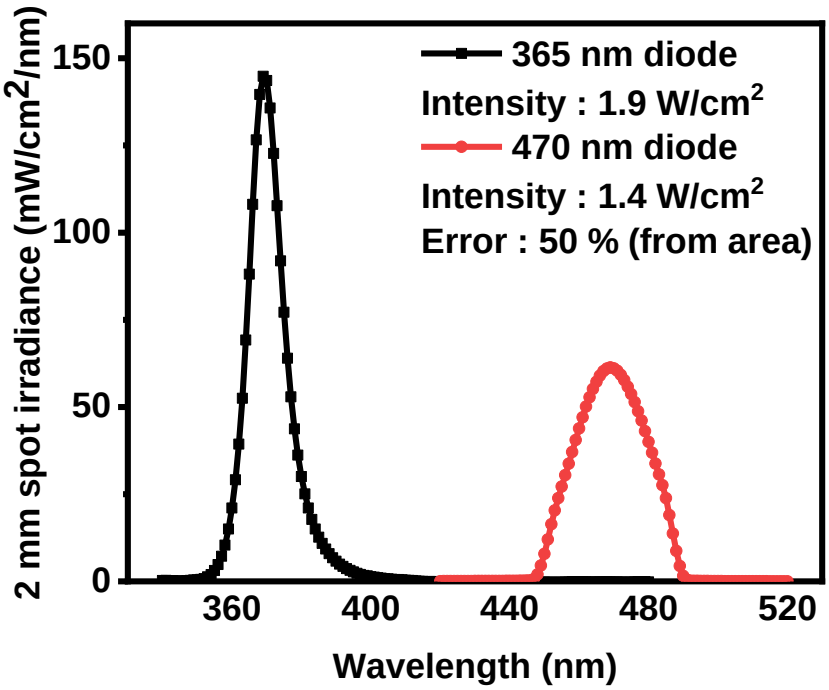

Figure 4.4 Spectral irradiance and resulting intensity of the light sources used for propulsion of the microswimmers, measured at the place of the sample.

4.5.2 Swimming behavior in water and water-alcohol mixtures

In order to enable the HER on PHI, an active catalyst such as Pt or Au is required owing to the high intrinsic overpotential of carbon nitrides for HER [207]. We hence illuminated the corresponding Janus microswimmers and measured their mean square displacement (MSD) in deionized (DI) water. On short time scales (~1 s), the motion is ballistic and hence mostly linear. The displacement is significantly enhanced by UV light, as shown in Figure 4.7a for all Janus microswimmers, along with a control experiment using the microscope light only. The mean speed can be extracted from the average slope. On longer time scales (~15 s), the speed of the UV illuminated PHI-Pt microswimmers was 10.4 ± 0.6 µm/s, while PHI-Au microswimmers swam with 9.1 ± 0.6 µm/s (13% slower), as shown in Figure 4.7b (left side). Interestingly, the SiO_2-PHI microswimmers were propelled at almost the same speed (8.6 ± 0.7 µm/s), without having a redox-active cap. Importantly though, this observation excludes HER as the source of self-diffusiophoresis, owing to the large overpotential of the HER on the PHI surface as shown in an earlier work [207]. Hence, another reductive process must be operative, which will be discussed further below. However, these results show that the capped PHI microswimmers can move even in the absence of a dedicated fuel and indicate that the

propulsion process is almost independent of the capping material when only water is used as fuel.

In order to check if and how these microswimmers can be moved in aqueous conditions, an additional thin Ni layer was deposited in between the PHI and the cap to enable magnetic control. The PHI-Ni-Pt microswimmers follow the direction of the applied magnetic field as shown in (Figure 4.5). Their speed is 12.1 ± 0.3 µm/s at an applied field of 8 mT, which is comparable to inorganic TiO_2 based microswimmers of similar size (13.3 ± 0.4 µm/s) [128].

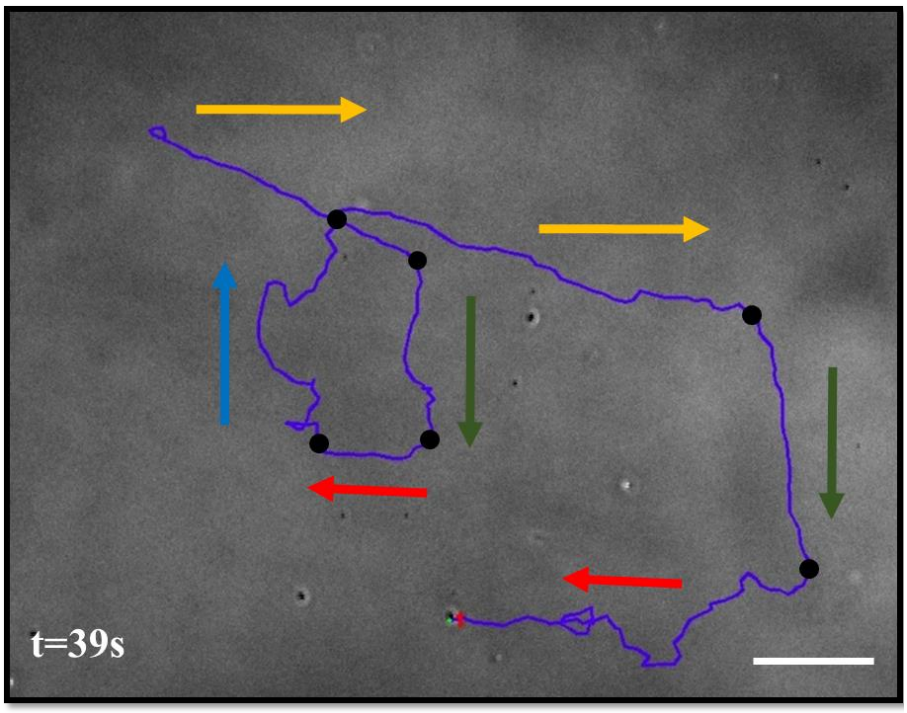

Figure 4.5 Video snapshots of the magnetically guided PHI-Ni-Pt microswimmer (from Supporting Movie 1) under the UV light at various time intervals with 5% methanol, with the black dots indicating the time points where the uniform 8 mT magnetic field changes direction (indicated by colored arrows). Scale bar: 5 µm.

In order to increase the propulsion activity of the microswimmers, which is limited by the sluggish kinetics of the hole extraction in pure water, alcohols like methanol (MeOH) or 4-methyl benzyl alcohol were added, which have been shown to reduce the lifetime of photogenerated holes on PHI efficiently to significantly below 3 µs [210]. With 5% MeOH added as a hole extraction fuel, the mean speed of the PHI-Pt microswimmers was almost doubled to 20.4 ± 1.3 µm/s (Figure 4.7b, left side). Increasing the MeOH concentration to 10% yielded comparable speeds of 20.6 ± 0.9 µm (Figure 4.6). Hence, a saturation of the rate limiting donor reaction can be estimated at 5% MeOH already.

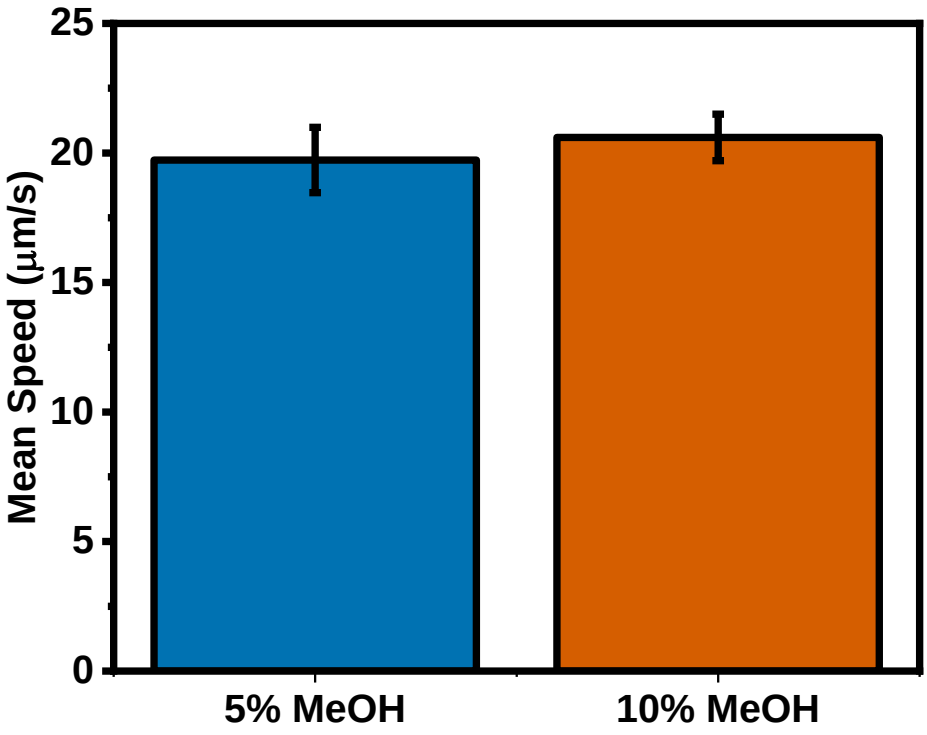

Figure 4.6 Average mean speed of PHI-Pt microswimmers under UV illumination with different MeOH concentrations.

Due to the biocompatibility of Au, its use as catalytically active cap material instead of Pt is also of interest, especially for biomedical applications [102, 211]. Again, the speed of PHI-Au microswimmers was found to be almost doubled to 16.3 ± 1.4 µm/s with 5% MeOH, i.e., 20% less than that observed with PHI-Pt microswimmers. The overall similar mean speed of both types of metal Janus microswimmers indicates similar surface reaction kinetics, despite the distinctly different catalytic activities of Pt and Au towards HER. The mean speed of SiO_2-capped microswimmers, however, increased only slightly upon addition of the alcohol (10.7 ± 0.5 µm/s with 5 % MeOH, +25%) and remains significantly below that of the metal capped microswimmers (47% less that Pt-PHI). The catalytic reactions that are responsible for propulsion hence rely on the complex interplay of both sides of the Janus particle.

The swimming speed of the PHI Janus microswimmers is approximately two times larger than for inorganic TiO_2-Au microswimmers with 1-2 µm diameter under the same illumination and donor conditions, which is 9.2 ± 0.5 µm/s [128], and of similar speed as TiO_2-Pt microswimmers (8.9 µm/s) in DI water under the same illumination conditions (1.9 W/cm²) [84], The PHI microswimmers are capable of active propulsion at the same speed as melon-type CN_x based microswimmers.[199] This more efficient use of light can be attributed to the

high quantum yield of the surface reaction occurring on PHI in comparison to other organic photocatalysts, possibly originating from the more efficient hole transfer to the alcohol [210], less recombination-active trap states in the material [212], and from better charge separation efficiencies at the metal-semiconductor junction in the Janus particle.

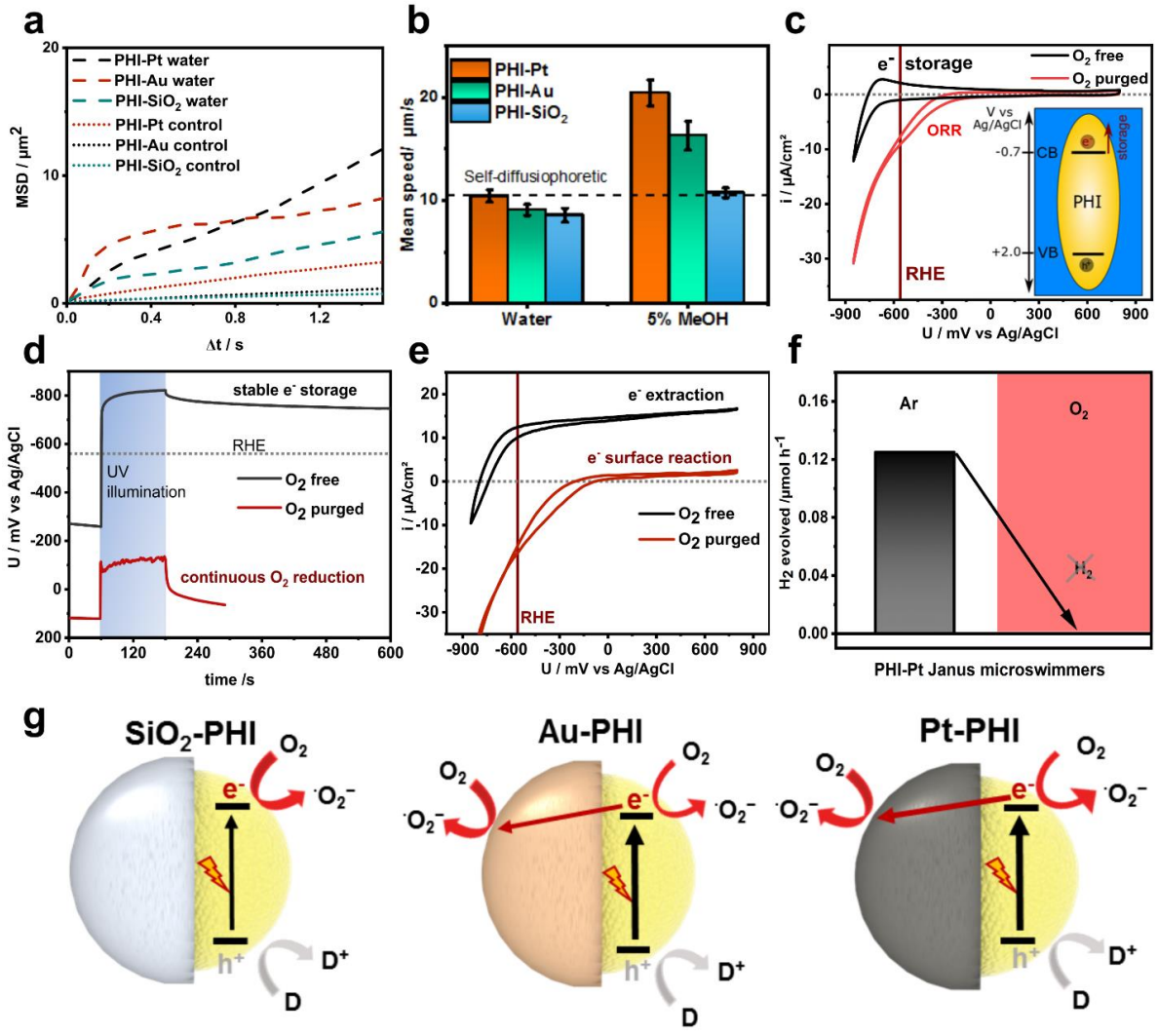

Figure 4.7 Characterization of the swimming behavior of different PHI-based Janus microswimmers in water and with alcohol. a: 2D mean-square-displacement (MSD) swimming trajectory data as a function of the time interval for the PHI-Pt, PHI-Au and PHI-SiO2 microswimmers in DI water with UV light on short time scales (~1 s) and the control experiment in the dark (dotted lines). b: Average (N=25) mean speed of the UV light-driven PHI-Pt, PHI-Au and PHI-SiO2 microswimmers on longer time scales (~15 s) in water and with MeOH. c-e: Electrochemical characterization of exfoliated PHI sheets deposited on FTO. c: Current-voltage measurement (CV) showing reversible electron storage and release above RHE upon cathodic cycling in O2-free electrolyte (black line) and the oxygen reduction

reaction (ORR, red line) occurring positive of the RHE under oxygen containing conditions, thus hindering charge accumulation and storage. The inset illustrates the positions of the valence band (VB) and conduction band (CB), where electron storage occurs. d: Open circuit potential (OCP) measurements for both conditions in the dark, under and after UV illumination. e: CV showing potential-dependent electron extraction current under UV illumination in the presence of an electron donor (MeOH), providing a measure of the charges available for diffusiophoresis under ambient and O2-free conditions. f: Hydrogen evolution measurement of Pt-PHI Janus microswimmers in degassed (left) and absence of hydrogen in oxygen containing conditions(right) with the black arrow indicating the absence of hydrogen. g: Schematics illustrating the major and minor light-induced redox-reactions on both sides of the three PHI-based Janus microswimmers. Reduction reactions (driven by electrons) are indicated by a red arrow (with Au and Pt caps), whereas the oxidation (driven by photogenerated holes) are highlighted in grey. Reproduced from reference [201].

4.6 Photoelectrochemical characterization with water and methanol as donor

The photoelectrochemical measurements were performed in a closed glass reactor equipped with a quartz window for side illumination. A Ag/AgCl reference electrode with saturated KCl (+0.197 V vs. NHE) was used with the different aqueous electrolytes. A Pt wire acted as counter electrode. To remove dissolved oxygen, the electrolyte was purged with >99% pure N_2 or Ar prior to the respective measurement through a porous glass frit for at least 1 h. Electrochemical measurements were recorded and analyzed using an IVIUM CompactStat potentiostat and the IviumSoft software. UV illumination was provided by a Thorlabs M365L2 (Germany) UV lamp at an operating current of 1.4 mA and a working distance of 20 cm (15 mW/cm²). PHI was deposited on FTO by drop casting nanosheets as reported previously [207].

To elucidate the nature of the electrochemical reactions occurring on the surface of PHI, we studied the photoelectrochemical (PEC) properties of PHI. To this end, exfoliated PHI nanosheets were deposited on a conductive fluorine-doped tin oxide glass (FTO) substrate and characterized electrochemically in the dark and with 15 mW/cm² during UV illumination at 365 nm from the same light source used for the swimming experiments, both in the presence and absence of oxygen (Figure 4.7c-e). As can be seen in the cyclic voltammogram (CV) in Figure 4.7c, anodic cycling of PHI in oxygen free conditions (black curve) in the dark leads to a reversible electron storage and retraction process (schematics in inset), which occurs at approximately -700 mV vs Ag/AgCl, well negative of the RHE, thus enabling electron transfer to a co-catalyst and HER, in principle. Illumination in the presence of a donor also enables

stable electrochemical electron storage [207] and yields a negative open circuit potential (OCP) of approximately -800 mV vs Ag/AgCl in the absence of O_2 (Figure 4.7d black curve), even after illumination. These photogenerated electrons can be extracted by applying more positive potentials, leading to photocurrents of 10-15 µA/cm^2 (Figure 4.7e black curve). However, the situation is distinctly different in the presence of oxygen (red curves); here, PHI neither shows electron storage upon electrical charging (Figures 4.7c and Figure 4.8 for different conditions) nor by photo-charging (Figures 4.7 d and Figure 4.9), which impedes electrical charge extraction, as shown in Figure 4.7 e. In other words, the ORR takes place predominantly at potentials of approximately -200 mV vs Ag/AgCl or more positive, i.e., well positive of the RHE and, hence, preferentially over the HER. Consequently, the accumulation of (photogenerated) electrons in the CB is impeded by rapid electron transfer to the oxygen present in solution, reducing it to water or forming ROS that then reacts further and as observed on other semiconductors [213].

In the case of inert SiO_2-capped Janus microswimmers, all photoelectrons are transferred to oxygen and, hence, it can be assumed that self-diffusiophoretic propulsion occurs from the PHI hemisphere only (Figure 4.7g). For Pt- or Au-capped Janus microswimmers, the same mechanism is possible, in principle, and probably dominates when no donor is present, since all swimming speeds are comparable (Figure 4.10). Since significantly increased swimming speeds have been observed only on metal-capped Janus microswimmers with MeOH, i.e., when the hole extraction from PHI is fast and not rate limiting, the cap must be active for charge separation and also drive a surface reaction under these conditions. Charge carrier separation at the metal-semiconductor interface decreases recombination and simultaneously enables reduction reactions on both Janus hemispheres. Internal electron transfer from PHI to the metal cap hence adds self-electrophoresis as a likely propulsion mechanism to the MSD (Figure 4.7g).

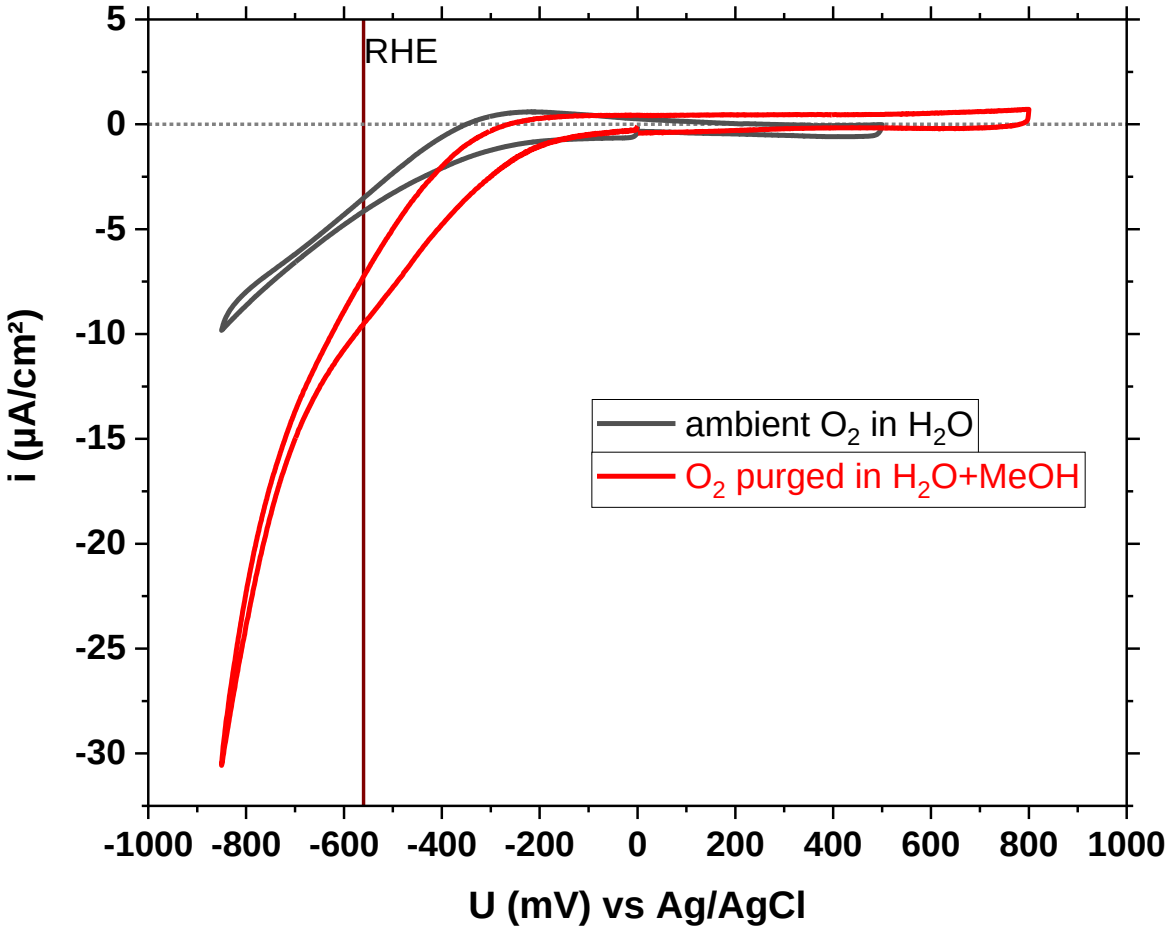

Figure 4.8 Electrochemical cyclic voltammogram (CV) of PHI deposited on fluorine-doped tin oxide glass (FTO) in deionized water. Purging with oxygen further increases the reductive currents, which start at approx. -200mV vs Ag/AgCl, i.e. well before the RHE. Methanol does not affect the currents in this potential window. The dark currents originating from FTO alone in O_2 containing conditions are of comparable magnitude to these with PHI deposited on FTO, which is attributed to comparably slow charge transfer kinetics of the PHI when reacting with oxygen.

4.6.1 Oxygen reduction reaction (ORR)

Upon photoexcitation, many semiconductors such as TiO_2 and CN_x can reduce dissolved oxygen on their own or on a Pt surface, by driving the oxygen reduction reaction (ORR) or by producing reactive oxygen species (ROS), which then react further and are often used for the removal of pollutants [213, 214]. This thermodynamically downhill reaction is in competition with solar fuel productions since the scavenging of electrons by O_2 impedes uphill

photosynthetic reactions, such as the hydrogen evolution reaction or the CO_2 reduction [215, 216].

The ORR has thermodynamically the highest driving force, but it requires the transfer of four electrons:

E^0 (O_2/H_2O) = +1.23 V vs SHE @ 1 bar O_2 (Nernstian pH dependence)

The main ROS formed upon reduction of O_2 are (1) superoxide radicals ($^{\bullet}O_2^-$), which are in equilibrium with (2) hydroperoxyl radicals ($^{\bullet}HO_2$) in acidic conditions ($^{\bullet}HO_2$ <-> $^{\bullet}O_2^- + H^+$), as well as (3) hydroxyl radicals ($^{\bullet}HO$), which are formed by the decomposition of hydrogen peroxide (H_2O_2 <-> 2 $^{\bullet}HO$). Hydrogen peroxide itself can be a product of the ROS formation and further reduction, as listed in the reduction reaction potentials below. The equilibrium potentials of the main ROS are:[217],[214]

E^0 ($O_2/^{\bullet}O_2^-$) = -0.33 V vs SHE @ 1 bar O_2 (constant if pH > 4.8)

E^0 ($O_2/^{\bullet}O_2^-$) = -0.16 V vs SHE @ 1 M O_2

E^0 ($O_2/^{\bullet}HO_2$) = -0.037 V vs SHE @ pH 0

These ROSs can then further react to form other radicals or hydrogen peroxide[213, 214]

E^0 ($^{\bullet}O_2^-/H_2O_2$) = +0.94 V vs SHE @ pH 7

E^0 ($^{\bullet}O_2^-/HO_2^-$) = +1 V vs SHE

E^0 ($^{\bullet}HO_2/H_2O_2$) = +1.42 V vs SHE @ pH 0; +1 V vs SHE @ pH 7

E^0 ($^{\bullet}HO_2/HO_2^-$) = +0.79 V vs SHE

Subsequent reactions with H_2O_2 are discussed in Supplementary Note 5. The hydroxyl radical, which is in equilibrium with H_2O_2 (H_2O_2 <-> 2 $^{\bullet}HO$), can also be reduced further:

E^0 ($^{\bullet}OH/OH^-$) = +1.9 V vs SHE

Besides, also the formation of the ROS singlet oxygen ($^1O_2$) via H_2O_2 is possible via photosensitization [218].

A more detailed overview of the energetics of reductive processes involving O_2 at pH 7 is reported elsewhere [219].

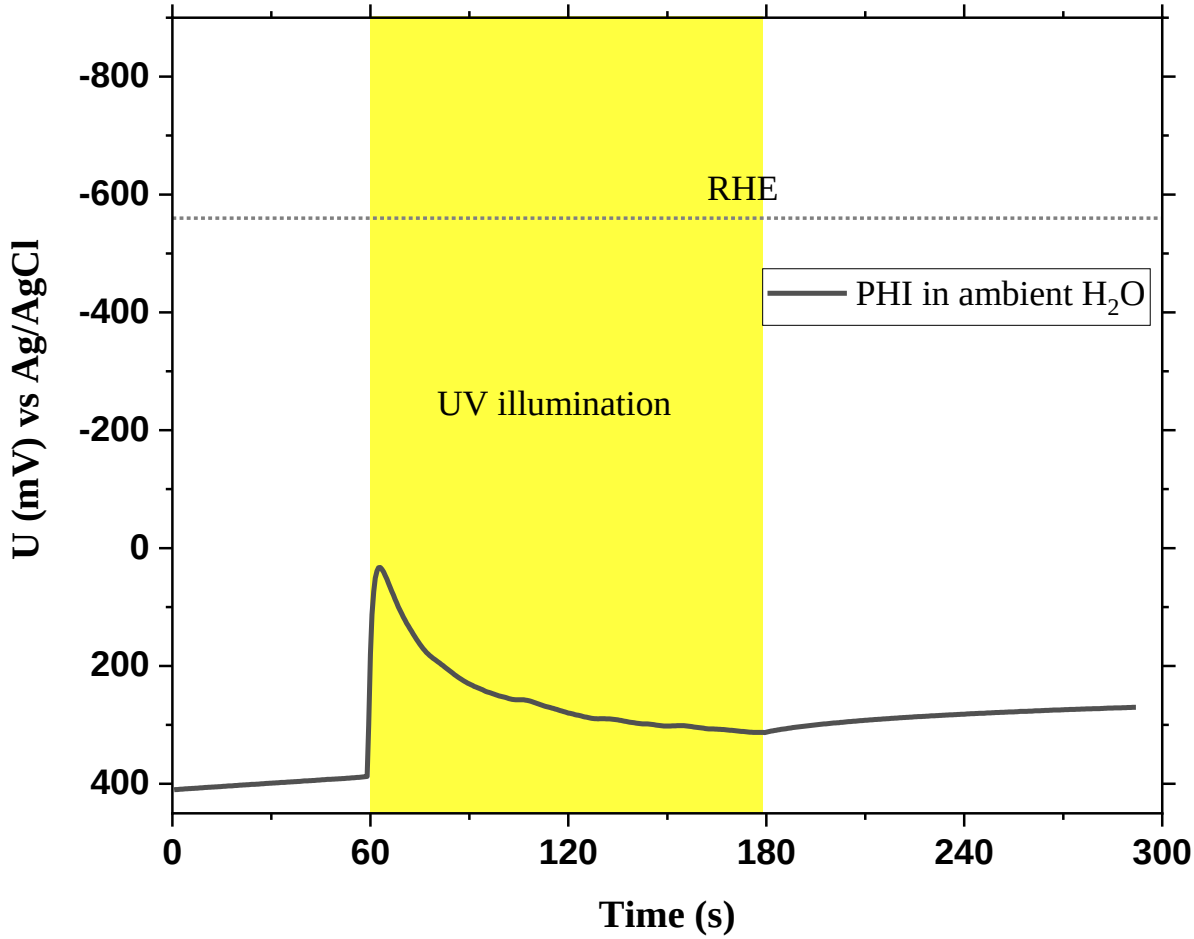

Figure 4.9 Transient open circuit potential (OCP) measurement of a thick layer of PHI deposited on FTO in DI water. Upon illumination, an OCP shift is generated by illumination. Subsequently, electrons react with oxygen, lowering the OCP under illumination.

4.6.2 Light-induced propulsion without added alcohol

To further investigate the propulsion without alcohol present, open circuit potential (OCP) measurements of a PHI film deposited on fluorine-doped tin oxide glass (FTO) were performed in water under ambient conditions (Figure 4.8). After a fast negative spike upon illumination towards 0 V vs Ag/AgCl due to photogeneration of charge carriers, a continuous positive shift down to +300 mV vs Ag/AgCl is observed, evidencing the extraction of electrons by oxygen, balancing the hole reaction entirely.

In order to evidence the water oxidation reaction (OER) enabling donor free propulsion with metal caps, cyclic voltammograms (CVs) were performed under chopped illumination under more oxidative potentials (Figure 4.10). An oxidative photocurrent could be measured at potentials more positive than +1V vs. Ag/AgCl, since only then, a high enough driving force

for electron extraction is provided, avoiding excessive charge recombination that also impedes the measurement of photocurrents at more negative potentials than +1V.

The fact that enhanced light induced propulsion in pure water was only observed with metal caps and not with SiO_2 can be rationalized by the fact that these metal caps act as electron sinks and hence decrease the charge recombination on the PHI side if the hole reaction is rate limiting. This enables enhanced oxidation reaction rates on the organic semiconductor part, while the metal caps also drive the reduction reaction, leading to self-electrophoretic propulsion with the charge carriers separated at the metal-semiconductor interface.

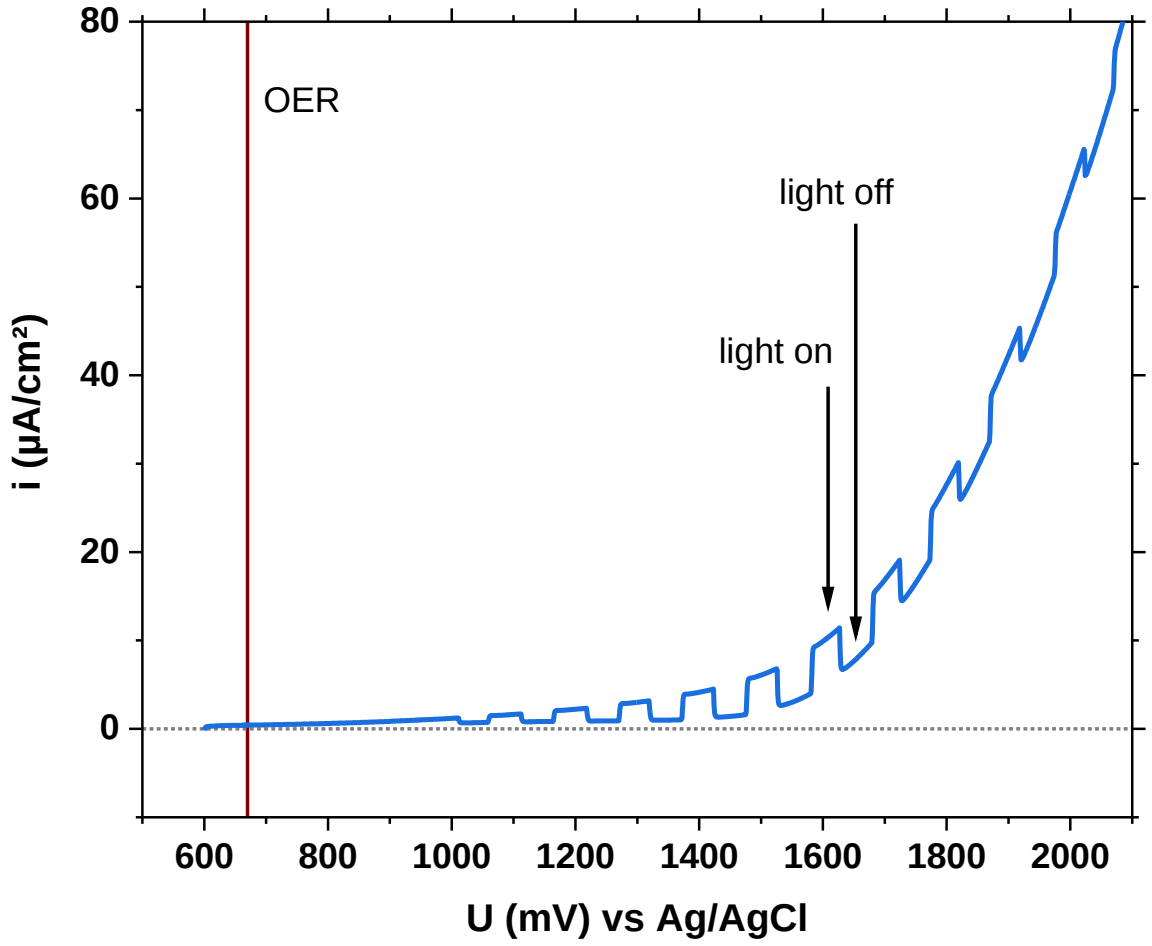

Figure 4.10 Cyclic voltammogram of PHI deposited on FTO substrate in deionized (DI) water in the oxidation region. As evidenced by the positive photocurrent upon chopped illumination, a water oxidation reaction can take place on the PHI surface after photon absorption. Since the photocurrents are comparably small and the reaction overpotential is rather high, it can be assumed that the water oxidation is rate limiting when no donor is present.

4.7 Hydrogen evolution reaction

Photocatalytic experiments were performed in a double-walled glass reactor with a quartz glass window on top, as previously reported [220]. The temperature within the reactor was thermostated by a water-cooling jacket to 25°C. Top-illumination of the reactor is performed with a xenon lamp (Newport, 300 W) with a water filter, or by a Thorlabs M365L2 UV lamp (Germany). To cut off some of the UV light, air mass filter (AM 1.5 G) was used in the respective experiments. If not stated otherwise, CN_x Janus microswimmers were suspended in water (9 ml) and methanol (1 ml). Prior to illumination, the head space of the reactor was evacuated and backfilled with Ar six times to remove oxygen. The headspace was periodically analyzed by a gas chromatograph (Thermo Scienific TRACE GC Ultra) equipped with a TCD detector using Ar as a carrier gas.

To obtain a full picture of the reduction products, we studied the gas formation of Pt-capped PHI Janus microswimmers. Illumination in the presence of methanol under oxygen-free conditions evidences the accumulation of hydrogen in the headspace of a sealed reactor, as shown in Figure 4.7f, black bar, for the full spectrum of a xenon lamp and SI Figure 4.11 for comparison to air mass filter (AM 1.5 G) and UV illumination conditions used to study the swimming. However, if oxygen was *not* removed from the suspension, no hydrogen whatsoever is observed over 23 h with the same Janus particle suspension. The same observation was made with photo-deposited Pt or Au on both PHI and TiO_2 (anatase), where HER was only observed when oxygen was removed from the suspension (Figure 4.12). ORR occurs in ambient conditions with water and/or alcohol donors present with Au and Pt used as reduction catalysts, which is evidenced on both PHI and TiO_2. Therefore, it can be expected that the preference of the ORR over HER in the presence of oxygen can be generalized. We thus conclude that the fastest swimming Pt-capped and Au-capped microswimmers are dominantly active for ORR/ROS formation in ambient conditions, which is happening on both sides as long as oxygen is present in the environment.

For HER measurements with photodeposited Pt or Au on PHI or TiO_2 (anatase, Sigma Aldrich 232033), the same reactor preparation and geometry was used, with full arc illumination by the same Newport Xe lamp, set to 100 mW/cm². For photodeposition of the co-catalyst Pt or Au, an optimized amount (8 wt% or 2 wt%) of H_2PtCl_6 or $HAuCl_4$ (Sigma Aldrich) was added to the suspension before the measurement in Argon containing conditions. After at least 6 h of measurement, the O_2 containing experiment was performed on the same material. The suspension was purged with O_2 through a needle for 20 min while stirring (1 ml

MeOH was added after 15 min to prevent its evaporation) and the reactor was left open for 10 min to equilibrate. In all cases, the HER rate was determined by the average slope after activation over at least 3 h, with a minimum sensitivity of 0.06 µmol H_2/h over 3 h.

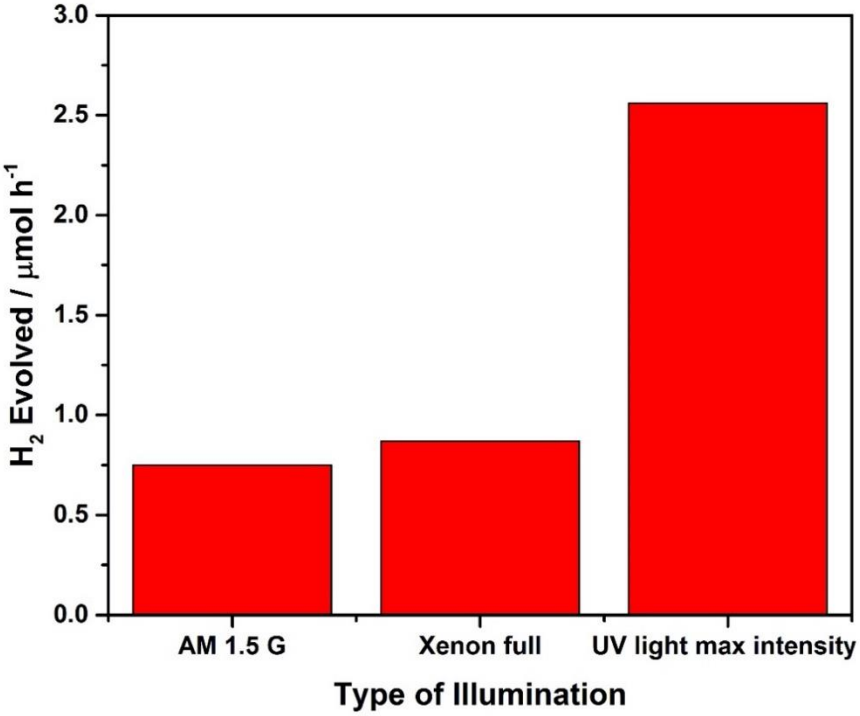

k

Figure 4.11 Hydrogen evolution measurements of PHI-Pt microswimmer with 10% methanol in O_2-free conditions, under AM 1.5 G illumination, with the full spectrum of the same xenon lamp and with UV light (same conditions as for light induced swimming measurements).

In oxygen free environments, the ORR can be excluded and the dominant surface reaction on the metal caps becomes the hydrogen evolution reaction, as long as only alcohol donors are used to quench photogenerated holes. PHI-Pt microswimmers were tested for hydrogen evolution with 10% methanol under different illumination intensities and their hydrogen evolution rates are shown in Figure 4.11. In general, more hydrogen was evolved with increasing intensity of UV light. The hydrogen evolution rate increased from 0.75 µmol h^{-1} with an AM1.5 G filter to 0.87 µmol h^{-1} with the full range illumination wavelength of a Xe-lamp. A further drastic increase was observed with the UV lamp (2.56 µmol h^{-1}). Comparing those hydrogen evolution rates to literature, the Janus PHI-Pt microswimmers show a lower photocatalytic activity in comparison to classical photocatalysis experiment with *in-situ* Pt photo-deposition (1200 µmol h^{-1} g^{-1}), although a normalization is difficult since the amount of PHI cannot be determined correctly after Pt cap deposition. A decrease in activity

with respect to in-situ Pt deposition might be due to different particle sizes and less accessible surface area of both, CN_x and Pt. Light is scattered or absorbed and thermalized by the sputtered metal cap instead of being absorbed by the PHI (see Figure 4.9). In the presence of ambient oxygen as seen in Figures 4.7 f and 4.12, no hydrogen evolution was observed further validating the role of ORR in the propulsion of microswimmers.

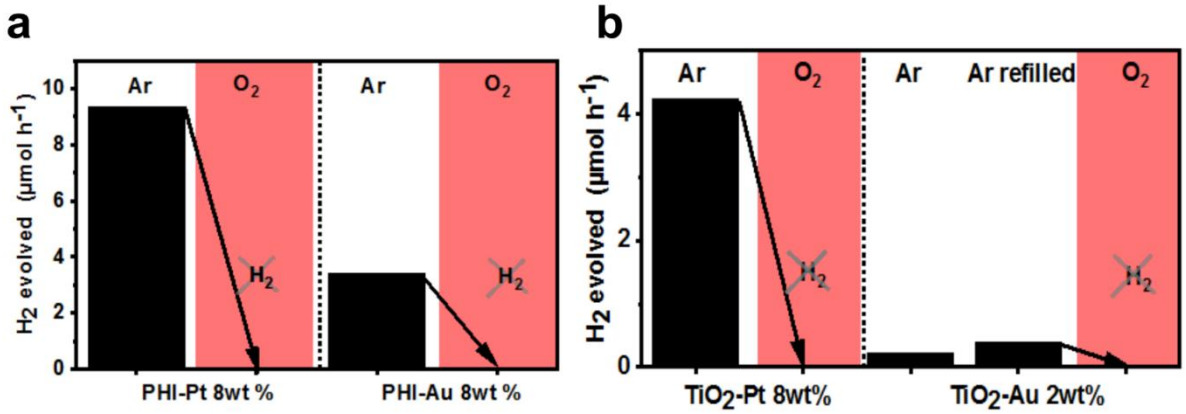

Figure 4.12 Hydrogen evolution measurements of PHI. (a) and anatase TiO_2 (b) with photo-deposited Pt or Au in water containing 10% methanol under Xe full arc illumination (100 mW/cm²). Hydrogen evolution is only observed in degassed conditions (Ar). In ambient, oxygen containing conditions (red background), no H_2 was observed.

4.8 Swimming with H_2O_2 as fuel

We also studied the active propulsion in H_2O_2, a widely used fuel for microswimmers. Since noble metals such as Pt also catalyze the decomposition of H_2O_2 in the absence of light, this fuel is commonly used for microswimmer propulsion without light [12]. H_2O_2 is redox amphoteric, i.e., it can be both oxidized and reduced, making swimming faster under appropriately chosen conditions. The activity of the microswimmers was tested in the presence of various concentrations of H_2O_2 to study concentration and illumination effects on the microswimmer speed and mechanism of propulsion. When PHI-Pt and PHI-Au microswimmers are illuminated with visible light at an intensity of 1.6 W/cm^2 in the presence of 2 vol% H_2O_2, they swim with a similar speed of 12.1 ± 0.6 µm/s and 11.9 ± 0.4 µm/s, respectively, significantly faster than without illumination (Figure 4.14 a). Hence, also visible light propulsion is possible with H_2O_2 as a fuel. The propulsion under UV illumination is shown in Figure 4.14b. The PHI-Pt swimmers move with a speed of 13.2 ± 0.9 µm/s already at a concentration of 0.05% H_2O_2, which slightly increases at 0.5% H_2O_2, saturating at 1% (13.6 ±

1.1 µm/s and 16.5 ± 1.1 µm/s, respectively, Figure 4.13 for saturation). The maximum speed of the illuminated Pt microswimmers is hence 33% lower than the mean speed with 5% methanol as a fuel.

The PHI-Au microswimmers move faster than the PHI-Pt ones with H_2O_2 (+10% at 0.05% H_2O_2, (14.6 ± 0.8 µm/s), and by +81% at 0.5% (24.6 ± 1.6 µm/s)). Unlike the Pt microswimmers, their speed is significantly increased with increasing the H_2O_2 concentration to 0.5 % (+68%), while being 51% faster than with 5% MeOH. The swimming trajectories of the PHI-Pt and PHI-Au microswimmers in 0.5% H_2O_2 are shown in Supplementary Movies 4 and 5. When the insulating SiO_2 cap is used, the microswimmer speeds are comparable to the metal-capped ones at low H_2O_2 concentrations (10.8 ± 0.7 µm/s at 0.05% H_2O_2). The speed is significantly increased with 0.5% H_2O_2 (19.4 ± 0.9 µm/s, +80%), which remains only 21% below the speed with Au caps and is much higher than with Pt caps at 0.5% H_2O_2 (+43%). Compared to 5% MeOH, the increase is most drastic for the SiO_2-capped microswimmers (+81%). The fundamentally different trends in propulsion with H_2O_2 compared to MeOH indicate a more complex interplay of the surface reactions, or competitive processes occurring simultaneously on both sides.

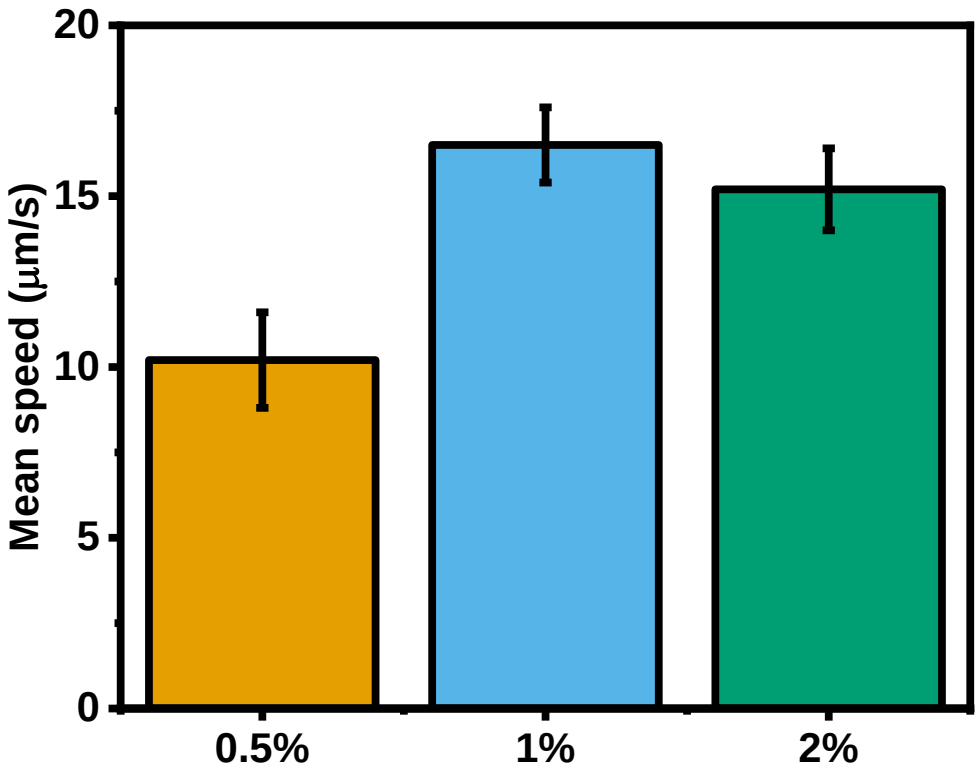

Figure 4.13 Mean speed of PHI-Pt microswimmers under different H_2O_2 concentrations under UV illumination.

4.9 Photoelectrochemistry with H_2O_2

The PEC characterization of PHI microswimmers with H_2O_2 relies predominantly on the photoresponse because the dark reduction and oxidation currents from the FTO substrate alone are of comparable size or even stronger than from the electrode containing PHI (Figure 4.15), which cannot be circumvented. Figure 4.14c contrasts the dark and illuminated OCP of PHI nanosheets on FTO in aqueous 1% H_2O_2. The negative shift from +340 to +70 mV vs. Ag/AgCl upon illumination proves the photoelectron generation, whereas the immediate decay shows that no charge accumulation is possible in the presence of H_2O_2. This is similar to MeOH and O_2 (Figures 4.7c), but at overall more positive potentials, since H_2O_2 is reduced more easily than O_2. Figure 4.14c illustrates the photocurrents negative and positive of the illuminated OCP value, which remain rather constant at -10 and +15 mA/cm², respectively and illustrate that both the light induced reduction and oxidation occur very efficiently on PHI, albeit with a slight asymmetry kinetically favoring the oxidation reaction. Similar findings are made with intermittent (chopped) illumination (Figure 4.15). Pt-capped PHI Janus microswimmers do not allow for the extraction of photocurrents due to strongly enhanced dark currents by the Pt (Figure 4.16). However, the observation of an initially weak negative and subsequently

transient positive OCP shift under UV illumination suggests the major photoreaction on PHI still being the H_2O_2, while Pt subsequently contributes more to the H_2O_2 reduction (Figure 4.17).

These findings help us pinpoint the propulsion mechanism. The PHI Janus microswimmers propulsion appears to occur predominantly due to photogenerated electrons and holes on the PHI surface, which drive redox-reactions with H_2O_2 at significantly faster kinetics compared to MeOH and dissolved O_2 due to lower reaction overpotentials and consequently, higher currents on the PHI hemisphere. Consequently, the pure symmetry-breaking propulsion mechanism (self-diffusiophoresis) in the PHI-SiO_2 system leads to enhanced MSD in H_2O_2 with respect to MeOH. Au and especially Pt however are redox-active materials supporting the disproportionate decomposition of H_2O_2 [221], and Pt is electrochemically much more active than Au, FTO or PHI, as evidenced by CV measurements (Figure 4.17). Consequently, competing reactions at both hemispheres of the Janus microswimmer, effectively lifting the symmetry breaking necessary for propulsion, can slow down the Janus particle under illumination in the presence of a metal cap. [77] Therefore, the propulsion with Pt caps is decreased over Au (Figure 4.14b) where the self-catalyzed and possibly thermally enhanced decomposition of H_2O_2 is less pronounced by more than two orders of magnitude [221].

The light-induced photocatalytic Janus particle propulsion with metal caps thus appears to mainly originate from the PHI hemisphere, like in the SiO_2 case. A slight increase in swimming speed with Au can again be attributed to a self-electrophoretic contribution enhancing charge separation at the metal semiconductor interface, akin to the metal-capped microswimmers in MeOH. A summary of the proposed light-induced propulsion mechanisms, which accounts for the complex interplay of the various competing surface catalytic processes of capped PHI microswimmers, is illustrated in Figure 4.14e for all three Janus particle cases.

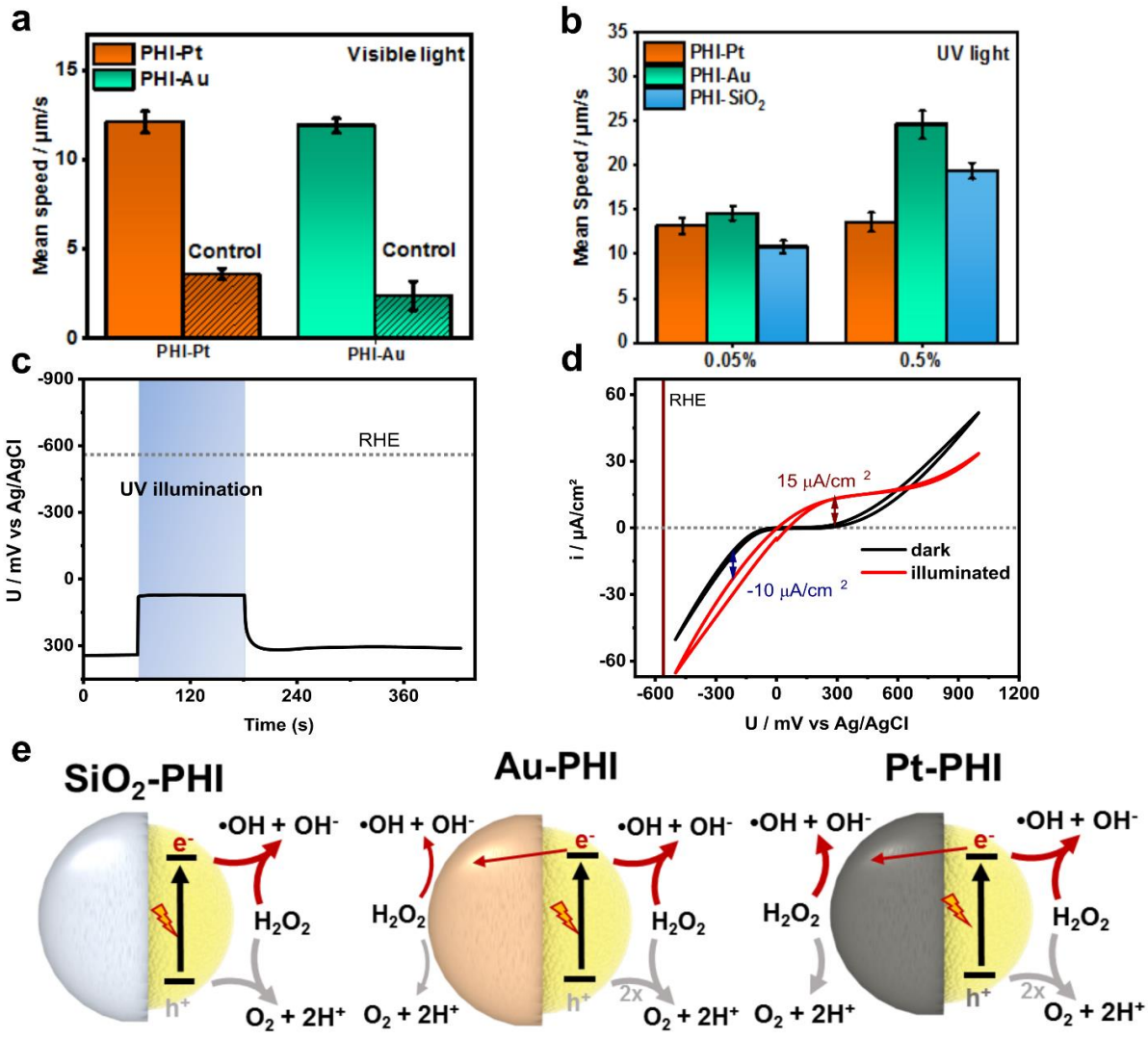

Figure 4.14 Characterization of the swimming behavior of PHI-based Janus microswimmers in H_2O_2. a: Average (N=25) mean speed of the visible light-driven PHI-Au and PHI-Pt microswimmers with 2% H_2O_2 as fuel and the control experiment in the dark. b: Average (N=25) mean speed of UV-light propelled PHI based microswimmers with Pt, Au and SiO_2 caps at low H_2O_2 concentrations (0.05 and 0.5%). c: OCP measurement of PHI nanosheets deposited on FTO in DI water containing 1 vol% H_2O_2 in the dark, under and after UV illumination. d: CV in dark (black curve) and under UV illumination (red curve) with the same conditions as in c. e: Schematics illustrating the (competing) major and minor redox-reactions with H_2O_2 on both sides of the three PHI-based Janus microswimmers. Reduction reactions (driven by electrons) are indicated by red arrows, whereas the oxidation reactions are highlighted in grey. The electron transfer between the PHI and the metal cap (straight red arrow) indicates a possible self-electrophoretic contribution. Reproduced from reference [201].

4.9.1 Possible redox-reactions with H_2O_2

As stated before, H_2O_2 can be a product of the formation of a ROS, but since the concentration of products formed due to photocatalytic propulsion with microswimmers stays rather very low, this discussion focusses on H_2O_2 being an added fuel in concentrations >0.01 vol%. Besides being used as donor species in order to facilitate hole extraction from semiconductor photocatalysts compared to the OER [222], it can also be reduced easily, acting as electron acceptor [215, 223].

The main reduction reactions with conduction band electrons (e^-_{CB}) are:[222]

$H_2O_2 + e^-_{CB} \rightarrow OH^- + OH^\bullet$ (1)

$OH^- + OH^\bullet + e^-_{CB} + 2H^+ \rightarrow 2\ H_2O$ (2)

Whereas the most dominant reactions with valence band holes (h^+_{VB}) are the following:

$H_2O_2 + h^+_{VB} \rightarrow O_2^{\bullet-} + 2H^+$ (3)

$H_2O_2 + 2\ h^+_{VB} \rightarrow 2H^+ + O_2$ (4)

Besides, hydrogen peroxide can react with its own ROS (H_2O_2 <-> 2 $^\bullet$HO):

$H_2O_2 + OH^\bullet \rightarrow {}^\bullet O_2H + H_2O$ (5)

${}^\bullet O_2H + OH^\bullet \rightarrow H_2O + O_2$ (6)

Further information about the reaction mechanisms that can occur on the surface of PHI microswimmers and their metal caps in the presence of H_2O_2 can be found in the literature [199, 200].

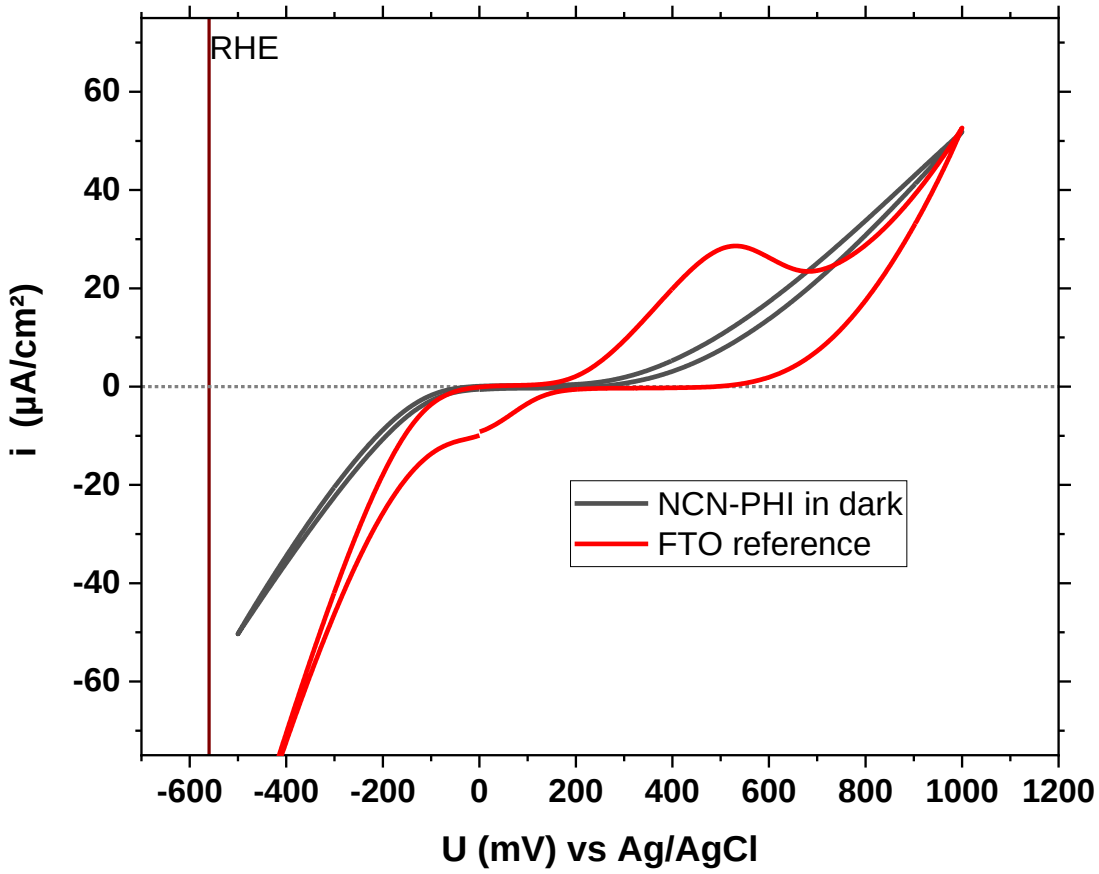

Figure 4.15 Dark currents of a bare FTO substrate and one covered with PHI nanosheets (10 µg) in DI water containing 1 vol% H_2O_2.

4.9.2 Photoelectrochemistry of FTO in H_2O_2

From the dark blank experiments (Figure 4.15), it can be seen that the reduction and oxidation of H_2O_2 in the dark occurs in a small voltage window (negative of -100 and positive of +300mV vs Ag/AgCl, respectively). Since H_2O_2 reduction occurs positive of the onset of ORR (-200 mV vs. Ag/AgCl), oxygen can play only a minor role in the propulsion mechanism in this case and is hence neglected in the following, since it does not affect the faster H_2O_2 reduction severely [223].

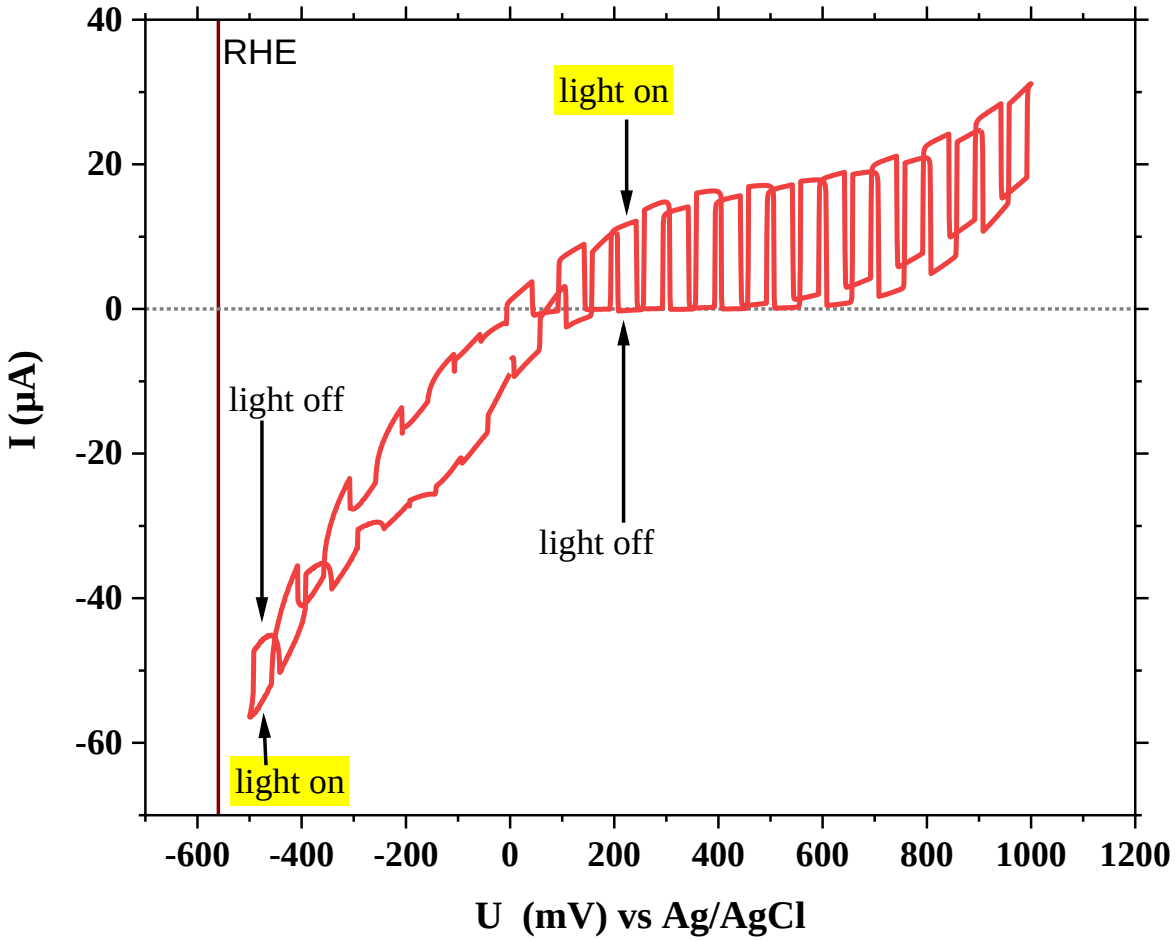

Figure 4.16 Cyclic voltammogram of PHI nanosheets (10 µg) deposited on FTO substrate in DI water containing 1 vol% H_2O_2 under intermittent UV illumination. A shift from photooxidation to photoreduction is visible at approximately 0 V vs. Ag/AgCl. A stronger oxidative photocurrent suggests this reaction to be more efficient on the surface of PHI. Since the photocurrent actually only shows the imbalance of photogenerated electrons or holes extracted by the potentiostat and both charges can react with H_2O_2, opposite to the case of MeOH without O_2, a photocurrent of similar size implies that the real surface reaction rate is much higher than the photocurrent alone with H_2O_2. Consequently, the light induced surface reaction kinetics are also much faster than the ones mesured with MeOH, since there, the electrons cannot decay by surface reactions.

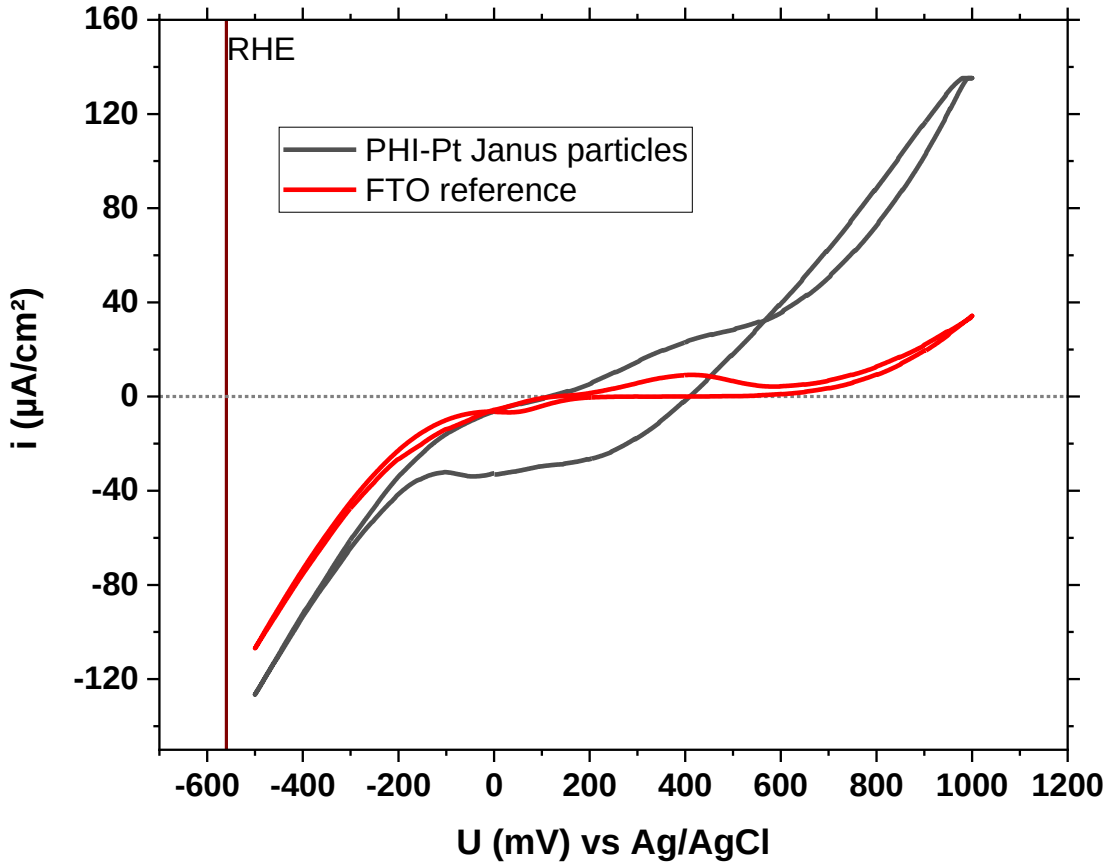

Figure 4.17 Cyclic voltammogram of PHI-Pt Janus particles deposited on FTO substrate in DI water containing 1 vol% H_2O_2 in comparison to a blank FTO substrate.

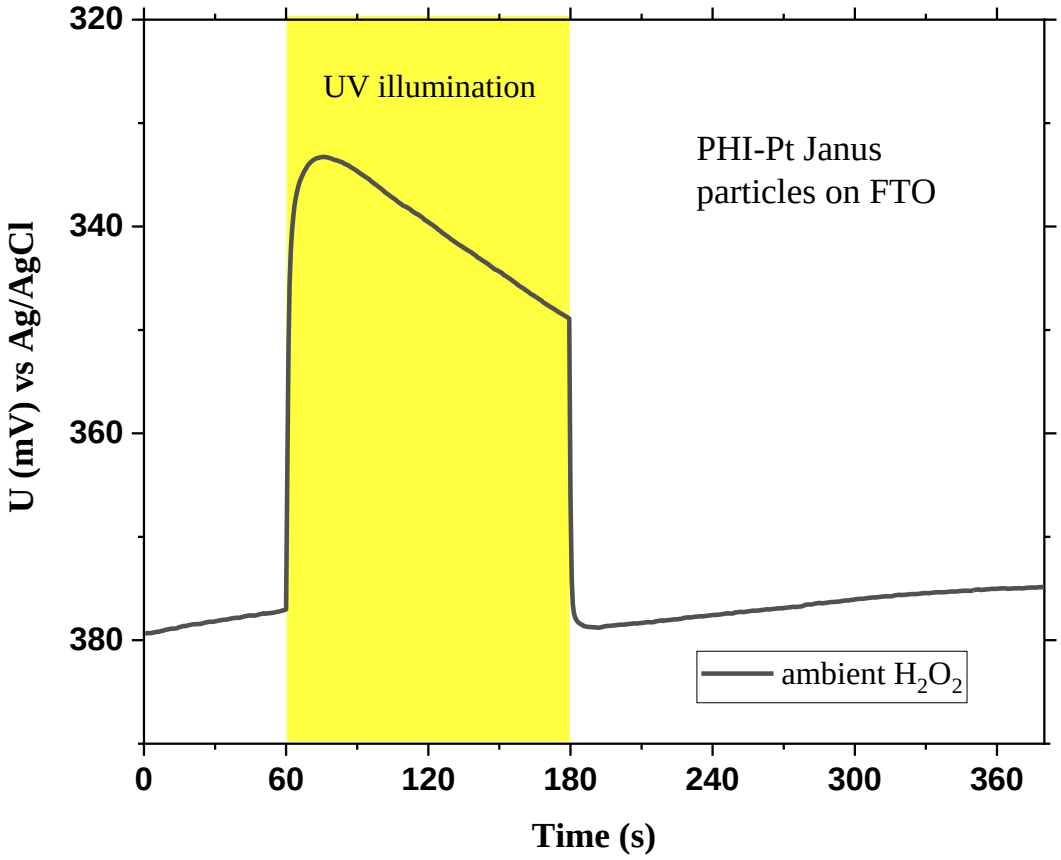

Figure 4.18 Open circuit potential measurement of Pt-PHI Janus particles deposited on FTO substrate before, during and after UV illumination.

4.9.3 Photoelectrochemistry with PHI in H_2O_2

In the case of a Pt or Au cap and a bulky Janus particle deposited on FTO, the situation is different from pure PHI sheets on FTO, since the cap material can accept the electrons and holes from PHI and drive the reduction or oxidation of H_2O_2, impeding the analysis of photoelectrochemical responses via the FTO substrate. Furthermore, the noble metal on the Janus particle increases the dark currents significantly, as shown in Figure 4.18 for Pt-PHI Janus particles, due to the high redox activity of Pt in contact with H_2O_2. Consequently, also most photogenerated charges react without being measured by the potentiostat. Hence, no reliable difference between the dark and illuminated currents could be measured in this case. Open circuit potential measurements of these Janus particles have shown a similarly positive potential value in the dark as PHI alone (-340 mV vs Ag/AgCl). Upon illumination however, a smaller negative shift can be observed (-40 mV vs -250 mV for PHI sheets without Pt), which is caused by the strong reduction activity of Pt, shifting the equilibrium value under illumination to more positive values than without the Pt cap (+340 mV vs +100mV vs Ag/AgCl). In the Pt-Janus particle case, the negative open circuit potential shift is followed by

a positive transient behavior, akin to Figure 4.9 for PHI alone in ambient water. It can hence be assumed that the PHI side of the Janus particle dominantly oxidizes H_2O_2, while electrons not only react on the PHI surface, but also on the Pt surface.

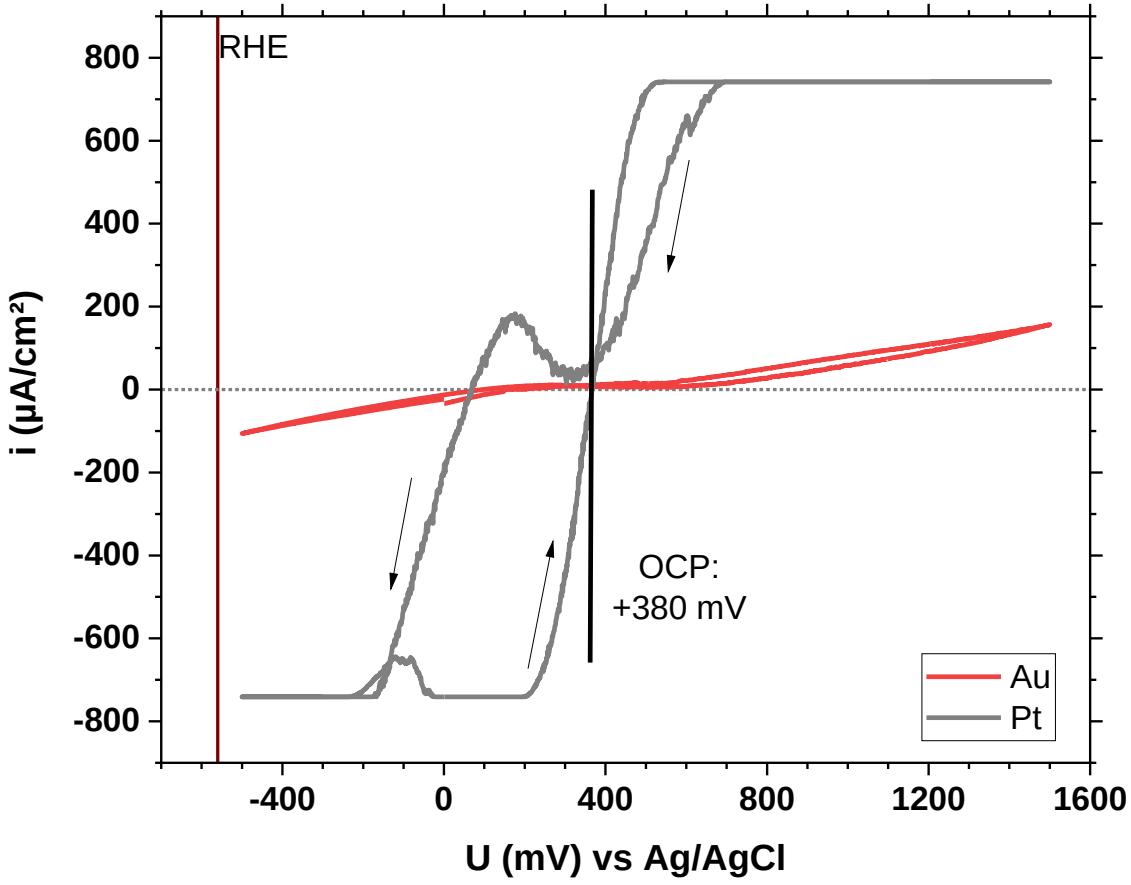

Figure 4.19 Cyclic voltammogram of a Pt wire and a gold plate in DI water containing 1 % H_2O_2. Pt (grey) catalyzes the reduction and oxidation of H_2O_2 more efficiently than Au (red). The depletion of reactants in the vecinity of Pt therefore causes a hysteresis and a catalytic wave. The open circuit potential is similar for both materials (+380 mV vs Ag/AgCl).

4.10 Solar battery swimming

An intriguing question is whether photocharging of PHI microswimmers – the basis for time-delayed photocatalysis in the dark as well as solar batteries based on PHI [206, 207] – could be used to realize a new propulsion mechanism: sustained swimming of light-driven PHI swimmers in the dark through time-delayed discharge, which we call *solar battery swimming*. However, the presence of ambient oxygen or H_2O_2, which act as electron scavengers on the PHI surface, would intuitively be expected to hinder charge accumulation of electrons in the conduction band of PHI. A way to circumvent this problem is to charge the bulky Janus particle

from inside, making use of sluggish electron transfer kinetics within PHI (from the inside to the surface) for delayed propulsion in the dark [206, 207].

As described before, the surface reactions on the Pt and PHI hemispheres in Pt-PHI Janus microswimmers are in strong competition in H_2O_2, which is not beneficial for fast light driven propulsion. However, the H_2O_2 decomposition reaction on the Pt surface becomes asymmetric if electrons are transferred away from Pt, as reported for Pt-Au nanorods where the Au hemisphere acts as an acceptor and drives the reduction reaction [121, 224]. Translating this effect to Pt-PHI microswimmers could enable electron transfer from Pt to photoexcited PHI, thus leading to hole quenching near the interface and hence, charge accumulation on PHI. We thus studied the propulsion behavior of PHI-Pt microswimmers at 1% H_2O_2 concentrations in more detail, i.e., before, during and after illumination, as shown in Figure 4.20. Figure 4.20 a visualizes the instantaneous speed of the microswimmers during an off/on/off cycle. Initially, when the light is off for 7 s, the microswimmers show enhanced Brownian motion due to the surface reaction of Pt with H_2O_2. When the light is turned on for 7 s, the swimmers increase their speed and swim due to reactions enabled by photogenerated charges, as described earlier. When the light is switched off again for 7 s, however, the swimmers continue to show enhanced ballistic motion, which is at least two times faster than the initial Brownian motion. Hence, the Pt-PHI Janus particle can actually be charged by light while increasing its swimming speed ballistically, which leads to enhanced and lasting propulsion in the dark. Figure 4.20b illustrates this continuous solar battery swimming process on longer time scales with 5 s of photocharging. The average instantaneous displacement of the microswimmers in the respective parts is illustrated in Figure 4.20c, highlighting that the microswimmers travel much faster and further after illumination than they would have done without it (solar battery displacement is 293 µm in 120s). The ballistic swimming during the dark is shown in orange in Figure 4b and c, the swimmers still show active Brownian motion even after the ballistic motion is stopped. The particle trajectory is shown in Figure 4.20d. Overall, a 5 s period of charging results in 120 – 160 s of enhanced MSD until the swimmers are discharged. This corresponds to a 24-32 times increased propulsion period compared to the illumination time.

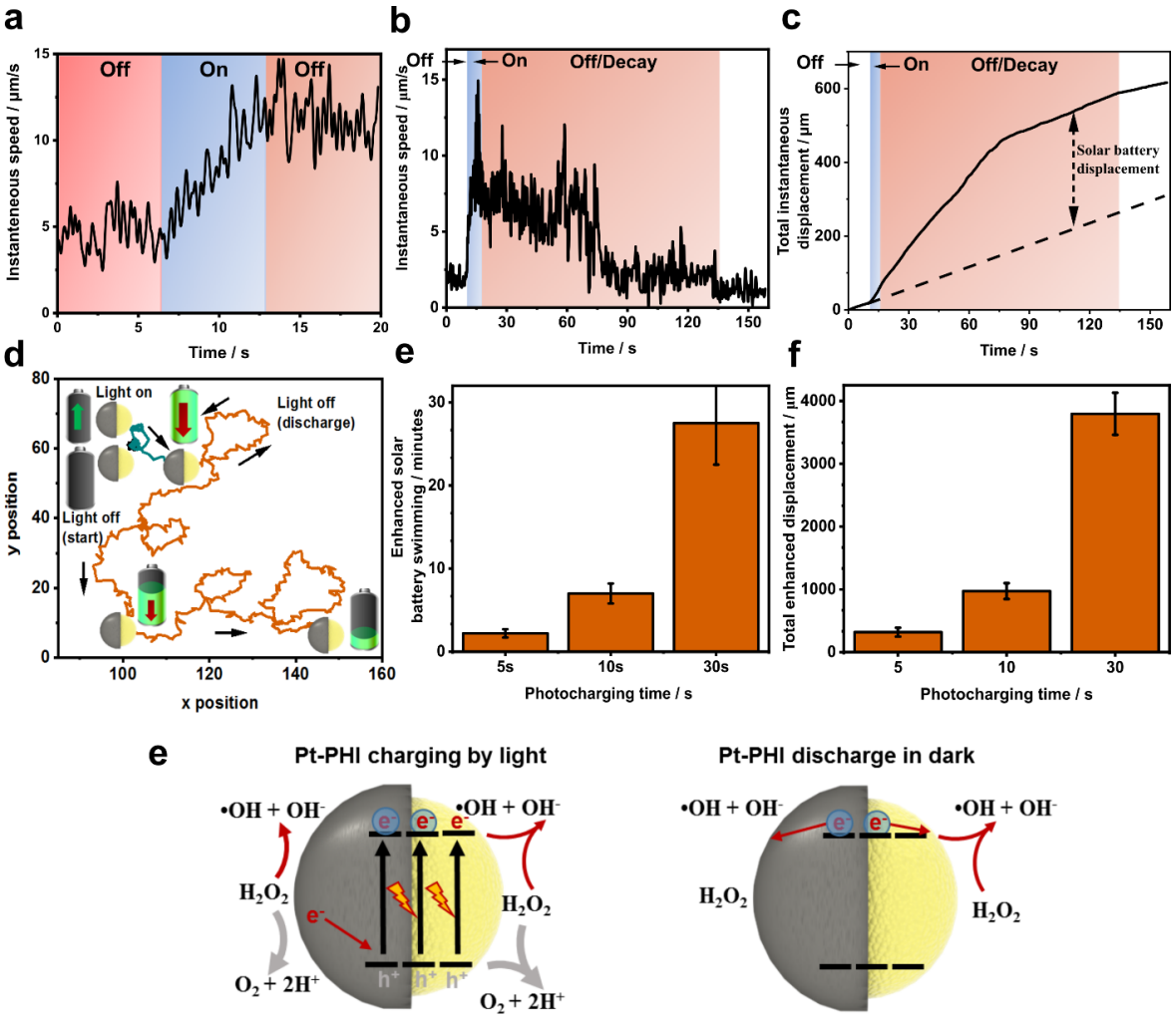

Figure 4.20 Light-enhanced swimming during and after UV illumination on Pt-PHI Janus microswimmers in H_2O_2. a: Continuous increase in swimming speed of a PHI-Pt microswimmer with 1% H_2O_2 under UV illumination (blue color), which leads to enhanced propulsion even after illumination is turned off (orange color) (Supplementary Movie 6). b: Solar battery swimming after 5s of illumination, which leads to light induced enhanced motion after UV illumination for periods up to 32x longer than the illumination time (up to 60 s shown here, see Supplementary Movie 7 for longer times). The data represents an averaged instantaneous speed (N=15). c: Microswimmer average total displacement (distance traveled) over time extracted from b. Dashed line: total displacement without illumination. d: Corresponding particle trajectory in the dark (0-10 s, in orange), under illumination (10 – 15 s, in blue) and during solar battery swimming (15 – 120 s, in brown). e: Schematic representation of the proposed reaction scheme enabling the solar battery charging mechanism on PHI and the subsequent discharge process enabling solar battery swimming in the dark, the arrows indicate the direction of the trajectory. Reproduced from reference [201].

To further study the solar battery swimming behavior and the relationship between charging and discharging times further, we have measured the solar battery swimming after 10 s and 30s of illumination. For 10s illumination, we observe the solar battery swimming effect for approximately 6.7 minutes, which is approximately 40 times the charge time as show on Figure 4.21a. The average instantaneous displacement of the microswimmers in the respective parts is illustrated in Figure 4.21b. As the charging time is increased to 30s we observe that the swimming slows down after 800s, which is about 27 times as the charge time as shown on Figure 4.21a, but the microswimmer does still not come back to mean speed before illumination. The microswimmer continuous to move ballistically, even though the mean speed was close to the initial one in the dark without ballistic motion, indicating that some discharge still continuous to occur in from the microswimmers, without significantly affecting the swimming speed directly. Some swimmers even continued to move even after 30 minutes after mere 30s of illumination. Their average instantaneous displacement of the microswimmers for 30s illumination in the respective parts is illustrated in Figure 4.21d. The summarized enhanced solar battery swimming times for 5s, 10s and 30s are shown on Figure 4.20e and their respective solar battery displacements are shown on Figure 4.20f. The electron accumulation process on the PHI during the illumination period, akin to the photocharging occurring prior to "dark photocatalysis" [206, 207], requires faster charging of the PHI compared to the intrinsic discharge rate of electrons driving self-diffusiophoresis or self-electrophoresis. Therefore, a high and asymmetric reaction rate on the Pt side is thus required that quenches the holes on PHI as shown in Figure 4.20g on the left. Alternatively, the slow electron transfer kinetics from the charged PHI volume to the Pt surface, together with the fast surface reaction on the Pt side may be the reason for the time-delayed discharge of the PHI particle after the illumination period. In any case, the drift of accumulated charge carriers to the surface enables the photocapacitive, enhanced motion without the presence of light, as shown on Figure 4.20g on the right, despite conditions that are not beneficial for charge accumulation *per se*.

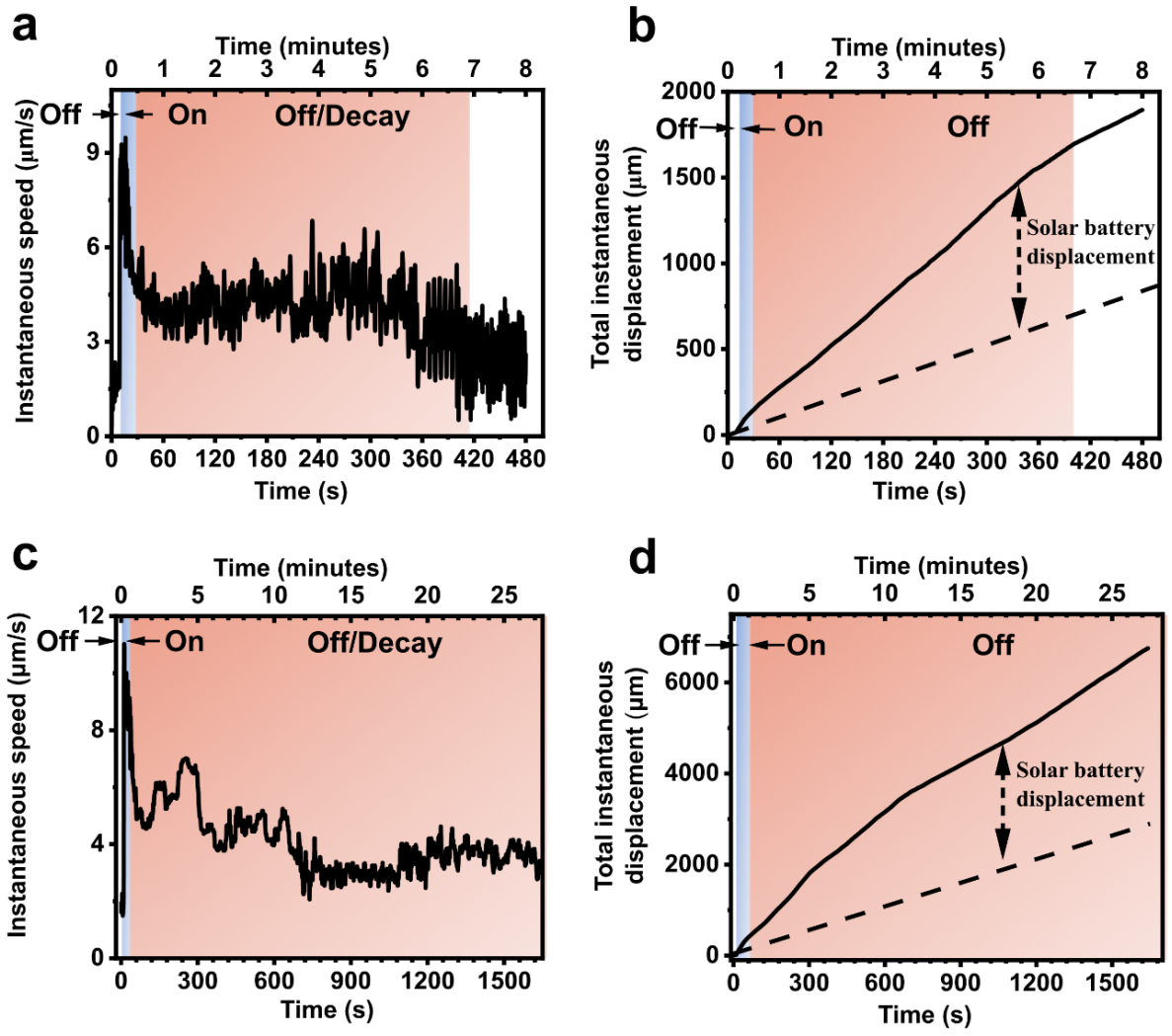

Figure 4.21 Solar battery swimming for longer prior illumination times. a) Solar battery swimming after 10 s of prior illumination, which leads to light-induced enhanced motion after UV illumination for 400 s (6.7 minutes, shown in orange-colored background). The active Brownian motion after the end of ballistic swimming (after 400 s) is shown with white background. The data represents an averaged instantaneous speed (N=5). b) Microswimmer total instantaneous displacement (distance traveled) over time extracted from a). Dashed line here represents the total displacement in dark without illumination, estimated from the passive Brownian displacement before illumination. The solar battery displacement is 767 μm (2.2 times further than the passive Brownian displacement) in 400 s. c) Solar battery swimming after 30 s of illumination, which leads to light induced enhanced motion after UV illumination for 600-800 s (13 minutes). The swimming slows down after 800 s but the swimmers continue to swim ballistically up to 1800 s. The data represents an averaged instantaneous speed (N=10). d) Microswimmer total instantaneous displacement as shown in c), reaching 3600 μm (2.16 times further than the passive Brownian displacement in the same duration) in 27 minutes.

Some swimmers continue to swim even longer than half an hour, which is beyond the possible analysis time of our equipment (30 minutes), hence making the propulsion time and total instantaneous displacement difficult to estimate for longer initial illumination times than 30 s.

4.11 Summary

In this chapter, we have studied the propulsion of carbon nitride-based light-driven microswimmers and demonstrated light-induced photocapacitive swimming under dark conditions, which originates from a solar battery functionality in poly(heptazine imide). The PHI-Janus microswimmers show efficient light-induced propulsion under visible light and UV illumination using both alcohols and H_2O_2 as fuels. Assisted by photoelectrochemical analysis, we elucidate the surface reactions being responsible for the predominantly self-diffusiophoretic propulsion with different caps (Pt, Au and SiO_2) in the presence of MeOH and H_2O_2 under ambient conditions. We find that PHI-Pt swims the fastest with water and alcohol as fuel, whereas PHI-Au, followed by PHI-SiO2 shows the fastest propulsion with H_2O_2 as fuel. Opposed to the mainstream assumption, we find that hydrogen is not evolved during the photocatalytically induced propulsion under ambient conditions, but oxygen serves as electron scavenger with alcohol donors used as fuels when Pt or Au are used as co-catalysts, even for the most widely used photocatalyst TiO_2. With H_2O_2, unexpected propulsion trends with different caps can be explained by competing surface reactions on both hemispheres. This interplay of different surface processes can be exploited to realize photocharging on PHI-Pt Janus microswimmers at H_2O_2 concentrations of 1% or above, enabling continued propulsion in the dark for up to 160 s after only 5 s of illumination, i.e., up to 32 times longer than the illumination period. The first observation of a solar battery swimming process is based on the dual light absorption and energy storage capability of PHI, akin to dark photocatalysis. However, its realization is a product of careful interfacial reaction studies and their rational tuning in order to enable the simultaneous charging and discharging of the PHI volume to achieve continued propulsion in the dark.

The unique properties of PHI-based microswimmers make them particularly promising for potential medical (e.g., targeted drug delivery) and environmental remediation applications, due to their sensitivity to visible light, their soft organic nature, and the possibility to use biocompatible caps such as Au or SiO_2. The solar battery swimming effect is anticipated to open new capabilities in diverse applications, where micro/nanomachines need to operate without continuous external fuel supply, and where environmentally or biologically benign materials are required. Finally, the charging effect reported here opens the door to the creation

of autonomous systems with built-in energy storage capabilities, since PHI can not only drive redox reactions in a time-delayed manner, but also provide an electrical potential, akin to a battery.

Chapter 5. High ion tolerance and stimuli-responsive drug delivery by biocompatible light-driven carbon nitride microswimmers

In this chapter, we demonstrate the versatile use of two-dimensional (2D) organic poly(heptazine imide) (PHI) carbon nitride particles as light-driven microswimmers in different ionic and biological media and cellular environments, such as diluted blood, without requiring additional fuels. The PHI microswimmers further show collective phototactic propulsion under UV and blue light illumination. These swimmers demonstrate unusually fast light-driven swimming in these multi-component ionic solutions up to concentrations as high as 1 M, thus overcoming one of the most critical limitations of many previous light-driven microswimmers towards biological applications. Biocompatibility of the organic PHI microswimmers is validated by viability studies with three different cell types and primary cells. Moreover, the swimmers can be loaded with a model cancer drug, doxorubicin (DOX), in large amounts (185% loading efficiency) without any passive release. Controlled drug release on demand is demonstrated in different pH conditions and can be triggered also by light. This environment-responsive drug release thus enables a theranostic function that can be crucial for the targeted therapy of tumour cells which contain reduced amounts of oxygen in their microenvironment.

5.1 Introduction

Microswimmers are cell-scale mobile machines that can be self-propelled by converting energy made available to them from their environment or remotely [12, 16, 202], such as chemical reagents, light, magnetic and acoustic energy [68, 225]. One of the main targeted applications of microswimmers is *in-vivo* local, active, and on-demand delivery of diagnostic or therapeutic cargos, such as drugs, imaging agents, and stem cells [226, 227]. Different propulsion methods impart different constraints on the possible uses and applications of microswimmers *in vivo* [228]. Nowadays, chemical propulsion, such as dissolution of metals (e.g., magnesium in acidic conditions), enzymatic and magnetic propulsion are the most widely used methods towards *in-vivo* medical applications [229]. Chemical propulsion is predominantly used for swimming in the stomach and gastrointestinal tract [229-232], whereas enzymatic propulsion can be used in

other body regions [43, 233, 234]. Both methods need sacrificial and usually toxic agents as fuels to enable swimming, which is disadvantageous for their prolonged use in biological conditions [77]. Light, however, is a viable energy source for the propulsion of microswimmers [85, 123], both with and without the use of additional fuels, enabling also propulsion control and steering [235, 236]. Photocatalytic swimmers can exhibit positive and negative phototaxis and gravitaxis [237], depending on their surface charge,[103] enabling collective steering and control of microswimmer swarms [194]. Despite many advantages over other methods of swimming propulsion, photocatalytic and chemical propulsion especially when diffusiophoretic and electrophoretic propulsion modes are operative suffer from fundamental limitations in electrolyte solutions[123] because the presence of ions hinders mobility of the microswimmers and, hence, the concentration gradients of starting materials and products involved in self-electrophoresis and self-diffusiophoresis [121, 238, 239].

5.2 Problems in swimming in biological media

Although different semi-conducting inorganic photocatalysts[112, 159, 168, 240-242] have been studied as light-driven microswimmers for potential biological applications[243], donor-free light-driven swimming in ionic media such as NaCl has been demonstrated with sophisticated geometries in Si and for concentrations below 10 mM. Thus, light-driven swimming in ionic media (NaCl, phosphate saline buffer (PBS) and Dulbeco's modified Engle's medium (DMEM) with concentrations over 200 mM, as present in various biological solutions or in real cell environment conditions), still remains an unresolved bottleneck. The EI50 number has been introduced previously as a measure of the ionic concentration at which the speed of the microswimmers is reduced by 50% [104]. EI50 is less than 0.1 mM for self-diffusiophoretic and self-electrophoretic swimmers [125], reaching up to ~4 mM for geometrically optimized systems addressing this problem [104]. For practical applications an EI50 value of more than 100 mM is needed. This limitation is attributed to the presence of a solid surface in the microswimmer, which does not allow fluids or ions to migrate through the particle. The presence of salt ions collapses the Debye layer of the microswimmers from hundreds of nm to ~1 nm [244], thereby collapsing also the ionic gradient around the particle under illumination, which is responsible for the propulsion force. Therefore, commonly, ions gradually stop the swimming for hard spheres, which are without any porosity. Besides, most light-driven microswimmers use high concentrations of H_2O_2 or alcohols as additional chemical fuels [245], which are toxic for their potential use in biological applications. The availability of potential biocompatible fuels that are present in large enough quantities has been

a pressing bottleneck in implementing light-driven microswimmers in such applications [123], which require concentrations as high as ~30 mM of fuel for effective light-driven propulsion, even in the presence of biocompatible fuels like glucose [126]. Furthermore, collective propulsion as well as controlled cargo uptake and release of active products are highly desired properties of medical microswimmers, which are usually studied and realized separately [246].

We have addressed all of the above issues by using photocatalytically highly active and texturally as well as structurally porous carbon nitrides (CN_x) as light-driven microswimmers. CN_x are a family of organic macromolecular photocatalysts that have gained attention because of their facile synthesis [220], chemical robustness, absorption of visible light and favorable band positions that enable various photocatalytic redox reactions, such as water splitting [247]. Besides, CN_x are widely used for environmental remediation[248], sensing applications and even as ion pumps recently [248, 249]. Most commonly, a one-dimensional (1D) carbon nitride called "melon" or "g-C_3N_4", is reported. However, the carbon nitride used in this study is the recently discovered and structurally characterized two-dimensional (2D) carbon nitride species poly(heptazine imide) (PHI) [198, 204, 250], which hosts hydrated alkali metal ions (typically K^+) or protons in its structural pores, resulting in an unusual blend of optoelectronic and optoionic properties [206, 207, 251]. PHI does not only show higher hydrogen evolution activity than Melon-type CN_x [198, 204, 252], but is also able to store light-induced electrons for subsequent use through electron-ion interactions [206, 207, 253]. Since PHI microswimmers exhibit not only structural but also textural porosity enabling ion intercalation and permeability that can be driven by light [207, 249-251], they are intriguing platforms for light-driven propulsion [253] and cargo delivery in various biological media. Hence, the development of biocompatible and highly ion tolerant, non-toxic light-driven microswimmers that can be propelled purely by light in naturally occurring bio-fuels while being able to carry and release a cargo in a controllable fashion combines many fundamental challenges [251].

In this work, we describe the phototactic propulsion of PHI microparticles in complex ionic solutions revealing efficient light-induced propulsion that decreases only slightly with increasing ion concentration of the liquid. In addition, biocompatibility of PHI microswimmers is evidenced with three different cell lines (HT-29, SKBR3 and fibroblasts) and primary cells from mice. Upon loading the model anti-cancer drug doxorubicin (DOX), stable physisorption without any passive release is observed, while active release can be triggered either by light or by a pH change in the cell culture medium. Moreover, *in vitro* experiments demonstrate the targeted delivery and uptake of DOX stimulated by the oxygen-depleted (hypoxic)

environment of cancer cells. These findings open up new avenues to the design of light-driven, biocompatible microswimmers that can move autonomously under conditions of high ionic strength and in the absence of dedicated fuels, which is highly relevant for targeted drug delivery, theranostics, and environmental applications.

5.3 PHI synthesis

PHI was synthesized according to a procedure described in the literature [198, 254]. Shortly, melamine (5.0 g) is heated in a tube furnace in a quartz glass boat to 550°C for 12 h with a heating rate of 5°C/min under Argon (Ar) flow. After cooling to ambient temperature, a yellow powder (2.0-2.5 g) is obtained. 1.5 g of this product (Melon) were thoroughly ground with KSCN (3.0 g), which was heated overnight to 140°C in vacuum to evaporate water. The mixture is heated in a tube furnace in an Alox boat to 400°C for 1 h and 500°C for 30 min with a heating rate of 30°C/min under Ar flow. The Alox boat with the CN_x is sonicated two times for 15 min in 80 mL of water to disperse the yellow product. This suspension is washed six times with DI water by centrifugation (20,000 rpm). The insoluble product is dried in vacuum at 60 °C overnight. SEM images of the microswimmers were captured by a Zeiss Merlin SEM. In order to capture the swimming of the microswimmers, a Zeiss Axio A1 inverted optical microscope was used.

5.4 PHI characterization

The PHI microparticles were obtained by sonication and centrifuge-assisted separation from the original suspension (see Materials and methods for details). Figure 5.1a shows a scanning electron microscopy (SEM) image of the PHI microparticles with a diameter ranging from 1-5 µm. As they represent agglomerates of smaller primary crystallites, the microswimmers have a slightly irregular spherical shape and textural pores occur naturally. These larger voids enable efficient fluid movement and entrapment. Figures 5.1b illustrates the schematic and underlying molecular structure of PHI microswimmers. Structural pores in the PHI backbone consisting of imide-bridged heptazine units are filled with hydrated ions that can be exchanged [250]. The absorbance spectrum in Figure 5.1c shows light absorption below 450 nm (band gap of 2.7 eV[206, 207]), enabling photocatalysis and, hence, propulsion driven by visible light. The strongly positive valence band position (+2.2 V versus Normal Hydrogen Electrode (NHE)[207]) gives rise to an even stronger oxidative power of light-generated holes than for Melon (Figure 5.1d), providing the thermodynamic driving force for various photocatalytic oxidation reactions including water oxidation, which are usually the bottleneck for light-generated charge extraction and photocatalytic propulsion[253].

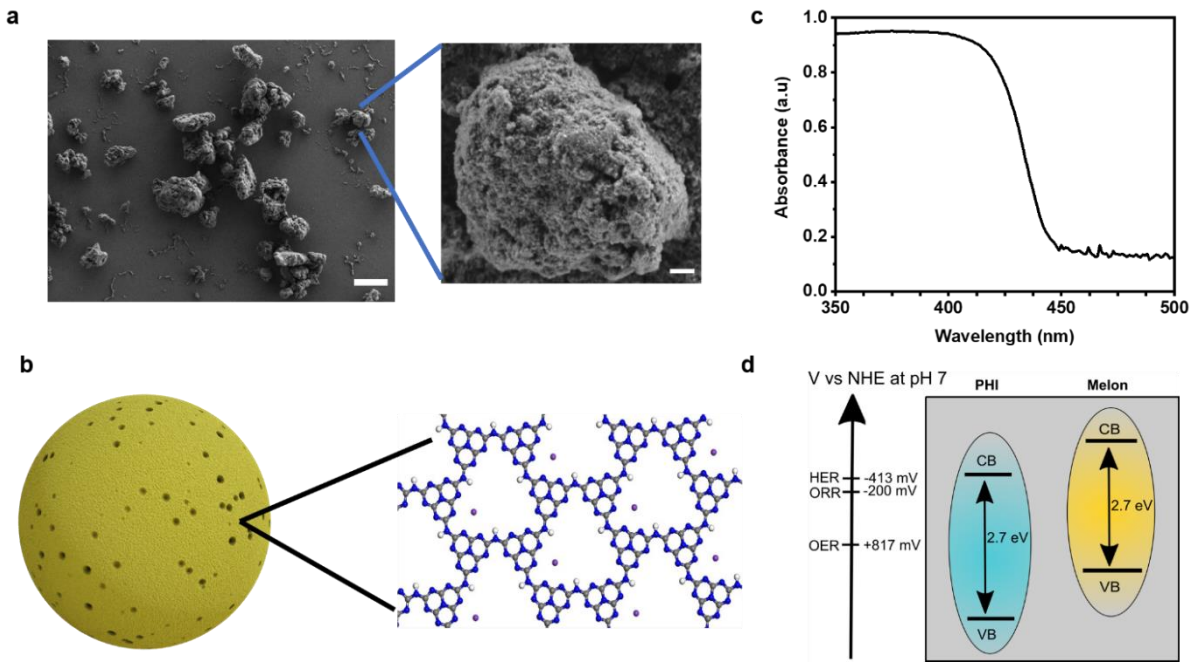

Figure 5.1 Structure, morphology and optical properties of poly(heptazine imide) (PHI)-based organic microswimmer particles. a) SEM image of representative PHI microparticles (grey) with a size distribution of 1-5 µm (scale bar: 5 µm) and close-up of one particle (scale bar: 400 nm), showing the porous morphology. b) Schematics of the PHI microswimmer and structure of the PHI macromolecules consisting of heptazine moieties comprising carbon (blue), nitrogen (grey) and hydrogen (white). Solvated potassium ions reside in structural pores (purple). c) Absorbance spectrum of PHI microswimmers, showing the onset of band gap absorption at 450 nm determined based on a Tauc plot. d) Band positions of PHI and Melon with a bandgap of 2.7 eV along with hydrogen evolution reaction (HER), oxygen reduction reaction (ORR) and oxygen evolution reaction (OER) potentials at pH7.

5.4.1 Pore size analysis

The physisorption isotherm of PHI obtained by BET analysis (Figure 5.2c) is best described as type II isotherm with a H3 hysteresis loop. Such a behavior is typical for plate like particle aggregates and non- or macroporous materials. In addition, the pore size distribution analysis reveals a small fraction of mesopores in the range of roughly 5-20 nm (Figure 5.2d). We therefore conclude that PHI is a material that contains meso- and macro-pores, in line with the results obtained from SEM analysis (Figure 5.2 a,b) [255].

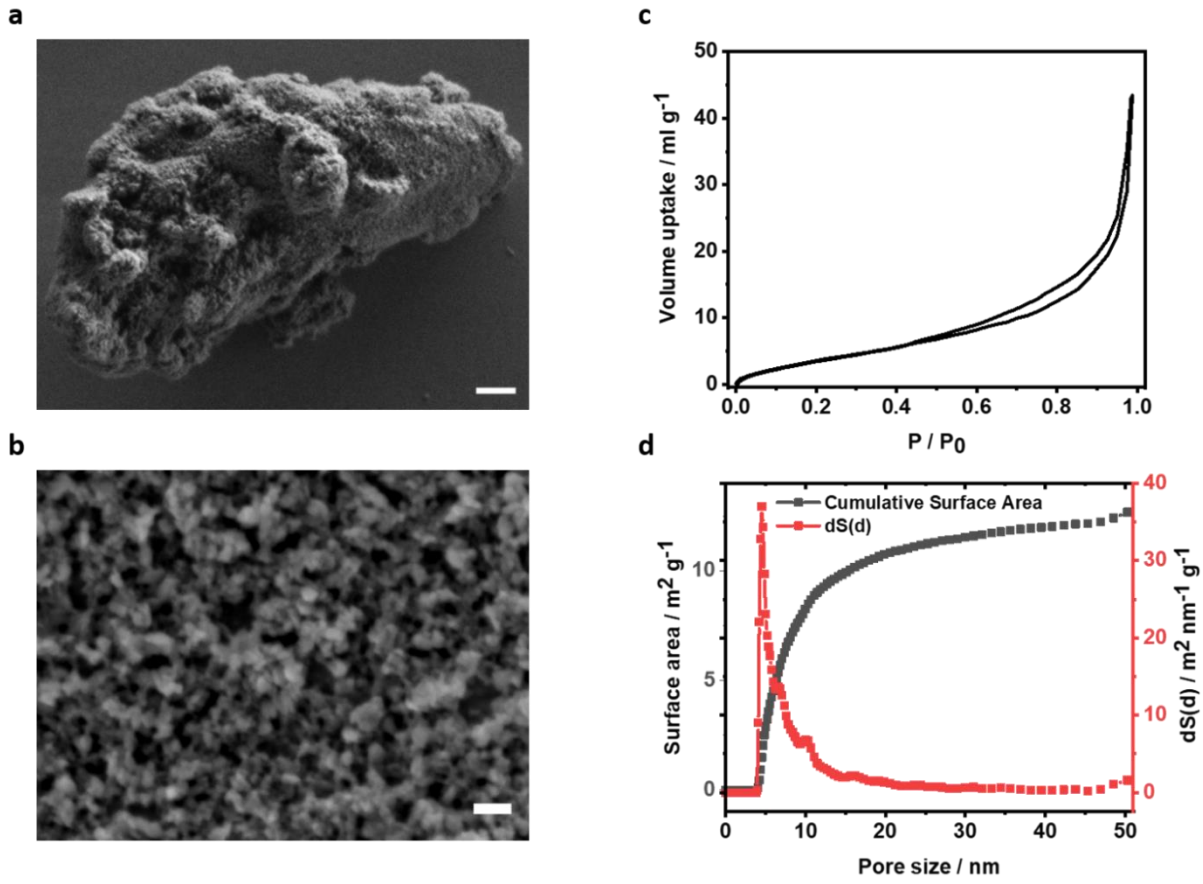

Figure 5.2 Structural analysis of PHI. a) Additional SEM image of a PHI microswimmer particle (scale bar: 400 nm). b) Close-up of a PHI particle showing the porous surface morphology (scale bar: 100 nm). c) Ar sorption isotherm for BET surface area determination of PHI. c) Specific surface area (~12.5 m^2/g) and pore size distribution (5-20 nm) of PHI obtained from BET analysis.

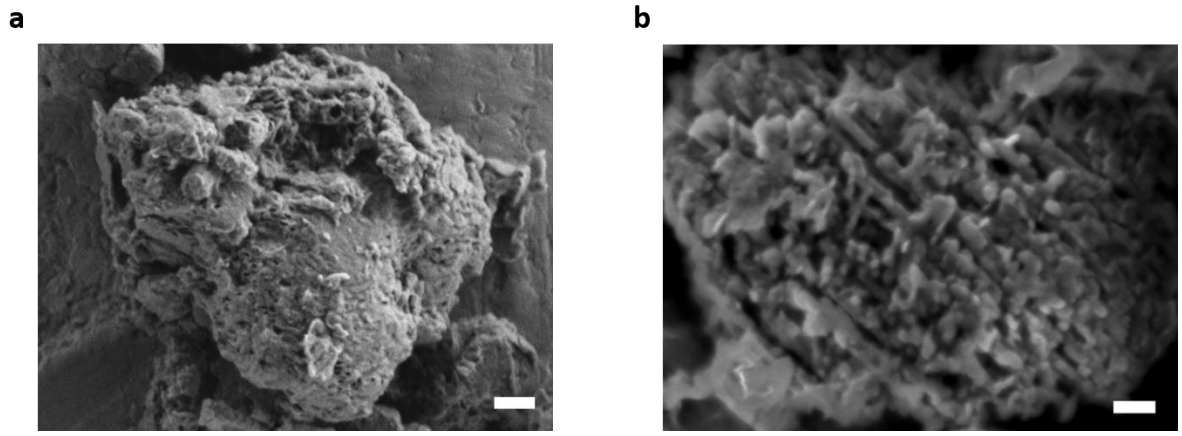

Figure 5.3 a) SEM image of a Melon microswimmer particle (scale bar: 400 nm). b) Zoom onto a Melon particle showing the porous surface morphology (scale bar: 100 nm).

5.5 Light-induced swimming in different biological media

In order to demonstrate the mechanism of propulsion of the PHI microswimmers, the light from a photodiode was focused with an intensity of 1.9 W/cm^2 at 385 nm on the particle chamber. The mean speed of illuminated microswimmers in deionized (DI) water was 24.2 ± 1.9 µm/s (Figure 5.4a). In this case, their photocatalytically induced motion is attributed to water oxidation and reduction of dissolved oxygen on the illuminated PHI hemisphere [253]. To explore and determine the influence of different ionic and biological constituents on the propulsion efficiency of PHI microswimmers, different pH neutral buffers and relevant biological media, such as Dulbeco's phosphate saline buffer (dPBS) and Dulbeco's modified Engle's medium (DMEM) were tested. In brief, dPBS was used as the buffer solution for cell washing and contains NaCl, KCl, Na_2HPO_4 and KH_2PO_4 at ca. 10 g/L (~150 mM) in total. DMEM, commonly used to culture cells, contains the same salts (~160 mM), amino acids (ca. 2 g/L, ~10 mM), trace amounts of vitamins and glucose (4.5 g/L, ~25 mM), some of which can be used as reducing agents and, hence, hole extraction fuel to power light-driven microswimmers [171]. However, the presence or absence of glucose in DMEM did not affect the propulsion speed of PHI microswimmers. Under illumination, the mean speed of the microswimmers in dPBS was 19.0 ± 3.3 µm/s (21% slower than in DI water) and comparable in DMEM (23.7 ± 2.6 µm/s, similar to DI water), as seen in Figure 5.4a. The ions present in dPBS (~150 mM) hence only have a relatively small influence on the speed of PHI, whereas the additional components in DMEM do not hamper the efficiency of photocatalytic reactions being responsible for the propulsion. To emulate a realistic cell environment, the growth-supplementing medium Fetal Bovine Serum (FBS) containing complex proteins and other

components [256] were added to DMEM. The illuminated PHI microswimmers still moved with a mean speed of 12.5 ± 3.1 µm/s in DMEM medium with 10% FBS, hence being 47% slower than in DMEM alone. This decrease in speed may be ascribed to the viscosity change, deposition of protein and other components on the PHI surface, thus blocking surface reactions partially [252]. Additionally, a high concentration (1 M) of sodium phosphate buffer, an important component of DMEM, was also used to test the propulsion of PHI microswimmers. We observed a mean speed of 9.4 ± 1.7 µm/s, which is 54% lower than in DMEM containing ~160 mM of salts. These findings show that PHI microswimmers can be used efficiently in many realistic biological environments and in salt buffers at concentrations even beyond biological systems.

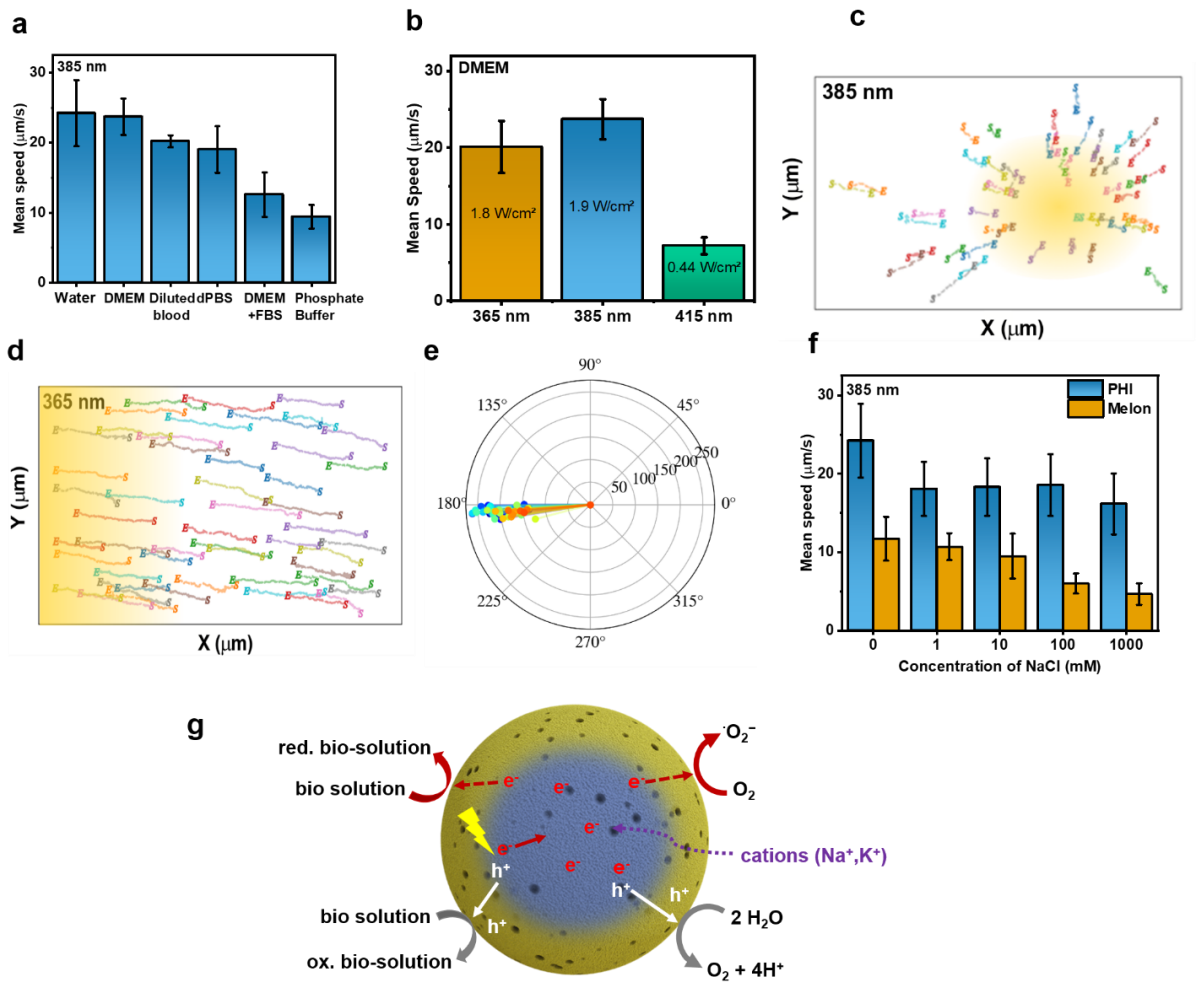

Figure 5.4 PHI microswimmer propulsion in different ionic fluids. a) Average mean speed (N=50) of PHI microswimmers in various biological media swimming under 385 nm illumination. b) Average mean speed (N=50) of PHI microswimmers in DMEM medium under

different illumination wavelengths. c) Sample trajectory of PHI microswimmers in DMEM medium swimming under 385 nm illumination showing swarming behavior. S and E indicate the start and end of the trajectories. d) Sample trajectory of PHI microswimmers in DMEM medium swimming under 365 nm illumination from the side with S and E indicating the start and end of trajectories showing positive phototactic behavior. e) Polar plot of PHI microswimmers' directed propulsion in the same conditions as d). f) Average mean speed (N=50) of the carbon nitrides PHI and Melon in different concentrations of NaCl under 385 nm illumination. g) Reactions affecting the photocatalytic propulsion of PHI microswimmers and the light induced movement of K^+ and Na^+ ions (purple) into the particle, enabled by textural, and structural porosity, which leads to photocharging in PHI (blue).

Active motion in heterogeneous and complex biological fluids, such as blood, is also crucial for future biomedical applications in the human body. To test the propulsion capability of the PHI microswimmers in blood, they were mixed with blood cells with a 25% hematocrit (in DMEM medium), which is in the physiological range. When illuminated with UV light (385 nm), the PHI microswimmers also moved in the diluted red blood cell (RBC) solution. Auto-fluorescence of the PHI microswimmers, i.e., the natural emission without any fluorescent markers, enabled their label-free imaging and detection even in the optically dense RBC solution. The mean speed of the PHI microswimmers in the dilute RBC solution, where viscosity remains the same in comparison with pure DMEM solution [257], was 20.2 ± 0.8 μm/s, comparable to their mean speed in DMEM medium. The RBCs in the solution were also observed to be moving, which appears to be caused by the fluidic flow fields arising from the collective propulsion of PHI microswimmers (vide infra). Of note, the PHI microswimmers were not able to swim in whole blood, which could be ascribed to the increased viscosity, heterogeneous non-Newtonian nature and possibly the lack of sufficient amounts of fuel in these conditions, making it impossible to swim effectively. A comparison of the available literature and the current work on ionic swimming is shown in Table 5.1.

Table 5. 1 Ion tolerance of light-driven microswimmers from the literature in comparison with this work.

Microswimmer type	*Ion tolerance*	*Mean speed*
Si with SPS coating [104]	up to 3 mM (EI50 at 0.25 mM)	~12 µm/s (0.32 mM NaCl and BQ/H_2Q as fuel)
Si with SPS coating(geometrically optimized) [104]	up to 40 mM (EI50 at ~4 mM)	~12 µm/s (0.32 mM NaCl and BQ/H_2Q as fuel)
Reduced Graphene oxide (with donor added and decomposition) [258]	up to 100 mM NaCl (no data on EI50)	~22 µm/s (100 mM NaCl)
PHI (this work)	up to 1 M NaCl (EI50 not reached even at 1 M)	23.7 ± 2.6 µm/s (1M DMEM)
Melon (this work)	>0.1 M and <1 M NaCl (EI50 at 100 mM)	6 ± 1.3 µm/s (100mM NaCl)

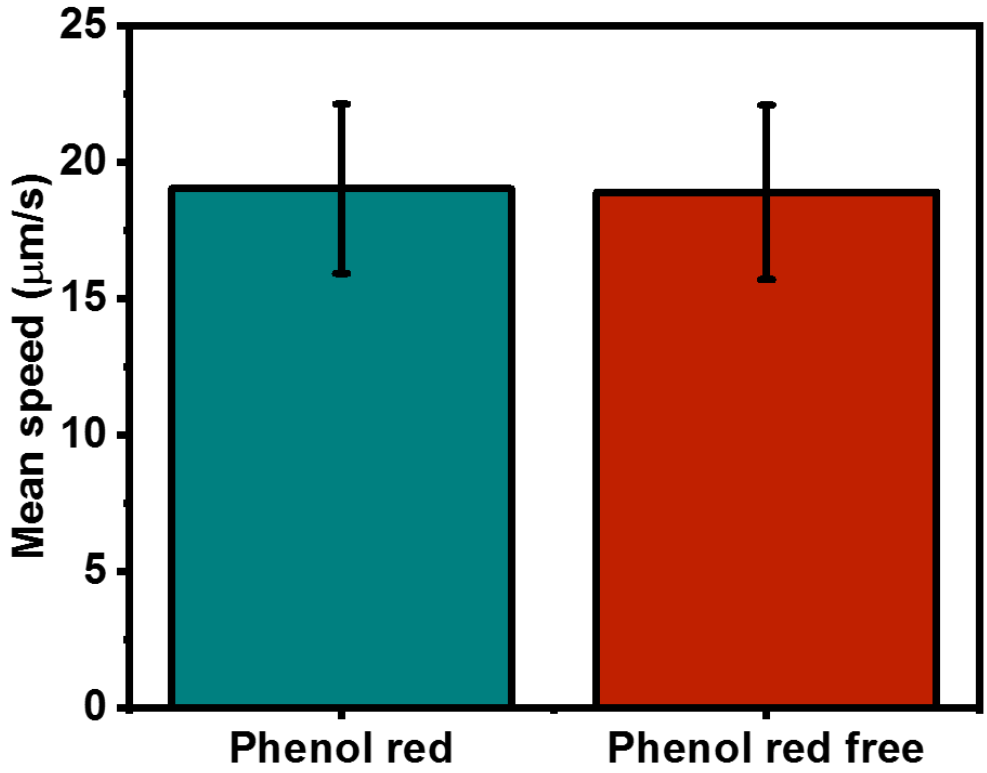

Figure 5.5 Average mean speed of PHI microswimmers in DMEM medium containing phenol red and phenol red-free solutions with same intensity of 385 nm.

5.6 Intensity and wavelength dependence

The light-intensity dependence of the PHI swimmer propulsion was studied under 385 nm UV light in DMEM medium and is shown in Figure 5.6 from 0 to 2 W/cm². The almost linear relation between intensity and propulsion speed suggests that the quantum efficiency of the propulsion process is not modified in this intensity range, even in the presence of the ions. The effect of illumination wavelength was also measured in DMEM by illuminating the microswimmers at four different wavelengths, 365 and 385 nm in the UV spectrum and blue light at 415 nm and 430 nm with intensities of 1.8, 1.9 and 0.44 W/cm² (~50% error from area of illumination), respectively, as shown in Figure 5.4b. The PHI microswimmers swam the fastest at 385 nm (23.7 ± 2.6 μm/s) and were slightly slower (20.1 ± 3.1 μm/s) at 365 nm, which corresponds to the slightly lower intensity of UV light. When illuminated at 415 nm, the speed was reduced to 7.2 ± 1.1 μm/s, which corresponds well to the mean speed at 385 nm at 0.4 W/cm². However, the microswimmers did not show any light-induced swimming with 430 nm illumination, despite the measured absorption edge of PHI at 450 nm. This indicates that the already decreasing absorbance of the material (Figure 5.1c) stems from states that are unproductive in terms of the photocatalytic reactions assisting propulsion. It can be

summarized that the efficiency of the light-induced swimming process is proportional to the light intensity up to 2 W/cm² and independent of the wavelength up to 415 nm in DMEM, highlighting that also harmless visible light can be used for efficient propulsion of PHI in biological solutions. There is also no effect of Phenol red – an ingredient of DMEM used to indicate the pH of the solution – on the swimming speed, as seen in Figure 5.4. A collection of the mean speeds in different fluids is shown in Tables 5.2-5.4.

Table 5. 2 Mean speed results of PHI microswimmers under illumination with different (ionic) media with illumination at 385 nm.

Media (illumination at 385 nm at 1.9 W/cm^2)	*Mean speed*
Pure DI water	24.2 ± 4.7 µm/s
DMEM	23.7 ± 2.6 µm/s
Dilute blood (25%)	20.2 ± 0.8 µm/s
dPBS	19.0 ± 3.3 µm/s
DMEM + FBS	12.5 ± 3.1 µm/s
Phosphate buffer	9.4 ± 1.7 µm/s
DOX loaded in DMEM	18.5 ± 1.0 µm/s

Table 5. 3 Mean speed results of PHI microswimmers in DMEM under illumination with different wavelengths.

DMEM under different wavelength	*Mean speed*
365 nm at 1.8 W/cm^2	20.1 ± 3.4 µm/s
365 nm (at ~45°) at 115 mW/cm^2	12.5 ± 0.4 µm/s
385 nm at 1.9 W/cm^2	23.7 ± 2.6 µm/s
415 nm at 0.42 W/cm^2	7.2 ± 1.1 µm/s
Dark (~25 mW/cm^2 white light, control)	3.2 ± 0.8 µm/s

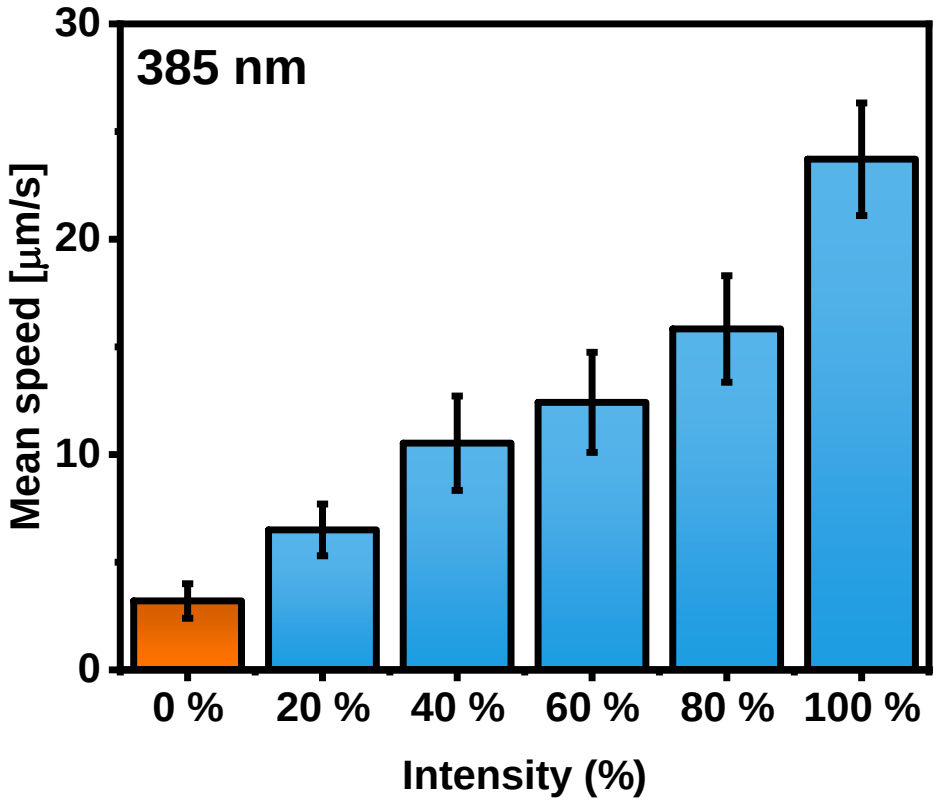

Figure 5.6 Average mean speed of PHI microswimmers in DMEM at 385 nm at different intensities. In order to test the effect of light intensity on the swimming speed of the PHI microswimmers, five different light intensities (1.9, 1.52, 1.14, 0.76 and 0.38 W/cm^2) were used in DMEM solution. The speed of the swimmers decreases in line with the UV light intensity. A decrease in swimming speed is expected because the lower photon flux (being proportional to intensity) leads to a decrease in photogenerated charges, hence affecting the photocatalytically generated proton or more generally, charge gradient responsible for the propulsion of the swimmers. However, the linear relation between intensity and propulsion speed suggests that the quantum efficiency of the propulsion process is not modified in this intensity range, even in the presence of the ions.

5.7 Phototaxis-based directional and collective control of PHI microswimmers

When a PHI microswimmer swarm was illuminated under the optical microscope, the particles moved towards the middle of the light beam (Movie S1 and Figure 2c). The light from the LED source was focused onto the image place from the objective. Since an inverted microscope was used, the light is focused from below on to the imaging plane containing the PHI microswimmers. Such behaviour is not only observed in DMEM alone, but in all tested fluids. Since PHI has a negative zeta potential (-40 mV) [198], enabling positive phototaxis [103], their motion towards the centre of the beam and then upwards was observed, causing a

phototactic swarming behaviour as seen in Figure 5.4c and discussed further below. Besides the ensemble control to reaccumulate the spread particles, this property can be beneficial for creating a convective flow also in the illuminated liquid, e.g., to stir it, as shown with red blood cells and drug-loaded microswimmers [259]. To test the phototactic properties of the PHI particles in more detail, they were illuminated with 365 nm UV light at an 45º angle from one side, with an intensity of 115±15 mW/cm^2, also in DMEM medium. This created a light gradient along the *x*-axis as shown in Figure 2d. The mean speed of the microswimmers was 12.5 ± 0.4 µm/s in this case, which is significantly higher (78%) compared to the lateral motion measurement with perpendicular illumination through the microscope objective at 400 mW/cm² (6.5 ± 1.2 µm/s,) and hence as fast as with 10x stronger illumination from the top (1.2 W/cm²).

This apparent increase in speed is attributed to a change in directional component of the measured speed. In the case of illumination from the side, there is a larger parallel component resulting in a higher lateral speed, whereas when illuminating from the bottom, the parallel component is slower while the *z*-component (parallel to the illumination) is not analysed, resulting in a lower effective speed. As can be seen from the trajectories in Figure 5.4d, the polar plot in Figure 5.4e, the PHI particles follow the direction of illumination precisely. Although the microswimmers are not Janus-type in structure, they show directional propulsion due to light being asymmetrically absorbed on one illuminated hemisphere only.[91]The amount of absorbed photons decreases with the increasing depth of penetration inside the microswimmers, giving rise to an asymmetry in charge generation in the microswimmers in the direction of illumination. The charge gradients that are created on the particle surface because of the asymmetric illumination are therefore sensitive to the direction of illumination. The side facing the light becomes the dominant side and shadows the other half of the particle, resulting in the creation of an artificial Janus-type structure due to illumination.

When the direction of illumination was changed, the direction of swimming also changed. Furthermore, it also explains the discrepancy between the speeds measured from the perpendicular illumination (from bottom) and from the side at 45º. When illuminated from the bottom, only the components arising from side-wise illumination (such as the planar intensity gradient causing swarming behaviour) actually contribute to the measured propulsion speed, which underestimates the real phototactic speed of the swimmers. Besides, tumbling and rotational motion may cause a sidewise motion with perpendicular illumination.[203]

However, also the generation of heat and convective flow can contribute to the propulsion and swarming behaviour, as observed during control experiments with PS particles that do not show phototaxis on their own, but are propelled as fast as PHI in their presence (Figures 5.9). These effects likely also explain the convective motion upwards, away from the bottom illumination. Nevertheless, phototactic properties of the PHI microswimmers originating dominantly from light-induced photocatalytic propulsion can be used to control their motion in a variety of future biological applications, such as targeted drug delivery and cargo transport, as we will investigate below.

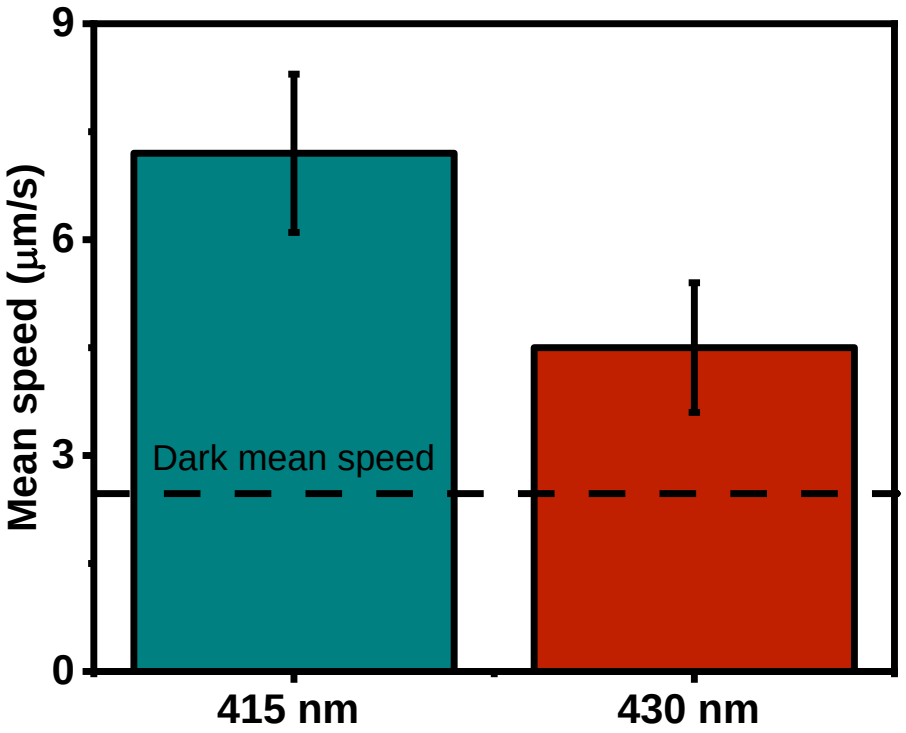

Figure 5.7 Average mean speed of PHI microswimmers in DMEM medium under different wavelength illumination with intensity of 440 mW/cm^2 and 1.4 W/cm^2 at 415 nm and 430 nm, respectively. At 430 nm only active Brownian motion, but no ballistic propulsion is observed.

5.8 Light-induced charging of PHI microswimmers

When a denser suspension of PHI microswimmers (100 mg/ml), dispersed in DMEM medium inside a closed microfluidic chamber, is illuminated under 385 nm light, the PHI microswimmers change their color and turn blue. This blue state, described previously to occur upon photocharging in the presence of alcohol donors [254, 260], is characteristic for electron storage in PHI. The change of color occurs in suspensions above 0.7 mg/ml, below which the solution is too dilute to visualize the color change. Since stable photocharging with electrons requires the absence of electron scavengers such as O_2, it appears that oxygen is consumed

initially by photocatalytic reactions [253] in crowded environments and so that the photoreduced state persists due to the low diffusion coefficient of O_2 in aqueous conditions (2.16×10^{-9} m^2/s) [261]. Indeed, the blue state, shown on Figure 5.8b and Figure 5.13c, is found to fade in ~10 s after illumination in the microfluidic chamber, further evidencing our previous findings that photocharging in ambient conditions can only result if a suitable balance between photocharging and decay processes is maintained [207, 253]. The charge storage in oxygen poor environments, which affects various material properties,[207] may further be interesting for responsive and possibly theranostic applications that are explored below. One area of such applications is cancer cells therapy, since an oxygen depleted environment is observed there and in many infected tissues [262].

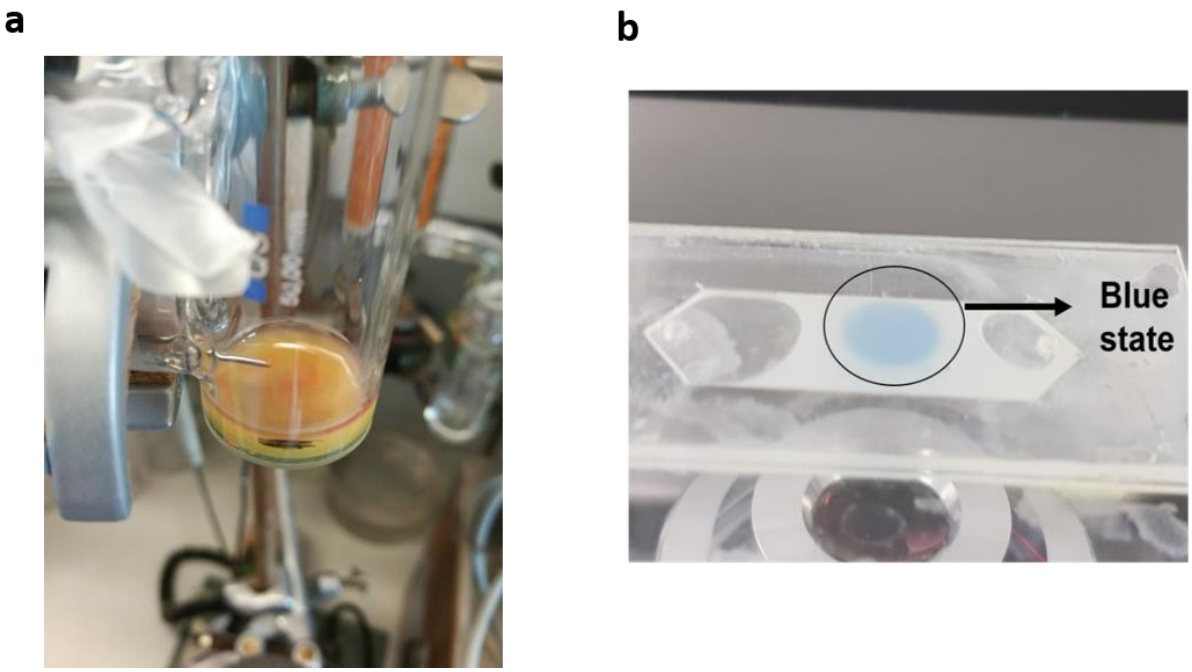

Figure 5.8 a) Experimental setup for studying the release of DOX from pre-loaded PHI microswimmers in DMEM after illumination under 415 nm light in ambient and oxygen deficient conditions by purging the suspension with Ar through a septum with a needle. b) Blue state of high concentrations of PHI microswimmers after illumination showing photo-charging in DMEM medium under 385 nm wavelength illumination.

5.9 Ionic tolerance for light-induced propulsion with NaCl

To better understand the ionic tolerance of PHI, the microswimmers were exposed to various NaCl concentrations and compared to the "sister material" Melon under 385 nm illumination, as shown in Figure 5.4f. In comparison with DI water (24.2 ± 1.9 μm/s), the PHI swimmers

show a 25% decreased speed (18.1 ± 3.4 μm/s) at 1 mM NaCl, with no obvious further decrease in speed observed until 100 mM (18.6 ± 3.4 μm/s). At 1 M NaCl, they show a further decrease (12%) in speed (16.1 ± 3.9 μm/s). Hence, the speed was reduced only by 33% with respect to DI water and the characteristic EI50 was not yet reached; thus, PHI's ion tolerance surpasses all reported light-driven microswimmers by two orders of magnitude, while maintaining fast light-induced propulsion above 100 mM salt concentrations. To further investigate the effect of textural porosity on the high ion tolerance, PHI and melon were tested under identical conditions. While both melon (Figure 5.3) and PHI exhibit textural porosity (see Figure 5.1a and 5.2 for SEM and BET measurements), melon has no structural porosity as it consists of close-packed 1D heptazine imide chains, hence enabling only surface ionic interactions. As can be seen from Figure 5.4f, the swimming speed of the Melon microswimmers under UV illumination is 43% lower than that of the speed(11.7 ± 2.9 μm/s) in DI water. The decrease is relatively weak up to 10 mM (9%), with EI50 being reached at ~100 mM (6 ± 1.3 μm/s). These findings show that also this form of carbon nitride has a high ion tolerance (higher than any other material reported except PHI), which we tentatively attribute to its textural porosity, enabling ionic permeation by an inner flow of liquid. However, at 1 M NaCl, the Melon microswimmers stop swimming, which may be due to a reduced driving force for hole extraction or surface poisoning in the presence of high salt concentrations.

In contrast to Melon, PHI has not only textural, but also structural pores with a radius on the order of 3.84 Å [198, 204, 207]. The pores are large enough to host and allow the passage of hydrated K^+ and Na^+ ions (hydrodynamic radius of 1.25 and 1.84 Å, respectively), making the molecular backbone of PHI permeable to ions. We have demonstrated in earlier work that the light-induced hole extraction and photo-charging ability of PHI is intimately linked to the presence of ions in the pores of PHI and the surrounding electrolyte, which may lead to light-induced ionophoretic ion transport throughout the structural and textural pores of PHI [204, 249-251, 260] as illustrated in Figure 5.4g. We believe it is these intrinsic optoionic properties of PHI - absent in melon - paired with porosity, that lead to sustained motion in high ionic strength media. Both the presence of textural as well as structural pores invalidates the assumption of a hard sphere (i.e., no liquid or ion flow through the volume of the particle), which is commonly used to describe phoresis. Hence the Helmholtz-Smoluchowski equation, $U=\mu_e E_0$, where μ_e is the electrophoretic mobility and E_0 is the magnitude of the electric field, cannot be used to sufficiently describe the motion and new computational models need to be developed to fully capture the reason for the high ion tolerance of this organic semiconductor.

Nevertheless, the propulsion of the PHI microswimmers in purely ionic solutions is reduced due to various ionic effects affecting the self-diffusiophoresis/electrophoresis mechanism, such as collapse of the Debye layer and reduction of available redox species, as assumed for hard spheres [125]. A distinction of textural and structural porosity effects remains to be verified with similarly optoionically interacting particles that correspond to a hard sphere while being suitable for light-induced propulsion once an appropriate material becomes available. In the case of buffers and biological fluidic media studied, the additional species, partially negate the speed reduction, presumably by offering additional redox reaction pathways with respect to water and NaCl, hence increasing the efficiency of the photocatalytic propulsion process.

Table 5. 4 Mean speed results of PHI and Melon microswimmers in different concentrations of NaCl under 385 nm illumination.

Media (illumination at 385 nm at 1.9 W/cm^2)	*Mean speed PHI microswimmers*	*Mean speed Melon microswimmers*
DI water (0 mM NaCl)	24.2 ± 4.7 µm/s	11.7 ± 2.8 µm/s
1 mM NaCl	18.1 ± 3.4 µm/s	10.7 ± 1.7 µm/s
10 mM NaCl	18.3 ± 3.6 µm/s	9.5 ± 2.8 µm/s
100 mM NaCl	18.5 ± 3.9 µm/s	6.0 ± 1.2 µm/s (EI50 is reached)
1 M NaCl	16.2 ± 3.9 µm/s	4.6 ± 1.3 µm/s (no swimming)

5.10 Thermal effects

The use of UV light illumination raises potential questions on the effect of the heat on the particles and thermophoresis. Polystyrene (PS) particles of 2 µm are used as control to determine the effect of heat from the UV light. PS particles have a poor thermal absorption coefficient resulting in reduced heat absorption by the particle. Similar experiments have been done previously in literature to rule out the effect of heat [104, 258, 263]. PS particles were dispersed in DMEM medium and illuminated under UV light. The particles did not show any swimming towards the center of the beam or any ballistic swimming in general, they only show an increased active Brownian motion without any active propulsion, thus ruling out direct thermal effects from the UV light during propulsion (Figure 5.5). The other potential thermal

effect could arise from the ability of PHI to absorb UV light more effectively. Some of this absorbed light irradiation can potentially be converted to heat, causing thermophoresis of the particles. The medium also plays a role in the heat transfer of the particles. In order to test the effect of heat transmission and thermophoresis on particles illuminated by UV light in DMEM medium, the swimming of PHI swimmers in high concentration (300 µg/ml) was observed in the presence of a thermal camera to observe if there is a heating of the solution. After 15 minutes of illumination under UV light, only a 2°C raise in temperature is measured, which is too low to cause thermophoresis of the particles.

This increase in temperature of the solution can be either due to the microfluidic chamber absorbing the light partially and generating heat, or due to heat generated from the photocatalytic reactions (photothermal effect), giving rise to a local heat gradient in addition to the phoretic gradient caused from the catalytic activity on the surface of the particle. Such heat generated on the particle or by the chamber itself combined with the closed nature of the chamber could give rise to the convective flows observed during the collective assembly of the microswimmers (Figure 5.4c), with hot liquid going upwards, but attracting surrounding liquid to the center. This could potentially explain the increased swimming speed of PS particles in presence of PHI (Figure 6) Once convective flows originate, the flows can be strong enough to negate the effects of phototactic activity, which is why a particle motion away from the bottom illumination was observed, although, generally, the PHI particles show a positive phototactic behaviour. However, the decrease in speed of melon, a material with similar absorption properties, in increasing concentrations of NaCl indicates that diffusio/electrophoresis still play a dominant role in the phototactic propulsion of the microswimmers, which can strengthen the convective flow when assembled towards a point (Figure 3c). If the swimming was caused due to heat only, no dependence on the ion concentration would be expected. In addition, such high concentrations of the microswimmers would cause a large heat difference (~30°C [264]), but we did not observe any significant increase in temperature when swimmers at concentrations as high as 0.1 mg/ml are dispersed and illuminated in DMEM. To further rule out collective heat generation from PHI particles as major reason for the propulsion, the effect of concentration on the propulsion speeds of the PHI microswimmers was also tested. When two different densities of 2 µg/ml and 30 µg/ml were used, no difference in their speeds was observed. If thermophoresis is a factor in propulsion of the microswimmers, the denser suspension would have shown higher mean speed due to the collective heating of the solution due to the heat radiated by the particles. Furthermore, when the microswimmers are

illuminated with a 430 nm light source, they did not show any phototactic swimming behaviour as shown on Figure 5.5, further evidencing that the surface catalytic activity occurring due to photocatalysis under illumination propels the microswimmer, and not the heat that is created due to absorption. This is rationalized by assuming that absorption near the experimentally estimated band gap of 450 nm stems from activation of recombination active trap states near the gap that do not add to propulsion, but yield recombination and hence add to heat generation most efficiently.

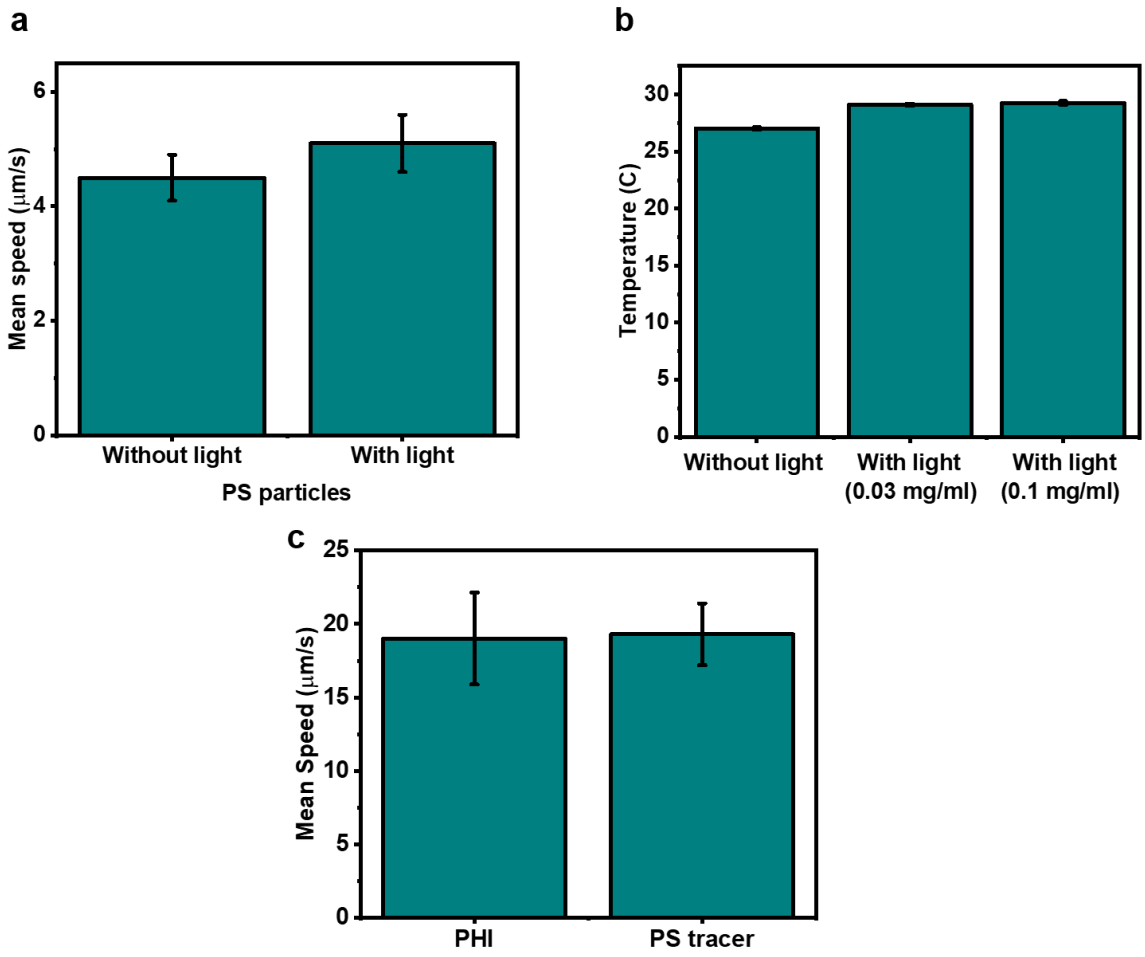

Figure 5.9 a) Average mean speed of Polystyrene (PS) 2 μm particles in DMEM medium under 385 nm illumination. b) Temperature measurements of PHI microswimmers without and with light at two different concentrations. c) Average mean speed of PHI microswimmers and PS tracers (2 μm) present in the same suspension under illumination with 385 nm light in DMEM, highlighting that the speed of the PS tracers is affected by the motion of PHI under illumination.

5.11 Cytotoxicity tests

A low cytotoxicity profile of the microswimmers is an essential requirement for biomedical applications. Therefore, we tested the cytotoxicity of the PHI microswimmers with a normal cell line (NIH 3T3 fibroblast cells) and two cancer cell lines (HT-29 colorectal cancer cells and SKBR3 breast cancer cells). Live/dead staining of the tested cell lines incubated with varying concentrations of PHI microswimmers (0-30 µg/mL) for 24 h showed no decrease in cell viability for all cell lines (Figure 5.10a,b). Other than particle cytotoxicity, we also tested the effect of illumination and catalytic activity of PHI microswimmers on cellular viability. Illumination at 415 nm (420 mW/cm^2) and 385 nm (1.1 W/cm^2) of high density of PHI microswimmers (30 µg/mL) on the fibroblast cells for varying durations (0-30 min) show no negative effects on the viability, both immediately after testing and after 24 h incubation (Figure 5.10c,d). Coupled to the efficient propulsion of the PHI microswimmers in biological media, their operation in cellular environments is highly promising. When illuminated at 415 nm, the cells retained viability up to 24 h for illumination times of 30 min. With 385 nm UV light, 24 h viability is retained up to 10 min of illumination. Since strong UV illumination for long durations is harmful for the cells [265], they are not viable anymore if illumination lasts for 30 min. Studies with primary cells from mouse splenocytes further confirmed the absence of an immune response.

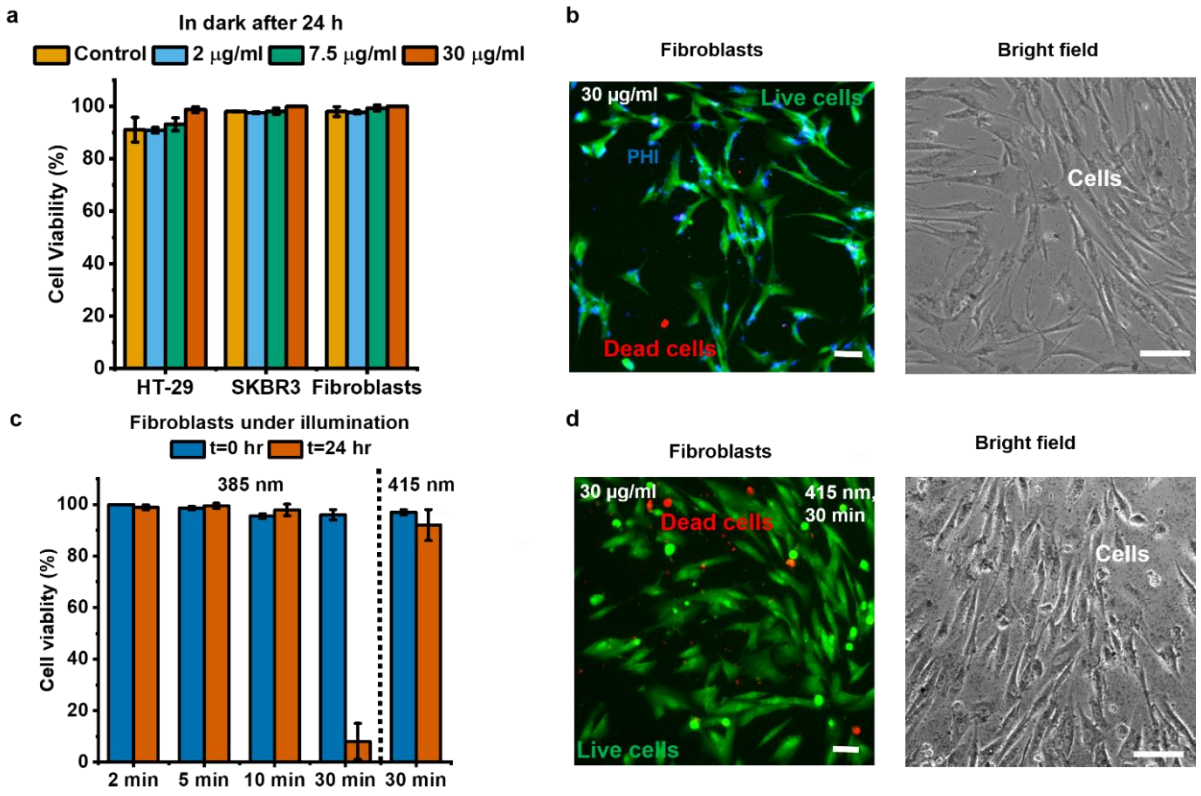

Figure 5.10 Cytotoxicity of PHI microswimmers. a) Cell viability of fibroblasts and cancer cells incubated with PHI microswimmers at varying concentrations after 24 hours. Data represents means ± standard deviation of ~300 cells. b) Live/dead staining of healthy BJ fibroblast cells following 24 h incubation with the PHI microswimmers. Green and red indicates the live cells and dead cells, respectively. Along with the bright field images in the same conditions indicating the cells and PHI (black dots). Scale bar: 100 μm. c) Cell viability of BJ fibroblast cells in presence of PHI microswimmers (30 μg/ml) right after and 24 h after illumination for varying durations at 385 nm and 415 nm. Data represents means ± standard deviation. d) Live/dead staining of BJ fibroblast cells following swimming of PHI swimmers, not in the picture (30 μg/mL) via light (415 nm) after 30 mins. Along with the bright field images in the same conditions indicating the cells and PHI (black dots). Scale bar: 100 μm.

5.12 Drug loading and hypoxically, pH- and light-triggered drug release

5.12.1 Drug loading

If the PHI microswimmers are capable of carrying and releasing cargo, along with its biocompatibility, they are promising candidates for targeted cargo (e.g., drug, gene, imaging agent) delivery applications. The idea behind the concept is shown in Figure 4a with the anti-cancer drug model, doxorubicin (DOX). The presence of textural pores present in Melon and PHI microswimmer particles is beneficial for enhanced drug loading efficiency (BET surface

area ~12 m^2/g and pore size distribution from 5-20 nm in PHI, Figure S7), enabling the adsorption of drugs within the microparticle [198, 266]. We further anticipate that the drug uptake is assisted by the negative zeta potential of PHI and free surface groups on the PHI, which intrinsically attracts the positively charged DOX molecules [266]. To test this hypothesis, 200 µg of DOX was added to a suspension of 100 µg of PHI microswimmers dispersed in 1 mL DMEM, resulting in 185 µg DOX encapsulated with a DOX loading efficiency of 185% (185 µg) on PHI after 24 hours. Figure 4b shows the fluorescent image of DOX loaded on PHI particles. For Melon, a loading efficiency of 110% (110 µg) resulted under the same conditions. Astonishingly, no passive release was observed for PHI in the absence of illumination, for more than 30 days. The stronger attachment of DOX to the surface of PHI is likely due to enhanced hydrogen bonding interactions between the oxygen-rich DOX backbone and the amine surface groups present on the PHI. [204] Moreover, the DOX molecules loaded on PHI particles had no negative effect on the propulsion speed of the PHI microswimmers in DMEM (18.5 ± 0.9 µm/s). This can be rationalized by the fact that DOX molecules are predominantly physisorbed in the particle volume, rather than on the outer surface, which does not affect the outer surface photocatalytic reactions of PHI with the surrounding medium that give rise to a field gradient around the particle and hence, propulsion.

5.12.2 Light-triggered release

Illuminating the particles triggers the release of DOX from both PHI and Melon, thus enabling a fully controlled, on-demand release of the drug. We used 415 nm blue light at an intensity of 170 mW/cm^2 to study the release of DOX and related products from the microswimmers in both ambient and O_2-free environments (Figure 5.13c, 5.11a). Band gap illumination of PHI microswimmers in oxygen-deficient suspensions triggers (oxidative) photocharging of the material, which is accompanied by a change of optoelectronic properties and a color change from yellow to blue. Hence, this effect is expected to influence the release, too (Figure 5.13a). Interestingly, the charging effect was also observed for denser PHI suspensions in DMEM even in ambient conditions (i.e. in the presence of oxygen), which appears to originate from photocatalytic oxygen consumption (Figure S9b). The cumulative release signal of DOX from PHI in DMEM is shown in Figure 5.13d for 3, 10 and 30 minute intervals of illumination in both ambient and O_2-free environments. Results of the DOX release with continuous illumination are shown in Figure 5.11. The released DOX was estimated by measuring the supernatant absorption in the PHI microswimmer suspension after centrifugation In ambient conditions, an optical equivalent of approximately 26 µg was released every 10 min, resulting

in 64 µg in 30 min cumulatively. When the amount of oxygen is decreased by purging the suspension with Ar 5 min prior and during the illumination, an increase (almost doubling) in stepwise and cumulative release was observed, resulting in 114.8 ± 5.2 µg of DOX equivalently being released after 30 min (Figure 5.13c). Tumor cells have oxygen-deficient hypoxic regions. Hence, a microswimmer which releases drugs faster in oxygen-deficient conditions is not only beneficial, but could even be used in a theranostic sense for hypoxically triggered drug delivery.

Beyond 60 minute illumination time intervals, the DOX amount released from PHI was reduced in ambient (O_2-rich) conditions, suggesting a light-triggered degradation process, similar to observations made on DOX-loaded TiO_2 microparticles [267]. A triggered release from Melon was also observed after 0 min (Argon purging in ambient light conditions), 3 and 10 min of illumination, albeit at lower amounts (~17 mg of DOX equivalent), however seemingly not significantly being from oxygen depletion (Figure 5.11). Since most of these products show similar absorption bands to DOX, a further quantification was only possible qualitatively by separation and mass spectroscopy, which was realized by high-performance liquid chromatography-mass spectroscopy (HPLC-MS) analysis of the supernatants after release. Besides pristine DOX, oxidatively modified DOX byproducts were indeed observed after release (Figure 5.13e and 5.12). The dominant decomposition products have molecular masses of 413, 399 and 143 (see Scheme 5.1 for visualization of the reaction). This clearly gives the evidence that, not only the release of DOX itself, but also of its oxidation products, which can act even more effectively on cells [267], can be intentionally tuned by the illumination time while being responsive to the presence of oxygen.

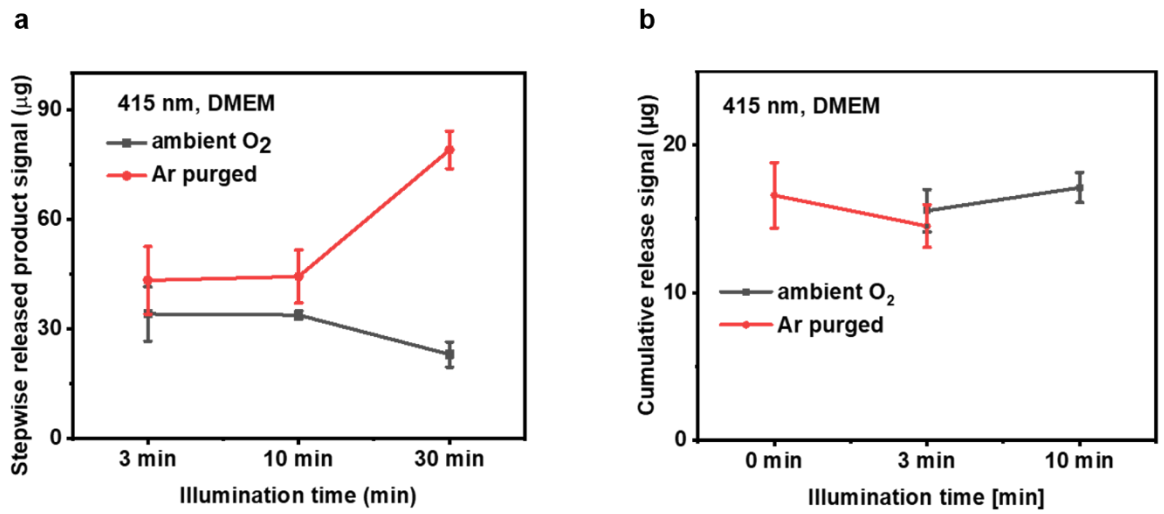

Figure 5.11 a) Stepwise release of the DOX-loaded PHI microswimmers in ambient and O_2 deficient conditions in DMEM medium under 415 nm illumination. b) Cumulative release signal of the DOX loaded Melon microswimmers (110 µg on 100 µg of Melon) in ambient and O_2 deficient conditions in DMEM medium under 415 nm illumination.

5.12.3 pH-based release

Besides, the PHI microswimmers are sensitive to acidic pH, which triggers protonation of the PHI backbone, with the protons blocking amine-acceptor sites on PHI, hence replacing the DOX [204]. Within 60 min at pH 3.5, induced by adding HCl to PBS, the microswimmers released the loaded DOX (116.2 ± 3.3 µg, 65%) without any light illumination (control) as shown in Figure 5.13f. In comparison, the control (pH 6.7) showed negligible release of ~2 %, within the margins of instrumental error.

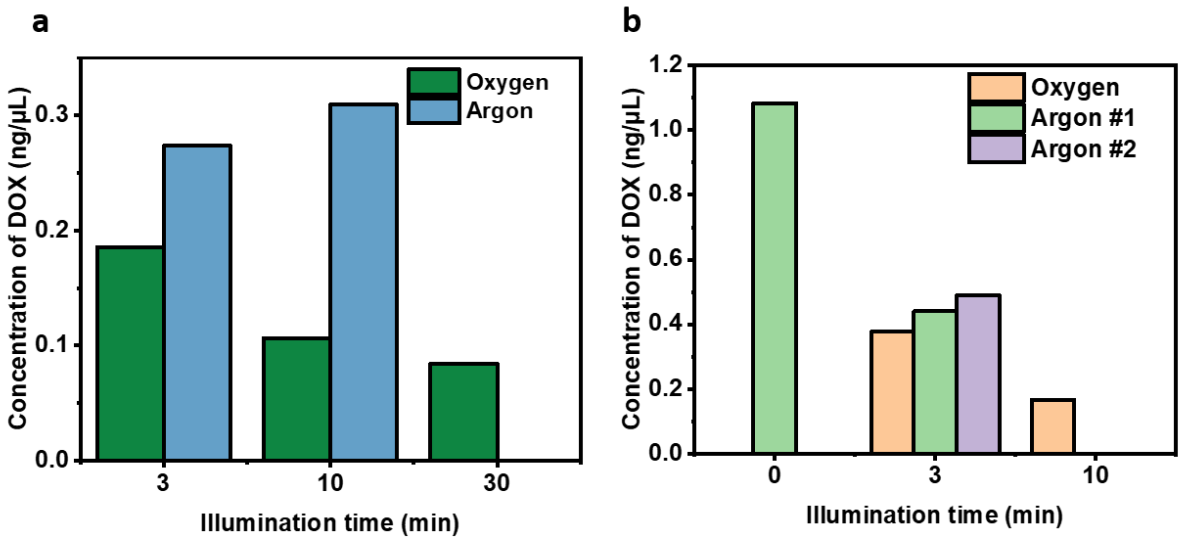

Figure 5.12 Additional HPLC-MS analysis of the release products after DOX loading of PHI (a) and Melon (b) after different illumination times.

5.12.4 Drug uptake by cells

Next, the ability of PHI microswimmers to deliver DOX or its active modifications to cancer cells under illumination was studied to provide a proof of concept. The bright field image of PHI microswimmers in a dense environment of cancer cells after 20 min of illumination (415 nm) is shown in Figure 5.13g. DOX or related products (red color) were released from the PHI microswimmers and taken up by the cancer cells after 24 hours incubation, while some amounts also diffused through the medium. Subsequently, the incubated cells died. The fluorescent image of the PHI microswimmers shows that the microswimmers are in the vicinity of the cancer cells (Figure 5.13h). This demonstrates that PHI microswimmers serve as smart light-driven cargo delivering agents in biological conditions. In fact, their stimuli-responsive behaviour triggers a theranostic function, making use of an intrinsic sensing property (i.e., charge accumulation enabled in oxygen-poor environments) that triggers an *enhanced* (and/or modified) release of the therapeutic agent.

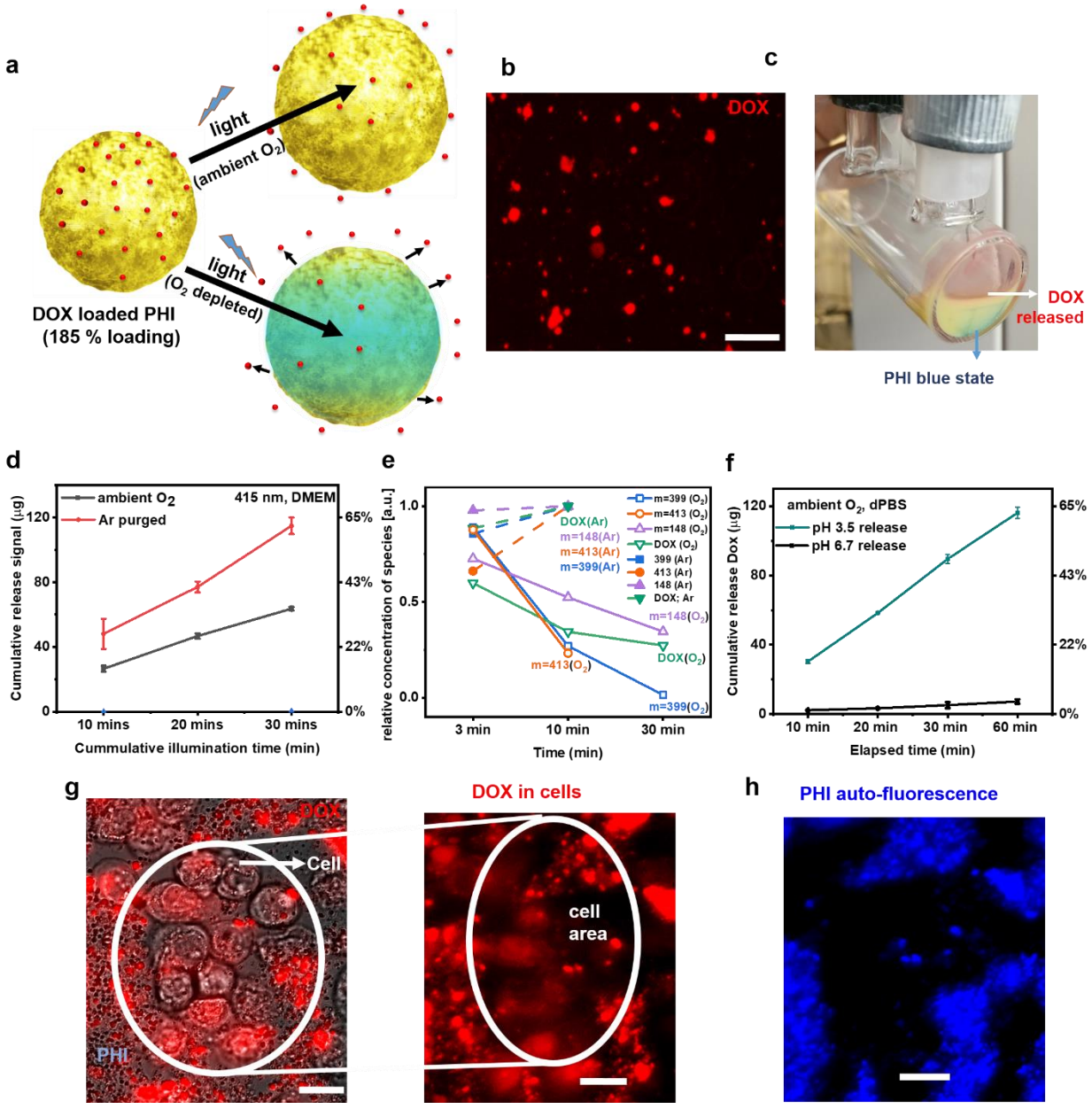

Figure 5.13 Drug loading and hypoxically, light- and pH-triggered drug release with PHI microswimmers. a) Schematic drug loading (DOX) and triggered release from PHI microswimmers in ambient and hypoxic conditions. b) Map of DOX loaded PHI microswimmers (185 μg/ml of DOX in 100 μg/ml PHI) showing DOX fluorescence emission at 595 nm. c) Image of the DOX-loaded PHI microswimmers (185 μg/ml of DOX in 100 μg/ml PHI) immediately after 30 min of illumination in oxygen deficient conditions showing the blue state of PHI and the released DOX and byproducts in red color. d) Light-triggered cumulative release signal of DOX and byproducts in DMEM medium at different time points under 415 nm illumination, with the supernatant being removed at each interval in ambient (black) and O_2 deficient conditions (red). The non-cumulative release data is shown in Supplementary

Figure S10. e) HPLC analysis of main products found after photocatalytic DOX release from PHI in ambient and Ar-purged conditions at different illumination times, normalized to the highest signal. f) pH-triggered release of DOX in PBS medium at pH 3.5 (green) with 54% of DOX being released after 60 min versus control (pH 6.7, black) showing negligible (~2%) release. g) Optical microscopy (bright field image) and fluorescence overlaid images of SKBR cancer cells (indicated within the circle) with PHI microswimmers under 415 nm illumination for 20 min showing DOX uptake under emission at 595 nm fluorescence in red. h) PHI autofluorescence image at 470 nm showing PHI microswimmers adhering to the cancer cells after some amount of DOX release. The two fluorescent images are taken from the same frame.

5.12.5 Release quantification

When the DOX loaded PHI microswimmers were illuminated continuously with light and their amount of DOX released was calculated based on the supernatant absorbance (calibrated to the DOX absorption peak at 480 nm), it was observed that in the presence of oxygen, at longer time intervals, the absorption signal of DOX, which had been released from PHI, was reduced by either direct photocatalytic interaction or by the formation of reactive oxygen species (ROS) that may react with the drug. [201] Although such behaviour was not directly observed in O_2-deficient conditions, similar effects may take place. To investigate this further, a product analysis of the supernatant by HPLC was performed. As the absorption of the products formed is similar to DOX (probably due to partially similar chemical structure, see Scheme 5.1), a distinction is not possible easily by UV/Vis spectroscopy. Thus, for quantification of the HLPC absorption signal after separating the products on columns, only relative intensities (and hence, relative amounts with a possible offset error) within every species can be given (Figure 5.13e). The mass analysis resulting from subsequent mass spectroscopy cannot be attributed unambiguously to a chemical structure and therefore, no reference material to calibrate the optical response is available. Besides, the role of the additional products presents in DMEM, possibly affecting the photocatalytic modification of DOX with PHI, is not yet reported. A DOX quantification based on mass spectroscopy analysis after dilution is shown in Figure 5.15 (which can potentially also have a systematic error). However, the general trend for light triggered DOX release on PHI described in Figure 5.11 is qualitatively reproduced by the corresponding HPLC measurement in Figure 5.14. In the case of Melon, the actual decomposition of DOX appears to be stronger than indicated by the absorption measurements as evidenced by HPLC (Figure 5.16) while only slightly benefiting from oxygen removal. These findings underline the importance and the benefits of the environmentally sensitive

photocharging ability of PHI for enhanced and responsive DOX (and related active product) release and the role of ROS on the degradation of DOX on the PHI especially in the presence of oxygen.

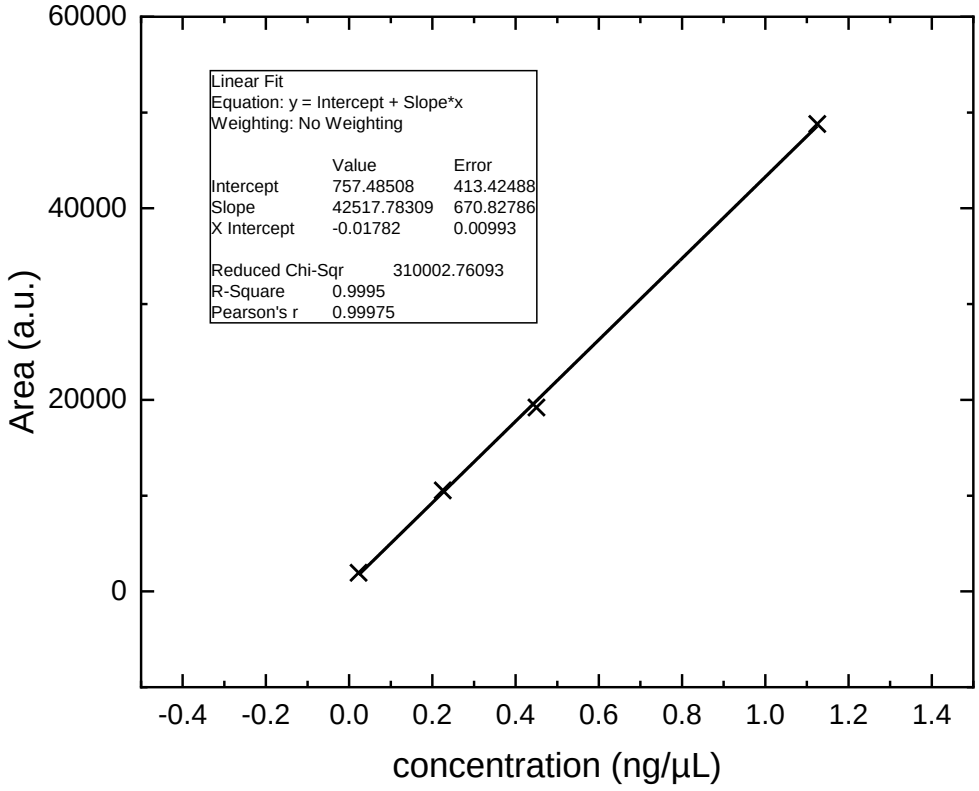

Figure 5.14 Calibration line for the quantification of doxorubicin showing a linear response. Area is obtained by peak integration (intensity) acquired at selective ion monitoring (SIM) mode (m/z = 544.18).

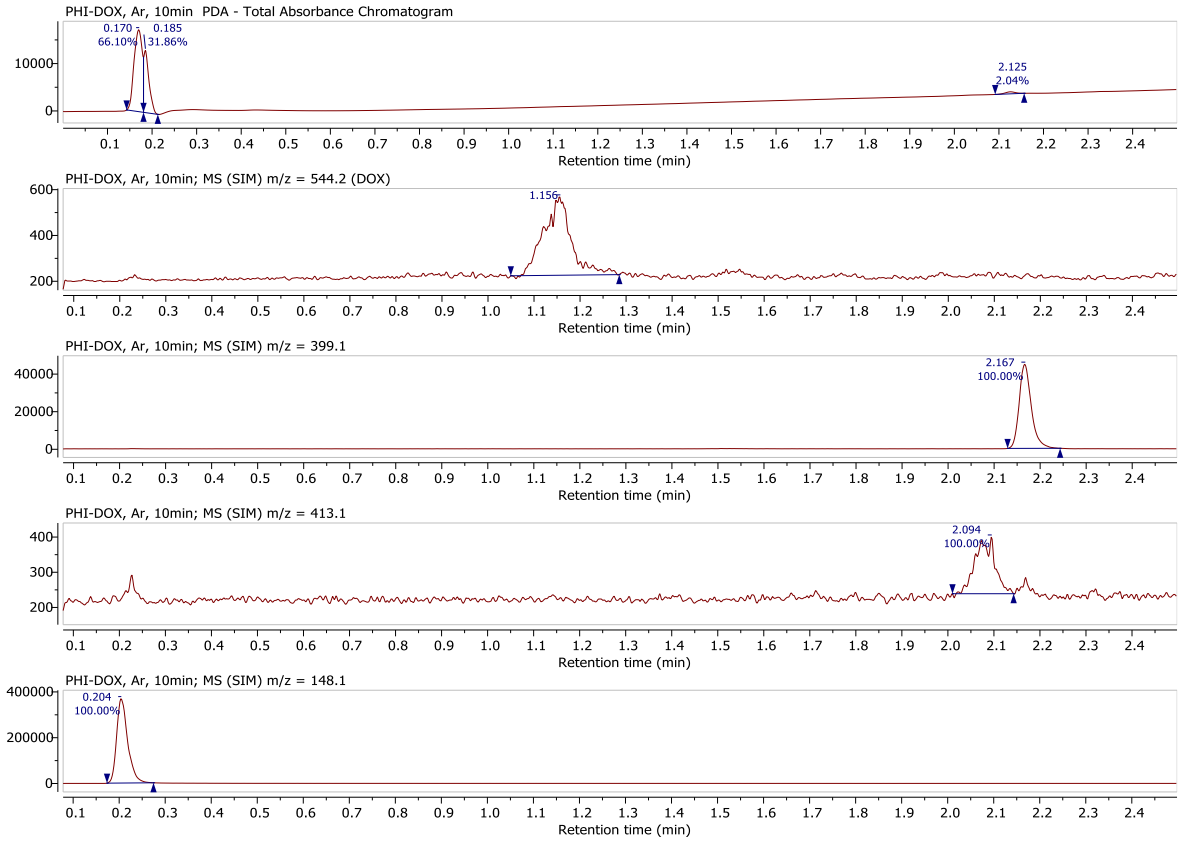

Figure 5.15 Chromatogram of PHI-DOX (Argon) after 10 min of illumination. DOX, as well as mass peaks of degradation products are visible at different retention times.

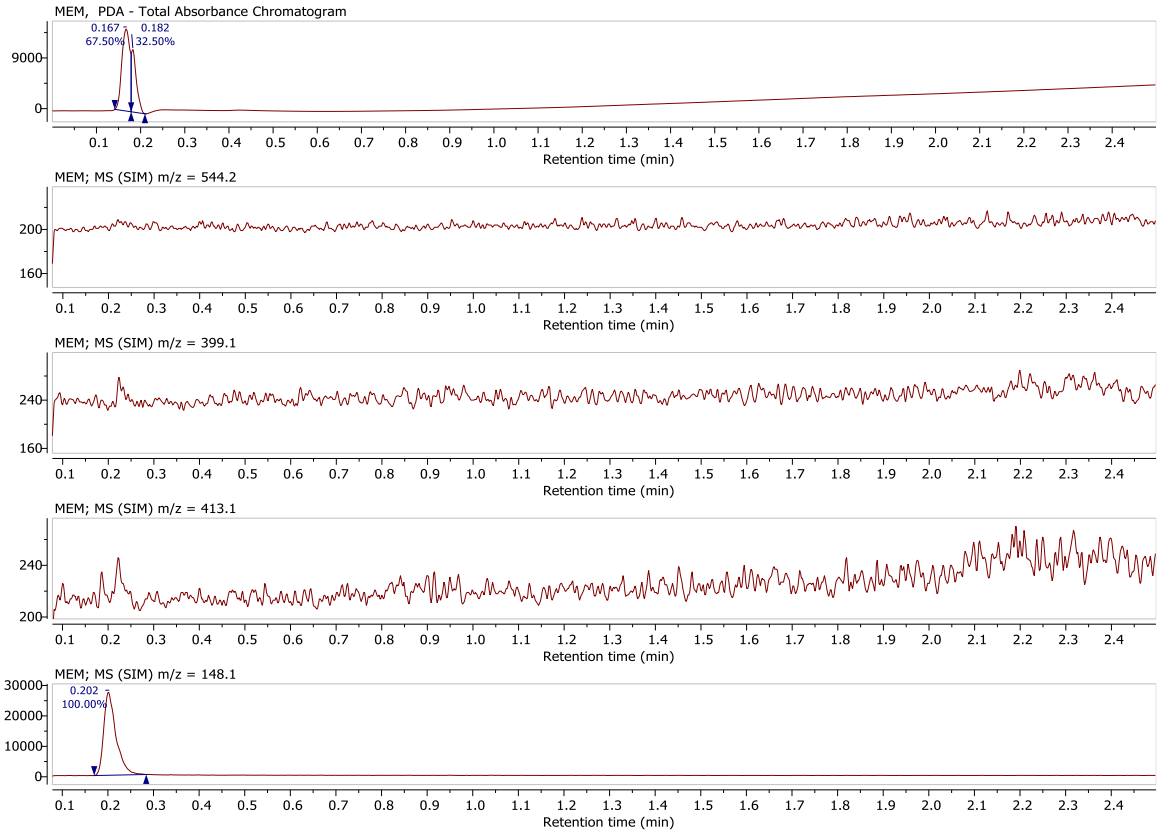

Figure 5.16 The chromatogram of MEM (blank) does not show signals at m/z = 544.1, 399.1 or 413.1, which excludes interference of the buffer solution with detected mass signals for quantification. The signal at m/z = 148.1 is subtracted in the analysis of samples to account for intensity caused by the buffer.

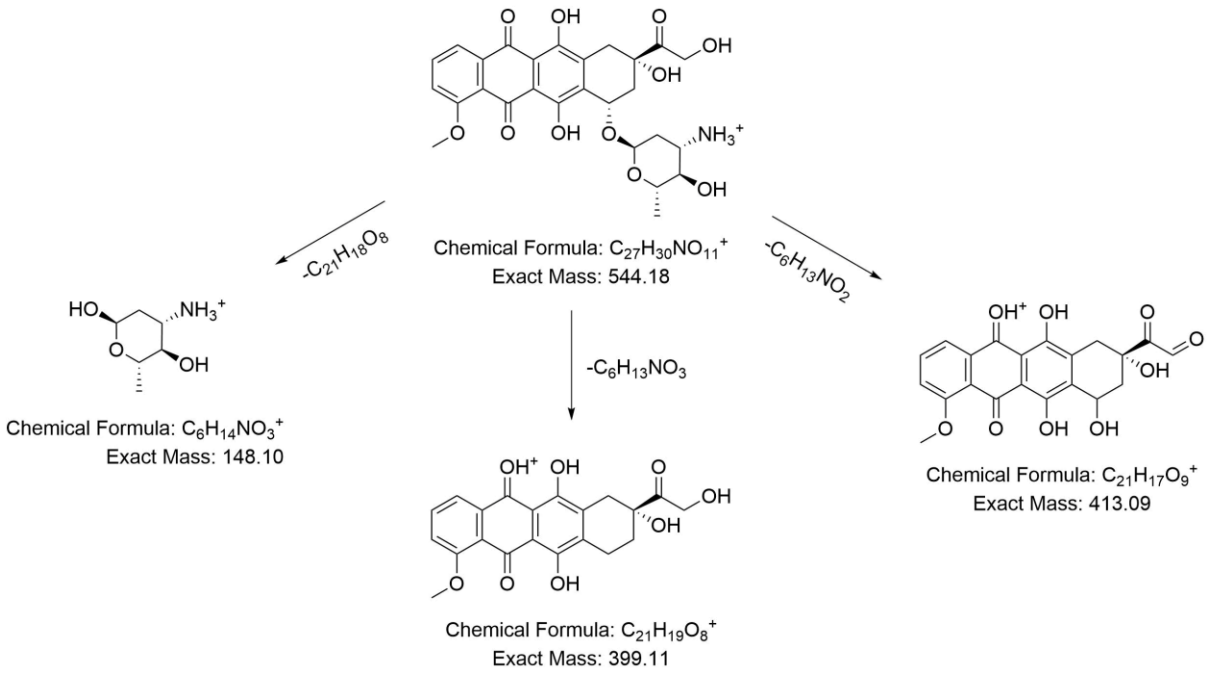

Scheme 5.1 Chemical structure of DOX and possible degradation products forming during photocatalytic release and modification of the drug in DMEM after loading on PHI or Melon. Especially for the element with unit mass 148, it cannot be excluded that other educts present in DMEM contribute to its formation.

Table 5. 5 Solvent composition timetable (HPLC-MS).

Time [min]	Water [%]	Water+1% FA [%]	MeCN [%]	MeCN+1% FA [%]
0	72	8	18	2
2.00	45	5	45	5
2.01	4.5	0.5	85.5	9.5
2.50	4.5	0.5	85.5	9.5

Table 5. 6 Concentration series of doxorubicin used for quantification of the mass signal during HPLC-MS analysis.

Index	c(initial) [µg/mL]	c(diluted) [ng/µL]	V(injected) [µL]	Area [a.u.]
C_1	75	1.125	1	48812.7
C_2	30	0.45	1	19208.6
C_3	15	0.225	1	10551.0
C_4	1.5	0.0225	1	1946.3

5. 13 Summary

We have developed highly efficient carbon-based PHI microswimmers that can be propelled phototactically with light in aqueous salt media with high molarity (up to 1 M NaCl) and realistic biological cell environments, such as dPBS, DMEM, DMEM + FBS as well as diluted blood, without any additional fuel. Such particle swarms exhibit phototaxis, which can be used to steer and locate the microswimmers into target locations [123]. The high ion tolerance for phototaxis is attributed to a favourable interplay between PHI's textural and structural porosity, as well as optoionic effects [207, 251]. Next, the biocompatibility of PHI swimmers was verified with three different cell lines without and with visible light illumination and primary cells. Besides, due to their textural porosity, PHI microswimmers have a very high capacity for drug uptake (~185% of their own mass using the example of the anti-cancer drug DOX), which stays bound stably to the particle over a month, until a fast release is triggered by a pH change or band gap illumination. Intriguingly, PHI shows stimuli responsive drug release, as the release can be enhanced or modified in oxygen-deficient conditions, which are prevalent e.g. in hypoxic tumor regions, thus enabling potential theranostic applications. In addition to the PHI microswimmers' multi-stimuli responsive drug release capability, we demonstrate their swimming and ease of tracking in crowded heterogeneous biological fluids, such as a dilute blood solution, by monitoring PHI's inherent autofluorescence. These capabilities make the PHI microswimmers promising candidates for biomedical applications, such as light-induced *in-vivo* propulsion and targeted drug delivery, especially for cancer cell environments, which tend to be oxygen deficient and low in pH, and for stomach and the GI tract which likewise feature low pH. Due to PHI's organic nature, we envision that the microswimmers can be further functionalized for tailored catalytic, morphological and optical properties [204, 252],

such as light absorption in the near-infrared (NIR) regions, which could enable up to several centimetres of tissue penetration for future biomedical applications.

Chapter 6. Conclusion and Future Outlook

6.1 Conclusion

Light as one of the most widely available energy sources provides for a good stimulus for the propulsion of the microswimmers [8]. Light allows for remote propagation, superposition along with spatial and temporal procession [85]. Due to all these advantages light-driven microswimmers are gaining increasing traction for the fabrication of microswimmers [236]. To design and fabricate light-driven microswimmers with flexible capabilities and new materials, different strategies have been developed over the past decade [122]. Thanks to rapid progress in photocatalytic nanoparticles, especially new design and fabrication methods, these methods can be applied onto fabrication of new light-driven micro swimmers [68, 236]. The availability of good material library allows for fabrication of new materials and structures. In this thesis we have explored the fabrication and design of new materials that can be used for light-driven microswimmers.

Firstly, a hollow mesoporous morphology made of TiO_2 is used for the fabrication of light-driven microswimmers is developed. Such morphology when designed as Janus structure along with noble metals like Au, allows for faster swimming under low intensity UV illumination, due to the enhanced surface area present on such mesoporous morphology. The higher surface area allows for better charge carriers separation, which in turn gives rise to a higher number of electrons on the surface which then reacts with the H_2O_2, resulting in the formation of product molecules. The resulting transfer of electrons from the TiO_2 side to the Au side results in the fluid flow in the opposite direction, propelling the microswimmers. The hollow mesoporous morphology showed four times faster speed in comparison with the solid morphology of the swimmers. Magnetic control of such swimmers is also made possible by the addition of Nickel layer. As a proof of concept, such microswimmers have shown enhanced environmental remediation. Drugs like DOX an anti-cancer drug, can also be loaded on their mesoporous hollow morphology.

Secondly, in order to negate the harmful effects of UV light, we design an inorganic visible light responsive microswimmers. CoO is used as a material for the fabrication of visible light responsive microswimmers. CoO is fabricated along with TiO_2 as Janus structure and the overall structure is visible light responsive at very low intensities of visible light. Such soft low light enables potential application in environmental and biomedical applications as the light

does not harm the cells and tissues. Their ability to be responsive in UV and visible light allows for wavelength steering of the microswimmers in addition to their magnetic steering.

Finally, we designed an organic light responsive microswimmer. PHI a 2D form of carbon nitride, which is an organic photocatalytic material is used for the fabrication the microswimmers. Janus structures using Au, Pt and SiO_2 are studied, in addition to being propelled by UV and visible light, their propulsion mechanism is studied in detail for all the cap structures and other inorganic light driven microswimmers using photoelectrochemistry. The resulting studies showed that, the light-driven microswimmers are propelled predominantly due to oxygen reduction reaction in water and other alcohol-based fuels. PHI has a unique ability to store charges under illumination and the charges can be released when the illumination stops enabling solar battery swimming in dark. The swimmers have shown propulsion for more than 30 minutes in the dark for a mere 30s illumination. In the second part of this work, the ability of PHI microswimmers to swimming without the cap structure is explored. They have structural and textural pores which enables their swimming in biologically relevant mediums, which has been a bottleneck till now. PHI microswimmers are biocompatible and show a higher drug uptake and release under illumination. The release is sensitive to pH and oxygen concentrations in the environment thus showing an intelligent behavior which can be harnessed for potential biomedical applications.

Hence in this thesis, we have used three different materials, two inorganic (TiO_2 and CoO) and one organic (PHI) material for the fabrication of light-driven microswimmers. The microswimmers could swim in both UV and visible light. Magnetic control of the swimmers was established using magnetic layers. The organic PHI also demonstrated optical control. The mechanism of propulsion of all light driven microswimmers is explored in detail and the unique charge storage ability of Phi enables it to swim in the dark even in the absence of illumination for more than 30 minutes for a mere 30s illumination which is astonishing. Finally, their potential application in drug delivery is explored by loading them with anti-cancer drugs such as Doxorubicin. They show intelligent release active to both pH and oxygen concentration in the environment enabling their future biomedical applications.

6.2 Future Outlook

In spite of the enormous progress that has been achieved in the propulsion of light-driven microswimmers a lot of potentially critical challenges that exist before the light-driven microswimmers can be used in practical applications, especially in biomedical applications

[122]. The multiple challenges that exist in light driven microswimmers are, the need to have highly efficient light-driven microswimmers that can be propelled under low intensity at NIR and IR wavelengths, the ability to detect light-driven microswimmers inside the body and the need for biocompatible material that would have a good drug uptake and allow for stable delivery of the drugs [24].

6.2.1 NIR and IR active microswimmers

One of the predominant issues that come with the use of the use light-driven microswimmers in biomedical and in vivo applications is the relative low penetration of light into living tissues [8]. The use of wavelength greatly affects the penetration depth of the microswimmers. For example, UV light can penetrate 0.5 to 2 mm, where as an NIR or IR can penetrate up to 10 mm [268]. The penetration depth would affect the type of biomedical application the microswimmers is tailored to be used [123]. The use of UV and blue light which have the high energy of the photons allows for faster swimming but they would limit their application due to penetration depth and the possible harm it could cause the tissues in the longer run. Though UV and blue light driven microswimmers can be used for propulsion in near skin or eye environments, this would limit their applications. Thus, the use of an NIR or IR active photocatalytic material that can be used for microswimmers allows for their use in applications deeper inside human body [57]. To this end the use of organic and tailorable photocatalytic material such as covalent organic frameworks (COF) can be used efficient tailoring of the NIR responsiveness. To this end, we have been working on a biocompatible COF based light-driven microswimmer that can be used for visible and NIR active swimming for biomedical applications.

6.2.2 Detection of light-driven microswimmers

The other major area that requires thrust is for the need to detect the light driven microswimmers inside crowded environments and inside the body [8]. Different strategies are being developed in this regard, the predominant of them is the use of fluorescence to detect the presence of the microswimmers. But fluorescence-based methods also suffer from the same penetration depth issue due to light. They cannot be used to visualize the swimmers deep inside the tissues. Hence in order to overcome them, new methods for the detection of the swimmers are needed. Photoacoustic tomography is an imaging method based on light and ultrasound. They have shown promising ability to image deep tissues either in vivo or ex vivo by using light to excite the molecules/materials and detect it using ultrasound which has a deeper penetration [246]. Specific molecules can be loaded along with drug cargo onto light-driven

microswimmers which would enable their detection in vivo. Other methods such as microCT can be used if magnetic materials can be loaded or deposited onto light-driven microswimmers [230]. The ability to detect magnetic materials deep inside human body have been established using many methods such as MRI and CT. Hence, there is a need for imaging methods to be developed to push light-driven microswimmers more towards practical applications [269].

6.2.3 Swarm control of light-driven microswimmers

The most commonly used methods are magnetic control and optical control. Magnetic control of such microswimmers is done by adding additional magnetic layer on the microswimmer surface. But the addition of magnetic layers affects the propulsion mechanism of the light-driven microswimmers lowering their propulsion efficiency in ionic environments [26]. Hence, newer methods of magnetic controls that do not affect the propulsion of light-driven microswimmers is needed. To this end, the use of iron platinum nanoparticles which are highly magnetic in nature could be used in such a way that they do not affect the propulsion mechanism of the swimmers [270]. The other method to get collective behavior is to use light by itself for collective assembly of the swimmers. The swimmers are phototactic in nature allowing for aggregation of the swimmers towards or away from the light, based on the zeta potential of the swimmers. But such behavior is difficult to achieve in biomedical applications where the penetration of light may be affected by the diffraction of the light by the tissues. To circumvent these problems newer methods which allow for manipulation and complex self-assembly is needed.

6.2.4 Sensing

Unlike microswimmers that are present in nature, synthetic micro swimmers suffer from the lack of on-board sensing. Sensing plays an important role in the effective targeting of the microswimmers in biomedical applications. Due to their smaller size, it is difficult to place complex sensors on the swimmer body. On-board power storage, like the one shown by PHI microswimmers in this thesis would allow for the powering of the sensors on the swimmer body. However practical fabrication challenges still exist.

Despite all the challenges that remain for light-driven microswimmers, the persistent endeavors of researchers would allow for the successful application of such swimmers in biomedical applications especially in the fields of drug delivery and sensing. Such intelligent swimmers are no more in the realm of science fiction but rather much closer to reality and with

the unremitting efforts of researchers, the realization of a fantastic voyager will happen much sooner.

Appendix A: Monolayer deposition for Janus microswimmer fabrication

The formation of monolayer is important in the fabrication of Janus microswimmers. The quality of the monolayer affects the amount of half cap coverage in the subsequent deposition steps. This is due to the fact that close packing of the monolayer leads to the shadowing effect on the next microswimmer. This leads to half capping of the microswimmers. If they layer is not tightly packed then it results in the Janus caps being more than half caps. Different methods have been developed for the fabrication of monolayers such as drop casting, dip coating, self-assembled monolayers, template assisted fabrication, Langmuir–Blodgett method and spin coating [271]. The most easy and versatile of these methods is the drop casting of microparticles onto the substrate. By controlling the concentration of the particles in the solution and regulating the evaporation rate of the solvent, the thickness of the monolayers can be controlled [272]. Throughout this thesis, drop casting was used to fabricate monolayers on which further deposition is carried out for the fabrication of Janus microswimmers. The substrate is treated with Ar plasma to make the surface hydrophobic. Different concentrations of the particles are tried to check the optimum concentration of the solutes in the solution. Ethanol, a fast evaporating solvent is used along with the microparticles. When the ethanol containing particles is drop cast on the surface, due to the hydrophobicity the droplets spread outward immediately and the subsequent evaporation forces the uniform distribution of the particles on the glass substrate [272].

Bibliography

1. Jager, E.W.H., O. Inganäs, and I. Lundström, *Microrobots for Micrometer-Size Objects in Aqueous Media: Potential Tools for Single-Cell Manipulation.* Science, 2000. **288**(5475): p. 2335.
2. Nelson, B.J., I.K. Kaliakatsos, and J.J. Abbott, *Microrobots for Minimally Invasive Medicine.* Annual Review of Biomedical Engineering, 2010. **12**(1): p. 55-85.
3. Ceylan, H., et al., *Translational prospects of untethered medical microrobots.* Progress in Biomedical Engineering, 2019. **1**(1): p. 012002.
4. Safdar, M., S.U. Khan, and J. Jänis, *Progress toward Catalytic Micro- and Nanomotors for Biomedical and Environmental Applications.* Advanced Materials, 2018. **30**(24): p. 1703660.
5. Junk, A. and F. Riess, *From an idea to a vision: There's plenty of room at the bottom.* American Journal of Physics, 2006. **74**(9): p. 825-830.
6. McCracken, J.M., B.R. Donovan, and T.J. White, *Materials as Machines.* Advanced Materials, 2020. **32**(20): p. 1906564.
7. Medina-Sánchez, M., et al., *Swimming Microrobots: Soft, Reconfigurable, and Smart.* Advanced Functional Materials, 2018. **28**(25): p. 1707228.
8. Wang, B., et al., *Trends in Micro-/Nanorobotics: Materials Development, Actuation, Localization, and System Integration for Biomedical Applications.* Advanced Materials, 2020. **n/a**(n/a): p. 2002047.
9. Parmar, J., et al., *Micro- and Nanomotors as Active Environmental Microcleaners and Sensors.* Journal of the American Chemical Society, 2018. **140**(30): p. 9317-9331.
10. Schmidt, C.K., et al., *Engineering microrobots for targeted cancer therapies from a medical perspective.* Nature Communications, 2020. **11**(1): p. 5618.
11. Soto, F., et al., *Medical Micro/Nanorobots in Precision Medicine.* Advanced Science, 2020. **7**(21): p. 2002203.
12. Sanchez, S., L. Soler, and J. Katuri, *Chemically powered micro- and nanomotors.* Angew Chem Int Ed Engl, 2015. **54**(5): p. 1414-1444.
13. Xu, T., et al., *Fuel-Free Synthetic Micro-/Nanomachines.* Advanced Materials, 2017. **29**(9): p. 1603250.
14. Sun, L., et al., *Biohybrid robotics with living cell actuation.* Chemical Society Reviews, 2020. **49**(12): p. 4043-4069.
15. Alapan, Y., et al., *Microrobotics and Microorganisms: Biohybrid Autonomous Cellular Robots.* Annual Review of Control, Robotics, and Autonomous Systems, 2019. **2**(1): p. 205-230.
16. Erkoc, P., et al., *Mobile Microrobots for Active Therapeutic Delivery.* Advanced Therapeutics, 2019. **2**(1): p. 1800064.
17. Wu, Z., et al., *Medical micro/nanorobots in complex media.* Chemical Society Reviews, 2020. **49**(22): p. 8088-8112.

18. Wang, H. and M. Pumera, *Micro/Nanomachines and Living Biosystems: From Simple Interactions to Microcyborgs.* Advanced Functional Materials, 2018. **28**(25): p. 1705421.
19. Ceylan, H., et al., *Mobile microrobots for bioengineering applications.* Lab on a Chip, 2017. **17**(10): p. 1705-1724.
20. Guix, M., et al., *Self-Propelled Micro/Nanoparticle Motors.* Particle & Particle Systems Characterization, 2018. **35**(2): p. 1700382.
21. Chen, X., C. Zhou, and W. Wang, *Colloidal Motors 101: A Beginner's Guide to Colloidal Motor Research.* Chemistry – An Asian Journal, 2019. **14**(14): p. 2388-2405.
22. Chen, C., et al., *Magnesium-Based Micromotors: Water-Powered Propulsion, Multifunctionality, and Biomedical and Environmental Applications.* Small, 2018. **14**(23): p. 1704252.
23. Zhao, X., et al., *Powering Motion with Enzymes.* Accounts of Chemical Research, 2018. **51**(10): p. 2373-2381.
24. Zhan, Z., et al., *Recent advances of light-driven micro/nanomotors: toward powerful thrust and precise control.* Nanotechnology Reviews, 2018. **7**(6): p. 555-581.
25. Sitti, M., et al., *Biomedical Applications of Untethered Mobile Milli/Microrobots.* Proceedings of the IEEE, 2015. **103**(2): p. 205-224.
26. Yang, Q., et al., *Recent Advances in Motion Control of Micro/Nanomotors.* Advanced Intelligent Systems, 2020. **2**(8): p. 2000049.
27. Wang, W., et al., *Small power: Autonomous nano- and micromotors propelled by self-generated gradients.* Nano Today, 2013. **8**(5): p. 531-554.
28. Purcell, E.M., *Life at low Reynolds number.* American Journal of Physics, 1977. **45**(1): p. 3-11.
29. Lauga, E., *Life around the scallop theorem.* Soft Matter, 2011. **7**(7): p. 3060-3065.
30. Shapere, A. and F. Wilczek, *Self-Propulsion at Low Reynolds Number.* Physical Review Letters, 1987. **58**(20): p. 2051-2054.
31. Lauga, E. and T.R. Powers, *The hydrodynamics of swimming microorganisms.* Reports on Progress in Physics, 2009. **72**(9): p. 096601.
32. Paxton, W.F., et al., *Catalytic Nanomotors: Autonomous Movement of Striped Nanorods.* Journal of the American Chemical Society, 2004. **126**(41): p. 13424-13431.
33. Wang, Y., et al., *Bipolar Electrochemical Mechanism for the Propulsion of Catalytic Nanomotors in Hydrogen Peroxide Solutions.* Langmuir, 2006. **22**(25): p. 10451-10456.
34. Zacharia, N.S., Z.S. Sadeq, and G.A. Ozin, *Enhanced speed of bimetallic nanorod motors by surface roughening.* Chemical Communications, 2009(39): p. 5856-5858.
35. Howse, J.R., et al., *Self-Motile Colloidal Particles: From Directed Propulsion to Random Walk.* Physical Review Letters, 2007. **99**(4): p. 048102.
36. Mei, Y., et al., *Versatile Approach for Integrative and Functionalized Tubes by Strain Engineering of Nanomembranes on Polymers.* Advanced Materials, 2008. **20**(21): p. 4085-4090.
37. Solovev, A.A., et al., *Catalytic Microtubular Jet Engines Self-Propelled by Accumulated Gas Bubbles.* Small, 2009. **5**(14): p. 1688-1692.

38. Simmchen, J., et al., *Effect of surfactants on the performance of tubular and spherical micromotors – a comparative study.* RSC Advances, 2014. **4**(39): p. 20334-20340.
39. Golestanian, R., T.B. Liverpool, and A. Ajdari, *Designing phoretic micro- and nano-swimmers.* New Journal of Physics, 2007. **9**(5): p. 126-126.
40. Gao, W., et al., *Cargo-Towing Fuel-Free Magnetic Nanoswimmers for Targeted Drug Delivery.* Small, 2012. **8**(3): p. 460-467.
41. Guix, M., et al., *Carbonate-based Janus micromotors moving in ultra-light acidic environment generated by HeLa cells in situ.* Scientific Reports, 2016. **6**(1): p. 21701.
42. Li, J., et al., *Water-Driven Micromotors for Rapid Photocatalytic Degradation of Biological and Chemical Warfare Agents.* ACS Nano, 2014. **8**(11): p. 11118-11125.
43. Ma, X., et al., *Enzyme Catalysis To Power Micro/Nanomachines.* ACS Nano, 2016. **10**(10): p. 9111-9122.
44. Ma, X., et al., *Motion Control of Urea-Powered Biocompatible Hollow Microcapsules.* ACS Nano, 2016. **10**(3): p. 3597-3605.
45. Ma, X., et al., *Enzyme-Powered Hollow Mesoporous Janus Nanomotors.* Nano Letters, 2015. **15**(10): p. 7043-7050.
46. Muddana, H.S., et al., *Substrate Catalysis Enhances Single-Enzyme Diffusion.* Journal of the American Chemical Society, 2010. **132**(7): p. 2110-2111.
47. Sengupta, S., et al., *Enzyme Molecules as Nanomotors.* Journal of the American Chemical Society, 2013. **135**(4): p. 1406-1414.
48. Somasundar, A., et al., *Positive and negative chemotaxis of enzyme-coated liposome motors.* Nature Nanotechnology, 2019. **14**(12): p. 1129-1134.
49. Mou, F., et al., *Self-Propelled Micromotors Driven by the Magnesium–Water Reaction and Their Hemolytic Properties.* Angewandte Chemie International Edition, 2013. **52**(28): p. 7208-7212.
50. Dey, K.K., et al., *Micromotors Powered by Enzyme Catalysis.* Nano Letters, 2015. **15**(12): p. 8311-8315.
51. Martella, D., et al., *Self-Regulating Capabilities in Photonic Robotics.* Advanced Materials Technologies, 2019. **4**(2): p. 1800571.
52. Peyer, K.E., L. Zhang, and B.J. Nelson, *Bio-inspired magnetic swimming microrobots for biomedical applications.* Nanoscale, 2013. **5**(4): p. 1259-1272.
53. Wang, B., et al., *Bioinspired Superhydrophobic Fe3O4@Polydopamine@Ag Hybrid Nanoparticles for Liquid Marble and Oil Spill.* Advanced Materials Interfaces, 2015. **2**(13): p. 1500234.
54. Walker, D., et al., *Optimal Length of Low Reynolds Number Nanopropellers.* Nano Letters, 2015. **15**(7): p. 4412-4416.
55. Ghosh, A. and P. Fischer, *Controlled Propulsion of Artificial Magnetic Nanostructured Propellers.* Nano Letters, 2009. **9**(6): p. 2243-2245.
56. Palagi, S., et al., *Structured light enables biomimetic swimming and versatile locomotion of photoresponsive soft microrobots.* Nature Materials, 2016. **15**(6): p. 647-653.
57. Sitti, M. and D.S. Wiersma, *Pros and Cons: Magnetic versus Optical Microrobots.* Advanced Materials, 2020. **32**(20): p. 1906766.

58. Zhang, L., et al., *Artificial bacterial flagella: Fabrication and magnetic control.* Applied Physics Letters, 2009. **94**(6): p. 064107.
59. Ceylan, H., et al., *3D-Printed Biodegradable Microswimmer for Theranostic Cargo Delivery and Release.* ACS Nano, 2019. **13**(3): p. 3353-3362.
60. Ahmed, S., et al., *Density and Shape Effects in the Acoustic Propulsion of Bimetallic Nanorod Motors.* ACS Nano, 2016. **10**(4): p. 4763-4769.
61. Ren, T., et al., *Soft Ring-Shaped Cellu-Robots with Simultaneous Locomotion in Batches.* Advanced Materials, 2020. **32**(8): p. 1905713.
62. Aghakhani, A., et al., *Acoustically powered surface-slipping mobile microrobots.* Proceedings of the National Academy of Sciences, 2020. **117**(7): p. 3469.
63. Xu, T., et al., *Ultrasound-Modulated Bubble Propulsion of Chemically Powered Microengines.* Journal of the American Chemical Society, 2014. **136**(24): p. 8552-8555.
64. Zhou, C., et al., *Twists and Turns of Orbiting and Spinning Metallic Microparticles Powered by Megahertz Ultrasound.* ACS Nano, 2017. **11**(12): p. 12668-12676.
65. Ren, L., et al., *3D steerable, acoustically powered microswimmers for single-particle manipulation.* Science Advances, 2019. **5**(10): p. eaax3084.
66. Rao, K.J., et al., *A Force to Be Reckoned With: A Review of Synthetic Microswimmers Powered by Ultrasound.* Small, 2015. **11**(24): p. 2836-2846.
67. Soto, F., et al., *Acoustic Microcannons: Toward Advanced Microballistics.* ACS Nano, 2016. **10**(1): p. 1522-1528.
68. Eskandarloo, H., A. Kierulf, and A. Abbaspourrad, *Light-harvesting synthetic nano- and micromotors: a review.* Nanoscale, 2017. **9**(34): p. 12218-12230.
69. Bregulla, A.P., H. Yang, and F. Cichos, *Stochastic Localization of Microswimmers by Photon Nudging.* ACS Nano, 2014. **8**(7): p. 6542-6550.
70. Bregulla, A.P. and F. Cichos, *Size dependent efficiency of photophoretic swimmers.* Faraday Discussions, 2015. **184**(0): p. 381-391.
71. Hong, Y., et al., *Biomimetic behavior of synthetic particles: from microscopic randomness to macroscopic control.* Physical Chemistry Chemical Physics, 2010. **12**(7): p. 1423-1435.
72. Yang, P.-P., et al., *NIR Light Propulsive Janus-like Nanohybrids for Enhanced Photothermal Tumor Therapy.* Small, 2016. **12**(39): p. 5423-5430.
73. Okawa, D., et al., *Surface Tension Mediated Conversion of Light to Work.* Journal of the American Chemical Society, 2009. **131**(15): p. 5396-5398.
74. Wu, Y., et al., *Near infrared-modulated propulsion of catalytic Janus polymer multilayer capsule motors.* Chemical Communications, 2015. **51**(3): p. 511-514.
75. Wu, Z., et al., *Near-Infrared Light-Triggered "On/Off" Motion of Polymer Multilayer Rockets.* ACS Nano, 2014. **8**(6): p. 6097-6105.
76. Wu, Z., et al., *Superfast Near-Infrared Light-Driven Polymer Multilayer Rockets.* Small, 2016. **12**(5): p. 577-582.
77. Šípová-Jungová, H., et al., *Nanoscale Inorganic Motors Driven by Light: Principles, Realizations, and Opportunities.* Chemical Reviews, 2020. **120**(1): p. 269-287.
78. Abid, J.-P., et al., *Light-Driven Directed Motion of Azobenzene-Coated Polymer Nanoparticles in an Aqueous Medium.* Langmuir, 2011. **27**(13): p. 7967-7971.

79. Shahsavan, H., et al., *Bioinspired underwater locomotion of light-driven liquid crystal gels.* Proceedings of the National Academy of Sciences, 2020. **117**(10): p. 5125.
80. Dong, R., et al., *Photocatalytic Micro/Nanomotors: From Construction to Applications.* Accounts of Chemical Research, 2018. **51**(9): p. 1940-1947.
81. Fujishima, A., T.N. Rao, and D.A. Tryk, *Titanium dioxide photocatalysis.* Journal of Photochemistry and Photobiology C: Photochemistry Reviews, 2000. **1**(1): p. 1-21.
82. Dong, S., et al., *Recent developments in heterogeneous photocatalytic water treatment using visible light-responsive photocatalysts: a review.* RSC Adv., 2015. **5**(19): p. 14610-14630.
83. Ni, M., et al., *A review and recent developments in photocatalytic water-splitting using for hydrogen production.* Renewable and Sustainable Energy Reviews, 2007. **11**(3): p. 401-425.
84. Maric, T., et al., *Tailoring Metal/TiO2 Interface to Influence Motion of Light-Activated Janus Micromotors.* Advanced Functional Materials, 2020. **n/a**(n/a): p. 1908614.
85. Xu, L., et al., *Light-driven micro/nanomotors: from fundamentals to applications.* Chemical Society Reviews, 2017. **46**(22): p. 6905-6926.
86. Gibbs, J.G., et al., *Engineering the Dynamics of Active Colloids by Targeted Design of Metal–Semiconductor Heterojunctions.* Advanced Materials Interfaces, 2019. **6**(6): p. 1801894.
87. Palagi, S., D.P. Singh, and P. Fischer, *Light-Controlled Micromotors and Soft Microrobots.* Advanced Optical Materials, 2019. **7**(16): p. 1900370.
88. Singh, D.P., et al., *Interface-mediated spontaneous symmetry breaking and mutual communication between drops containing chemically active particles.* Nature Communications, 2020. **11**(1): p. 2210.
89. Ibele, M., T.E. Mallouk, and A. Sen, *Schooling behavior of light-powered autonomous micromotors in water.* Angew Chem Int Ed Engl, 2009. **48**(18): p. 3308-3312.
90. Carp, O., C.L. Huisman, and A. Reller, *Photoinduced reactivity of titanium dioxide.* Progress in Solid State Chemistry, 2004. **32**(1): p. 33-177.
91. Chen, C., et al., *Light-Steered Isotropic Semiconductor Micromotors.* Adv Mater, 2017. **29**(3).
92. Enachi, M., et al., *Light-Induced Motion of Microengines Based on Microarrays of TiO2 Nanotubes.* Small, 2016. **12**(39): p. 5497-5505.
93. Singh, D.P., et al., *Non-Equilibrium Assembly of Light-Activated Colloidal Mixtures.* Advanced Materials, 2017. **29**(32): p. 1701328.
94. Singh, D.P., et al., *Photogravitactic Microswimmers.* Advanced Functional Materials, 2018. **28**(25): p. 1706660.
95. Yu, T., et al., *Microchannels with Self-Pumping Walls.* ACS Nano, 2020. **14**(10): p. 13673-13680.
96. Dong, R., et al., *Highly Efficient Light-Driven TiO2-Au Janus Micromotors.* ACS Nano, 2016. **10**(1): p. 839-44.
97. Wang, L., et al., *Cu@TiO2 Janus microswimmers with a versatile motion mechanism.* Soft Matter, 2018. **14**(34): p. 6969-6973.
98. Jang, B., et al., *Multiwavelength Light-Responsive Au/B-TiO2 Janus Micromotors.* ACS Nano, 2017.

99. Giudicatti, S., et al., *Photoactive rolled-up TiO2 microtubes: fabrication, characterization and applications.* J Mater Chem C Mater Opt Electron Devices, 2014. **2**(29): p. 5892-5901.
100. Mou, F., et al., *Single-Component TiO2 Tubular Microengines with Motion Controlled by Light-Induced Bubbles.* Small, 2015. **11**(21): p. 2564-70.
101. Hong, Y., et al., *Light-Driven Titanium-Dioxide-Based Reversible Microfireworks and Micromotor/Micropump Systems.* Advanced Functional Materials, 2010. **20**(10): p. 1568-1576.
102. Dong, R., et al., *Highly Efficient Light-Driven TiO2–Au Janus Micromotors.* ACS Nano, 2016. **10**(1): p. 839-844.
103. Dai, B., et al., *Programmable artificial phototactic microswimmer.* Nat Nanotechnol, 2016. **11**(12): p. 1087-1092.
104. Zhan, X., et al., *Enhanced ion tolerance of electrokinetic locomotion in polyelectrolyte-coated microswimmer.* Nat Commun, 2019. **10**(1): p. 3921.
105. Dong, R., et al., *ZnO-based microrockets with light-enhanced propulsion.* Nanoscale, 2017. **9**(39): p. 15027-15032.
106. Wolff, N., et al., *Advanced Hybrid GaN/ZnO Nanoarchitectured Microtubes for Fluorescent Micromotors Driven by UV Light.* Small, 2020. **16**(2): p. 1905141.
107. Pourrahimi, A.M., et al., *Catalytic and Light-Driven ZnO/Pt Janus Nano/Micromotors: Switching of Motion Mechanism via Interface Roughness and Defect Tailoring at the Nanoscale.* Advanced Functional Materials, 2019. **29**(22): p. 1808678.
108. Zhou, C., et al., *Photochemically Powered AgCl Janus Micromotors as a Model System to Understand Ionic Self-Diffusiophoresis.* Langmuir, 2018. **34**(10): p. 3289-3295.
109. Zhou, D., et al., *Visible-light controlled catalytic Cu2O-Au micromotors.* Nanoscale, 2017. **9**(1): p. 75-78.
110. Wang, J., et al., *A Silicon Nanowire as a Spectrally Tunable Light-Driven Nanomotor.* Adv Mater, 2017. **29**(30).
111. Zhou, D., et al., *Visible-light driven Si–Au micromotors in water and organic solvents.* Nanoscale, 2017. **9**(32): p. 11434-11438.
112. Wang, X., et al., *High-Motility Visible Light-Driven Ag/AgCl Janus Micromotors.* Small, 2018. **14**(48): p. e1803613.
113. Solovev, A.A., S. Sanchez, and O.G. Schmidt, *Collective behaviour of self-propelled catalytic micromotors.* Nanoscale, 2013. **5**(4): p. 1284-1293.
114. Simmchen, J., et al., *Dynamics of Novel Photoactive AgCl Microstars and Their Environmental Applications.* ChemNanoMat, 2017. **3**(1): p. 65-71.
115. Altemose, A., et al., *Chemically Controlled Spatiotemporal Oscillations of Colloidal Assemblies.* Angewandte Chemie International Edition, 2017. **56**(27): p. 7817-7821.
116. Wang, X., et al., *High-Motility Visible Light-Driven Ag/AgCl Janus Micromotors.* Small, 2018. **14**(48): p. 1803613.
117. Pacheco, M., B. Jurado-Sánchez, and A. Escarpa, *Lab-on-a-micromotor: catalytic Janus particles as mobile microreactors for tailored synthesis of nanoparticles.* Chemical Science, 2018. **9**(42): p. 8056-8064.

118. María Hormigos, R., B. Jurado Sánchez, and A. Escarpa, *Multi-Light-Responsive Quantum Dot Sensitized Hybrid Micromotors with Dual-Mode Propulsion.* Angewandte Chemie International Edition, 2019. **58**(10): p. 3128-3132.
119. Zheng, J., et al., *Orthogonal navigation of multiple visible-light-driven artificial microswimmers.* Nat Commun, 2017. **8**(1): p. 1438.
120. Dai, B., et al., *Programmable artificial phototactic microswimmer.* Nature Nanotechnology, 2016. **11**(12): p. 1087-1092.
121. Kuron, M., P. Kreissl, and C. Holm, *Toward Understanding of Self-Electrophoretic Propulsion under Realistic Conditions: From Bulk Reactions to Confinement Effects.* Accounts of Chemical Research, 2018. **51**(12): p. 2998-3005.
122. Dong, R., et al., *Photocatalytic Micro/Nanomotors: From Construction to Applications.* Acc Chem Res, 2018. **51**(9): p. 1940-1947.
123. Wang, J., et al., *Light-Driven Micro/Nanomotor for Promising Biomedical Tools: Principle, Challenge, and Prospect.* Acc Chem Res, 2018. **51**(9): p. 1957-1965.
124. Luo, M., et al., *Micro-/Nanorobots at Work in Active Drug Delivery.* Advanced Functional Materials, 2018. **28**(25): p. 1706100.
125. Moran, J.L. and J.D. Posner, *Role of solution conductivity in reaction induced charge auto-electrophoresis.* Physics of Fluids, 2014. **26**(4): p. 042001.
126. Wang, Q., et al., *Glucose-Fueled Micromotors with Highly Efficient Visible-Light Photocatalytic Propulsion.* ACS Applied Materials & Interfaces, 2019. **11**(6): p. 6201-6207.
127. Wang, J., et al., *Rational Design of Reversible Redox Shuttle for Highly Efficient Light-Driven Microswimmer.* ACS Nano, 2020. **14**(3): p. 3272-3280.
128. Sridhar, V., B.W. Park, and M. Sitti, *Light-Driven Janus Hollow Mesoporous TiO2-Au Microswimmers.* Advanced Functional Materials, 2018. **28**(25): p. 1704902.
129. Li, Y., et al., *Light-controlled bubble propulsion of amorphous TiO2/Au Janus micromotors.* RSC Adv., 2016. **6**(13): p. 10697-10703.
130. Mou, F., et al., *Light-controlled propulsion, aggregation and separation of water-fuelled TiO2/Pt Janus submicromotors and their "on-the-fly" photocatalytic activities.* Nanoscale, 2016. **8**(9): p. 4976-83.
131. Zhang, Q., et al., *Light-Driven Au-WO3@C Janus Micromotors for Rapid Photodegradation of Dye Pollutants.* ACS Appl Mater Interfaces, 2017.
132. Dong, R., et al., *Visible-Light-Driven BiOI-Based Janus Micromotor in Pure Water.* J Am Chem Soc, 2017.
133. Dai, B., et al., *Programmable artificial phototactic microswimmer.* Nat Nano, 2016. **11**(12): p. 1087-1092.
134. Elham Ghadiri, N.T., Shaik M. Zakeeruddin, Michael Gratzel, and Jacques-E. Moser, *Enhanced Electron Collection Efficiency in Dye-Sensitized Solar Cells Based on Nanostructured TiO2 Hollow Fibers.* Nano Lett. , 2010. **10**: p. 1632–1638.
135. Gao, W., S. Sattayasamitsathit, and J. Wang, *Catalytically propelled micro-/nanomotors: how fast can they move?* The Chemical Record, 2012. **12**(1): p. 224-231.
136. Zhang, Y., et al., *Prolonged Electron Lifetime in Ordered TiO2 Mesophyll Cell-Like Microspheres for Efficient Photocatalytic Water Reduction and Oxidation.* Small, 2016. **12**(17): p. 2291-9.

137. Koo, H.J., et al., *Nano-embossed Hollow Spherical TiO2 as Bifunctional Material for High-Efficiency Dye-Sensitized Solar Cells.* Advanced Materials, 2008. **20**(1): p. 195-199.
138. Shiraishi, Y., N. Saito, and T. Hirai, *Adsorption-Driven Photocatalytic Activity of Mesoporous Titanium Dioxide.* Journal of the American Chemical Society, 2005. **127**(37): p. 12820-12822.
139. Lou, X.W., L.A. Archer, and Z. Yang, *Hollow Micro-/Nanostructures: Synthesis and Applications.* Advanced Materials, 2008. **20**(21): p. 3987-4019.
140. Pan, J.H., et al., *Self-Etching Reconstruction of Hierarchically Mesoporous F-TiO2 Hollow Microspherical Photocatalyst for Concurrent Membrane Water Purifications.* Journal of the American Chemical Society, 2008. **130**(34): p. 11256-11257.
141. Pang, H., et al., *Nanoparticle self-assembled hollow TiO2 spheres with well matching visible light scattering for high performance dye-sensitized solar cells.* Chemical Communications, 2012. **48**(70): p. 8832-8834.
142. Yao, Y., et al., *Broadband light management using low-Q whispering gallery modes in spherical nanoshells.* 2012. **3**: p. 664.
143. Jiang, X., T. Herricks, and Y. Xia, *Monodispersed Spherical Colloids of Titania: Synthesis, Characterization, and Crystallization.* Advanced Materials, 2003. **15**(14): p. 1205-1209.
144. S. Eiden-Assmann, J.W., and G. Maret, *Synthesis and Characterization of Porous and Nonporous Monodisperse Colloidal TiO2 Particles.* Chem. Mater 2004. **16**(1): p. 6-11.
145. Yang, D., et al., *An external template-free route to uniform semiconducting hollow mesospheres and their use in photocatalysis.* Nanoscale, 2015. **7**(30): p. 12990-12997.
146. Kim, D.S., S.J. Han, and S.Y. Kwak, *Synthesis and photocatalytic activity of mesoporous TiO(2) with the surface area, crystallite size, and pore size.* J Colloid Interface Sci, 2007. **316**(1): p. 85-91.
147. Wu, Y., et al., *Dye-Enhanced Self-Electrophoretic Propulsion of Light-Driven TiO2–Au Janus Micromotors.* Nano-Micro Letters, 2017. **9**(3): p. 30.
148. Wang, H., et al., *Semiconductor heterojunction photocatalysts: design, construction, and photocatalytic performances.* Chem Soc Rev, 2014. **43**(15): p. 5234-44.
149. Bannat, I., et al., *Improving the Photocatalytic Performance of Mesoporous Titania Films by Modification with Gold Nanostructures.* Chemistry of Materials, 2009. **21**(8): p. 1645-1653.
150. Wang, H., et al., *Mesoporous Au/TiO2 composites preparation, characterization, and photocatalytic properties.* Materials Science and Engineering: B, 2012. **177**(11): p. 913-919.
151. Xuan, M., et al., *Near Infrared Light-Powered Janus Mesoporous Silica Nanoparticle Motors.* J Am Chem Soc, 2016. **138**(20): p. 6492-7.
152. Zheng-Hui Ren, H.-T.L., Qiang Gao ,Hao Wang ,Bo Han , Kai-Sheng Xia , Cheng-Gang Zhou *Au nanoparticles embedded on urchin-like TiO2 nanosphere: An efficient catalyst for dyes degradation and 4-nitrophenol reduction.* Materials and Design, 2017. **121**: p. 167-175.
153. Parmar, J., et al., *Reusable and Long-Lasting Active Microcleaners for Heterogeneous Water Remediation.* Advanced Functional Materials, 2016. **26**(23): p. 4152-4161.

154. Park, B.-W., et al., *Multifunctional Bacteria-Driven Microswimmers for Targeted Active Drug Delivery.* ACS Nano, 2017. **11**(9): p. 8910-8923.
155. Yang, P., S. Gai, and J. Lin, *Functionalized mesoporous silica materials for controlled drug delivery.* Chemical Society Reviews, 2012. **41**(9): p. 3679-3698.
156. Chen, Y., et al., *Hollow/Rattle-Type Mesoporous Nanostructures by a Structural Difference-Based Selective Etching Strategy.* ACS Nano, 2010. **4**(1): p. 529-539.
157. Ren, W., et al., *Enhanced doxorubicin transport to multidrug resistant breast cancer cells via TiO2 nanocarriers.* RSC Advances, 2013. **3**(43): p. 20855-20861.
158. Yin, M., et al., *Upconverting Nanoparticles with a Mesoporous TiO2 Shell for Near-Infrared-Triggered Drug Delivery and Synergistic Targeted Cancer Therapy.* Chemistry – A European Journal, 2014. **20**(43): p. 14012-14017.
159. Sridhar, V., et al., *Multiwavelength-Steerable Visible-Light-Driven Magnetic CoO–TiO2 Microswimmers.* ACS Applied Materials & Interfaces, 2020. **12**(21): p. 24149-24155.
160. Carlsen, R.W. and M. Sitti, *Bio-hybrid cell-based actuators for microsystems.* Small, 2014. **10**(19): p. 3831-3851.
161. Hosseinidoust, Z., et al., *Bioengineered and biohybrid bacteria-based systems for drug delivery.* Advanced Drug Delivery Reviews, 2016. **106**: p. 27-44.
162. Wang, J., et al., *Light-Driven Micro/Nanomotor for Promising Biomedical Tools: Principle, Challenge, and Prospect.* Accounts of Chemical Research, 2018. **51**(9): p. 1957-1965.
163. Wang, X., et al., *Fuel-Free Nanocap-Like Motors Actuated Under Visible Light.* Advanced Functional Materials, 2018. **28**(25): p. 1705862.
164. O'Neel-Judy, É., et al., *Light-Activated, Multi-Semiconductor Hybrid Microswimmers.* Small, 2018. **14**(32): p. 1801860.
165. Jang, B., et al., *Multiwavelength Light-Responsive Au/B-TiO2 Janus Micromotors.* ACS Nano, 2017. **11**(6): p. 6146-6154.
166. Zhou, C., et al., *Photochemically Excited, Pulsating Janus Colloidal Motors of Tunable Dynamics.* ACS Nano, 2019. **13**(4): p. 4064-4072.
167. Dong, R., et al., *Visible-Light-Driven BiOI-Based Janus Micromotor in Pure Water.* J Am Chem Soc, 2017. **139**(5): p. 1722-1725.
168. Villa, K., et al., *Visible-Light-Driven Single-Component BiVO4 Micromotors with the Autonomous Ability for Capturing Microorganisms.* ACS Nano, 2019. **13**(7): p. 8135-8145.
169. Mallick, A. and S. Roy, *Visible light driven catalytic gold decorated soft-oxometalate (SOM) based nanomotors for organic pollutant remediation.* Nanoscale, 2018. **10**(26): p. 12713-12722.
170. Maria Hormigos, R., B. Jurado Sanchez, and A. Escarpa, *Multi-Light-Responsive Quantum Dot Sensitized Hybrid Micromotors with Dual-Mode Propulsion.* Angew Chem Int Ed Engl, 2019. **58**(10): p. 3128-3132.
171. Pacheco, M., B. Jurado-Sanchez, and A. Escarpa, *Visible-Light-Driven Janus Microvehicles in Biological Media.* Angew Chem Int Ed Engl, 2019. **58**(50): p. 18017-18024.

172. Zheng, J., et al., *Full Spectrum Tunable Visible-Light-Driven Alloy Nanomotor.* Advanced Functional Materials, 2019. **29**(27): p. 1901768.
173. Tong, J., et al., *Visible-Light-Driven Water-Fueled Ecofriendly Micromotors Based on Iron Phthalocyanine for Highly Efficient Organic Pollutant Degradation.* Langmuir, 2019.
174. Wang, H. and M. Pumera, *Emerging materials for the fabrication of micro/nanomotors.* Nanoscale, 2017. **9**(6): p. 2109-2116.
175. Liao, L., et al., *Efficient solar water-splitting using a nanocrystalline CoO photocatalyst.* Nat Nanotechnol, 2014. **9**(1): p. 69-73.
176. Park, K.-W. and A.M. Kolpak, *Mechanism for spontaneous oxygen and hydrogen evolution reactions on CoO nanoparticles.* Journal of Materials Chemistry A, 2019. **7**(12): p. 6708-6719.
177. Zhang, J., et al., *Porous TiO2 Nanotubes with Spatially Separated Platinum and CoOx Cocatalysts Produced by Atomic Layer Deposition for Photocatalytic Hydrogen Production.* Angew Chem Int Ed Engl, 2017. **56**(3): p. 816-820.
178. Shi, W., et al., *New Insight of Water-Splitting Photocatalyst: H2O2-Resistance Poisoning and Photothermal Deactivation in Sub-micrometer CoO Octahedrons.* ACS Applied Materials & Interfaces, 2017. **9**(24): p. 20585-20593.
179. Gaya, U.I. and A.H. Abdullah, *Heterogeneous photocatalytic degradation of organic contaminants over titanium dioxide: A review of fundamentals, progress and problems.* Journal of Photochemistry and Photobiology C: Photochemistry Reviews, 2008. **9**(1): p. 1-12.
180. Zhan, X., et al., *Efficient CoO nanowire array photocatalysts for H2 generation.* Applied Physics Letters, 2014. **105**(15).
181. Ramakrishnan, V., et al., *Cobalt oxide nanoparticles on TiO2 nanorod/FTO as a photoanode with enhanced visible light sensitization.* RSC Advances, 2016. **6**(12): p. 9789-9795.
182. Savio, A.K.P.D., et al., *Environmentally effective photocatalyst CoO–TiO 2 synthesized by thermal precipitation of Co in amorphous TiO 2.* Applied Catalysis B: Environmental, 2016. **182**: p. 449-455.
183. Ngo, T.Q., et al., *Atomic layer deposition of photoactive CoO/SrTiO3 and CoO/TiO2 on Si(001) for visible light driven photoelectrochemical water oxidation.* Journal of Applied Physics, 2013. **114**(8).
184. Risbud, A.S., et al., *Wurtzite CoO.* Chemistry of Materials, 2005. **17**(4): p. 834-838.
185. Safdar, M., J. Simmchen, and J. Jänis, *Light-driven micro- and nanomotors for environmental remediation.* Environmental Science: Nano, 2017. **4**(8): p. 1602-1616.
186. Zhang, J., et al., *Porous TiO2 Nanotubes with Spatially Separated Platinum and CoOx Cocatalysts Produced by Atomic Layer Deposition for Photocatalytic Hydrogen Production.* Angewandte Chemie International Edition, 2017. **56**(3): p. 816-820.
187. Zhang, G., et al., *Enhanced photocatalytic activity of CoO/TiO2 nanotube composite.* Electrochimica Acta, 2012. **81**: p. 117-122.
188. Savio, A.K.P.D., et al., *Environmentally effective photocatalyst CoO–TiO2 synthesized by thermal precipitation of Co in amorphous TiO2.* Applied Catalysis B: Environmental, 2016. **182**: p. 449-455.

189. Brown, A.T., et al., *Ionic screening and dissociation are crucial for understanding chemical self-propulsion in polar solvents.* Soft Matter, 2017. **13**(6): p. 1200-1222.
190. Zhan, X., et al., *From Strong Dichroic Nanomotor to Polarotactic Microswimmer.* Adv Mater, 2019. **31**(48): p. e1903329.
191. Shi, H. and X. He, *Large-scale synthesis and magnetic properties of cubic CoO nanoparticles.* Journal of Physics and Chemistry of Solids, 2012. **73**(5): p. 646-650.
192. Simoncelli, S., et al., *Combined Optical and Chemical Control of a Microsized Photofueled Janus Particle.* Small, 2016. **12**(21): p. 2854-8.
193. Chen, X., C. Zhou, and W. Wang, *Colloidal Motors 101: A Beginner's Guide to Colloidal Motor Research.* Chem Asian J, 2019. **14**(14): p. 2388-2405.
194. You, M., et al., *Intelligent Micro/nanomotors with Taxis.* Acc Chem Res, 2018. **51**(12): p. 3006-3014.
195. Wang, Y., X. Wang, and M. Antonietti, *Polymeric graphitic carbon nitride as a heterogeneous organocatalyst: from photochemistry to multipurpose catalysis to sustainable chemistry.* Angew Chem Int Ed Engl, 2012. **51**(1): p. 68-89.
196. Cui, Y., et al., *Metal-free activation of H2O2 by g-C3N4 under visible light irradiation for the degradation of organic pollutants.* Physical Chemistry Chemical Physics, 2012. **14**(4): p. 1455-1462.
197. Lotsch, B.V., et al., *Unmasking Melon by a Complementary Approach Employing Electron Diffraction, Solid-State NMR Spectroscopy, and Theoretical Calculations—Structural Characterization of a Carbon Nitride Polymer.* Chemistry – A European Journal, 2007. **13**(17): p. 4969-4980.
198. Lau, V.W.-h., et al., *Rational design of carbon nitride photocatalysts by identification of cyanamide defects as catalytically relevant sites.* Nature Communications, 2016. **7**: p. 12165.
199. Ye, Z., et al., *A phototactic micromotor based on platinum nanoparticle decorated carbon nitride.* Nanoscale, 2017. **9**(46): p. 18516-18522.
200. Villa, K., et al., *Metal-Free Visible-Light Photoactivated C3N4 Bubble-Propelled Tubular Micromotors with Inherent Fluorescence and On/Off Capabilities.* ACS Nano, 2018. **12**(12): p. 12482-12491.
201. Sridhar, V., et al., *Carbon nitride-based light-driven microswimmers with intrinsic photocharging ability.* Proceedings of the National Academy of Sciences, 2020. **117**(40): p. 24748.
202. M.Sitti, *Mobile microrobotics.* MIT Press, Cambridge, MA, 2017.
203. Uspal, W.E., *Theory of light-activated catalytic Janus particles.* J Chem Phys, 2019. **150**(11): p. 114903.
204. Schlomberg, H., et al., *Structural Insights into Poly(Heptazine Imides): A Light-Storing Carbon Nitride Material for Dark Photocatalysis.* Chemistry of Materials, 2019. **31**(18): p. 7478-7486.
205. Markushyna, Y., et al., *Green radicals of potassium poly(heptazine imide) using light and benzylamine.* Journal of Materials Chemistry A, 2019. **7**(43): p. 24771-24775.
206. Lau, V.W.-h., et al., *Dark Photocatalysis: Storage of Solar Energy in Carbon Nitride for Time-Delayed Hydrogen Generation.* Angew Chem Int Ed Engl, 2017. **56**(2): p. 510-514.

207. Podjaski, F., J. Kroger, and B.V. Lotsch, *Toward an Aqueous Solar Battery: Direct Electrochemical Storage of Solar Energy in Carbon Nitrides.* Adv Mater, 2018. **30**(9): p. 1705477.
208. Savateev, A., et al., *Potassium Poly(heptazine imides) from Aminotetrazoles: Shifting Band Gaps of Carbon Nitride-like Materials for More Efficient Solar Hydrogen and Oxygen Evolution.* Chemcatchem, 2017. **9**(1): p. 167-174.
209. Savateev, A., et al., *Highly crystalline poly(heptazine imides) by mechanochemical synthesis for photooxidation of various organic substrates using an intriguing electron acceptor – Elemental sulfur.* Journal of Catalysis, 2017. **350**: p. 203-211.
210. Kasap, H., et al., *Solar-Driven Reduction of Aqueous Protons Coupled to Selective Alcohol Oxidation with a Carbon Nitride–Molecular Ni Catalyst System.* Journal of the American Chemical Society, 2016. **138**(29): p. 9183-9192.
211. Wang, X., et al., *Fuel-Free Nanocap-Like Motors Actuated Under Visible Light.* Advanced Functional Materials, 2018. **28**(25): p. 1705862.
212. Rahman, M.Z., et al., *A Benchmark Quantum Yield for Water Photoreduction on Amorphous Carbon Nitride.* Advanced Functional Materials, 2017. **27**(39): p. 1702384.
213. Nosaka, Y. and A.Y. Nosaka, *Generation and Detection of Reactive Oxygen Species in Photocatalysis.* Chemical Reviews, 2017. **117**(17): p. 11302-11336.
214. Schneider, J.B., D.; Ye, J.; Puma, G. L.; Dionysiou, D. D., Eds., *Photocatalysis: Fundamentals and Perspectives*. Royal Society of Chemistry: Cambridge. 2016. - 436.
215. Park, H., et al., *Photoinduced charge transfer processes in solar photocatalysis based on modified TiO2.* Energy & Environmental Science, 2016. **9**(2): p. 411-433.
216. Kang, U., et al., *Photosynthesis of formate from CO2 and water at 1% energy efficiency via copper iron oxide catalysis.* Energy & Environmental Science, 2015. **8**(9): p. 2638-2643.
217. Wardman, P., *Reduction Potentials of One-Electron Couples Involving Free Radicals in Aqueous Solution.* 1989. **18**(4): p. 1637-1755.
218. Evans, D.F. and M.W. Upton, *Studies on singlet oxygen in aqueous solution. Part 1. Formation of singlet oxygen from hydrogen peroxide with two-electron oxidants.* Journal of the Chemical Society, Dalton Transactions, 1985(6): p. 1141-1145.
219. Dey, S., et al., *Molecular electrocatalysts for the oxygen reduction reaction.* Nature Reviews Chemistry, 2017. **1**(12): p. 0098.
220. Lau, V.W.-h., et al., *Low-Molecular-Weight Carbon Nitrides for Solar Hydrogen Evolution.* Journal of the American Chemical Society, 2015. **137**(3): p. 1064-1072.
221. McKee, D.W., *Catalytic decomposition of hydrogen peroxide by metals and alloys of the platinum group.* Journal of Catalysis, 1969. **14**(4): p. 355-364.
222. Chen, Z., H. Dinh, and E. Miller, *Photoelectrochemical water splitting*. 2013: Springer publishing house New York. 124.
223. Yi, J., et al., *Photocatalytic Decomposition of H2O2 on Different TiO2 Surfaces Along with the Concurrent Generation of HO2 Radicals Monitored Using Cavity Ring Down Spectroscopy.* The Journal of Physical Chemistry C, 2012. **116**(18): p. 10090-10097.
224. Wang, W., et al., *Understanding the Efficiency of Autonomous Nano- and Microscale Motors.* Journal of the American Chemical Society, 2013. **135**(28): p. 10557-10565.

225. Alapan, Y., et al., *Microrobotics and Microorganisms: Biohybrid Autonomous Cellular Robots.* 2019. **2**(1): p. 205-230.
226. Luo, M., et al., *Micro-/Nanorobots at Work in Active Drug Delivery.* 2018. **28**(25): p. 1706100.
227. Ma, X. and S. Sánchez, *Self-propelling micro-nanorobots: challenges and future perspectives in nanomedicine.* Nanomedicine, 2017. **12**(12): p. 1363-1367.
228. Li, J., et al., *Micro/nanorobots for biomedicine: Delivery, surgery, sensing, and detoxification.* Science Robotics, 2017. **2**(4): p. eaam6431.
229. de Ávila, B.E.-F., et al., *Micromotor-enabled active drug delivery for in vivo treatment of stomach infection.* Nature Communications, 2017. **8**(1): p. 272.
230. Wu, Z., et al., *A microrobotic system guided by photoacoustic computed tomography for targeted navigation in intestines in vivo.* Science Robotics, 2019. **4**(32): p. eaax0613.
231. Wang, J. and W. Gao, *Nano/Microscale Motors: Biomedical Opportunities and Challenges.* ACS Nano, 2012. **6**(7): p. 5745-5751.
232. Gao, W., et al., *Artificial Micromotors in the Mouse's Stomach: A Step toward in Vivo Use of Synthetic Motors.* ACS Nano, 2015. **9**(1): p. 117-123.
233. Llopis-Lorente, A., et al., *Enzyme-Powered Gated Mesoporous Silica Nanomotors for On-Command Intracellular Payload Delivery.* ACS Nano, 2019. **13**(10): p. 12171-12183.
234. Hortelão, A.C., et al., *Enzyme-Powered Nanobots Enhance Anticancer Drug Delivery.* Advanced Functional Materials, 2018. **28**(25): p. 1705086.
235. Zhang, D., et al., *A phototactic liquid micromotor.* Journal of Materials Chemistry C, 2018. **6**(45): p. 12234-12239.
236. Kong, L., et al., *Photocatalytic Micromotors Activated by UV to Visible Light for Environmental Remediation, Micropumps, Reversible Assembly, Transportation, and Biomimicry.* Small, 2019: p. e1903179.
237. Uspal, W.E., *Theory of light-activated catalytic Janus particles.* 2019. **150**(11): p. 114903.
238. Moran, J.L. and J.D. Posner, *Role of solution conductivity in reaction induced charge auto-electrophoresis.* 2014. **26**(4): p. 042001.
239. Brown, A. and W. Poon, *Ionic effects in self-propelled Pt-coated Janus swimmers.* Soft Matter, 2014. **10**(22): p. 4016-4027.
240. Sridhar, V., B.-W. Park, and M. Sitti, *Light-Driven Janus Hollow Mesoporous TiO2–Au Microswimmers.* 2018. **28**(25): p. 1704902.
241. Wang, X., et al., *Fuel-Free Nanocap-Like Motors Actuated Under Visible Light.* 2018. **28**(25): p. 1705862.
242. Wang, J., et al., *A Silicon Nanowire as a Spectrally Tunable Light-Driven Nanomotor.* 2017. **29**(30): p. 1701451.
243. Gibbs, J.G., *Shape- and Material-Dependent Self-Propulsion of Photocatalytic Active Colloids, Interfacial Effects, and Dynamic Interparticle Interactions.* Langmuir, 2019.
244. Wei, M., et al., *Catalytic Micromotors Moving Near Polyelectrolyte-Modified Substrates: The Roles of Surface Charges, Morphology, and Released Ions.* ACS Applied Materials & Interfaces, 2018. **10**(3): p. 2249-2252.

245. Palacci, J., et al., *Light-activated self-propelled colloids.* Philos Trans A Math Phys Eng Sci, 2014. **372**(2029).
246. Aziz, A., et al., *Medical Imaging of Microrobots: Toward In Vivo Applications.* ACS Nano, 2020. **14**(9): p. 10865-10893.
247. Wang, X., et al., *A metal-free polymeric photocatalyst for hydrogen production from water under visible light.* Nature Materials, 2009. **8**(1): p. 76-80.
248. Ong, W.-J., et al., *Graphitic Carbon Nitride (g-C3N4)-Based Photocatalysts for Artificial Photosynthesis and Environmental Remediation: Are We a Step Closer To Achieving Sustainability?* Chemical Reviews, 2016. **116**(12): p. 7159-7329.
249. Xiao, K., et al., *Artificial light-driven ion pump for photoelectric energy conversion.* Nature Communications, 2019. **10**(1): p. 74.
250. Savateev, A., et al., *Towards Organic Zeolites and Inclusion Catalysts: Heptazine Imide Salts Can Exchange Metal Cations in the Solid State.* Chemistry – An Asian Journal, 2017. **12**(13): p. 1517-1522.
251. Podjaski, F. and B.V. Lotsch, *Optoelectronics Meets Optoionics: Light Storing Carbon Nitrides and Beyond.* Advanced Energy Materials, 2021. **11**(4): p. 2003049.
252. Kröger, J., et al., *Interfacial Engineering for Improved Photocatalysis in a Charge Storing 2D Carbon Nitride: Melamine Functionalized Poly(heptazine imide).* Advanced Energy Materials, 2020. **n/a**(n/a): p. 2003016.
253. Sridhar, V., et al., *Carbon nitride-based light-driven microswimmers with intrinsic photocharging ability.* Proceedings of the National Academy of Sciences, 2020: p. 202007362.
254. Lau, V.W.-h., et al., *Dark Photocatalysis: Storage of Solar Energy in Carbon Nitride for Time-Delayed Hydrogen Generation.* 2017. **56**(2): p. 510-514.
255. Thommes, M., et al., *Physisorption of gases, with special reference to the evaluation of surface area and pore size distribution (IUPAC Technical Report).* Pure and Applied Chemistry, 2015. **87**(9-10): p. 1051-1069.
256. Honn, K.V., J.A. Singley, and W. Chavin, *Fetal Bovine Serum: A Multivariate Standard.* Proceedings of the Society for Experimental Biology and Medicine, 1975. **149**(2): p. 344-347.
257. Singh, M. and N.A. Coulter, *Rheology of blood: Effect of dilution with various dextrans.* Microvascular Research, 1973. **5**(2): p. 123-130.
258. Qin, H., et al., *Light actuated swarming and breathing-like motion of graphene oxide colloidal particles.* Communications Chemistry, 2018. **1**(1): p. 72.
259. Karshalev, E., B. Esteban-Fernández de Ávila, and J. Wang, *Micromotors for "Chemistry-on-the-Fly".* Journal of the American Chemical Society, 2018. **140**(11): p. 3810-3820.
260. Podjaski, F., J. Kröger, and B.V. Lotsch, *Toward an Aqueous Solar Battery: Direct Electrochemical Storage of Solar Energy in Carbon Nitrides.* 2018. **30**(9): p. 1705477.
261. Xing, W., et al., *1 - Oxygen Solubility, Diffusion Coefficient, and Solution Viscosity*, in *Rotating Electrode Methods and Oxygen Reduction Electrocatalysts*, W. Xing, G. Yin, and J. Zhang, Editors. 2014, Elsevier: Amsterdam. p. 1-31.
262. Brown, J.M., *The Hypoxic Cell.* A Target for Selective Cancer Therapy—Eighteenth Bruce F. Cain Memorial Award Lecture, 1999. **59**(23): p. 5863-5870.

263. Hu, Y., W. Liu, and Y. Sun, *Multiwavelength Phototactic Micromotor with Controllable Swarming Motion for "Chemistry-on-the-Fly".* ACS Applied Materials & Interfaces, 2020. **12**(37): p. 41495-41505.
264. Hao, D., et al., *Bifunctional Fabric with Photothermal Effect and Photocatalysis for Highly Efficient Clean Water Generation.* ACS Sustainable Chemistry & Engineering, 2018. **6**(8): p. 10789-10797.
265. Bryant, S.J., C.R. Nuttelman, and K.S. Anseth, *Cytocompatibility of UV and visible light photoinitiating systems on cultured NIH/3T3 fibroblasts in vitro.* Journal of Biomaterials Science, Polymer Edition, 2000. **11**(5): p. 439-457.
266. Gao, Y., et al., *Controlled Intracellular Release of Doxorubicin in Multidrug-Resistant Cancer Cells by Tuning the Shell-Pore Sizes of Mesoporous Silica Nanoparticles.* ACS Nano, 2011. **5**(12): p. 9788-9798.
267. Calza, P., et al., *Photocatalytic degradation of selected anticancer drugs and identification of their transformation products in water by liquid chromatography–high resolution mass spectrometry.* Journal of Chromatography A, 2014. **1362**: p. 135-144.
268. Douplik, A., et al., *3 - The response of tissue to laser light*, in *Lasers for Medical Applications*, H. Jelínková, Editor. 2013, Woodhead Publishing. p. 47-109.
269. Erin, O., et al., *Magnetic Resonance Imaging System–Driven Medical Robotics.* Advanced Intelligent Systems, 2020. **2**(2): p. 1900110.
270. Giltinan, J., et al., *3D Microprinting of Iron Platinum Nanoparticle-Based Magnetic Mobile Microrobots.* Advanced Intelligent Systems, 2021. **3**(1): p. 2000204.
271. Wang, H. and M. Pumera, *Fabrication of Micro/Nanoscale Motors.* Chemical Reviews, 2015. **115**(16): p. 8704-8735.
272. Kaliyaraj Selva Kumar, A., et al., *A mini-review: How reliable is the drop casting technique?* Electrochemistry Communications, 2020. **121**: p. 106867.